THE GYRACC

AN INTEGRATED SENSOR FOR 3D RATE OF TURN AND ACCELERATION

BEREND JAN KOOI

Samenstelling promotie commissie:

voorzitter	
Prof. dr. ir. A.J. Mouthaan	Universiteit Twente
promotoren	
Prof. dr. ir. P. Bergveld	Universiteit Twente
Prof. dr. ir. P. H. Veltink	Universiteit Twente
assistent promotor	
Dr. ir. W. Olthuis	Universiteit Twente
leden	
Prof. dr. N.F. de Rooij	University of Neuchâtel
Prof. dr. P.J. French	TU Delft
Prof. dr. M.C. Elwenspoek	Universiteit Twente
Prof. dr. F.C.T. van der Helm	Universiteit Twente

The research described in this thesis was funded by the Dutch Technology Foundation (STW) project: TEL.4167. The research was carried out at the Sensor systems for Biomedical and Environmental applications group (BIOS), of the MESA$^+$ research institute, University of Twente.

Title: The Gyracc, an integrated sensor for 3D rate of turn and acceleration.

Author: Berend Jan Kooi (Bart)

ISBN: 90-365-2219-6

Cover : The Gyracc sensor, artist impression by Sebastiaan Herber.

Printed by Wöhrmann Print Service, Zutphen

THE GYRACC
AN INTEGRATED SENSOR FOR 3D RATE OF TURN AND ACCELERATION

PROEFSCHRIFT

ter verkrijging van
de graad van doctor aan de Universiteit Twente,
op gezag van de rector magnificus,
prof. dr. W.H.M. Zijm,
volgens besluit van het College voor Promoties
in het openbaar te verdedigen
op donderdag 23 juni 2005 om 16.45 uur

door

Berend Jan Kooi
geboren op 18 augustus 1970
te Slochteren

Dit proefschrift is goedgekeurd door:

de promotoren:	Prof. dr. ir. Piet Bergveld
	Prof. dr. ir. Peter H. Veltink
de assistent-promotor:	Dr. ir. Wouter Olthuis

Voor pap, mam en Ard

1 Introduction 1
1.1 The biological 3D inertial sensor 1
1.2 The man-made 3D inertial sensor 2
1.3 Motivation for developing a new IMU 2
1.4 Possible application areas for the Gyracc 4
1.5 Outline of this thesis 5
1.6 References 5
2 Gyroscopes - An overview 7
2.1 Introduction 7
2.2 Gyroscope principles 8
2.3 Essential gyroscope performance parameters 17
2.4 Commercially available Coriolis-based rate of turn sensors 18
2.5 Transduction in Coriolis-based rate of turn sensors 18
2.6 Coriolis-based rate of turn sensors in open literature 22
2.7 The Gyracc 30
2.8 Conclusions 32
2.9 References 32
3 Operating principle of the Gyracc 35
3.1 Introduction 35
3.2 The mass-spring-damper system 46
3.3 The Coriolis effect 49
3.4 Combined acceleration and rate of turn measurement 51
3.5 Uniaxial rate of turn detection 54
3.6 Multiple axis rate of turn detection 55
3.7 Cross-axis movement of the mass 57
3.8 The output signal of the sensor 58
3.9 Conclusions 66
3.10 References 67
Appendix Closed box damping estimation 69
A.1 Simplified structure 69
A.2 Simulation results 70
A.3 References 72
4 The actuator 73
4.1 The maximum actuation force 73
4.2 The optimal spring constant in the Gyracc 74
4.3 Electrostatic actuation of the seismic mass 74
4.4 Electromagnetic actuation of the seismic mass 79

4.5 The actuation force of the E-core electromagnet 86
4.6 Conclusions 94
4.7 References 95
5 Simulations of Gyracc behavior 97
5.1 Introduction 97
5.2 The simulation parameters 98
5.3 Single axis simulation 99
5.4 The Coriolis simulation 106
5.5 Triaxial simulation 113
5.6 Conclusions 116
5.7 References 117
6 Design and realization 119
6.1 Inertial sensor structure 119
6.2 The electromagnet 120
6.3 The original triaxial accelerometer 121
6.4 Sensor box with pre-defined dimensions 123
6.5 Dimension-tolerant sensor box design 127
6.6 Conclusions 135
6.7 References 136
7 Measurements on the Gyracc 137
7.1 Characterization of the electronic measurement system 137
7.2 Acceleration measurements 139
7.3 Actuation of the mass 142
7.4 Rate of turn measurements 151
7.5 Conclusions 161
7.6 References 162
8 Conclusions and suggestions for further research 163
8.1 Conclusions 163
8.2 Suggestions for future research 167
Summary 169
Samenvatting 171
Dankwoord 173
About the author 177

Chapter 1

1 INTRODUCTION

The whereabouts of an object with respect to a certain reference is of interest in many applications. If one is interested in the position and orientation of an object in the 3 dimensional space during a specific span of time without continuously having the availability of a fixed reference, then its position and orientation can be predicted by means of integrating the linear- and angular motions in the 3 dimensional space over the period of measurement.

1.1 The biological 3D inertial sensor

The human being owns an organ that senses movement of the head by means of the inertial properties of mass. This organ is called the vestibular system and is located in the inner ear. It is able to detect angular motion (rotation) as well as linear acceleration, see figure 1-1.

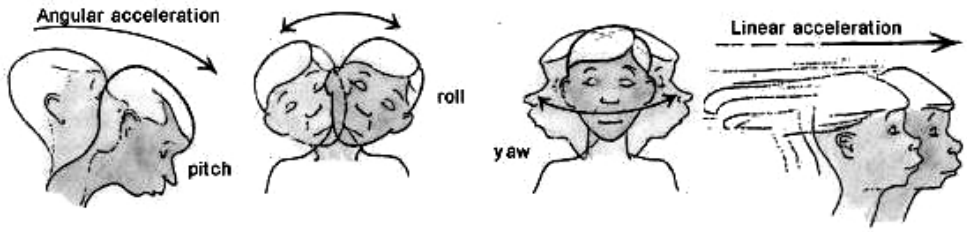

Figure 1-1: Definitions of the motions of the head.

With the knowledge of the motion of the head one is able to maintain balance and to stabilize the eyes relative to the environment.

Figure 1-2 shows that the vestibular system comprises 3 semicircular canals and 5 sense-organs, 3 ampullae, the utricle and the saccule respectively.

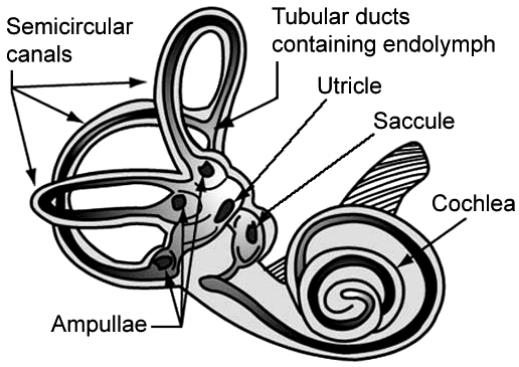

Figure 1-2: The vestibular system with the semicircular canals and sense-organs.

The three semi-circular canals are positioned roughly at right angles with respect to each other and detect any kind of rotational motion of the head. The canals react when we nod in an up and down motion (pitch), when we tilt our head towards our shoulders (roll), and when we shake our head in a side to side motion (yaw).

The semi-circular canals are filled with a liquid called endolymph. When a semicircular canal experiences a rotation around its central axis then inertia causes the endolyph to flow along the inner walls of the semi-circular canals. Each semi-circular canal contains an ampulla (organ) with hairs on top. The flow of the endolymph with respect to the inner canal walls induces the bending of the hairs on top of the ampullae. The bending of the hairs is transferred in to a signal that the brains interpret as a rotation.

Linear accelerations of the head are detected by means of the organs called utricle and saccule. The inside walls of the utricle as well as the saccule contain a bed of several thousand hair cells covered by small flat piles of calcium carbonate crystals imbedded in a gel-like substance. When the head experiences acceleration the gel substance will displace and makes the hairs to bend, resulting in a signal that the brains interpret as a linear acceleration.

The head is the only part of the human body in which such a sophisticated movement detection system is available for posture control. The position and movement of the other elements of the body (with respect to the head) is determined by the eyes and by interpreting the sensed muscle length and its derivative.

1.2 The man-made 3D inertial sensor

A man-made sensor which has the same sensing properties as the vestibular system would be valuable for many applications [1]. Applications in the medical field include human movement analysis, artificial feedback in human motor control and virtual reality. Other possible applications involve navigation of cars, missiles and airplanes.

A sensing system based on inertial sensors, which is able to measure movements in the 6 degrees of freedom, is called an Inertial Measurement Unit (IMU). In practice an IMU consists of rate of turn sensors and accelerometers which are mounted very close together, in one point ideally. An IMU fixed on an object, in combination with signal interpretation, will be able to predict the orientation and position of a moving object.

1.3 Motivation for developing a new IMU

Biomechanical engineering departments at the University of Twente are involved in movement analyses of human body posture control. In the 90's posture control was mainly analyzed in optical gait analysis laboratories. A gait analysis

laboratory consists of a designated area in which the movement of the person under investigation can be measured continuously. The movement of the person is registered by means of infrared cameras which are positioned at fixed positions around the designated area, whereas the person carries markers which reflect the infrared light of an infrared source. The information from the cameras is processed by means of a dedicated gait analysis computer. Such a measurement system is expensive and can only be used in the restricted area.
Lately small reliable inertial sensors have become commercially available and are combined into a single package resulting in an IMU. Currently commercial IMUs with outer dimensions of approximately 4x5x3 cm^3 are available with one digital output that represents the 6 degrees of freedom [2]. These small IMUs can be used in ambulatory systems, which opens the possibility to perform posture control measurements independently of restricted areas. IMUs are for instance used in the control loop of a drop-foot stimulator [3].

The following two criteria withhold the miniature IMUs from being the ideal biomechanical measurement system:
1. The inaccuracy in the signal from the sensing elements, which results in a discrepancy between the predicted and the actual position of the moving object.
2. The size of IMUs is still unpractical for external use and far too large for implantation in humans.

Ad1. In the biomechanical group of Prof. Dr. Ir. P.H. Veltink algorithms have been developed to reduce the amount of error built up in time by combining the information from the six sensor signals that represent the six degrees of freedom. This resulted in an estimate of the 3D orientation of the IMU. These algorithms, which are Kalman filter-based, were implemented by Dr. Ir. H.J. Luinge and provide an optimal estimate of 3D orientation. Luinge developed a stochastic sensor model, based on the physical relations between relevant kinematic variables, 3D orientation, angular velocity, acceleration and the sensor signals [4,5,6,7]. The performance of these algorithms has been evaluated in functional human movements by comparing the estimated orientation with measurements performed by a state-of-the-art optical measurement system regularly used in human movement laboratories. The IMU based measurements provided a nearly drift-free and accurate estimate of inclination, but had remaining drift in the estimate of heading. A 3D magnetic sensor system (electronic compass) was subsequently integrated with the IMU system, providing a more drift-free and accurate estimate of 3D orientation. Currently, this procedure is extended to on-body estimation of relative positions. Application development of this technology is performed in corporation with Roessingh Research and Development. The research results have been transferred to the company Xsens, a start-up company of the University of Twente. Xsens produces inertial sensor modules and related measurement and analysis systems. The sensors in their program are a purely inertial sensor

module (MT6) and an inertial sensing module that is extended with magnetic field sensors (MT9).

Ad2. In the biosensors group of Prof. Dr. Ir. P. Bergveld a first step to decreasing the size of the IMU was performed by Dr. Ir. J.C. Lötters. He was able to produce a 2x2x2 mm^3 triaxial sensing device which is capable to detect accelerations in the three major axes [8]. This triaxal accelerometer is constructed around one single seismic mass.
The present thesis will show that the single mass based inertial sensor can be extended with rate of turn sensing properties. An IMU based on a single seismic mass would result in an almost single point sensing element, which comes close to a perfect IMU. This sensor will be further called Gyracc, which name is a combination of the first three letters of gyroscope and accelerometer.

1.4 Possible application areas for the Gyracc

In 1994 a technical paper of J. Söderkvist included a nice overview of applications with their requirements [1]; this is shown in Table 1-1.

Table 1-1: Applications that need small or inexpensive inertial sensors [1]

Area	Example of applications	Range	Accuracy
Automotive			
reliable, inexpensive,	improved control for airbags	50 g, 200 °/s	500 mg, 10 °/s
lifetime	anti-collision systems	100 °/s	1 °/s
rough environment	active suspension	50 °/s	2 °/s
	anti-skid	100 °/s	1 °/s
Consumer			
inexpensive	free-space pointers	100 °/s	1 °/s
small, lifetime	remote control (TV)	100 °/s	2 °/s
low-power	video camera (anti-jitter)	50 °/s	0.5 °/s
	navigation (GPS)	50 °/s	0.5 °/s
	toys and sport equipment	varies	Varies
Industrial			
reliable, small,	machine control	10 °/s	0.01 °/s
rough environment	Angular vibration measurements	varies	Varies
	attitude control of flying objects	20 °/s	0.02 °/s
	automatic guided vehicles	50 °/s	0.2 °/s
	stabilized platforms	20 °/s	0.2 °/s
	robotics	10 °/s	0.01 °/s
Medical			
reliable, small,	monitoring of body-movement	10 g, 100 °/s	100 mg, 1 °/s
low-power	vibration diagnostics	0.1 g, 50 °/s	1 mg, 0.5 °/s
	controls for paralyzed patients	2 g, 100 °/s	20 mg, 2 °/s
	surgical instruments	20 °/s	0.1 °/s
	wheel-chairs	2 g, 50 °/s	20 mg, 0.2 °/s
Military			
reliable, small,	new weapon systems		
rough environment	smart ammunition		

From this overview it can be concluded that a small sized Gyracc would also be of interest for applications outside the biomedical field.

1.5 Outline of this thesis

Chapter 2 explains the physics behind measuring angular motion, followed by an overview of the existing basic MEMS structures that are able to sense rate of turn. With the knowledge of the boundary conditions of measuring rate of turn it is shown how harmonic actuation of the seismic mass in Lötters's triaxial accelerometer opens the possibility to sense rate of turn. Chapter 3 explains the theory behind the vibrating pathway of the seismic mass. Chapter 4 shows the possibilities of integrating electrostatic and/or electromagnetic actuation in the passive inertial sensor. Chapter 5 shows simulation results of the vibrating behavior of the seismic mass during the experience of a rate of turn in the two and three dimensional space. In chapter 6 two realized constructions of the sensor are described. The constructions consist of a combination of MEMS and precision engineered elements. Chapter 7 shows measurement results performed with the two types of inertial sensors. In chapter 8 conclusions are drawn and presented and suggestions for future research are proposed.

1.6 References

[1] Söderkvist, J., Micromachined gyroscopes. Sensors and Actuators A, 1994. 43: p. 65-71.

[2] Products MT6 and MT9, Inertial based sensing modules, Xsens, Enschede, the Netherlands, 2002

[3] Veltink, P.H., Three dimensional inertial sensing of foot movements for automatic tuning of a two-channel implantable drop-foot stimulator, Medical Engineering & Physics, vol. 25, 2003, pp. 21-28.

[4] Luinge, H.J., Inertial sensing of human movement, Ph.D. thesis, University of Twente, 30 October 2002

[5] Luinge, H.J., Veltink, P.H., Inclination Measurement of human movement using a 3-D accelerometer with auto-calibration, IEEE Transactions on Neural Systems and Rehabilitation Engineering, vol. 12, 2004, pp. 112-121.

[6] Luinge, H.J., Veltink, P.H., Measuring orientation of human body segments using miniature gyroscopes and accelerometers, Medical and Biological Engineering and Computing, vol. 43, 2005, pp. 273-282.

[7] Luinge, H.J., Veltink, P.H., Baten, C.T.M., Ambulatory Measurement of Arm orientation, J. Biomechanics, provisionally accepted.

[8] Lötters, J., et al., Design, fabrication and characterization of a highly symmetrical capacitive triaxial accelerometer. Sensors and Actuators A, Physical, 1998. 66(1-3): p. 205-212.

Chapter 2

2 GYROSCOPES - AN OVERVIEW

This chapter shows the principles of rotation sensing. An overview of Coriolis based micromachined rate of turn sensors in open literature is presented and rate of turn sensing with a modified triaxial accelerometer is introduced.

2.1 Introduction

"Gyroscope" is a combination of the two Greek words *gyros* for "revolution" and *scopein* for "to view". The French physicist Jean Bernard Leon Foucault introduced the word gyroscope in 1852 for his discovery, which successfully demonstrated that the earth rotates around its axis. This discovery is generally known as the Foucault pendulum. However, in 1810 the German scientist G. C. Bohnenberger invented already the first device resembling today's mechanical gyroscope, which consists of a gimbaled rotating disk. Once the disk is rotating it resists any attempt to change the direction of the rotation axis. This principle only became useful after 1890 when G. M. Hopkins introduced an electric motor, which continuously drove the rotating disk of the gyroscope. Dr. H. Anschutz from Germany (1908) and Elmer Sperry from Great Britain (1909) both used the stability and precession properties of the gyroscope. They both developed systems, which used the gyroscope as a reference: to keep track of the position of the objects the gyroscope was placed on.
Gyroscopes ("gyros") are instruments, which are used to measure angular motion. Their traditional market is for navigation as well as guidance and stabilization of military systems. There are many types of gyroscopes available today. Most familiar for many people is the spinning mass. Spinning mass gyros first came into high volume production during the Second World War in an aircraft attitude determination instrument [1]

In recent years there has been increasing pressure in the military field of motion sensors to provide less expensive gyroscopes and accelerometers while maintaining a good performance [2]. A micromachined gyroscope is very attractive for space navigation and automobile applications, because of its size, weight, cost and low power consumption. Micromachined accelerometers in silicon and quartz have already been successfully transferred into mass production and are nowadays commercially available [3]. There are two main branches of gyroscope design: mechanical gyros that use the inertial properties of matter, and optical gyros that operate using the propagation properties of light.

There is a functional difference between the "old fashioned" gyroscopes and the "modern" gyroscopes. The first measures the turn (rad) made by the gyroscope, with respect to the object it is placed on, and the latter measures the rate of turn made by the gyroscope ($rad \cdot s^{-1}$). By means of signal processing the output signal of the rate of turn sensor is modified into an equivalent gyroscope signal.
In this chapter a new type of gyroscope is proposed, after explaining the working principles of the existing gyroscopes and showing an overview of micro machined gyroscopes in open literature.

2.2 Gyroscope principles

Chapter one showed the necessity of a sensor that is able to measure the rotation of an object, without reference points outside the rotating body. This section shows the available techniques to measure rotation without any external reference point or system. The available techniques are:

- Centripetal force
- Conservation of angular momentum
- Constant velocity of light
- Coriolis effect

The fundamentals of these physical methods will be explained in the following sections. It is to be noted that there are also sensors that sense rotation by using an external reference. Examples of these sensors are inclinometers and compasses which use gravitation and the earth magnetic field, respectively. A drawback of these sensor types is that they do not sense rotations around all axes.

2.2.1 Centripetal force

Figure 2-1a shows a setup by which the rate of turn of a rotating system can be measured by means of an accelerometer. The seismic mass m [kg] in the accelerometer will transduce the force F_{cp1} into a measurable output signal. The output of the accelerometer is a function of the distance r_1 [m] from the mass of the accelerometer to the center of the rotating axis (O) and the rate of turn Ω [rad/s] (equation 2-1).

$$F_{cp1} = m \cdot r_1 \cdot \Omega^2 \qquad (2\text{-}1)$$

The fact that this sensing method is depending on the position of the accelerometer with respect to the rotating axis is an undesired complication. To bypass the necessity to know the distance r_1 an extra accelerometer is placed on the line between the rotating axis and the first accelerometer (Figure 2-1b).

These two identical accelerometers can be constructed into one housing. The mass displacement due to non-centripetal forces is considered to be identical in both accelerometers.

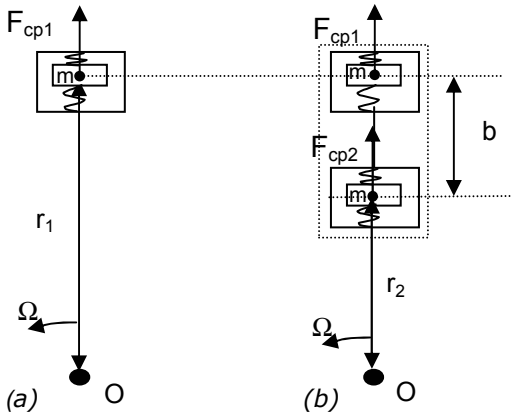

Figure 2-1: The accelerometer as a rate of turn sensor.

As a result the differential output, of the by a distance b separated accelerometers (equation (2-2)), is a function of the angular velocity (equation (2-3)).

$$b = r_1 - r_2 \tag{2-2}$$

$$F_{cp1} - F_{cp2} = m \cdot r_1 \cdot \Omega^2 - m \cdot r_2 \cdot \Omega^2 = m \cdot \Omega^2 \cdot (r_1 - r_2) = m \cdot \Omega^2 \cdot b \tag{2-3}$$

Angular rate is detected through the effect of centrifugal forces on the two seismic masses. When the sensitivity for both accelerometers is S [$V \cdot N^{-1}$]:

$$V_{out} = S.(F_{cp1} - F_{cp2}) \tag{2-4}$$

Rewriting results in the rate of turn:

$$V_{out} = S \cdot m \cdot \Omega^2 \cdot b \tag{2-5}$$

$$\Omega = \sqrt{\frac{V_{out}}{m \cdot b \cdot S}} \tag{2-6}$$

Now an angular rate sensor is obtained (equation (2-6)), but this sensor is hardly used, because the two accelerometers in the sensor have to be positioned accurately along the radius of the rotational point (O). Moreover, if we would like to measure the rate of turn of a body that has a variable rotational point O we need the use of other physical properties.

The rate of turn sensor can be transformed into a gyroscope, by integrating the rate of turn signal over time:

$$\theta(t) = \int_{t_0}^{t} \Omega(t)dt \qquad (2\text{-}7)$$

2.2.2 Conservation of angular momentum

The original gyroscopes make use of inertial properties of angular motion instead of the linear displacement due to centripetal forces as described in 2.2.1. An example of a gyroscope based on angular motion is shown in Figure 2-2.

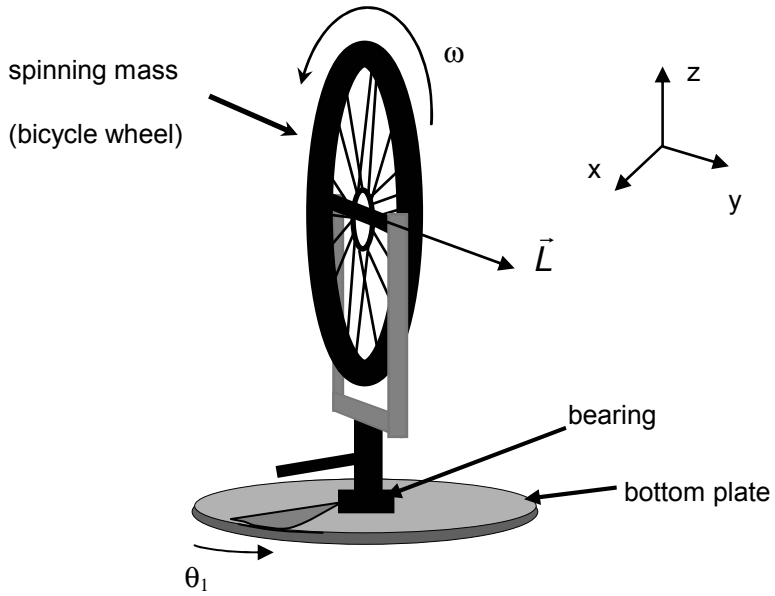

Figure 2-2: A spinning mass (wheel) on top of a rotating disk.

It shows a homogenous body (wheel), spinning around its symmetry axis in a fork shaped holder. This fork shaped holder is connected to the bottom plate by means of a bearing. If the bottom plate experiences an angular acceleration ($\vec{\alpha}$) in the x-y plane, then the wheel will resist this change in orientation, due to inertial forces. A torque ($\vec{\tau}$) will be induced across the bearing. If the bearing is friction free, then the wheel will keep its original orientation. If the bottom plate is turned over an angle θ_1 in the x-y plane then the angle between the spinning wheel and the rotating platform will also be θ_1.

The general term inertia refers to the resistance of the body to change in motion. In this sense, the moment of inertia fulfils the same role for rotational motion as the mass of a body in translational motion. It is possible to obtain the basic equations for angular motion by simply transforming the equations for linear motion into equations for angular motion, as shown in Table 2-1.

Table 2-1: The analogy between linear- and angular motion

Linear variables		***Angular variables***
Force, $\vec{F}$ [N]	⟶	Torque, $\vec{\tau}$ [Nm]
Mass, m [kg]	⟶	Moment of inertia, I [kg.m^2]
Velocity, $\vec{v}$ [m/s]	⟶	Angular velocity, $\vec{\omega}$ [rad/s]
Momentum, $\vec{p}$ [kg m/s]	⟶	Angular momentum, $\vec{L}$ [kg.m^2/s]
Acceleration, $\vec{a}$ [m/s^2]	⟶	Angular acceleration, $\vec{\alpha}$ [rad/s^2]

The analogy needs to be treated with care; e.g. I *is not a constant property of the body, as is mass, since its value depends on the axis around which is measured.*

With the equations in Table 2-1, Newton's law $\vec{F} = m \cdot \vec{a}$ becomes:

$$\vec{\tau} = I \cdot \vec{\alpha} \tag{2-8}$$

with

$\vec{\tau}$	*the dynamical torque of the system*	*[N.m]*
I	*the moment of inertia of the rigid body*	*[kg.m^2]*
$\vec{\alpha}$	*the angular acceleration of the rotating platform*	*[rad/s^2]*

The angular moment ($\vec{L}$) of the rotating mass (e.g., the wheel of Figure 2-2) is the product of the moment of inertia (I), which describes the distribution of mass of the rotating body relative to the rotating axis, and the rate of turn of the wheel ($\vec{\omega}$), see equation 2-9.

$$\vec{L} = I \cdot \vec{\omega} \tag{2-9}$$

with

$\vec{L}$	*the angular momentum of the rigid body*	*[kg.m^2/s]*
I	*the moment of inertia of the rigid body*	*[kg.m^2]*
$\vec{\omega}$	*the rate of turn of the rigid body*	*[rad/s]*

A torque force applied perpendicular to the direction of $\vec{L}$, does not change the amplitude of $\vec{L}$, but does change its direction. Therefore the gyroscope based on a rotating wheel is based on the conservation of the angular momentum.

Figure 2-3 shows a conventional gyroscope. In addition to the example of the spinning wheel, this system has extra bearings, which makes it possible to detect angular turns around the two axes θ_1 as well as θ_2. It is not possible to detect the angular turn θ_3 of the axle around which the rotor is spinning. It can be concluded that with a single rotating disk only the turn around the two axes perpendicular to the wheel axis can be measured.

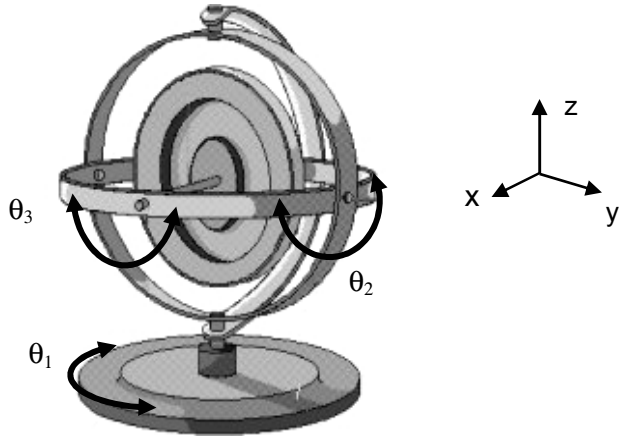

Figure 2-3: A conventional spinning wheel gyroscope.

Conventional gyroscopes are expensive, bulky, have a short working life due to mechanical wear and contain many components that require high precision in fabrication and assembly. Their performance however is excellent. Conventional gyroscopes are widely used in automatic steering systems in airplanes, missiles and torpedoes.

Though the application of a spinning wheel is a nice concept, which directly shows the angular turn in two planes, it is not applicable in a micro systems yet, because of the wearing of the bearings of the rotating mass of micro-motors developed up to now, although Shearwood et al. [4] reported a wear-free micromachined rotating disk.

2.2.3 Constant velocity of light

Gyroscopes based on the principle of constant velocity make use of the propagation principle of electromagnetic waves (radio waves, light) through an electromagnetic wave-guide medium (vacuum, glass). The propagation of electromagnetic waves is not disturbed by the possible displacement of the conducting medium. Figure 2-4 shows the basic concept of a setup (sensor), which can detect angular rotation by means of a system that is based on the principle of constant velocity. The setup contains a circularly bent glass fiber with a light source (laser) at one end and a light detector (PN-junction) at the other end.

In case the system is not experiencing a rotation, it will take a certain time for an injected light pulse to reach the detector. If the setup is experiencing a rotation in the direction of the light pulse then the traveling time of the light pulse will increase and if the setup rotates in the opposite direction the traveling time of the light pulse to reach the light detector will decrease. The traveling time of the light pulse is a measure for the experienced rate of turn (Ω [rad/s]) instead of the absolute angle made by the setup (θ [rad]).

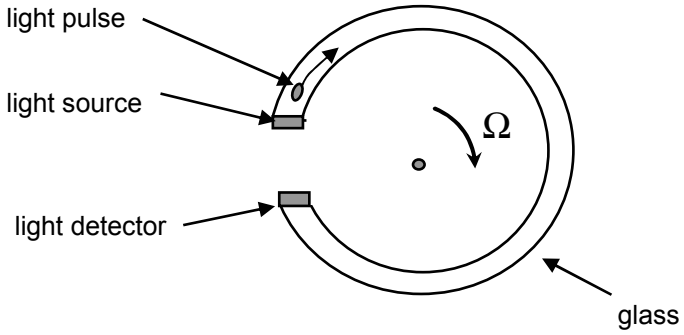

Figure 2-4: Example of a system which measures the rate of turn by means of measuring the traveling time of a light pulse through a circularly shaped wave guide.

The angular rate detection can be turned into turn detection by means of integrating the angular rate over time (equation (2-7)). An angular rate sensor, which makes use of propagating light through a glass fiber, is called a "fiber optic gyroscope" (FOG). Real FOGs do not function the way as previously mentioned, because the traveling time of the light pulse is too small to be detected by present electronic systems.

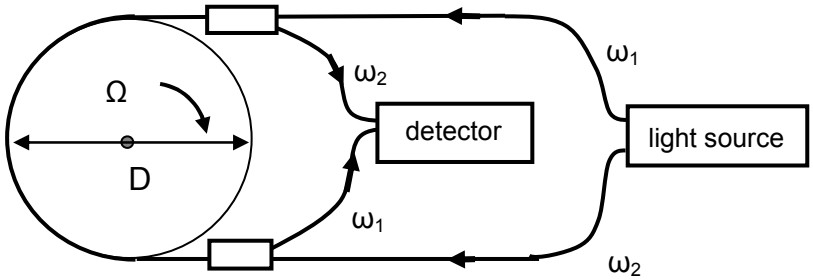

Figure 2-5: Schematic view of a fiber optic gyroscope (FOG).

Instead of this, existing fiber-optic gyroscopes are based on the interference between two light waves (the Sagnac-effect). In Figure 2-5 a simple schematic of such a fiber-optic gyroscope is shown. In order to determine the rate of turn, the output from a light source is split into two waves (ω_1 and ω_2), which simultaneously propagate through a circular path in opposite directions. If the gyro is rotating, the split/recombine point will move in space during the time that the light wave is traveling along the optical path. Since the speed of light is a constant factor, the time will be increased for the light wave traveling in the direction of the rate of turn (Ω), and decreased for the wave traveling in the opposite direction. When the two beams meet again they will no longer be in phase, but a phase difference ($\Delta\varphi$) will occur as given in equation (2-10). The phase difference is equal to:

$$\Delta\varphi = 2\pi LD\Omega/c\lambda \qquad (2\text{-}10)$$

with		
L	*length of fibre coil*	*[m]*
D	*effective coil diameter*	*[m]*
λ	*mean optical wavelength*	*[m]*
c	*velocity of light in vacuum*	*[m/s]*
Ω	*angular velocity around sensitive axis*	*[rad/s]*

The phase difference between the light-waves at the light detector will cause a decrease in the light intensity. The measured light intensity is a measure for the experienced rate of turn [5].

Fiber Optic Gyroscopes have a major advantage in the sense that they do not contain any moving parts. A drawback is that commercially available FOGs are relatively expensive and use much more power as compared to the rate of turn sensors based on the Coriolis effect discussed in the next paragraph.

2.2.4 The Coriolis effect

Micromachined gyroscopes, based on rate of turn sensing, are at present mainly based on the principle of Coriolis force [6-15]. The Coriolis force is an inertial force on a mass with a certain velocity within a rotating reference system. In order to understand in more detail the Coriolis effect, the experiment as represented in Figure 2-6 and Figure 2-7 may be useful. It shows the top view of a merry-go-round on which a person A and a person B are sitting opposite to each other.

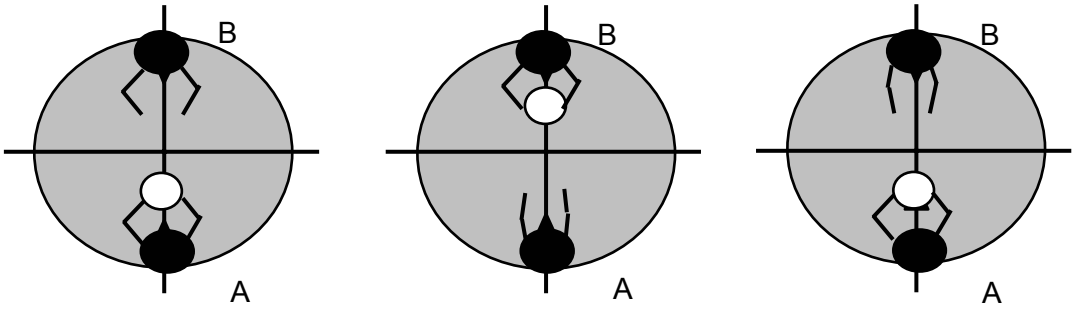

Figure 2-6: Two persons A and B, sitting on stationary merry-go-round, throwing a ball to each other.

The persons throw a ball back and forth towards each other. In case the merry-go-round is not experiencing a rate of turn, the ball's pathway is straight from person A to the person B (Figure 2-6). In case the merry-go-round is rotating and persons A and B are still throwing the ball towards each other, the pathway of the ball will deviate from a straight line to person B, as shown in Figure 2-7.

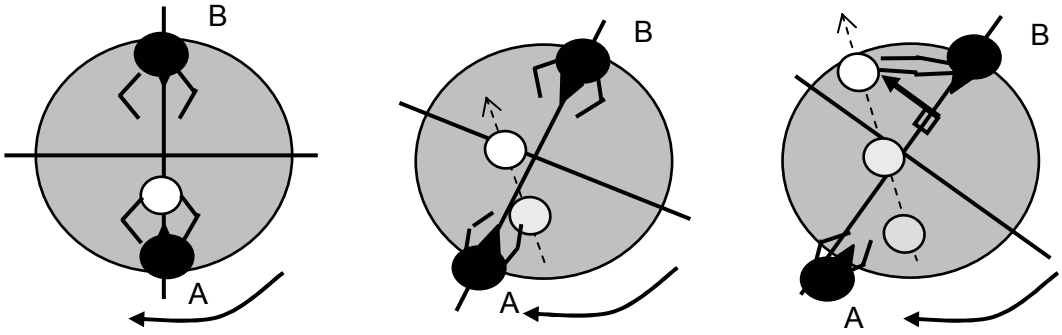

Figure 2-7: Two persons, sitting on a rotating merry-go-round and person A is throwing a ball to person B.

Although person A made an attempt to throw the ball towards person B, the ball will have a deflection to the left. The dotted line shows the actual pathway of the ball. The ball will have an additional velocity due to the rotation with respect to the initial velocity given by ball thrower A. Furthermore the receiving person B is moving away from the arriving ball. If person B is throwing the ball back to person A then the ball will be received on the right of person A. The deflection of the ball with respect to the straight line between the persons is a measure for the rate of turn of the merry-go-round. The French mathematician Gustave Gaspard de Coriolis (1792-1843) showed that the laws of motion could be used in a rotating frame of reference if an extra element called the Coriolis acceleration is added to the equations of motion, as illustrated in Figure 2-8.

$$\vec{a}_c = -2\vec{\Omega} \times \vec{v} \qquad (2\text{-}11)$$

with

$\vec{a}_c$	*the acceleration of the ball with respect to the rotating reference frame*	*[m/s²]*
$\vec{\Omega}$	*the rate of turn of the merry-go-round*	*[rad/s]*
$\vec{v}$	*the velocity of the ball with respect to the rotating reference frame*	*[m/s]*

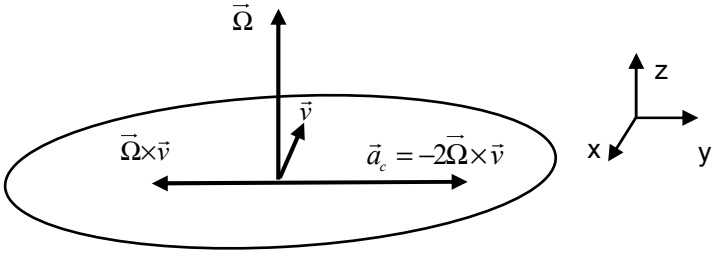

Figure 2-8: A representation of the vectors concerning the Coriolis force.

The acceleration the ball experiences as seen from the rotating merry-go-round can be used to define the Coriolis force.

$$\vec{F}_c = -2m\vec{\Omega} \times \vec{v} \qquad (2\text{-}12)$$

with

m *the mass of the bal* *[kg]*

Now suppose that the ball is periodically bounced from A to B along the x-axis of Figure 2-8. In this case the ball is vibrating with a certain frequency. If the vibration frequency of the ball (ω [Hz] or [rad/s]) is much larger than the experienced rate of turn around the z-axis (Ω [rad/s]) of the merry-go-round, then the Coriolis force acts perpendicular to the x-z plane (Figure 2-8). Therefore the force experienced on the ball in the y-axis direction is a measure for the angular rate of the merry-go-round. In case the velocity of the thrown ball is a constant, then the Coriolis force is linearly related to the rate of turn of the system. Coriolis based gyroscopes are also referred to as vibrating rate of turn gyroscopes. When the mass of the gyroscope is vibrating, an angular rate induces Coriolis forces and thus a vibration perpendicular to the original vibration (Figure 2-9).

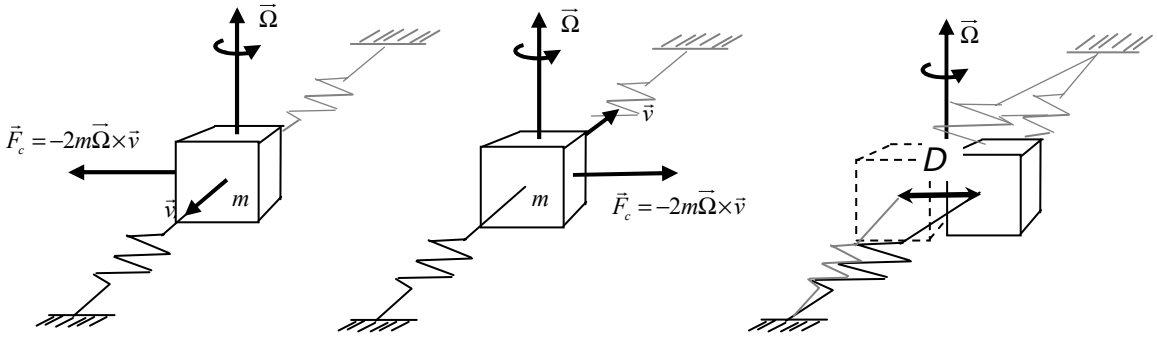

Figure 2-9: (a, b) The Coriolis force acting on a moving mass in a specific direction (c) the position of the mass during different moments in time.

The amplitude of the vibration (*D)* is a function of the experienced rate of turn (*Ω*). The larger the rate of turn the larger the amplitude (*D*), as shown in Figure 2-9(c).

2.2.5 Conclusions

Four physical principles to sense a rotation or a rate of turn have been described. The sensor based on the use of centripetal force has the disadvantage that its rate of turn sensing property is depending on the positioning of the sensor with respect to the rotational axis (a reference point outside the sensor). In case of a body with a non pre-defined rotational axis, a sensor based on Centripetal force is of no use.

The remaining three physical principles are sensors based on: Conservation of angular momentum, Constant velocity and Coriolis effect.
A sensor based on the conservation of angular moment has the disadvantage of being a non solid-state sensor, showing wear of the bearings and having a lack of robustness. Depending on the number of bearings a sensor based on this principle can measure the turn around one or two axis.

A sensor based on constant velocity has the disadvantage of relatively large power consumption. Furthermore there have been no reports on any micromachined rate of turn sensors based on the constant velocity principle yet. This type of sensor can only measure the rotation around one axis.

A sensor based on the Coriolis effect gives the best opportunity to make a rate of turn sensor, which has a low power consumption, is small, light of weight and is able to sense rotations in two directions perpendicular to the vibration axis.

2.3 Essential gyroscope performance parameters

There are many types of rate of turn sensors on the market nowadays and presently being developed. Choosing a rate of turn sensor for a certain application does not only depend on its size and price, but also on its performance. General performance parameters of rate of turn sensors are shown in Table 2-2.

Table 2-2: General rate of turn sensor parameters and their definitions.

Parameter	Definition	Unit
(Linear) range	The minimum and maximum rate of turn that give an output voltage as a (linear) function of the experienced rate of turn.	rad/s
Bandwidth	The maximum frequency at which rates of turn can be measured	Hz
Detection limit	The minimum rate of turn that the can be detected.	rad/s
Bias stability	Range of (unwanted) output signal at zero rate of turn.	(rad/s)/h
Run up time	The time until the rate of turn sensor gives a reliable signal after power on.	s
Cross-axis sensitivity	The relative amount of sensed rate of turn in the detection axis with respect to the other axes than the mentioned axis.	%
Volume	The size of the sensor length × height × width.	m^3
Weight	The mass of the sensor.	kg
Power consumption	The product of the voltage [V] and current [A], during operation.	W
Sensitivity	The change in output voltage of the rate of turn sensor as a function of the experienced rate of turn.	V/(rad/s)
Number of detection axes	Single axis, Biaxial or Triaxial rate of turn sensor.	-

Besides the parameters mentioned in Table 2-2 other parameters like the sensitivity of the sensor to experienced accelerations or temperature could be essential for the applicability of the rate of turn sensor. As with all sensors one

has to know exactly under which environmental conditions the sensor has to operate.

2.4 Commercially available Coriolis-based rate of turn sensors

There are only a few companies producing commercially available rate of turn sensors. Table 2-3 shows the commercially available rate of turn sensors, with dimensions smaller than $5\times5\times5cm^3$, which are suitable for portable applications.

Table 2-3: Overview of small commercially available rate of turn sensors.

Producing company	Sensor reference	Size (cm)	Range (rad/s)	Power consumption	Production Technology	Nr. of axes
SSS + BAE	CRS03-02	2.9 ×1.8×2.9	± 1.7	5V × 50mA	Precision engineering	1
Murata	ENC-03J	1.5×0.8×0.5	± 5.4	5V × 5mA	Precision engineering	1
NEC-Tokin	Ceramic Gyro	0.8 × 2 × 0.8	± 1.5	5V × 7mA	Precision engineering	1
Gyration	Microgyro 100	2.3×2.3×2.0	± 2.8	2.2V-5.5V 2.7mA	Precision engineering	2
Temic	DRS 75	3×2×1	± 1.3	5 V × 35mA	Micro machining	1
Micro-sensors	Silicon Micro-Ring Gyro	2×1×0.5	± 1	5V × 15mA	Micro machining	1
Panasonic	EWTS82	1×1.3 × 1.8	?	5V × 50mA	Micro machining	1
BEI	QRS11	4.1ø×1.5	± 1.8	± 5V × 80mA	Micro machining	1
Analog Devices	ADXRS150	0.7×0.7×0.3	± 2.6	5V × 7mA	Micro machining	1
Kionix	KX210	1.5×0.8×0.3	± 5.2	5V × 15mA	Micro machining	1

The table shows two groups of differently produced Coriolis based rate of turn sensors. One group is produced by means of precision engineering techniques and the other with micromachining techniques. The table further shows that only one commercially available sensor has the ability to detect the rate of turn around two axes. If the rate of turn around more axes has to be measured then more sensors have to be used, with an increase in volume and power consumption as result.

2.5 Transduction in Coriolis-based rate of turn sensors

The Coriolis principle is applied in many micromachined angular rate sensors [1-3, 6-33, 38, 40, 42, 44-49]. In these micromachined rate of turn sensors different methods are used to actuate and sense the vibration of the mass. An overview of these methods is shown before various concepts of Coriolis based rate of turn sensors in open literature are reviewed (section 2.6).

2.5.1 Actuating the vibration

In case of Coriolis based rate of turn sensors there is a need for actuating the vibration of the mass. The most energy effective vibration is reached, if the mass is actuated in its mechanical vibration resonance frequency. There are several ways of actuation; a short overview of actuation methods used in the Coriolis based rate of turn sensors is given in this paragraph.

2.5.1.1 Electrostatic actuation

The use of an electrostatic force is the most commonly used actuation method in micromachining. It is a force that arises between two conductors, which have a potential difference (see also Chapter 3). A drawback of this actuation method is that the produced force is the square of the potential difference. Furthermore, to stay within reasonable values of the actuation voltage (<16 Volts), the distance between the two conductors must therefore be small (<5 μm). Therefore a drawback (in poorly designed sensors) with electrostatic actuation is the risk of fusing the two conducting surfaces during operation. At the moment of physical contact between the two surfaces, a large current will occur and the surfaces might be bonded. A situation like this might appear at the moment that the sensor is experiencing inertial forces far beyond the safe operating region [7, 13, 15-29].

2.5.1.2 Piezoelectric actuation

Piezoelectric actuation uses the force that is generated by applying a potential difference (V) over a piezoelectric material like BaTi, ZnO or PZT. Depending on the polarity of the potential difference, the material will slightly increase or decrease in size (<0.01%). The piezoelectric material has to be in contact with the mass which should vibrate. The generated forces are large, but there are disadvantages in the use of this type of actuation. Piezoelectric actuation is mainly used in hand assembled sensors, because piezoelectric materials are poorly compatible with cleanroom technology. Furthermore the piezoelectric effect is very temperature dependent. Therefore rate of turn sensors with piezoelectric materials will be temperature sensitive [2, 30-34].

2.5.1.3 Electromagnetic actuation

It is possible to generate push and pull forces with an electromagnet. Electromagnets are mainly used for their ability to attract ferro-magnetic materials (Fe, Co, Ni) along the B-field of a permanent magnet, which is connected to the object to be moved. Electromagnets are actuated by means of a current through the coil of the electromagnet. The voltage across the coil is low compared to the voltages applied in the electrostatic and piezoelectric actuation method. The force produced by electromagnets is insensitive to changes in temperature. The main drawback in the use of electromagnets is the

non-compatibility of the materials used with present cleanroom technology, although there is a trend towards better compatibility [8, 14, 34, 35].

2.5.1.4 Lorentz force actuation

Lorentz force is the force acting on a charge, which flows with a certain velocity, through a magnetic field. A current through a wire is equal to a line of charges traveling with a certain velocity and thus when the current conducting wire is positioned in a magnetic field, it will experience a Lorentz force. Lorentz forces provide large displacements of the wire (mass) with relatively low currents (<10mA). The magnetic field is applied with a permanent magnet [35-37].

2.5.2 Sensing the vibration

There are several methods to sense the displacement and position of the vibrating mass. The used methods as mentioned in the literature are briefly summarized in the following subsections.

2.5.2.1 Capacitive sensing

The position of an object with respect to a reference point can be measured contact-less by means of the capacitive principle. To realize this, one capacitor plate is connected to the moving object (mass) and the other capacitor plate is fixed to the reference point. The capacitance of the capacitor is a function of the distance between these two plates. The capacitive sensing method is well suited for micromachined batch fabrication, but it requires high-resolution measurement circuitry to detect the fairly small capacitive changes, with usually parasitic capacitors and interfering electrostatic fields. The energy consumption for displacement detection with capacitive sensing is low. Unfortunately, the transfer of object displacement to a change in capacitance is non-linear, especially for relatively large displacements.

2.5.2.2 Inductive sensing

Besides for displacement actuation, electromagnets can be used for displacement sensing. The induction of the coil of the electromagnet is a measure of the distance between the core of the electromagnet and the moving object if the mass is part of the electromagnetic pathway. Another sensing principle is the detection of a changing magnetic field through a coil itself. A change of electromagnetic field through a coil produces a voltage. This detection principle can only be used for dynamic measurements. Inductive sensing has several advantages. It is contact-less, thus there is no friction. Additionally the dependence on temperature of the sensing elements is negligible [6]. Dynamic magnetic field detection can obtain relatively large output voltages compared with other methods. Unfortunately it is hard to implement in a micromachined structure.

2.5.2.3 Piezo-resistive sensing

The stress in a structure can be measured by means of a beam of a piezo-resistive material, which is mounted in the region under stress. The resistance of the piezo-resistive beam is a function of the length and thus the stress of the beam. The resistance can be measured by means of measuring the voltage over the piezo-resistive beam, which conducts a fixed bias current. As a result there will be a continuous dissipation of energy.

In general, piezo-resistive detection is more sensitive than capacitive detection for small resonant amplitudes. Piezo-resistive sensing methods are accurate but have highly temperature dependent output characteristics, except for crystalline piezoelectric materials such as quartz [34]. The effect of the temperature dependence of the piezo-resistive material is commonly reduced by means of integrating the resistive material in a Wheatstone-bridge. The Weatstone-bridge is also used for nulling the offset.

2.5.2.4 Piezo-electric sensing

Most of the piezoelectric rate of turn sensors use relatively small piezoelectric elements attached to a large non-piezoelectric resonator. The piezoelectric material gives a potential difference across the material e.g. Barium-Titanate, Zinc-Oxide and Lead-Zirconate-Titanate, in the case of deformation. Differences in expansion coefficients of the piezo-electric material and the material of the non-piezoelectric resonator will degrade the sensor performance when temperature changes [31].

2.5.2.5 Optical sensing

The moving mass is positioned between a light emitting diode (LED) and a photodiode. The further the mass is positioned between the two elements the lower the photocurrent through the photodiode will be. This current is a measure for the position of the mass [16].

2.5.2.6 Electron tunnelling

Electron tunneling is the most sensitive displacement measuring method. Its operation is based on the principle of quantum tunneling. This method can measure displacements at the atomic scale and thus measure down to the thermal noise floor of the mechanical system. Electron tunneling is very popular for Atomic Force Microscopy (AFM) measurements and is now also used for displacement sensing inside a rate of turn sensor [29]. The operating principle of electron tunneling is relatively simple; a conducting tip is brought close to a current conducting surface and a voltage is applied between the tip and the displacing material. At a distance of about 0.5-1.0 nm, electrons tunnel from one side to the other. The resulting tunnel current depends on the tunneling distance. In the most usual mode of operation, the tunnel current through the tip is kept constant via a feedback circuit.

2.6 Coriolis-based rate of turn sensors in open literature

The actuation and sensing methods mentioned in the previous section can all be used to actuate the vibration of mass and for the sensing of the vibration of the mass. The following paragraphs show the various concepts of rate of turn sensors based on the Coriolis effect published in the open literature.

2.6.1 Vibrating single mass

The most elementary configuration of a rate of turn sensor is a suspended single mass; an example is given in Figure 2-10. In this example the mass (m) may readily vibrate along the x-axis and z-axis. The mass is vibrating along the x-axis, at a certain frequency, by means of electrostatic AC actuation. The electrostatic force is imposed on the mass by means of the comb-like structures on the left and right side of the mass. A Coriolis force imposes a vibration along the z-axis, in case the mass is subjected to a constant angular rate around the y-axis. The Coriolis vibration frequency in the z-axis direction is equal to the frequency of vibration along the x-axis. The capacitance between the mass and a capacitor plate under the mass senses the movements of the mass in the direction of the z-axis.

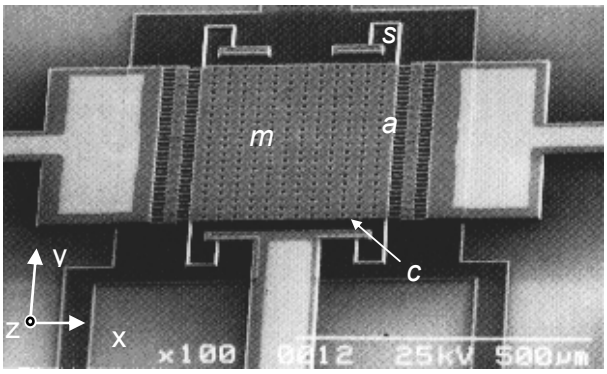

Figure 2-10: Top view of a micromachined y-axis vibrating mass rate of turn sensor [13].

If the amplitude of the drive vibration is constant, then the amplitude of the resulting oscillatory motion in the z-direction is proportional to the angular rate. Examples of the rate of turn sensors, which are based on a single vibrating mass with several relevant parameters, are given in Table 2-4.

These single mass rate of turn sensors are only able to detect rotations around one single axis. A note can be made on the vibrating mass rate of turn sensor described in reference 38. This gyroscope is operating under atmospheric pressure, which is quite unique for micro machined rate of turn sensors.

Table 2-4: Several relevant parameters of a single vibrating mass rate of turn sensor.

Reference	Type of actuation	Type of sensing	Resonance frequency	Quality factor	Power supply parameters	Resolution
13	Electrostatic	Capacitive	-	2.800-16.000	5 V_{DC}+5 V_{AC}	-
27	Electrostatic	Capacitive	9.07 kHz	-		1 ^{0}/s
28	Electrostatic	Capacitive	8.3 kHz	1000	6 V_{AC}+15 V_{DC}	
29	Electrostatic	Electron tunneling	48 kHz	1000-2000		0.07 ^{0}/s
16	Electrostatic	Optical	1.2 kHz	1000	6 W	1 ^{0}/s
25	Electrostatic	Capacitive	5.3 kHz	2000		
38	Electrostatic	Piezo resistive	593 Hz	260		

2.6.2 Vibrating dual mass

This type of sensor consists of two masses vibrating in anti phase. This sensor actually consists of two, single mass, rate of turn sensors (as mentioned in the previous section) positioned along the same axis. An example of a vibrating dual mass rate of turn sensor is given in Figure 2-11. It consists of two surface micromachined masses. The masses are brought into vibration along the x-axis, by means of electrostatic forces. A rotation around the z-axis imposes a Coriolis force in the y-axis direction on the masses. [36]. The resulting anti-phase vibration of the masses is capacitively detected by means of the comb-shaped structures in the masses.

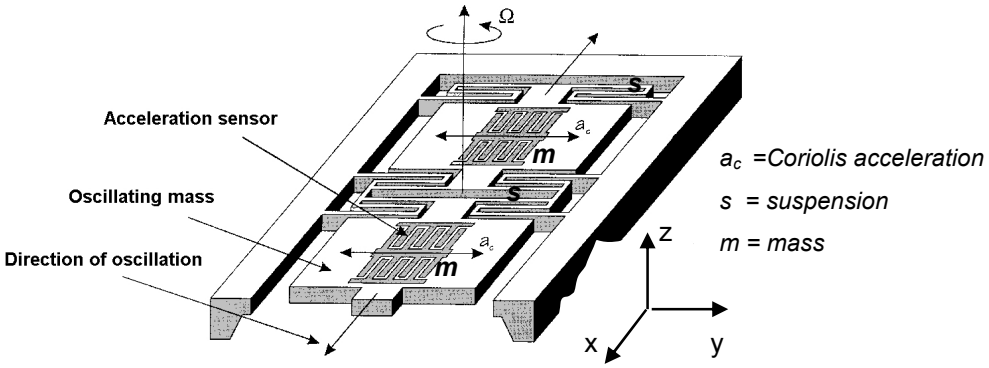

Figure 2-11: Two anti-phase vibrating masses as a z-axis rate of turn sensor [36].

This type of construction has two fundamental differences as compared to a single axis rate of turn sensor. First there is no net vibration experienced outside the sensor, because the masses are vibrating in anti-phase. For this reason it is possible to place more of these sensors on an object, without the problem of vibration coupling between the different sensors**.** Secondly, differential measurement of the Coriolis signal of the two vibrating masses filters out the signals originating from linear accelerations experienced by the sensor.

Several relevant parameters of dual-vibrating mass rate of turn sensors are listed in Table 2-5.

Table 2-5: Several relevant parameters of the dual vibrating mass rate of turn sensor.

Reference	Type of actuation	Type of sensing	Resonance frequency	Quality factor	Power supply parameter
17	Electrostatic	Capacitive	5 kHz	-	2.4 [V]
35	Lorentz	Capacitive	2.4 kHz	366	
36	Lorentz	Capacitive	2.1 kHz	1200	
37	Lorentz	Capacitive	470 Hz	100	
15	Electrostatic	Capacitive	12 kHz	10.000	

The rate of turn sensor described in reference 36 is operating under atmospheric pressure.

2.6.3 Tuning-fork

Probably the most popular micromachined rate of turn sensor is the tuning-fork rate of turn sensor. It has the same advantages as the dual mass rate of turn sensor. The difference between the dual mass rate of turn sensor and the tuning fork rate of turn sensor is the suspension of the masses and the Coriolis detection principle. An example of a tuning fork rate of turn sensor is shown in Figure 2-12. The sensor has two tines (masses) that are forced to vibrate along the z-axis. The vibration frequency of the two tines in the z-axis direction is called the excitation mode or primary mode. The two tines are forced to vibrate in opposite directions (anti-phase). An angular rate, applied around the y-axis, will generate a Coriolis force in the tines in the x-direction. The Coriolis forces have opposite direction for the two tines and will generate a periodic torque in the stem of the tuning fork as a consequence (detection mode or secondary mode). The resulting shear stress in the stem of the tuning fork is proportional to the angular rate.

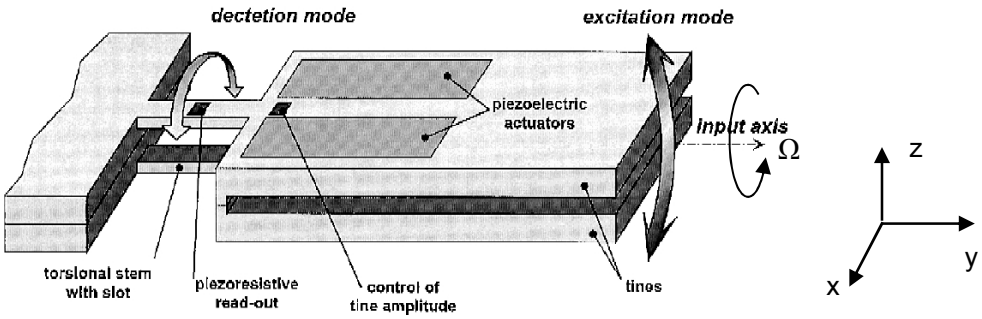

Figure 2-12: Tuning-fork rate of turn sensor [32].

The shear stress in the stem of the fork is sensed by a piezo-resistive read-out structure [32]. To ensure a good performance of the vibrating rate of turn sensor the tines of the tuning fork have to be balanced and for a high sensitivity

the frequencies of the two resonant modes have to be equal. Tuning forks are mainly designed with piezo-electric actuators and piezo-resistive sensors. Their resonance frequency is tens of kHz and they have a quality factor of about 10.000.

2.6.4 Rotary oscillating wheel

The rotary oscillating wheel is a vibrating sensor, which consists of an inner wheel and of an outer rectangular structure (Figure 2-13) [7]. The two structures are interconnected by means of a torsion spring. The entire movable structure is electro-statically driven to a rotary oscillation around the z-axis by the comb drives (primary mode). When the device is experiencing a rotation around its x-axis, Coriolis forces arise and the two masses will consequently displace in the z-axis direction in anti-phase. This anti-phase vibration causes a rotary oscillation around the y-axis (secondary mode). The position of the masses in the z-axis is measured by means of capacitor plates under the masses. The high stiffness of the inner wheel suspension suppresses an oscillation of the inner wheel in the Coriolis direction. Only the rectangular structure can follow the Coriolis forces, because it is decoupled from the inner wheel by torsion springs.

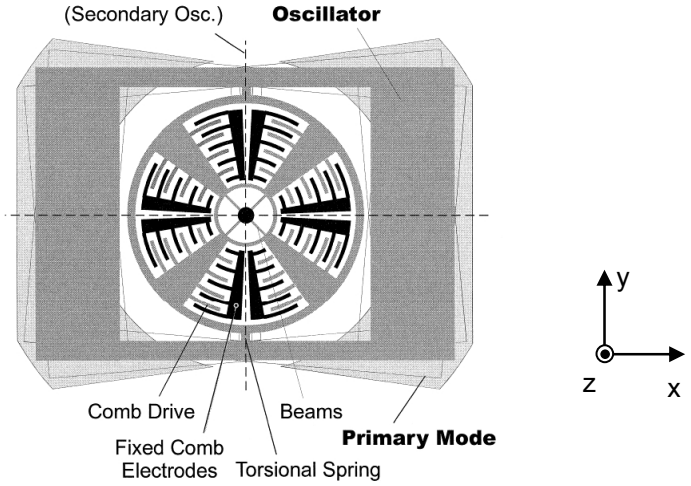

Figure 2-13: Oscillating wheel rate of turn sensor [7].

This rate of turn sensor has electrostatic actuation and capacitive detection. Its resonance frequency is 1.4 kHz and its resolution is 0.008 ^{0}/s [7,23].

2.6.5 Rotary vibrating plate

Figure 2-14 shows the angular rate of turn sensor, which is based on a rotary vibrating plate or mass [39]. The structure is composed of an outer gimbal fixed to the substrate via anchors, an inner gimbal connected to the outer gimbal through torsional support flexures, drive electrodes below and above the outer gimbal, and sense electrodes under the inner gimbal.

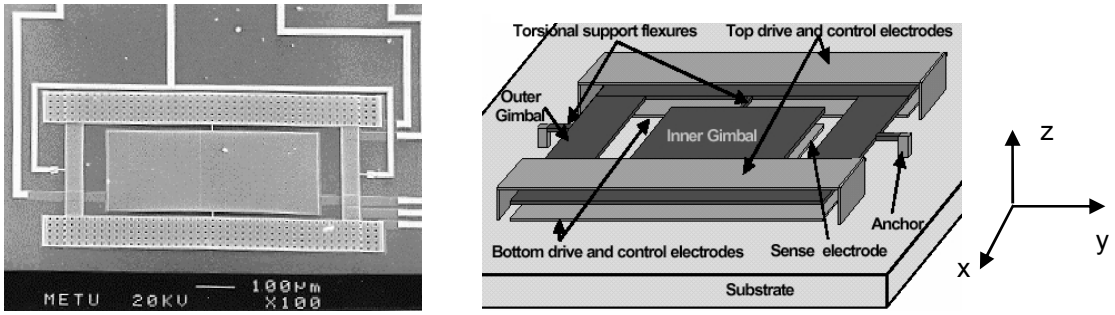

Figure 2-14: Photo and drawing of a rotary vibrating plate rate of turn sensor [39].

When the outer gimbal is excited to vibrate torsionally and an input rotation rate is applied around an axis perpendicular to the substrate (z-axis), the inner gimbal starts vibrating torsionally. By sensing the motion of the inner gimbal with a capacitive readout circuit, the rotation information is obtained. There are two isolated electrodes under the inner gimbal, allowing differential displacement sensing. Excitation of the outer gimbal can be achieved with both the top and bottom drive electrodes. Having two electrodes allows more efficient electrostatic feedback control and better adjustment of resonant frequency of the drive vibration mode. Typical parameters of this type of rate of turn sensor are given in Table 2-6.

Table 2-6: Several relevant parameters of rotary vibrating plate rate of turn sensors

Paper	Type of actuator	Type of sensing	Resonance frequency	Quality factor [-]	Power supply parameters
19	Electrostatic	Capacitive	2.5 – 4.7 kHz	1.000-70.000	36 V
33	Electromagnetic	Inductive	29 –34 Hz	18 – 40	
38	Electrostatic	Capacitive	5 kHz		

The rate of turn sensor, with reference nr. 33, is operating under atmospheric pressure and is not fully micromachined.

2.6.6 Vibrating ring

Figure 2-15 shows a micromachined ring rate of turn sensor [34]. The vibrating ring rate of turn sensor differs in operation, as compared to the rate of turn sensors mentioned in the previous sections. In the case of a vibrating ring rate of turn sensor a flexible ring (non-solid mass) is brought into its resonance vibration. The ring shaped rate of turn sensor vibrates in a similar way as a resonating wineglass.

Figure 2-16 shows an electrostatically in the xy-plane driven ring. The vibration of the ring results in an elliptical shape of the ring. The four points on the ring that have no radial deflection are the nodes. In an open-loop driven mode the

position of the nodes is a measure for the experienced rate of turn around the z-axis.

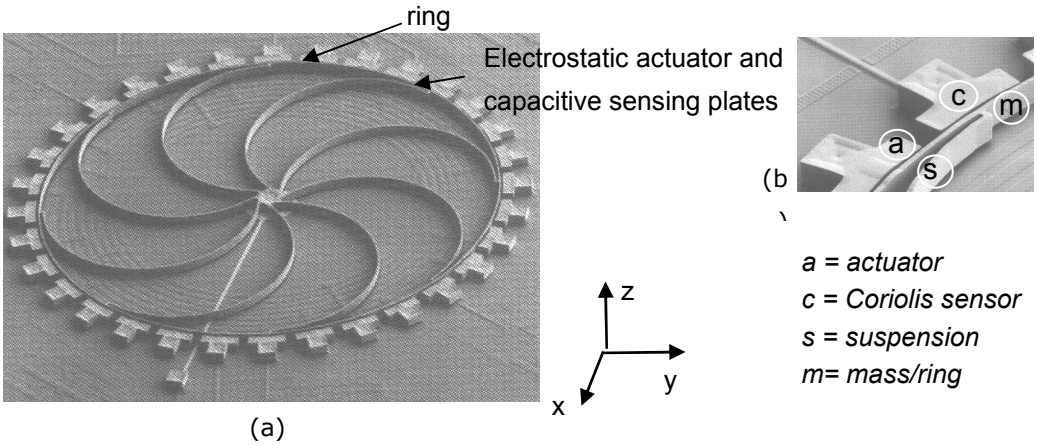

Figure 2-15: (a) The suspended flexible vibrating ring rate of turn sensor. (b) Close-up of the actuation and sensing points of the vibrating ring [34].

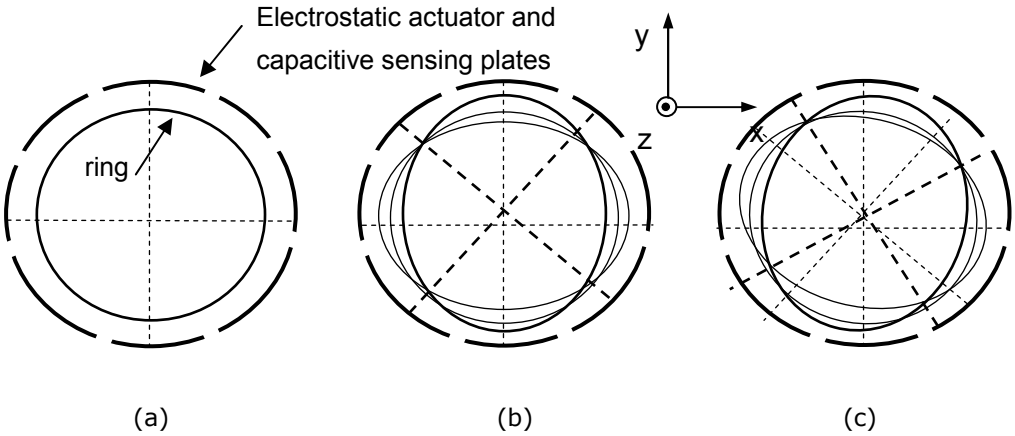

Figure 2-16: The ring and the surrounding actuator and sensor plates of the vibrating ring rate of turn sensor (a) not vibrating (b) vibrating and not experiencing a rate of turn (c) vibrating and experiencing a rate of turn.

In a closed-loop mode of operation the nodal points are held stationary by means of electrostatic forces. In this mode of operation the angular rate is related to the force necessary to keep the points stationary [16,21].

2.6.7 Dual axis rate of turn sensors

All previously mentioned rate of turn sensors are only able to detect rotations around a single axis. Depending on the structure, they can detect the rate of turn in the plane of the fabricated rate of turn sensor (z-axis) or in the direction perpendicular to the plane (x- or y-axis). Two perpendicularly positioned rate of turn sensors of the single sensor type are able to detect the rate of turn in two

directions. An example of two integrated perpendicularly positioned rate of turn sensors is shown in Figure 2-17.

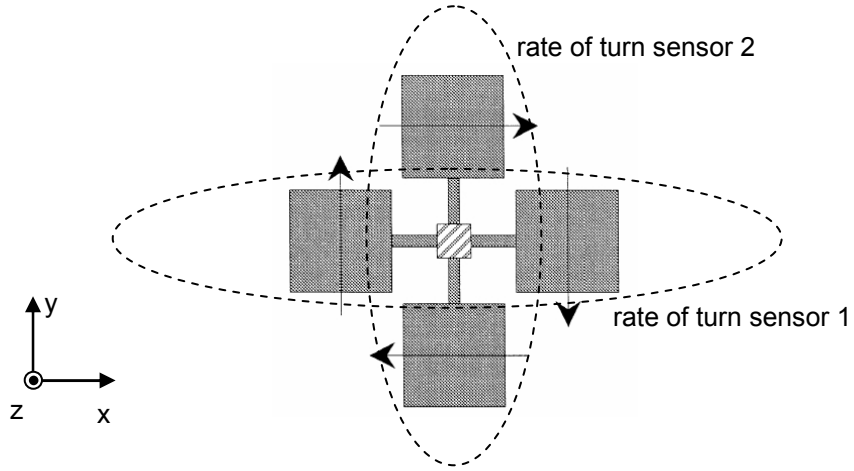

Figure 2-17: The configuration of a two-axial rate of turn sensor consists of two pairs of masses vibrating in anti-phase [24].

Vibrating rate of turn sensor 1 is vibrating along the y-axis and is able to detect rate of turn around the x-axis and vibrating rate of turn sensor 2 is vibrating along the x-axis and is able to detect rate of turn around the y axis.

Table 2-7: Several relevant parameters of dual axis rate of turn sensors.

Reference	Type of Actuator	Type of Sensing	Resonance frequency [kHz]	Quality factor [-]	Power supply parameters	Resolution
18	Electrostatic	Capacitive	56	950		0.004 ^{rad}/s (1 Hz BW)
39	Electrostatic	Capacitive	3.4	-		-
23	Electrostatic	Capacitive	9.8	4000	2.5 V_{DC}-0.3 V_{AC}	-
40	Electrostatic	Capacitive	3.7	30	7.5DC-15V_{ppAC}	-

2.6.8 Triaxial rate of turn sensors

There are no reports on three axes rate of turn sensors. If a multi-axis rate of turn sensor would be made by combining different rate of turn sensors, special attention has to be taken to circumvent the problem of cross sensitivity.

2.6.9 Other concepts

In addition to the micromachined rate of turn sensors described in the previous sections, rate of turn sensors have been designed that theoretically should be able to sense a rate of turn, but once produced showed no measurable output in practice. Two of them are discussed in this section.

2.6.9.1 Surface Acoustic Wave rate of turn sensor

A rate of turn sensor based on surface acoustic waves (SAWS) can have a two-dimensional construction like SAW filters. In SAW filters a plate of an elastic

material is provided with piezo electric elements. These elements impose standing waves through the elastic material (primary mode). An experienced rate of turn will impose a second SAW. The distribution of this new secondary oscillation results in a new stress pattern in the piezoelectric material. This stress can be measured by means of electrodes on top of the surface [42].

2.6.9.2 Piezoelectric thickness extension

A rate of turn sensor based on the thickness extension in the vibration mode of a piezo electric plate has also been described [31]. In contrast to all other piezoelectric rate of turn sensors it does not use any elastic elements. It is referred to as a piezoelectric–plate micro rate of turn sensor, because it has the ability to be reduced in size. A macro rate of turn sensor according to this concept is tested and is shown to work, however there are no reports about a working mini rate of turn sensor yet.

2.6.10 Discussion and additional remarks

In the previous sections different sensor concepts have been described. The micromachined rate-of-turn sensors are all based on inertial forces acting on a vibrating mass. In normal working mode the mass vibrates at its mechanical resonance frequency, because then the amplitude of the vibration is maximal. Electrostatic forces are small and therefore the mass is actuated at its mechanical resonance for the lowest possible energy consumption. Mechanical resonance in the direction of Coriolis displacement raises the displacement of the mass further above the detection noise level. The larger the quality factor of the resonance in Coriolis direction, the lower the minimum detectable rate of turn. To achieve the highest possible sensitivity and energy efficiency, the resonance frequency in the direction of the applied vibration (first mode resonance) should be equal to the resonance frequency in the direction of the Coriolis force (secondary vibration mode). Tuning of these frequencies is achieved by means of etching the springs during pre-processing of the silicon structures or by means of biasing the resonance frequency by putting the mass spring structure under a pre-stress condition, thus raising the resonance frequency. An exact frequency matching is difficult to maintain. This difficulty is caused by the etching process of the different parts and by stress occurring during assembly of the whole system. The problems may increase by aging and temperature effects. The necessity of a large quality factor in the Coriolis sense direction decreases with an increase in the weight of the seismic mass, because the Coriolis force on a mass is linearly depending on its weight.

2.6.11 Conclusions

All Coriolis based rate of turn sensors are based on the inertial properties of suspended vibrating rigid masses or on vibrating flexible structures. The quality factor of the vibrating systems compensates for the low mass of silicon

structures. The highest sensitivity and energy efficiency of a rate of turn sensor is reached when the resonance frequencies in the applied and in the sensing direction are the same. Electrostatic actuation and capacitive detection are most commonly used in micro machined rate of turn sensors. Some rate of turn sensors consist of two anti phase vibrating masses to eliminate the influence of external vibrations. Some sensors mechanically separate the movement of the mass in the applied direction and Coriolis detection direction to reduce the influence of mechanical cross axis movement. Most rate of turn sensors can detect the rate of turn around one axis and some can detect rate of turn around two axes. Sensors that can detect the rate of turn in two directions consist of two smartly integrated single axis rate of turn sensors. Triaxial rate of turn sensors are not reported yet. None of the reported inertial sensors was able to detect rate of turn as well as linear accelerations, thus the need for such a sensor still exists. A concept of a 3D movement sensor, consisting of a triaxial rate of turn sensor (gyroscope) and a triaxial accelerometer is shown in paragraph 2.7. The development of such a sensor is the main goal of this thesis.

2.7 The Gyracc

Our goal is to apply the Coriolis phenomenon in the symmetrical triaxial acceleration sensor as developed by Lötters et al. [43]. The drawings in Figure 2-18 show the transformation of the merry-go-round system as mentioned in 2.2.4 to the triaxial accelerometer.

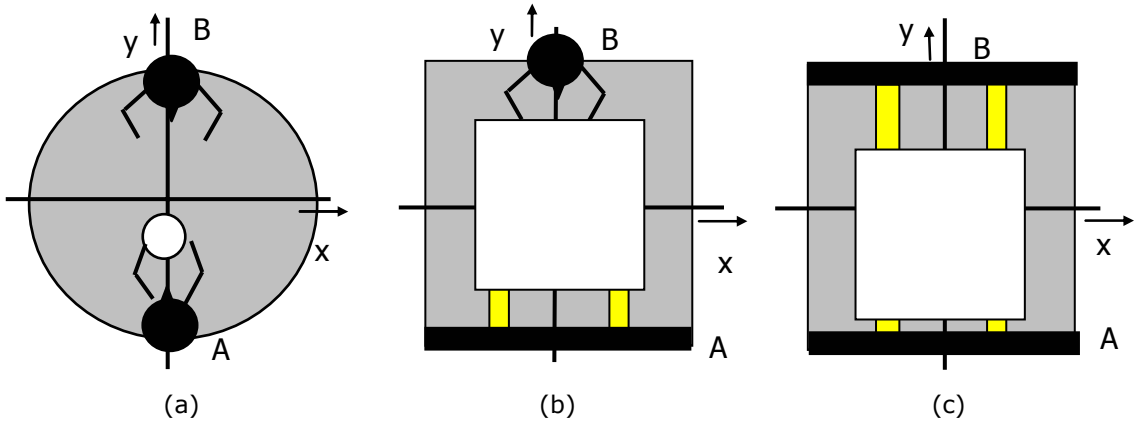

Figure 2-18: The stepwise transformation of a merry-go-round to an accelerometer.

Figure 2-18a shows the merry-go-round. Figure 2-18b shows that the round merry-go-round disk is replaced by a square shaped platform, whereas the round ball is replaced by a cubic mass and person A is replaced by a plate and the arms of person A are replaced by springs. In Figure 2-18c the same conversion is made with respect to person B. In principle Figure 2-18 is a cross section of the tri-axial accelerometer as shown in Figure 2-19 [36,44,45], from which it can easily be concluded that if the mass should vibrate in one direction,

the Coriolis effect will cause a vibration perpendicular to the actuated vibration axis in case the system experiences a rotation. This system is called the Gyracc (Figure 2-20).

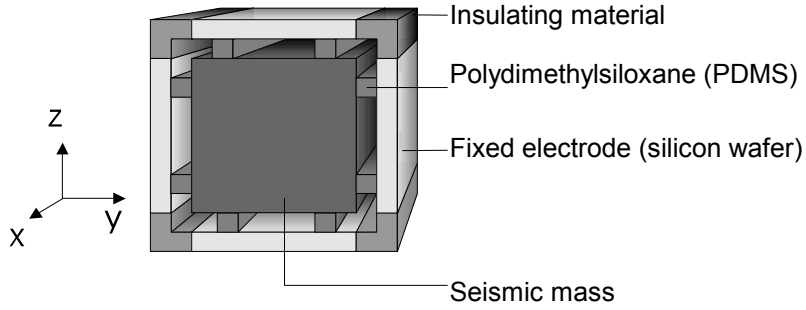

Figure 2-19: Schematic representation of the tri-axial accelerometer.

The major difference between the merry-go-round and the Gyracc is the way to throw the ball/mass to the opposite person/plate. It will be necessary to actuate the mass in such a way that it can be "thrown" forward and backward between the opposing plates. Possible methods are electrostatic actuation, piezoelectric actuation or electromagnetic actuation.

If the mass inside the box is vibrating and the system is experiencing a rate of turn in the same plane as the mass is vibrating, then the pathway of the mass is influenced by Coriolis forces. This pathway is shown in Figure 2-20.

The Coriolis force makes the seismic mass to move in a direction perpendicular to the actuated direction. This results in a vibration of the mass in the perpendicular direction. The combination of the applied vibration and of the movement due to the Coriolis force results in an elliptical movement of the mass.

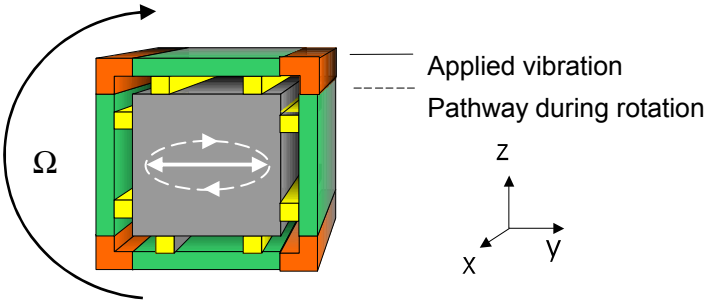

Figure 2-20: Movement of the mass inside the box with and without experiencing a rotation.

The width of the ellipse is a measure for the rate of turn. The direction of the rotation can be deduced from the clockwise or anti-clockwise displacement of the mass with respect to the silicon box. These parameters open the possibility to measure rate of turn by means of the vibrating mass. A detailed description of the movement of the mass is explained in Chapter 3.

2.8 Conclusions

The performances of different types of rate of turn sensors are shown and discussed. The different types of functioning do not cause a large difference in performance. On these grounds it is hard to say which type would be the best to use for the construction of a triaxial rate of turn sensor. Some sensors are able to measure in two, and some can only measure rate of turn in one direction. If one wishes to measure the rate of turn around three axes, then one has to combine at least a biaxial rate of turn sensor and a uniaxial rate of turn sensor. Thus increased power consumption and size are to be expected.

Paragraph 2.7 showed a concept of a single mass inertial sensor based on an existing triaxial accelerometer, which might be able to detect accelerations as well as rotations in 3 directions. The capabilities of the sensor are investigated in chapter 3. The construction of the sensor will be influenced by the actuation method of the mass. The two most likely actuation methods are electrostatic or electromagnetic. Research is needed to know which of the two is more appropriate (chapter 4). Chapter 5 will be devoted to simulations, chapter 6 to the actual design and construction, whilst chapter 7 will show the preliminary measurement results of two types of realized Gyracc 's.

2.9 References

[1] Reunert, M., I and Yoshida, B., II, "Fiber-optic gyroscopes: a new sensor for robotics and autonomous vehicles," Sensor Review, vol. 16, no. 1, pp. 32-34, 1996.

[2] Langmaid, C., "Vibrating structure gyroscopes," Sensor Review, vol. 16, no. 1, pp. 14-17, 1996.

[3] Söderkvist, J., "Micromachined Gyroscopes," Sensors and Actuators A, vol. 43 pp. 65-71, 1994.

[4] Shearwood, C., I, Ho, K. Y., I, Williams, C. B., II, and Gong, H., I, "Development of a levitated micromotor for application as a gyroscope," Sensors and Actuators A, vol. 83 pp. 85-92, Dec.1999.

[5] Reunert, M., I and Yoshida, B., II, "Fiber-optic gyroscopes: a new sensor for robotics and autonomous vehicles," Sensor Review, vol. 16, no. 1, pp. 32-34, 1996.

[6] Ferraris, F., Grimaldi, U., and Parvis, M., "Procedure for Effortless In-Field Calibration of Three-Axis Rate Gyros and Accelerometers," Sensors and Materials, vol. 7, no. 5, pp. 311-330, Dec.1994.

[7] Geiger, W., Folkmer, B., Merz, J., Sandmaier, H., and Lang, W., "A new silicon rate gyroscope," Sensors and Actuators A, vol. 73 pp. 45-51, Oct.1998.

[8] Kaienburg, J. R. and Schellin, R., "A novel silicon surface micromachining angle sensor," Sensors and Actuators A, vol. 73 pp. 68-73, Oct.1998.

[9] Sparks, D. R., Huang, X., Higdon, W., and Johnson, J. D., "Angular rate sensor and accelerometer combined on the same micromachined CMOS chip," Microsystem Technologies, vol. 4 pp. 139-142, Oct.1997.

[10] Barshan, B. and Durrant-Whyte, H. F., II, "Inertial Navigation Systems for Mobile Robots," IEEE Transactions on Robotics and Automation, vol. 11, no. 3, Oct.1994.

[11] Barshan, B. and Durrant-Whyte, H. F., II, "Evolution of a solid-state Gyroscope for Robotics Applications," IEEE Transactions on Instrumentation and Measurement, vol. 44, no. 1, June1994.

[12] Hashimoto, M., Cabuz, C., Minami, K., and Esashi, M., "Silicon resonant angular rate sensor using electromagnetic excitation and capacitive detection," Micromechanical Microengineering, vol. 5 Jan.1995.

[13] Tanaka, K., Mochida, Y., Sugimoto, M., Moriya, K., Hasegawa, T., Atsuchi, K., and Ohwada, K., "A micromachined vibrating gyroscope," Sensors and Actuators A, vol. 50 pp. 111-115, Sept.1995.

[14] Ansel, Y., Lerch, P., and Renaud, P., "Mode coupling aspects in a vibrating gyroscope," Sensors and Actuators A, vol. 62 pp. 576-581, 1997.

[15] Clarke, W. A., I, Howe, R. T., I, and Horowitz, R., II, "Surface Micromachined Z-Axis Vibratory Rate Gyroscope," IEEE, 1996.

[16] Bochobza-Degani, O., I, Seter, D. J., II, Socher, E., I, and Nemirovsky, Y., I, "A novel micromachined vibrating rate-gyroscope with optical sensing and electrostatic actuation," Sensors and Actuators A, vol. 82 pp. 54-60, Dec.1999.

[17] Kang, M. S., Youn, S. K., Cho, Y. H., and Lee, K. B., "Dynamic modelling of a Tuneable Microgyroscope," Sensors and Materials, vol. 10, no. 7, pp. 413-424, Dec.1997.

[18] Mengnian, I., Xue, W., II, Wang, X., I, Xie, J., I, Yang, G., I, and Wang, W., I, "Design and Characteristics of Two-Gimbals Micro-gyroscopes Fabricated with quasi-LIGA Proces," Transducers, vol. 97 1997.

[19] Junau, T., I, Pisano, A. P., II, and Smith, J. H., III, "Dual Axis Operation of a Mircomachined Rate Gyroscope," Transducers, vol. 97, no. 3B3.03, pp. 883-886, 1997.

[20] Kuisma, H., I, Ryhänen, T., II, Lahdenperä, J., I, Punkka, E., I, Ruotsalainen, S., I, Sillanpää, T., II, and Seppä, H. I., "A Bulk Micromachined Silicon Angular Rate Sensor," Transducers, vol. 97, no. 3B3.01, pp. 875-878, 1997.

[21] Sparks, D. R., Zarabadi, S. R., Johnson, J. D., Jiang, Q., Chia, M., Larsen, O., Higdon, W., and Castillo-Borelley, P., "A CMOS Integrated Surface Micromachined Angular Rate Sensor: It's Automotive Applications," Transducers, vol. 97, no. 3B1.04, pp. 851-854, 1997.

[22] Geiger, W., Folkmer, B., Sobe, U., Sandmaier, H., and Lang, W., "New Designs of Micromachanical Vibrating Rate Gyroscopes with Decoupled Oscillation Modes," Transducers, vol. 97, no. 4A2.10P, pp. 1129-1132, 1997.

[23] Geiger, W., Folkmer, B., Sobe, U., Sandmaier, H., and Lang, W., "The silicon angular rate sensor system DAVED (r)," Sensors and Actuators A, vol. 84 pp. 280-284, Jan.2000.

[24] An, S., I, Oh, Y. S., I, Park, K. Y., II, Lee, S. S., III, and Song, C. M., I, "Dual-axis microgyroscope with closed-loop detection," Sensors and Actuators A, vol. 73 pp. 1-6, Oct.1998.

[25] Li, Z., Yang, Z., Xiao, Z., Hao, Y., Wu, G., and Wang, Y., "A bulk micromachined vibratory lateral gyroscope fabricated with wafer bonding and deep trench etching," Sensors and Actuators A, vol. 83 pp. 24-29, Nov.1999.

[26] Fujita, T., Maenaka, K., Mizuno, T., Matsuoka, T., Oshima, T., and Maeda, M., "Disk-shaped bulk micromachined gyroscope with vacuum sealing," Sensors and Actuators A, vol. 82 pp. 198-204, Nov.1999.

[27] Tsuchiya, T., Kageyama, Y., Funabashi, H., and Jiro, S., "Vibrating gyroscope consisting of three layers of polysilicon thin films," Sensors and Actuators A, vol. 82 pp. 114-119, Oct.1999.

[28] Mochida, Y., Tamura, M., and Ohwada, K., "A micromachined vibrating rate gyroscope with independent beams for the drive and detection modes," Sensors and Actuators A, vol. 80 pp. 170-178, July1999.

[29] Kubena, R. L., Vickers-Kirby, D. J., Joyce, R. J., Stratton, F. P., and Chang, D. T., "A new tunneling-based sensor for inertial rotation rate measurements," Sensors and Actuators A, vol. 83 pp. -117, Dec.1999.

[30] Voss, R., I, Bauer, K., I, Ficker, W., I, Gleissner, T., I, Kupke, W., I, Rose, M., I, Sassen, S., I, Schalk, J., II, Siedel, H., I, and Stenzel, E., I, "Silicon Angular Rate Sensor for Automotive Applications with Piezoelectric Drive and Piezoresistive Read-out," Transducers, vol. 97, no. 3B3.02, pp. 879-882, 1997.

[31] He, G. H., Nguyen, C. T., Hui, J., Wong, M. S., Ng, A. F. L., Luong, H. C., and Ling, C., "A Piezoelectric-Plate Microgyroscope," Transducers, vol. 97, no. 3B3.06P, pp. 895-898, 1997.

[32] Sassen, S., I, Voss, R., I, Schalk, J., I, Stenzel, E., I, Gleissner, T., I, Gruenberger, R., I, Neubauer, F., I, Ficker, W., I, Bauer, K., I, and Rose, M., II, "Tuning fork silicon angular rate sensor with enhanced performance for automotive applications," Sensors and Actuators A, vol. 83 pp. 80-84, Dec.1999.

[33] Wakatsuki, N., Kudo, S., and Chiba, M., "Temperature self-compensated lithium tantalate piezoelectric gyroscope for higher sensitivity and stability," Ultrasonics, vol. 38 pp. 46-50, 2000.

[34] Lee, S. H., I, Hong, S. W., II, Kim, Y. K., I, and Lee, S. K., III, "A planar vibratory gyroscope using electromagnetic force," Sensors and Actuators A, vol. 65 pp. 101-108, Aug.1997.

[35] Grétillat, F., I, Grétillat, M. A., II, and Rooij, N. F., "Improved Design of a Silicon Micromachined Gyroscope with Piezoresistive Detection and Electromagnetic Exitation," IEEE Journal of Microelectromechanical Systems, vol. 8, no. 3, June1999.

[36] Lutz, M., Golderer, W., Gerstenmeier, J., Marek, J., Maihöfer, B., Mahler, S., Münzel, H., and Bishof, U., "A Precision Yaw Rate Sensor in Silicon Micromachining," Transducers, vol. 97, no. 3B1.03, pp. 847-850, 1997.

[37] M Hashimoto, et al., Silicon resonant angular rate sensor using electromagnetic excitation and capacitive detection, JMM 5, pp. 219-225, 1995

[38] Li, X., I, Bao, M., I, Yang, H., I, Shen, S., II, and Lu, D., I, "A micromachined piezoresistive angular rate sensor with a composite beam structure," Sensors and Actuators A, vol. 72 pp. 217-223, June1998.

[39] S.E. Alper, A planar gyroscope using a standard surface micromachining process, Eurosensors XIV, Copenhagen, Denmark, 2000, pp. 387-390

[40] Fujita, T., I, Mizuno, T., II, Kenny, R., I, Maenaka, K., I, and Maeda, M., I, "Two-Dimensional Micromachined Gyroscope," Transducers, vol. 97, no. 3B3.04, pp. 887-890, 1997.

[41] T. Fujita, et al., Disk-shaped bulk micromachined gyroscope with vacuum sealing, Sensors and Actuators A, vol. 82, pp. 198-204, 2000

[42] Kurosawa, M., I, Fukuda, Y., II, Takasaki, M., I, and Higuchi, T., II, "A Surface Acoustic Wave Gyro Sensor," Transducers, vol. 97, no. 3B2.03, pp. 863-866, 1997.

[43] J. C. Lötters, et al., Design, fabrication and characterization of a highly symmetrical capacitive triaxial accelerometer, Sensors and Actuators A, vol. 66, Issues 1-3, 1 April 1998, Pages 205-212

[44] Mizuno, J., I, Nottmeyer, K., II, Cabuz, I, Kobayashi, T., II, and Esashi, M., I, "Fabrication and characterization of a silicon capacitive structure for simultaneous detection of acceleration and angular rate," Transducers '95, Eurosensors IX, vol. 95 pp. 679-682, 1995.

[45] Verplaetse, C., "Inertial proprioceptive devices: Self-motion-toys and tools," IBM Systems Journal, vol. 35, no. 3, May1996, pp. 639-650

[46] Fang, H., I, Yang, J., I, and Jiang, Q., II, "Rotation-perturbed surface acoustic waves propagating in piezoelectric crystals," International Journal of Solids and Structures, vol. 37 pp. 4933-4947, June1999.

[47] Annovazzi, V. and Merlo, S., "Mechanical-thermal noise in micromachined gyros," Microelectronics Journal, vol. 30 pp. 1227-1230, 1999.

[48] Kasahara, M., I, Kurosu, S., I, Adachi, M., II, and Kamimura, K., III, "Analysis of a gyroscopic force measuring system in three-dimensional space," Measurement, vol. 28 pp. 235-247, Jan.2000.

[49] Dong, Y., I, Tay, F. E. H., II, Wen, Y., III, Yuan, X., I, and Chen, W. T., I, "Optimal design of a tuning fork gyroscope and its testing experiment", Journal of Modeling and Simulation of Microsystems, 2000. pp. 621-623.

Chapter 3

3 OPERATING PRINCIPLE OF THE GYRACC

In this chapter the different elements in the sensor are theoretically described and subsequently combined to predict the behavior of the Gyracc during the experience of accelerations and rates of turn.

3.1 Introduction

Knowledge of the behavior of the different elements in the inertial sensor makes it possible to understand the influence of the different design parameters. The Gyracc is based on a mass-spring-damper system. The model shown in Figure 3-1 is used to describe the dynamic and static behavior of the mass along a single axis.

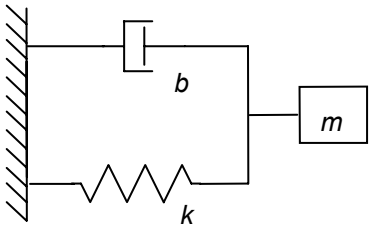

Figure 3-1: The mass-spring-damper model in one dimension, with m, k and b being the mass, spring and damping constant respectively.

In the Gyracc the mass can move along three axes. Such movements can be described as a superposition of the movement along the three separate axes [1]. The mechanical structure of the Gyracc is shown in Figure 3-2a and the movement of the mass of the Gyracc can be analyzed by the schematical mechanical model of Figure 3-2b.

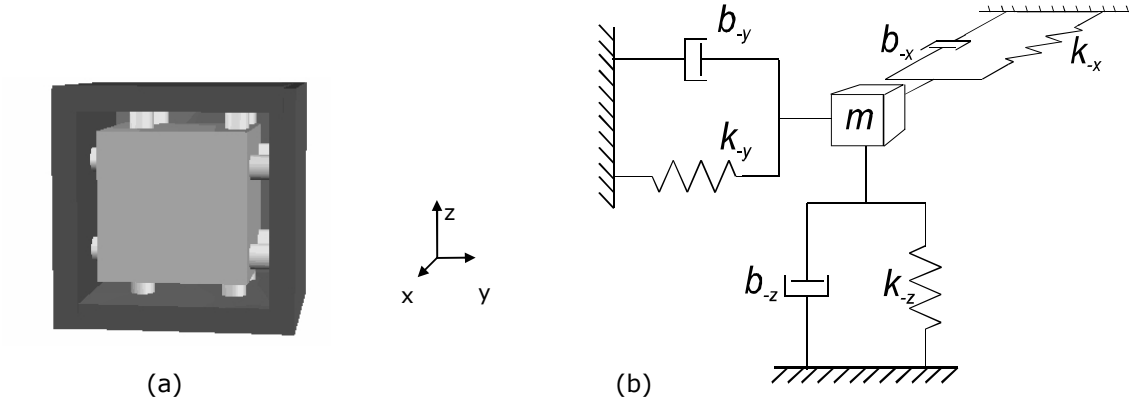

(a) (b)

Figure 3-2: (a) Cross section of the 3D inertial sensor and (b) schematical mechanical model.

The spring and damping constants along one separate axis are influenced by the springs and damping parameters of the two other axes. The mechanical behavior of the mass movement along one axis can be investigated if the total spring and damper constants along that axis are known. The characteristics of the mass, spring and damper are explained in the following sections.

3.1.1 The mass

The mass of the sensor is solid and cubic shaped with rib length *l*. It is made of a material with a certain mass density *ρ*; therefore the weight *m* of the mass is:

$$m = \rho \cdot l^3 \tag{3-1}$$

m	=	*mass weight*	*[kg]*
ρ	=	*density*	*[kg/m^3]*
l	=	*rib length*	*[m]*

3.1.2 The spring

The height (*d*) of a spring is modified by the application of a mechanical force (*F*) to this spring. The ratio between the change in spring height and the applied force is referred to as the spring constant (k).

$$k = \frac{F}{\Delta d} \tag{3-2}$$

k	=	*spring constant*	*[N/m]*
F	=	*force*	*[N]*
Δd	=	*change in height of the spring*	*[m]*

This relation holds as long as the spring behaves linearly (Hook's law) and is therefore only applicable for a limited change in the height of the spring (Δd). The force necessary to compress or strain the PDMS springs in the Gyracc is a non-linear function of Δd. This type of spring material is almost free of viscoelastic behavior, creep and stress relaxation. The mathematical expression for a spring made of PDMS is shown in Equation (3-3) [2].

$$F_{PDMS} = A_{PDMS} \cdot G_{PDMS} \cdot \left(\left(1 + \frac{\Delta d}{d_0} \right) - \frac{1}{\left(1 + \frac{\Delta d}{d_0} \right)^2} \right) \tag{3-3}$$

F_{PDMS}	=	*the tensile force acting on the spring*	*[N]*
A_{PDMS}	=	*the area of the PDMS*	*[m^2]*
G	=	*shear modulus of the PDMS*	*[N/m^2]*
d_0	=	*height of the PDMS in rest*	*[m]*
Δd	=	*change in height of the spring*	*[m]*

The first order Taylor approximation of this equation is the linear equivalent of this non-linear equation.

$$F_{PDMS,LIN} = \frac{3GA_{PDMS}\Delta d}{d_0} \tag{3-4}$$

Figure 3-3 shows the non-linear function of the compression and extension as a function of the applied force, using equation (3-3). The difference between a compressive and an extension force is defined by the change in the sign of the applied force [F]. The change in thickness of the rubber elastic material [Δd] is expressed likewise.

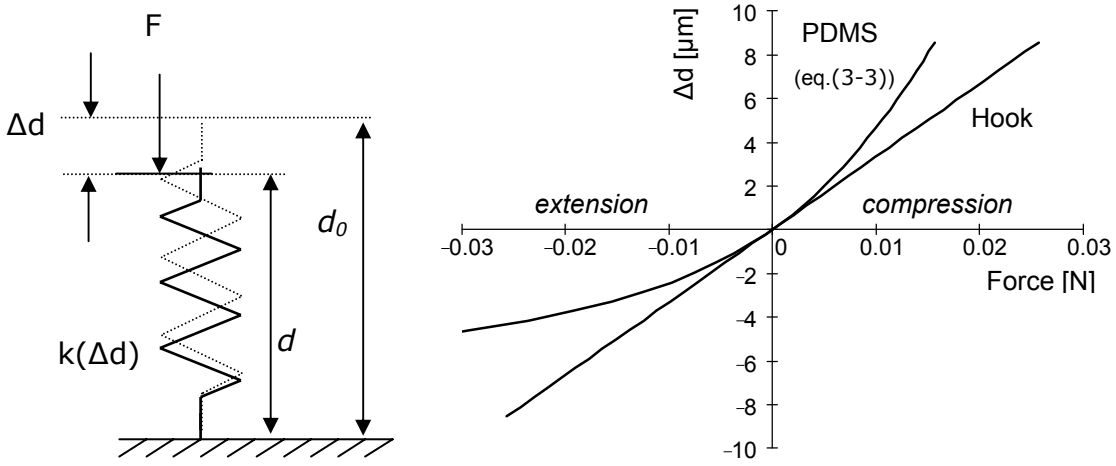

Figure 3-3: The compression of a linear spring (Hook) and a non-linear PDMS spring as a function of the applied force, using G=*250 kPa,* d_0 *= 10 µm and* A_{PDMS} *=4×10^{-8} m^2.*

Figure 3-3 shows that it is harder to compress the PDMS spring a certain distance than to extend it.

3.1.2.1 Springs in series

This section describes the mechanical behavior of two springs connected in series, as shown in Figure 3-4.

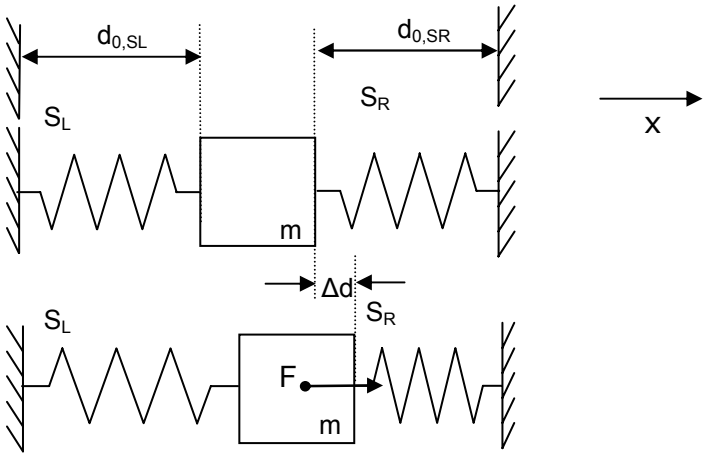

Figure 3-4: The mass is double-sided suspended by springs with equal initial spring constants (k_0).

The mass in Figure 3-4 is displaced with respect to the surrounding walls by for instance an inertial force which occurred while the system is experienced acceleration in the x-axis. The total force within the mass-spring system, in the x-axis direction is zero.

$$\vec{F}_{mass}(x) + \vec{F}_{SL}(x) + \vec{F}_{SR}(x) = \vec{0} \tag{3-5}$$

with

$\vec{F}_{SL}$	=	*Force on spring on the left*	*[N]*
$\vec{F}_{SR}$	=	*Force on spring on the right*	*[N]*

In case the spring on the left is extended by a length Δd, then the spring on the right is compressed over a length Δd, because the springs are mechanically interconnected by the mass. By combining equation (3-3) and equation (3-5) the force, as a function of a certain displacement, acting on the mass is derived.

$$F_{mass}(x) = F_{PDMS\_L}(x) - F_{PDMS\_R}(x)$$

$$F_{mass} = GA_{PDMS\_SR}\left(\left(1+\frac{\Delta d}{d_{0,SR}}\right)-\frac{1}{\left(1+\frac{\Delta d}{d_{0,SR}}\right)^2}\right) - GA_{PDMS\_SL}\left(\left(1+\frac{-\Delta d}{d_{0,SL}}\right)-\frac{1}{\left(1+\frac{-\Delta d}{d_{0,SL}}\right)^2}\right) \tag{3-6}$$

If the springs on the left and right side of the seismic mass are identical then the equation can be rewritten as

$$F_{mass} = GA_{PDMS}\left[\frac{2\cdot\Delta d}{d_0}+\frac{1}{\left(1-\frac{\Delta d}{d_0}\right)^2}-\frac{1}{\left(1+\frac{\Delta d}{d_0}\right)^2}\right] \tag{3-7}$$

The displacement of the mass as a function of the spring compression is shown in Figure 3-5. The data used in the calculations are: the shear elastic modulus of PDMS G = 250 kPa, the nominal thickness (d_0) of the PDMS structures is 10 µm and the area of a PDMS structure (A_{PDMS}) is 4×10^{-8} m^2.

The first order Taylor approximation of the previous equation yields:

$$F_{mass,LIN} = \frac{6\cdot GA_{PDMS}\Delta d}{d_0} \tag{3-8}$$

which is the linear equivalent of the non-linear equation. As a result the spring-constant for the two springs in series is:

$$k_0 = \frac{6\cdot GA_{PDMS}}{d_0} \tag{3-9}$$

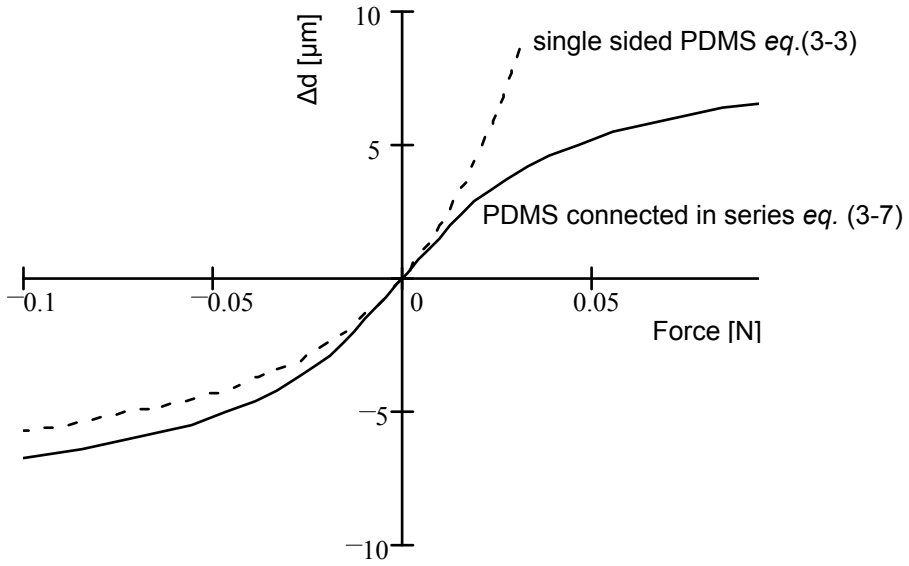

Figure 3-5: The displacement of the mass as a function of the applied force.

3.1.2.2 Linear displacement range

A truly linear spring does not exist in practice, but all springs can be defined as being linear for a limited compression/extension range. The definition of the linear spring range is:

The linear spring range is the range of compression/extension around the initial spring height in which the compression/extension of the spring as a function of the applied force does not deviate more than 1% from a spring obeying Hook's law (a true linear spring).

Thus, a spring is linear in a certain range in case the following equation holds:

$$\left|\left(\frac{\Delta d_{true}(F)}{\Delta d_{lin}(F)} - 1\right) \times 100\,\%\right| \leq 1\,\% \qquad (3\text{-}10)$$

with

F	=	*the force applied to the spring*	*[N]*
Δd_{true}	=	*change in height of the used spring*	*[m]*
Δd_{lin}	=	*change in height of a linear spring*	*[m]*

This equation is equivalent to:

$$\left|\left(\frac{F_{true}(\Delta d)}{F_{lin}(\Delta d)} - 1\right) \times 100\,\%\right| \leq 1\,\% \qquad (3\text{-}11)$$

with

Δd	=	*the applied spring compression/extension*	*[N]*
F_{true}	=	*the force necessary to realize the compression in the used spring*	*[m]*
F_{lin}	=	*the force necessary to realize the compression in a linear spring*	*[m]*

Figure 3-6 shows the linear range of a single spring and of two springs in series.

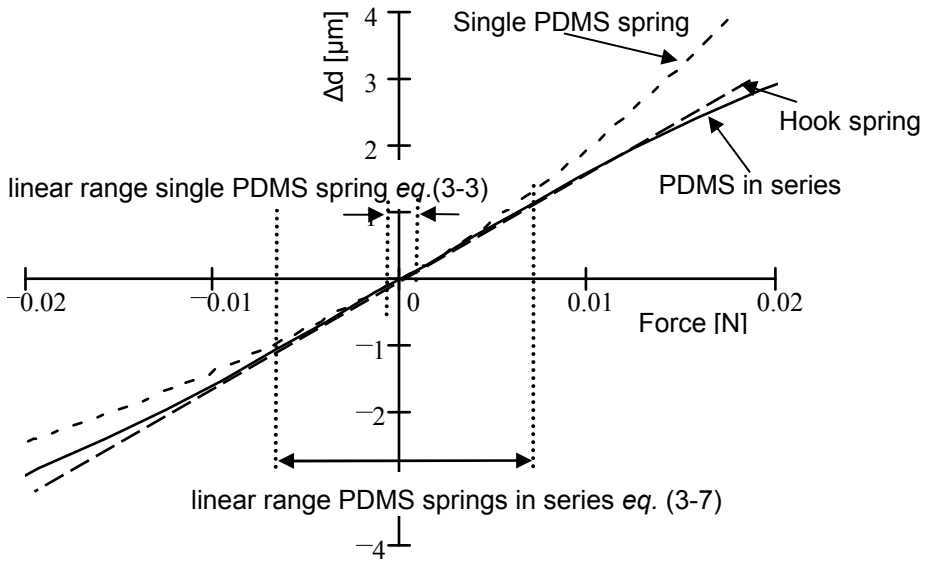

Figure 3-6: The linear range of the non-linear spring.

Superposition of equation (3-3) and (3-4) in equation (3-11) shows that the single PDMS spring behaves as a linear spring for:

$$-0{,}01 \cdot d_0 \le \Delta d \le d_0 \cdot 0{,}01 .$$

Superposition of equation (3-7) and (3-8) in equation (3-11) shows that the PDMS springs in series behave as a linear spring for:

$$-0{,}09 \cdot d_0 \le \Delta d \le d_0 \cdot 0{,}09 .$$

Thus due to the series connection of the PDMS springs according to the configuration, shown in Figure 3-4, the linear range is extended with a factor of nine. Figure 3-7 shows its behavior for a wider range.

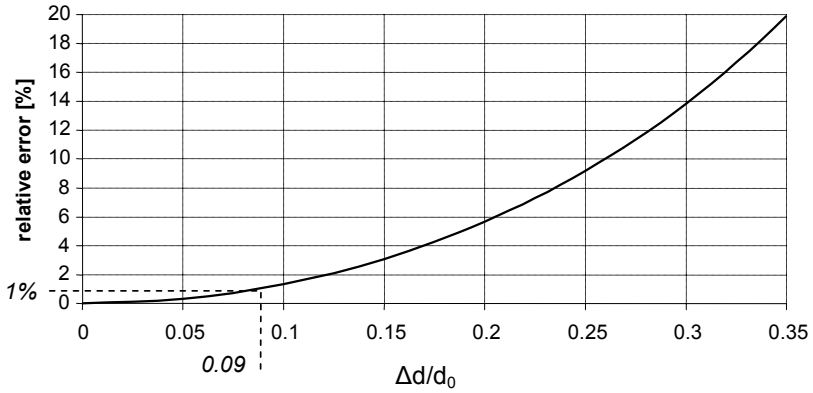

Figure 3-7: The relative error in the spring compression as a function of the relative spring compression.

From this graph it can be deduced that a 25% compression of the PDMS will result in a 10% error in the displacement as compared to a true linear spring.

3.1.2.3 Pre-compression

A displacement of the mass might result in loss of contact of the mass from the springs as illustrated in Figure 3-8.

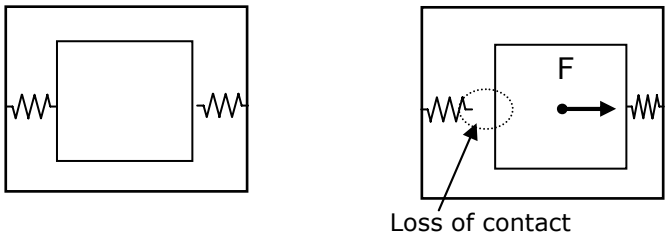

Figure 3-8: The spring-mass contact for different mass positions in the case of a non-mechanical interconnection between the mass and the springs.

To prevent this situation, the springs are made higher than the distance between the mass and the inner box walls. This results in a pre-compression of the springs in the sensor, even if the mass does not experience a force. The ratio between the change in height of the spring caused by the pre compression (Δd_{PCR}) and the initial height of the spring (d_0) is referred to as the pre-compression ratio (PCR) of the spring.

$$PCR = \frac{\Delta d_{PCR}}{d_0} \tag{3-12}$$

PCR	*the pre-compression ratio*	*[-]*
Δd	*change in length due to the compression of the spring*	*[m]*
d_0	*the initial height of the unloaded spring*	*[m]*

The pre-compression has its influence on the relation between the resulting mass displacement and the experienced force. A displacement of the mass will be added to the amount of pre-compression of the springs:

$$\Delta d_{total,L} = d_0 \cdot PCR - \Delta d \text{ and } \Delta d_{total,R} = d_0 \cdot PCR + \Delta d \tag{3-13}$$

The force acting on the mass, enclosed by two springs ($F_{mass,enc}$), as a function of the displacement of the mass (equation (3-7)) can therefore be rewritten as:

$$F_{mass,enc} = GA_{PDMS}\left(\frac{2\Delta d}{d_0} - \frac{1}{\left(1+\frac{d_0 \cdot PCR + \Delta d}{d_0}\right)^2} + \frac{1}{\left(1+\frac{d_0 \cdot PCR - \Delta d}{d_0}\right)^2}\right) \tag{3-14}$$

The influence of the pre-compression of the PDMS structures on the seismic mass displacement as a function of the applied force is shown in Figure 3-9.

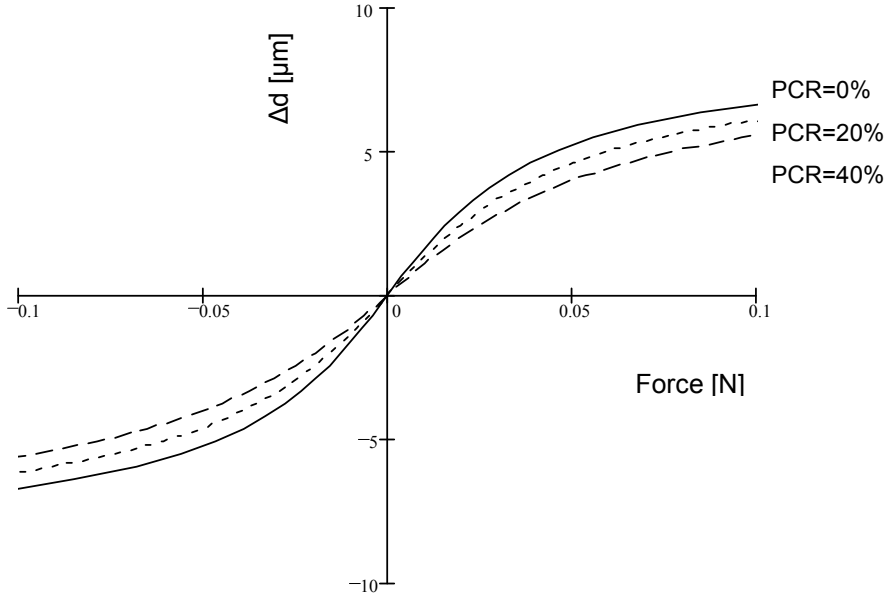

Figure 3-9: Displacement of the seismic mass as a function of applied force for different amounts of pre-compression.

It should be noted that the height of the springs is for all three pre-compressed states the same, but the initial height is different: 10, 12 and 14 micrometer respectively. The first order approximation of equation (3-14) results in:

$$F_{mass,enc,LIN} = \frac{2GA_{PDMS}}{d_0}\left(1 + \frac{2}{(1-PCR)^3}\right)\cdot \Delta d \qquad (3\text{-}15)$$

As a result the linearized spring-constant for the spring-construction in series is:

$$k_{enc,LIN} = \frac{2GA_{PDMS}}{d_0}\left(1 + \frac{2}{(1-PCR)^3}\right) \qquad (3\text{-}16)$$

With substitution of equation (3-14) and (3-15) in equation (3-11), the linear range of the springs in series can be calculated. The linear range slightly decreases with a higher PCR. Note that for PCR=0 equation (3-16) becomes equation (3-9), with $k_{enc,lin} = k_{0.}$

3.1.2.4 Shear force

Shear is a type of strain, which is represented by the sliding of planes which are parallel to a given plane, see Figure 3-10.

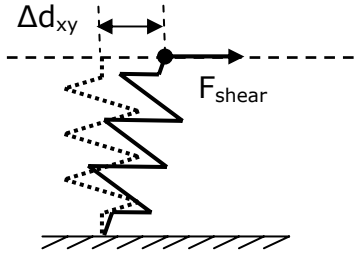

Figure 3-10: Shear force acting on a spring.

The shear force necessary for a displacement in the transverse direction is 1/3 [th] of the force necessary for an equal displacement in the compression direction [2]. Therefore the shear force acting on the two springs enclosing the mass at two opposite sides during a transverse displacement is:

$$F_{shear,enc} = \frac{GA_{PDMS}}{3}\left(\frac{2\Delta\Delta_{xy}}{d_0} - \frac{1}{\left(1+\frac{d_0 \cdot PCR + \Delta d_{xy}}{d_0}\right)^2} + \frac{1}{\left(1+\frac{d_0 \cdot PCR - \Delta d_{xy}}{d_0}\right)^2}\right) \quad (3\text{-}17)$$

G = *shear modulus of the PDMS* [N/m^2]
A_{PDMS} = *area of the PDMS spring on one side of the mass* [m^2]
Δd_{xy} = *top of the spring displaced in the transverse plain* [m]

The linear approximation of this function is the first order Taylor approximation of the shear stress on a single spring:

$$F_{shear,enc} = \frac{2 \cdot GA_{PDMS}}{3 \cdot d_0}\left(1 + \frac{2}{(1-PCR)^3}\right) \cdot \Delta d \quad (3\text{-}18)$$

3.1.2.5 The total spring constant in the inertial sensor

The force that displaces the seismic mass with respect to the inner walls of the box is fully absorbed by the PDMS springs surrounding the mass.

$$F_{total} = F_x + F_y + F_z \quad (3\text{-}19)$$

If for example the mass is experiencing a force along the x-axis of the inertial sensor then the springs in this direction will be extended or compressed and the springs in the perpendicular direction (y- and z-axes) will experience shear displacement.

$$F_{total} = F_{mass,enc} + 2 \times F_{shear,enc} \quad (3\text{-}20)$$

The total force absorbed by the springs as a function of the mass displacement (Δd) with respect to its original position is:

$$F_{mass} = GA_{PDMS}\left(\frac{2\Delta d_{xy}}{d_0} - \frac{1}{\left(1+\frac{d_0 \cdot PCR + \Delta d_{xy}}{d_0}\right)^2} + \frac{1}{\left(1+\frac{d_0 \cdot PCR - \Delta d_{xy}}{d_0}\right)^2}\right) \cdot \left(1+\frac{2}{3}\right) \quad (3\text{-}21)$$

The linear approximation of this equation is:

$$F_{total} = 10 \cdot \frac{GA_{PDMS}}{3 \cdot d_0}\left(1 + \frac{2}{(1-PCR)^3}\right) \cdot \Delta d \quad (3\text{-}22)$$

Therefore the spring constant is:

$$k_{total} = 10 \cdot \frac{GA_{PDMS}}{3 \cdot d_0}\left(1 + \frac{2}{(1-PCR)^3}\right) \qquad (3\text{-}23)$$

This equation holds for the linear displacement region of the displacing mass.

3.1.3 The damper

The distance between the mass and the inner walls of the box is filled with air, causing a certain amount of damping. Furthermore the springs themselves show some damping during dynamic use. The damping in the system is thus a combination of the air flowing between the mass and the box surrounding the mass and the damping in the spring material. The connection layer between the springs and the housing, the interconnection layer between the springs and the mass and the housing itself are expected to be rigid without introducing damping. The damping origins are shown in Figure 3-11.

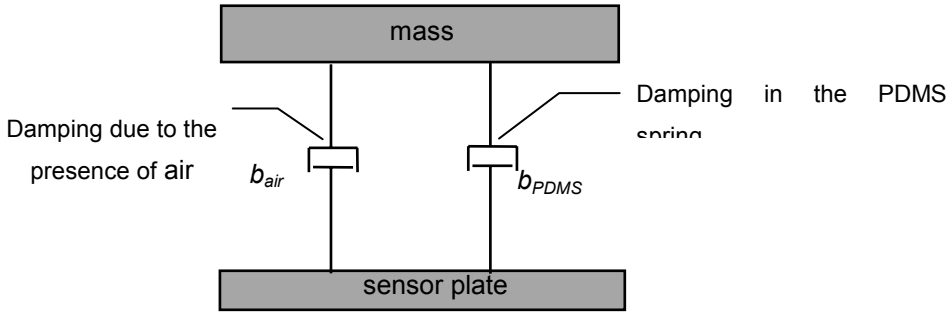

Figure 3-11: Origins of damping.

The damping results in a counter force on the mass equal to:

$$F_d = -b.v$$

b	*the damping constant*	*[N.s/m]*
v	*the displacement velocity of the mass with respect to the surrounding box*	*[m/s]*

The damping that the mass experiences is a summation of different damping mechanisms. The damping due to air is a summation of the radiation resistance, lateral film damping and squeeze film damping, as discussed in the next paragraphs.

3.1.3.1 Radiation resistance

The vibration of the mass in air experiences a frequency depending resistance. This is independent of the presence of the box walls and is valid for $2.\pi.l / \lambda << 1$, with l the rib length of the mass and λ the wave length of sound in air [3].

$$b_{RR} = \frac{\rho_a \omega^2 l^4}{8c} \qquad (3\text{-}24)$$

b_{RR}	*damping constant due to radiation resistance*	*[N.s/m]*
ρ_a	*the density of air*	*[kg/m^3]*
c	*the velocity of sound in air*	*[m/s]*
λ	*wavelength of sound*	*[m]*
ω	*frequency of vibration of the mass*	*[rad/s]*
l	*rib length of mass*	*[m]*

3.1.3.2 Lateral film damping

When the seismic mass is vibrating in parallel with the fixed capacitor plate, the air in the air gap starts vibrating with the velocity of the seismic mass at the interface with the seismic mass and with velocity 0 at the interface with the fixed capacitor plate (box wall). The velocity gradient in the air causes a damping mechanism, which is called lateral film damping. The resulting damping constant is [1]:

$$b_{LFD} = \frac{\eta_{eff} l^2}{d} \tag{3-25}$$

with

$$\eta_{eff} = \frac{\eta}{1 + 9.638 \cdot \left(\frac{\lambda_0 P_0}{d P_A} \right)^{1.159}}$$

η_{eff}	*the effective gas viscosity constant*	*[Pa·s]*
η	*the gas viscosity constant at 101Pa (18.5×10^{-6} Pa.s)*	*[Pa·s]*
l	*rib length of the mass*	*[m]*
d	*distance between capacitor plates*	*[m]*
λ_0	*mean free path of the gas at pressure P_0 (58.5×10^{-9} m)*	*[m]*
P_0	*atmospheric pressure (101k Pa)*	*[Pa]*
P_a	*the actual pressure*	*[Pa]*

3.1.3.3 Squeeze film damping

Because there is a small air gap between the seismic mass and the fixed capacitor plates, the vibration of the mass causes an air flow in or out of the capacitor: when the mass moves towards the capacitor plate the air is squeezed out of the capacitor and when the mass moves away from the capacitor plate the air is forced to flow into the capacitor. This airflow causes damping. The corresponding damping mechanism is called squeeze film damping. The squeeze film damping constant b_{SFD} [N·s/m] can be described as [4]:

$$b_{SFD} = \frac{12 \eta_{eff} A^2}{\pi^3 d^3} \tag{3-26}$$

with

A	*the area of the capacitor plate*	*[m^2]*

Equation (3-26) holds for two plates surrounded by a constant pressure. However in the cube with a box design, the air surrounding the nearing plates is not a fixed pressure. Instead, the air pushed away by the plates cannot freely move into the surroundings but flows up and down through the side channels. These channels set the boundary conditions for the damping. Therefore the influence of the side channels on the squeezed film damping is investigated in more detail in Appendix A. It shows that for a fully closed box surrounding the mass the damping dramatically increases for a distance between the capacitor plates smaller than 20 micrometer.

3.1.3.4 Damping in the rubber elastic material

All materials have a certain phase shift between an applied stress and the resulting strain. The phase shift is represented by the loss tangent *tanδ* of the material. Most rubber elastic materials have a very low loss tangent, *tanδ* << 0.001 [5]. The expression for the damper constant of a rubber elastic material b_{PDMS} [N.s/m] is found by:

$$b_{PDMS} = \tan\delta \cdot \sqrt{k \cdot m} \tag{3-27}$$

3.1.3.5 Total damping in the sensor

The radiation resistance, the lateral film damping, the squeezed film damping and the damping inside the PDMS springs all contribute to the damping of the mass vibration. If for example the seismic mass of the inertial sensor is vibrating in the x-axis, then the mass experiences squeeze film damping on both sides of the mass in the x-axis direction and lateral film damping will be experienced along planes in the y- and z-axes. In addition radiation resistance and damping in the PDMS springs will be experienced:

$$b_{total} = b_{RR} + 4 \times b_{LFD} + 2 \times b_{SFD} + b_{PDMS} \tag{3-28}$$

For a distance between the mass and the inner box walls of $5\mu \le d_0 \le 30\mu m$, $b_{SFD} >> b_{LFD}$, $b_{SFD} >> b_{PDMS}$ and $b_{SFD} >> b_{RR}$. Therefore the total damping within the system can be approximated by:

$$b_{SFD} = \frac{24.\eta_{eff} A^2}{\pi^3 d^3} \tag{3-29}$$

3.2 The mass-spring-damper system

In the previous section a mass, a spring and a damper have been described separately with their physical characteristics. The combination of these components in a mass-spring-damper system is characterized in terms of resonance frequency and mechanical quality factor.

3.2.1 Resonance frequency

The resonance frequency (ω_0) of the vibrating mass is [6]:

$$\omega_0 = \frac{1}{2m}\sqrt{4km - b^2} \tag{3-30}$$

ω_0	*the frequency at which the mass is vibrating*	*[rad/s]*
m	*the mass of the seismic mass*	*[kg]*
k	*the spring constant*	*[N/m]*
b	*the damping constant*	*[Ns/m]*

The resonance frequency of the mass decreases, under the influence of damping. Its influence is shown in Figure 3-12.

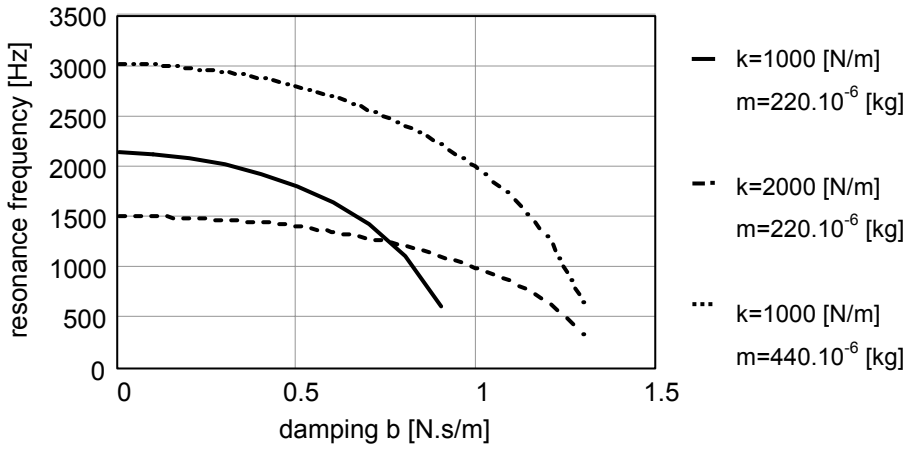

Figure 3-12: The resonance frequency as a function of damping and mass

The resonance frequency of the system while it is not experiencing any damping is its natural frequency.

$$\omega_n = \sqrt{\frac{k}{m}} \tag{3-31}$$

Figure 3-12 shows that for damping constants below 0.3 N.s/m the resonance frequency is almost equal to the natural frequency and can then be estimated by means of equation (3-31).

3.2.2 Mechanical quality factor

The quality factor (*Q*) is a measure for the amount of energy lost during a mechanical vibration. The amount of energy lost during a vibration is due to the damping in the system [6].

$$Q = \frac{\textit{maximum stored energy per period}}{\textit{lost energy per period}} \tag{3-32}$$

With the system parameters this is written as [6]:

$$Q = \frac{\sqrt{k.m}}{b} \tag{3-33}$$

The quality factor can be determined from a Bode diagram being the ratio between the displacement of the mass at its natural frequency and the displacement during static actuation, with the same actuation force.

$$Q = \frac{\hat{x}_n}{\hat{x}_{static}} \tag{3-34}$$

$\hat{x}_n$ *amplitude of vibration at its natural frequency* *[m]*
$\hat{x}_{static}$ *amplitude of displacement during statically applied force* *[m]*

The quality factor can also be determined from a damped vibration. In this case the quality factor is:

$$Q = \frac{\pi}{\ln 2} \cdot \frac{T_{1/2}}{T} \approx 4.5 \cdot \frac{T_{1/2}}{T} \tag{3-35}$$

with

$T_{1/2}$ *time in which the amplitude drops to half its original value* *[s]*
T *period time of the vibration* *[s]*

3.2.3 Amplitude and phase shift as a function of damping

The displacement of the mass (Δd_X) as a function of the frequency is described with [6]:

$$\Delta d_X = \frac{F_X}{k_{total}} \cdot \frac{1}{j^2 \frac{\omega^2}{\omega_n{}^2} + \frac{1}{Q} \cdot j \frac{\omega}{\omega_n} + 1} \tag{3-36}$$

The amplitude and phase of this complex number are:

$$\Delta \hat{d}_X = \frac{\hat{F}_X}{k_{total}} \cdot \frac{1}{\sqrt{\left(1 - \frac{\omega^2}{\omega_n{}^2}\right)^2 + \left(\frac{1}{Q} \cdot \frac{\omega}{\omega_n}\right)^2}} \tag{3-37}$$

$$\varphi = \tan^{-1}\left[\frac{\frac{1}{Q} \cdot \frac{\omega}{\omega_n}}{1 - \left(\frac{\omega}{\omega_n}\right)^2}\right] \tag{3-38}$$

Figure 3-13 shows the graphical representation of these equations as a function of the applied frequency for several values of Q, with m=220mg and k=800 N/m.

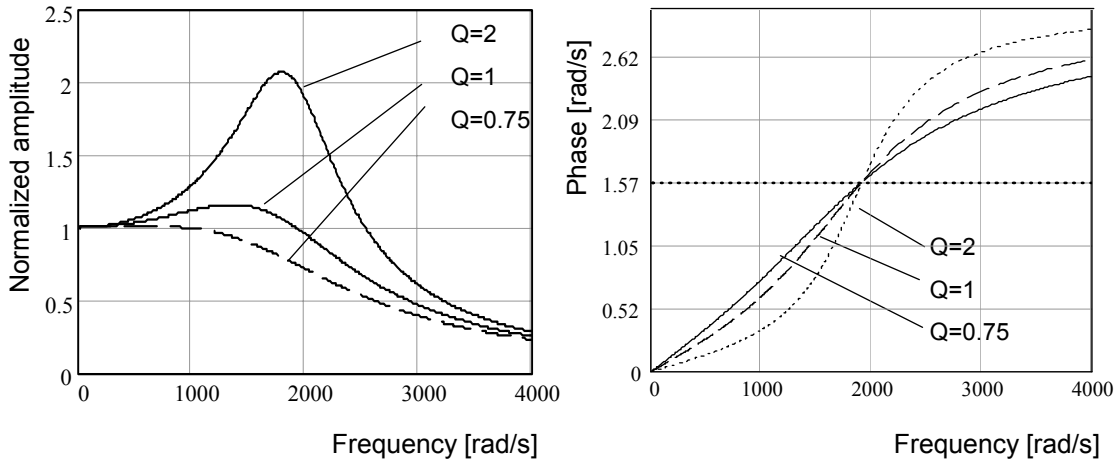

Figure 3-13: The normalized amplitude and phase diagram of the vibrating mass as a function of the applied frequency, ω_n= 1907 $^{rad}/_{s}$.

Figure 3-13 shows that the phase shift between the force applied to the mass and its actual displacement is 1/2 π at the natural resonance frequency and approaching π for frequencies far above the natural resonance frequency. Furthermore the graphs show that the phase difference between the actuation vibration force and the realized actuated vibration for systems with a higher quality factor is more sensitive to small changes in the actuation frequency.

3.3 The Coriolis effect

Chapter 2 showed the origin of the Coriolis effect. The Coriolis effect is responsible for the mass displacement orthogonal to the direction of vibration, during the experience of a rotation. The mathematical description for this force is shown in equation (3-39):

$$\vec{F}_c(t) = -2m.\vec{\Omega}(t) \times \vec{v}(t) \tag{3-39}$$

$\vec{F_c}$	*the Coriolis force acting on the mass*	*[N]*
m	*the mass*	*[kg]*
$\vec{\Omega}$	*the experienced rate of turn*	*[rad/s]*
$\vec{v}$	*velocity of the mass*	*[m/s]*

In case the mass is vibrating in the x direction in a sinusoidal way, the vibration can be expressed as:

$$\vec{x}(t) = \vec{\hat{x}} \sin(\omega t) \tag{3-40}$$

The velocity of the mass:

$$\vec{v}(t) = \frac{\delta \vec{x}}{\delta t} = \vec{\hat{x}}.\omega \cos(\omega t) \tag{3-41}$$

This results in a Coriolis force of:

$$\vec{F}_c(t) = -2m.\vec{\Omega}(t) \times \vec{\hat{x}}\omega \cos(\omega t) \tag{3-42}$$

If $\vec{\Omega}$ is in the z direction (meaning a rate of turn around the z-axis), then the Coriolis force in the y direction is equal to:

$$F_{c,y}(t) = -2m.\Omega(t)\hat{x}\omega \cos(\omega t) \tag{3-43}$$

Introducing this force in equation (3-36) results in;

$$\Delta d_{c,y}(t) = \frac{-2m.\Omega(t)\hat{x}\omega \cos(\omega t)}{k_{total}} \cdot \frac{1}{j \cdot \frac{1}{Q} \cdot \frac{\omega}{\omega_n} - \frac{\omega^2}{\omega_n{}^2} + 1} \tag{3-44a}$$

The amplitude of this complex variable is:

$$\Delta \hat{d}_{c,y}(t) = \frac{-2m.\Omega(t)\hat{x}\omega}{k_{total}} \cdot \frac{1}{\sqrt{\left(1 - \frac{\omega^2}{\omega_n{}^2}\right)^2 + \left(\frac{1}{Q} \cdot \frac{\omega}{\omega_n}\right)^2}} \tag{3-44b}$$

Figure 3-14 shows the Coriolis amplitude of a vibrating mass as a function of the experienced rate of turn.

Simulation parameters for Figure 3-14

System parameter	Symbol	
spring constant	K	8685 N/m
actuation amplitude	$\hat{x}$	1 µm
vibrating frequency	Ω	2π.1000
(resonance)		rad/s
quality factor	Q	1
mass	M	220 mg

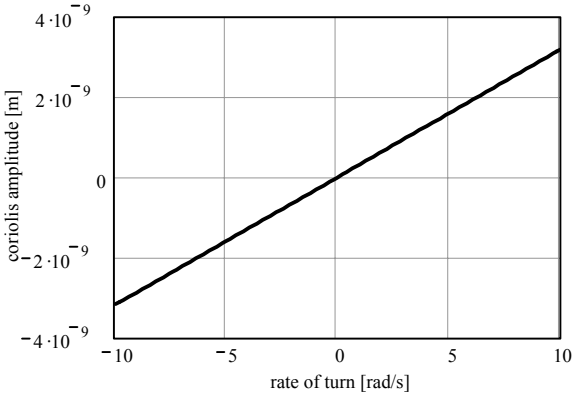

Figure 3-14: The Coriolis displacement amplitude of the mass as a function of the experienced rate of turn.

The mass displacement due to the Coriolis force is $0.3 \cdot 10^{-9}$ [m] for an experienced rate of turn of 1 rad/s. So for a symmetric vibrating system the displacement in the Coriolis direction is 3/10,000st of the amplitude of the applied vibration for the given parameters. A graphical explanation of the mass behaviour is shown in Figure 3-15.

The applied displacement along the x-axis $x(t)=1.10^{-6}.\sin(2\pi.1000.t)$

[equation (3-40)]

The resulting Coriolis force due to a rate of turn of Ω= 1[rad/s] experienced in the y-axis.

[equation (3-43)]

The resulting displacement of the mass due to the Coriolis force in the y axis for Ω = 1 [rad/s] (and Ω = -1 [rad/s]), in the case that the frequency of the applied vibration is equal to the natural vibration frequency in the Coriolis axis direction [equation (3-44)]. The displacement in the Coriolis direction is 180^0 out of phase with the applied vibration.

The displacement of the mass due to the Coriolis force in the y-axis for Ω = 1 [rad/s] at a frequency below the natural vibration frequency in the Coriolis axis direction (solid line). Due to the [equation (3-44)]

($\omega=\omega_n$: dashed line)

The displacement of the mass due to the Coriolis force in the y-axis for Ω = 1 [rad/s] at a frequency above the natural vibration frequency in the Coriolis axis direction (solid line). [equation (3-44)]

($\omega=\omega_n$: dashed line)

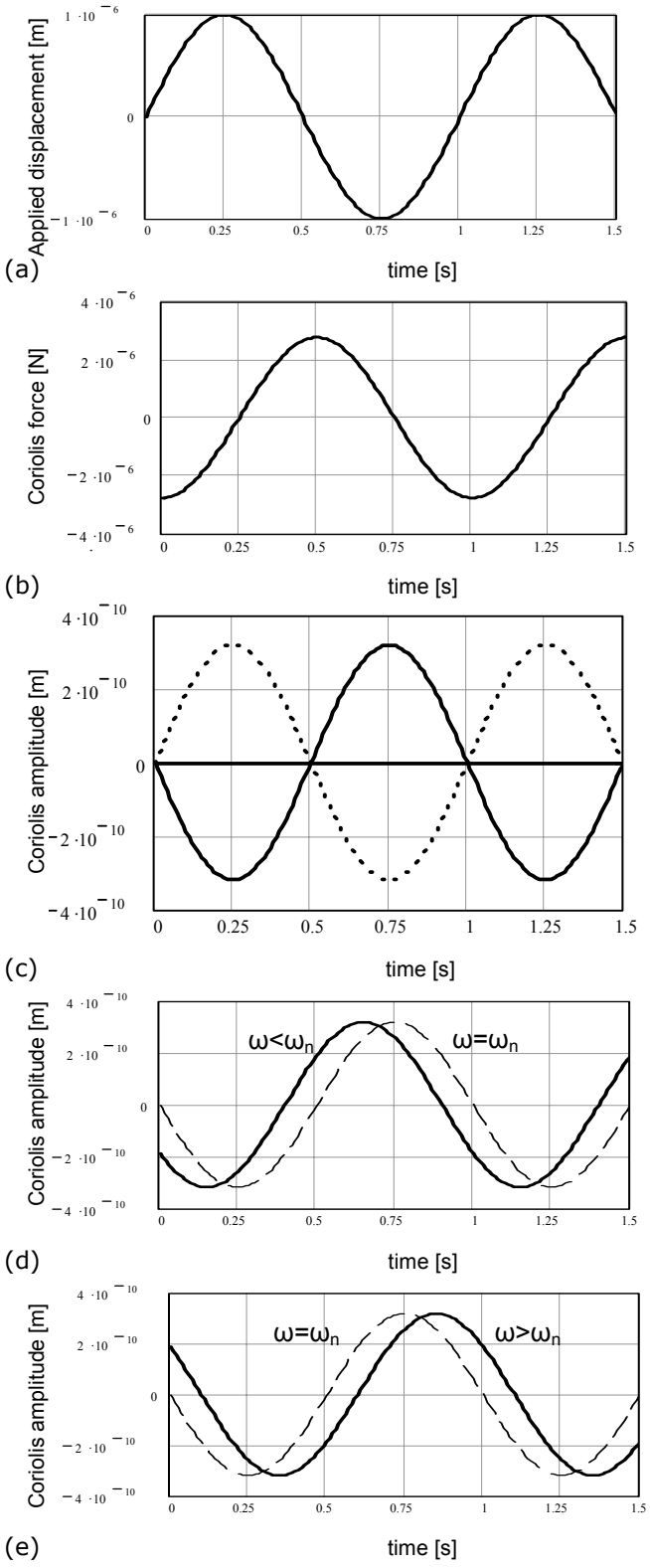

Figure 3-15: The stepwise development of the applied vibration to a Coriolis signal.

3.4 Combined acceleration and rate of turn measurement

The position of the mass in the inertial sensor is a superposition of the vibration due to the actuator, the Coriolis effect, gravity and inertial forces. The actuation

vibration of the mass and the Coriolis vibration have a chosen frequency (e.g. 1 kHz). The change in the gravity and other inertial accelerations take place well below the vibrating frequency of the mass and free movements of the mass appear at the resonance frequency of the system. Equation (3-45) shows the summation of the total force acting on the mass, which induces the resulting displacement of the mass.

$$F_{m,x,y,z}(t) = F_{a,x,y,z}(t) + F_{g,x,y,z}(t) + F_{v,x}(t) + F_{C,y,z}(t) + F_{r,x,y,z}(t) \qquad (3\text{-}45)$$

with

$F_{a,x,y,z}(t)$	*= Force experienced on the mass due to externally applied accelerations*	*[N]*
$F_{g,x,y,z}(t)$	*= Force experienced on the mass due to gravity*	*[N]*
$F_{v,x}(t)$	*= Force experienced on the mass due to applied vibration for rate of turn sensing*	*[N]*
$F_{C,y,z}(t)$	*= Force experienced by the mass due to Coriolis acceleration*	*[N]*
$F_{r,x,y,z}(t)$	*= Force experienced on the mass due to the damped natural frequency of system, after a disturbance*	*[N]*

An overview of the possible signals in the y-direction is graphically shown in Figure 3-16.

The actuation vibration is not taken into account, because it is not shown in the Coriolis sensing axis. The resonance vibration, due to a disturbance, is clearly visible in the resulting mass movement. The Coriolis signal is not visible at first sight.

Figure 3-17 illustrates the accelerations, the resonance and the rate of turn signal that occur at different frequencies. The signals can be separated by means of filtering.

A randomly chosen acceleration profile of approximately 5 g is experienced in the y-axis direction, which results in a mass displacement of approximately 1 µm.

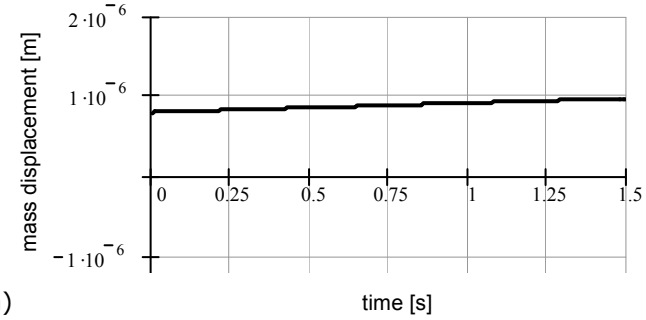

(a)

The inertial sensor is positioned in such a way that the gravity displaces the mass for about 0.2 µm in the y-axis direction.

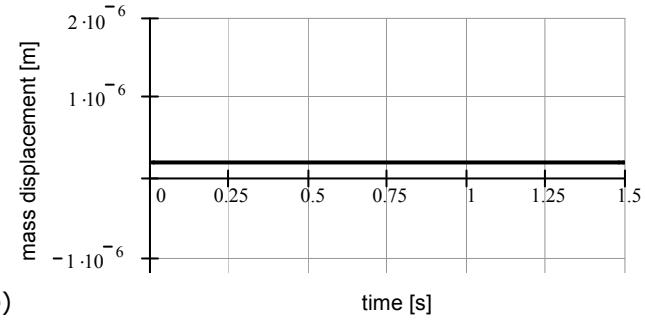

(b)

The resulting Coriolis force due to a rate of turn of 1 [rad/s] experienced in the y-direction. Note: The y-axis scale is 1000 times amplified with respect to figure a.

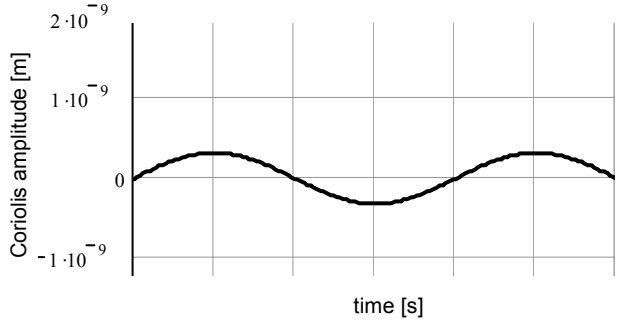

(c)

The movement of the mass in the Coriolis direction (y-axis) at the damped natural frequency after a disturbance.

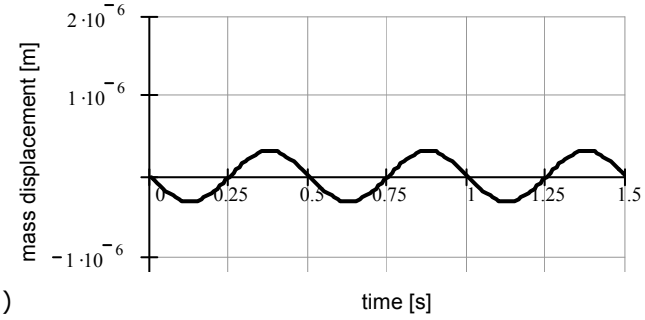

(d)

The total movement of the mass, which is a summation of figures a, b, c and d.

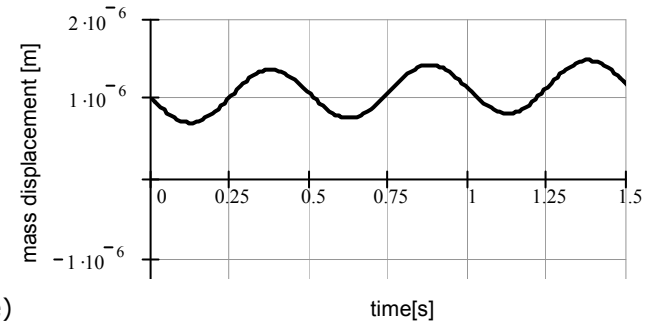

(e)

Figure 3-16: Summation of the different signals.

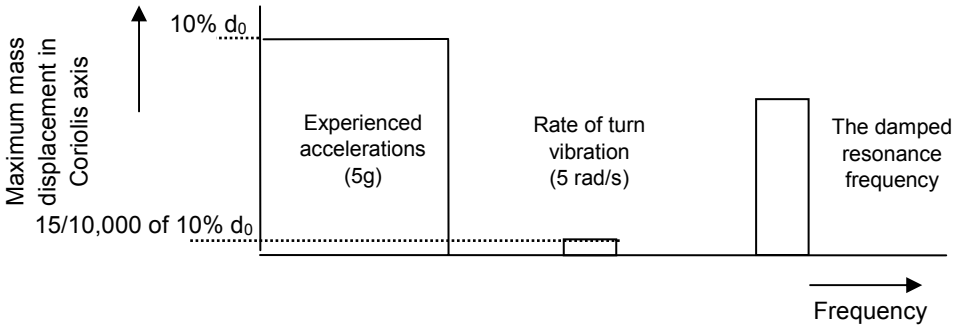

Figure 3-17: Overview of y-axis mass displacement factors in the frequency domain.

The movement of the mass inside the sensor box is measured by means of capacitive position measurement (section 3.8). The corresponding capacitance is converted into a voltage by means of a Capacitance to Voltage Converter (CVC). Accelerations experienced by the inertial sensor are measured by means of the Low Pass Filter (LPF) and the Coriolis vibration is measured by means of a Band Pass Filter (BPF).
For a quality factor of one and an experienced rate of turn of 1 rad/s the amplitude of the rate of turn signal is 3/100,000th of the initial spring height d_0 or 0.03% of the amplitude of the actuated vibration. The Coriolis signal can be extra amplified, as the Band Pass Filter for the rate of turn signal and the Low Pass Filter for the acceleration signal can operate independently.

3.5 Uniaxial rate of turn detection

Paragraph 3.3 showed that the rate of turn is a function of the ratio between the vibration in the Coriolis direction and the vibration in the actuated direction, with regards to the amplitude and phase (see Figure 3-15). Paragraph 3.4 showed that movements of the mass in the axes perpendicular to the axis of the actuation do not solely consist of movements induced by Coriolis forces. But as the Coriolis vibration has the same frequency as the vibration in the actuated direction it is possible to reject vibrations with frequencies that differ from the Coriolis vibration frequency. This signal at this specific frequency is measured by means of a lock-in amplifier (Figure 3-18).

A lock-in amplifier compares the vibration in the actuated direction (the reference signal) with the vibration in the perpendicular direction (the input signal). The lock-in amplifier gives two output signals. One output gives the amplitude of the input signal at the frequency of the reference signal and the other gives the phase-shift between the reference and input signal. The phase and amplitude output of the lock-in amplifier are a measure for the rate of turn.
Besides the continuous signal interpretation the output of the lock in amplifier has a low pass filter, which makes it possible to detect trends in noisy input

signal. Note that an increased time constant of the low pass filter decreases the bandwidth of rate of turn sensing.

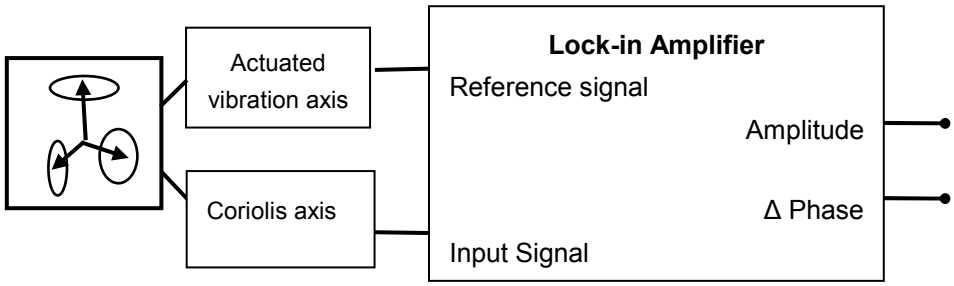

Figure 3-18: Connection scheme of the rate of turn sensor with the lock-in amplifier.

3.6 Multiple axis rate of turn detection

3.6.1.1 Biaxial rate of turn sensing

With the Gyracc it is possible to detect the rate of turn simultaneously around the axes perpendicular to the axis of vibration.

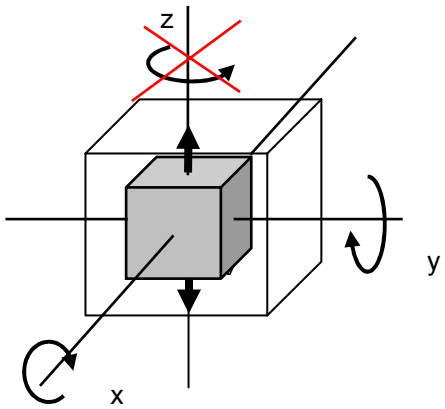

Figure 3-19: The mass vibrating along the z-axis and the x and y-axes in which the rate of turn around the y and x-axes can be detected.

In general it can be stated that the rate of turn can be measured in all axes as long as the next equation holds:

$$\vec{v} \times \vec{\Omega} \neq \vec{0} \tag{3-46}$$

For this reason it will be impossible to measure the rate of turn around the vibrating axis, being the z-axis in Figure 3-19.

3.6.1.2 Tri-axial rate of turn sensing

If the rate of turn is to be sensed around all axes in the 3D space, then the mass has to vibrate in the direction of more than one axis. This can be achieved by actuating the mass in a time multiplexed or in a continuous way.

3.6.1.3 Time multiplexed sensing

It is possible to detect the rate of turn around the 3 axes by means of time multiplexed sharing of at least two vibrations along different axes. It is for example possible to vibrate the mass along the x-axis and subsequently vibrate it in the y-axis. Note that this method results in a decrease in the bandwidth of the rate of turn signal to be detected.

3.6.1.4 Continuous sensing

It is possible to vibrate the mass around more than one axis by means of applying an extra vibration in the direction perpendicular to the first axis of actuation. If the vibrations have the same frequency and have a 90 degrees phase shift, then this will result in a circular (vibration) pathway of the mass as shown in Figure 3-20. During a rotation around the x-axis the vibration in the y-axis will result in a Coriolis effect in the z-axis, whereas the simultaneous vibration in the z direction will results in Coriolis signals in the y-axis.

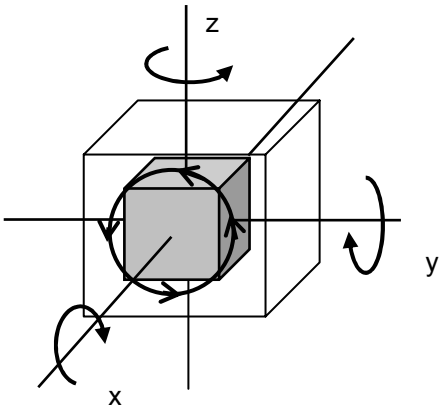

Figure 3-20: The circular vibrating mass for the three axes rate of turn detection principle.

As a consequence the diameter of the circular pathway of the mass (Figure 3-21) will increase or decrease. The change in diameter of the circle is a measure for the rate of turn around the x-axis.

Besides the increase or decrease of the circle in the y-z plane the ability to sense rotations around the y- and z-axis hold. The rates of turn around all three axis can be measured simultaneously.

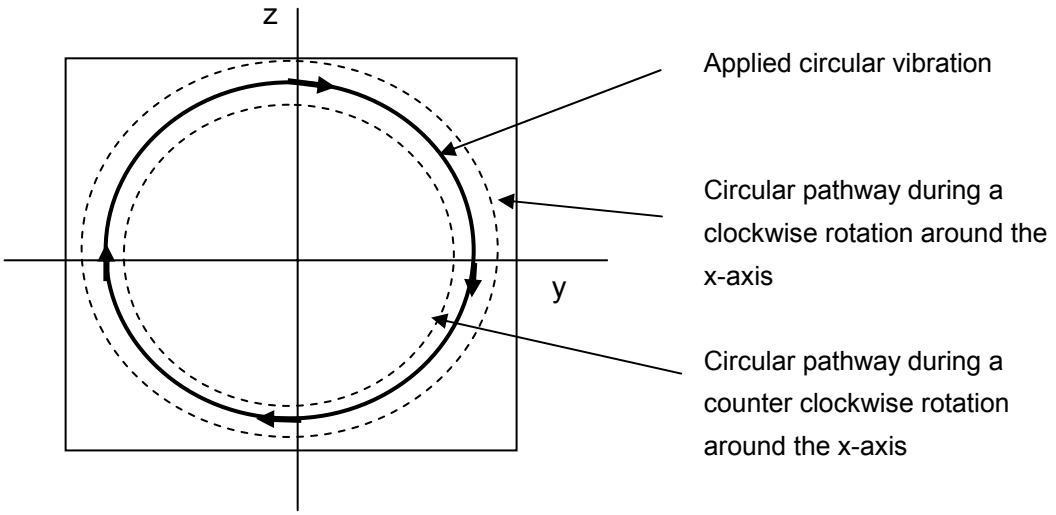

Figure 3-21: The increase and decrease of the rotationally vibrating mass, due to the experience of clockwise and counter clockwise rate of turn.

3.7 Cross-axis movement of the mass

The previous paragraphs assumed that the actuated mass vibrates perfectly along one axis (x-axis), but in practice the vibrating mass will also move in the axis perpendicular to the axis of actuation. This is schematically illustrated in Figure 3-22.

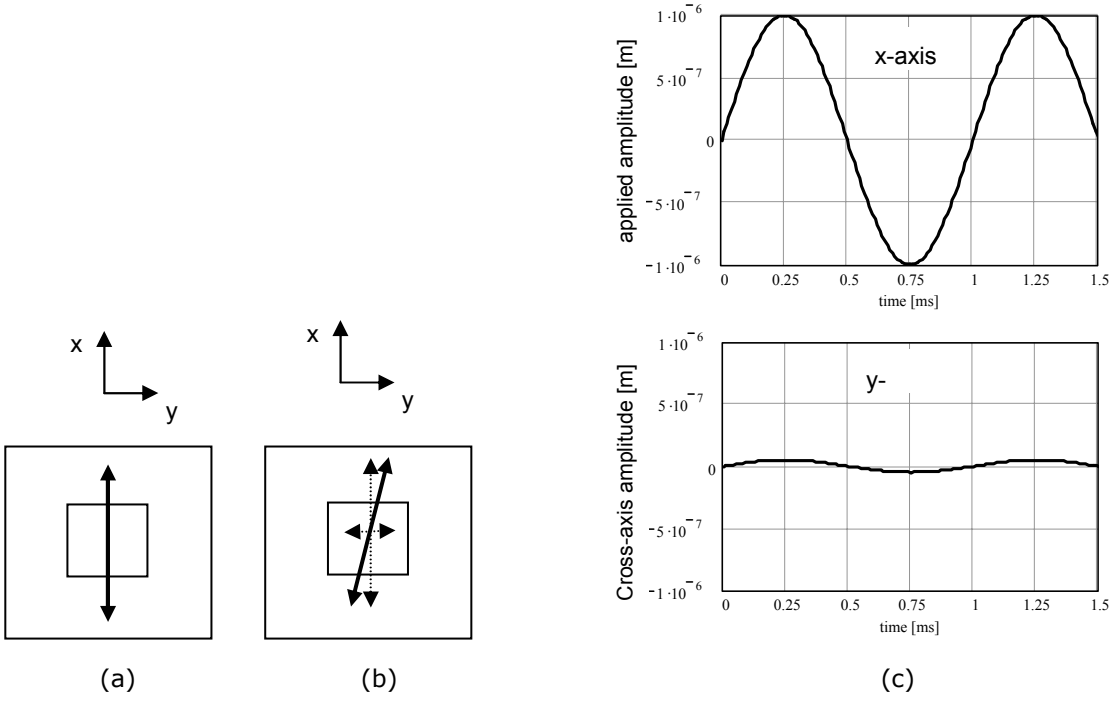

Figure 3-22: (a) The movement pathway of the mass in theory (ideal) and (b) practice (non-ideal). (c) Possible movements of the mass in the x- and y-axis.

This cross axis movement of the mass is due to mounting tolerances in the sensor construction. The Coriolis signal will be superimposed on top of this cross-axis signal.

3.8 The output signal of the sensor

The output signal of the sensor can be calculated by analysing the different stages in the transduction of the input signal (Ω or a) to the output signal (V). The stages of transformation are:

1. Transducing the input signal to the force acting on the mass.
2. The force acting on the mass results in a displacement of the mass.
3. The displacement of the mass results in a change in capacitance of the sensing capacitor.
4. The change in capacitance of the sensing capacitor results in a change in output voltage of the signal modifier.

The output signal of the sensor as a function of the input signal (rate of turn or acceleration) is referred to as the overall sensitivity of the sensor. All different stages in transducing the input signal to the ultimate output signal have their specific sensitivity. Multiplication of these sensitivities results in the overall sensitivity of the sensor.

$$S_{sensor} = S_{iF} S_M \cdot S_{ME} \cdot S_E \tag{3-47}$$

S_{iF} = *change in force / change in input (Ω or a)* *[ΔN/Δinp]*
S_M = *displacement of mass / change in force* *[Δd/ΔN]*
S_{ME} = *change in sense capacitance / displacement of mass* *[ΔC/Δd]*
S_E = *change in output voltage / change in sense capacitance* *[ΔV/ΔC]*

The different signal transduction stages are discussed in the following paragraphs.

3.8.1 Force acting on the mass/input-quantity (S_{iF})

The sensor is exposed to rates of turn (Ω) and accelerations (a). These motions result in a force acting on the mass.
The force on the mass as a result of an experienced acceleration is:

$$\vec{F}_a = m \cdot \vec{a} \tag{3-48}$$

The sensitivity of the force as a function of the acceleration acting on the mass is therefore:

$$S_{aF} = \frac{\left|\delta \vec{F}_a\right|}{\left|\delta \vec{a}\right|} = m \tag{3-49}$$

The force acting on the mass as a result of the rate of turn acting on the mass is:

$$\vec{F}_{\Omega} = 2m\vec{\Omega} \times \vec{\hat{x}}\omega \cos(\omega t) \tag{3-50}$$

The maximum sensitivity of the force on the mass as a function of the rate of turn is therefore:

$$S_{\Omega F} = \frac{\left|\delta \vec{F}_{\Omega}\right|}{\left|\delta \vec{\Omega}\right|} = 2m.\hat{x}.\omega \tag{3-51}$$

This sensitivity holds for ω>>Ω (see chapter 2).

3.8.2 Displacement of the mass/change in inertial force (S_M)

The force acting on the mass results in a displacement of the mass, which is influenced by the stiffness and damping of the springs and the damping of the air between the mass and the sensor box.

$$\Delta\hat{d} = F_{mass} \cdot \frac{1}{k_{total}} \cdot \frac{1}{\sqrt{\left(1 - \frac{\omega^2}{\omega_n{}^2}\right)^2 + \left(\frac{1}{Q} \cdot \frac{\omega}{\omega_n}\right)^2}} \tag{3-52}$$

with

$$k_{total} = 10 \cdot \frac{GA_{PDMS}}{3 \cdot d_0}\left(1 + \frac{2}{(1+PCR)^3}\right)$$

Therefore the sensitivity:

$$S_M = \frac{\delta\Delta\hat{d}}{\delta F_{mass}} = \frac{1}{k_{total}} \cdot \frac{1}{\sqrt{\left(1 - \frac{\omega^2}{\omega_n{}^2}\right)^2 + \left(\frac{1}{Q} \cdot \frac{\omega}{\omega_n}\right)^2}} \tag{3-53}$$

3.8.3 Change in sense capacitance/displacement of mass (S_{ME})

Capacitive measurement techniques are used to measure the position of the mass inside the box. The inner-side walls of the box are covered with capacitor plates (Figure 3-23a). All inner-walls of the box contain two capacitor plates parallel to the surface of the metal mass. The surface areas of the metal mass act as the opposite capacitor plate (Figure 3-23 b and c). On one terminal of the capacitor plates (C_{couple}) a high frequency carrier signal (100kHz) is applied and on the other a low ohmic terminal of a measurement circuit (C_{sense}) is connected. The current from the couple plates to the sensing capacitor plate is a measure for the distance of the cubic mass to the sensing plate in the specific sensing direction. The closer the mass gets to an inner-wall of the sensor-box the larger the capacitance between that wall and the conductive mass, the larger the current through the sense terminal of the measurement electronics.

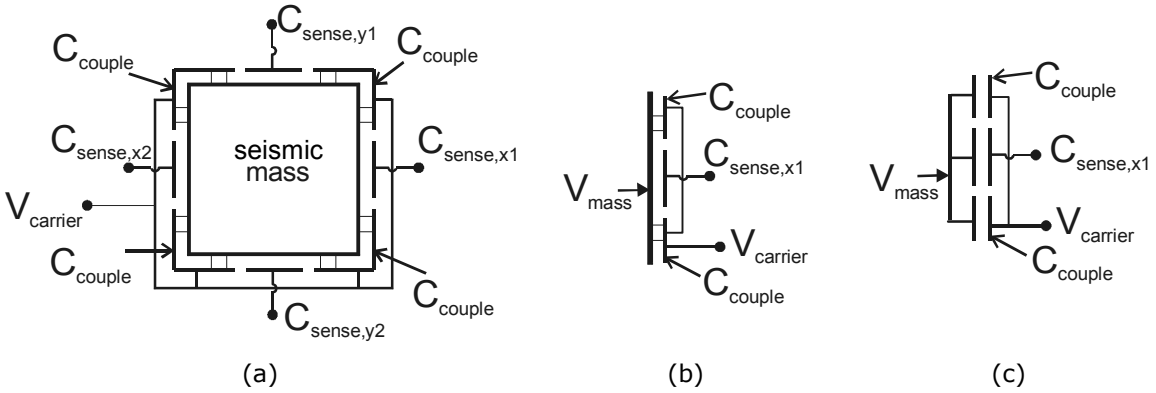

Figure 3-23: Cross-sectional view of the capacitor plates surrounding the mass (a) and a conservative view of the electrical circuitry (b, c).

The distance between the conductive plates is equal to the height of the PDMS structure by which the mass is suspended. The capacitance $C_{sense}(d)$ between sense plate and the mass (plate) is:

$$C_{sense}(d) = \frac{\varepsilon_0.[A_{sense} - A_{PDMS}] + \varepsilon_0.\varepsilon_{r,PDMS}.A_{PDMS}}{d} \tag{3-54}$$

with	ε_0	*=permittivity of vacuum*	*[F/m]*
	$\varepsilon_{r,PDMS}$	*=relative dielectric constant of PDMS (ε_r =2.5 [5])*	*[-]*
	A_{sense}	*=surface area of the sense plate*	*[m^2]*
	A_{PDMS}	*=surface area of the PDMS*	*[m^2]*
	d	*=distance between the conductive plates*	*[m]*

For $\varepsilon_{r,PDMS}.A_{PDMS} << (A_{sense}-A_{PDMS})$ the equation can be simplified to:

$$C_{sense}(d) = \frac{\varepsilon_0.A_{sense}}{d} \tag{3-55}$$

The sensitivity of the capacitive sensor with an initial plate distance $d=d_0$ is:

$$S_{ME} = \frac{\delta C_{sense}}{\delta d} = \frac{C_{sense}}{d_0} = \frac{\varepsilon_0 \cdot A_{sense}}{{d_0}^2} \tag{3-56}$$

3.8.4 Output voltage change/sense capacitance change (S_E)

Due to the symmetry of the capacitor plates surrounding the metal mass the voltage on the mass is equal to [7]:

$$V_{mass}(t) = K.V_{carrier}(t) \tag{3-57}$$

with

$$K = \frac{C_{couple,total}}{C_{couple,total} + C_{sense,total}} \tag{3-58}$$

$C_{couple,total}$ is the summation of all coupling capacitors surrounding the seismic mass and $C_{sense,total}$ is the summation of all six sensing capacitors surrounding

the mass. Figure 3-24 shows an extra capacitor $C_{par,x1}$, which is the parasitic capacitance between the coupling plate and the virtual ground of the signal modifier ($V_{sense,x1} \approx 0V$).

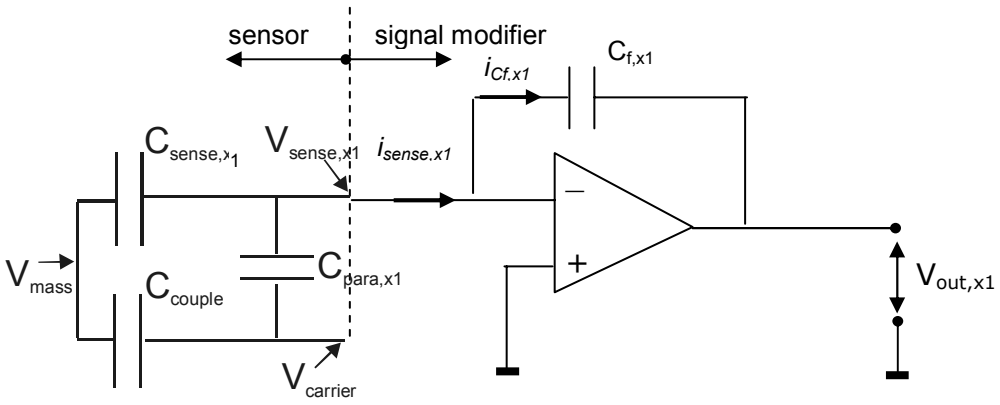

Figure 3-24: The current to voltage converter.

Therefore the current through the sensing terminal is equal to:

$$i_{sense,x1}(t) = i_{C,sense,x1}(t) + i_{C,para,x1}(t) \tag{3-59}$$

$$i_{C,sense,x1} = \frac{V_{mass}}{\frac{1}{j\omega C_{sense,x1}}} \quad and \quad i_{C,para} = \frac{V_{carrier}}{\frac{1}{j\omega C_{para,x1}}} \tag{3-60}$$

$$i_{sense,x1}(t) = j\omega . V_{carrier}(t) \left[K . C_{sense,x1}(t) + C_{para,x1}(t)\right] \tag{3-61}$$

The current through the feedback capacitor ($i_{Cf,x1}$) is equal to the current from the "sense" terminal of the sensor ($i_{C,sense,x1}$) and according to Kirchhoff's law:

$$i_{Cf,x1} = -i_{C,sense,x1} \tag{3-62}$$

As the sense terminal is connected to the virtual ground of the opamp, the current through the feedback capacitor is:

$$i_{Cf,x1} = \frac{-V_{out,x1}}{\frac{1}{j\omega C_{f,x1}}} = -j\omega C_{f,x1} V_{out,x1} \tag{3-63}$$

The output voltage of the current to voltage converter is therefore:

$$V_{out,x1}(t) = -\frac{i_{C,sense,x1}(t)}{j\omega C_{f,x1}} \tag{3-64}$$

Thus the output voltage is linearly depending on the current through the sense capacitance. In combination with equation (3-61) the output voltage is:

$$V_{out,x1}(t) = -\frac{V_{carrier}(t)}{C_{f,x1}} \left[K \cdot C_{sense,x1}(t) + C_{para,x1}(t)\right] \tag{3-65}$$

with $C_{sense,x1} = \dfrac{\varepsilon_0 \cdot A_{sense}}{d_0 + \Delta d}$

The same approach holds for terminal x_2:

$$V_{out,x2}(t) = -\frac{V_{carrier}(t)}{C_{f,x2}}\left[K \cdot C_{sense,x2}(t) + C_{para,x2}(t)\right] \tag{3-66}$$

with $C_{sense,x2} = \dfrac{\varepsilon_0 \cdot A_{sense}}{d_0 - \Delta d}$

The output voltage of terminal x_1 is a function of the current through $C_{sense,x1}$ and $C_{para,x1}$. A small change in C_{sense}, as a result of a small mass displacement, will result in a small change in the output voltage. The electrical sensitivity at a terminal is:

$$S_E = \frac{\delta V_{out,x1}}{\delta C_{sense,x1}} = \frac{K \cdot V_{carrier}}{C_{f,x1}} \tag{3-67}$$

Sense terminal x_1 as well as sense terminal x_2 have an offset voltage in common. This common voltage can be rejected by subtracting the signals of sense terminal x_1 and x_2. This is electronically realized by means of differential amplification, with an amplification factor A_{diff} (see Figure 3-25).

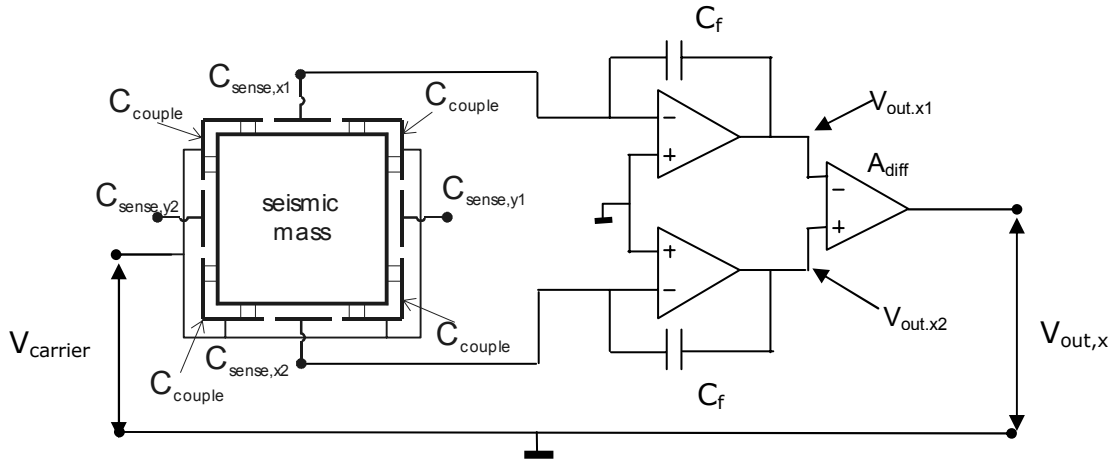

Figure 3-25: Circuit of two opposing sensor plates connected to a differential amplifier.

This differential signal is a measure for the position of the inertial mass in the sensor box. The output voltage of this differential measuring method is:

$$V_{out,x} = A_{diff}.[V_{out,x1} - V_{out,x2}] \tag{3-68}$$

with $C_f = C_{f1} = C_{f2}$ and $C_{para,x1} = C_{para,x2}$ the electrical sensitivity for the differential measured change in capacitance is:

$$S_{E,diff} = \frac{\delta V_{out,x}}{\delta C_{sense}} = 2 \cdot \frac{K \cdot A_{diff} \cdot V_{carrier}}{C_f} \tag{3-69}$$

which is twice the sensitivity of a non-differentially measured mass displacement.

3.8.5 Total sensor sensitivity to rate of turn (S_{sensor})

The total sensitivity of the sensor can be calculated by means of multiplying the sensitivity of the different transduction stages.

$$S_{sensor} = S_{\Omega F}.S_M \cdot S_{ME} \cdot S_E \tag{3-70}$$

with

$$S_{\Omega F} = \left\| \frac{\delta \vec{F}_{\Omega}}{\delta \vec{\Omega}} \right\| = 2m.\hat{x}.\omega \tag{3-71}$$

$$S_M = \frac{\delta \Delta d}{\delta F} = \frac{1}{k_{total}} \cdot \frac{1}{\sqrt{\left(1 - \frac{\omega^2}{\omega_n{}^2}\right)^2 + \left(\frac{1}{Q} \cdot \frac{\omega}{\omega_n}\right)^2}} \tag{3-72}$$

$$S_{ME} = \frac{\delta C}{\delta d} = \frac{C_{sense}}{d} = \frac{\varepsilon_0.A_{sense}}{d^2} \tag{3-73}$$

$$S_{E,diff} = \frac{\delta V_{out,x}}{\delta C_{sense}} = 2 \cdot \frac{K \cdot A_{diff} \cdot V_{carrier}}{C_f} \tag{3-74}$$

The total sensitivity for a rate of turn is therefore:

$$S_{sensor} = \frac{\delta V}{\delta \Omega} = \frac{4 \cdot m \cdot \hat{x} \cdot \omega}{C_f \cdot k_{total}} \cdot \frac{\varepsilon_0.A_{sense}}{d^2} \cdot V_{carrier}.K \cdot \frac{A_{diff}}{\sqrt{\left(1 - \frac{\omega^2}{\omega_n{}^2}\right)^2 + \left(\frac{1}{Q} \cdot \frac{\omega}{\omega_n}\right)^2}} \tag{3-75}$$

with

$$K = \frac{C_{couple,total}}{C_{couple,total} + C_{sense,total}}$$

$$k_{total} = 10 \cdot \frac{GA_{PDMS}}{3 \cdot d_0}\left(1 + \frac{2}{(1 - PCR)^3}\right)$$

$$d = d_0(1 - PCR)$$

A good estimation of the sensitivity of the sensor is calculated by substitution of the parameters of Table 3-8 in equation (3-75). This results in a rate of turn sensitivity of: $S_{\Omega,sensor}$= 6 mV $^{s}/_{rad}$

Table 3-8: Sensor parameters.

parameter	*definition*	*value*
d_0	uncompressed spring height	10.10^{-6} m
d	Initial spring height in compressed state	$d=d_o(1-PCR)$
PCR	Pre-Compression Ratio of springs	0.1
$\hat{X}$	vibration amplitude	$0.1\times d_0$ m
K	capacitor plate ratio	0.5
m	mass	220.10^{-6} kg
ω	vibration frequency	$2.\pi.1000$ rad/s
A_{sense}	sense capacitor plate area	$0.4\times3.10^{-3}\times3.10^{-3}$ m^2
$V_{carrier}$	carrier wave amplitude	5 V
A_{PDMS}	PDMS area at one side of the mass	$4\times100\times10^{-6}\times100\times10^{-6}$ m^2
ε_0	dielectric constant of vacuum	$8.85.10^{-12}$ F/m
G	shear elastic modulus of PDMS	250.000 Pa
C_f	feed back capacitor	10.10^{-12} F
A_{diff}	amplification factor of differential amplifier	100
Q	mechanical quality factor	1

3.8.6 The relation between mass position and output voltage

This paragraph takes a closer look at the output voltage as a function of the mass position. A linear relation between the output voltage (V_{out}) and the mass displacement (Δd) is desirable for a clear understanding of the mass vibration behaviour.

The output of a single side connected capacitance to voltage converter, with $C_{para,x1}=0$ (Figure 3-24) is equal to equation (3-65):

$$V_{out,x1}(t) = -\frac{V_{carrier}(t)}{C_{f,x1}}\left[K \cdot \frac{\varepsilon_0 A_{sense}}{d_0 - \Delta d(t)}\right] \tag{3-76}$$

The output voltage of the two differentially connected sensing terminals (Figure 3-25) as a function of the displacement of the mass is found by substitution of equation (3-65) and (3-66) in equation (3-68).

$$V_{out,x}(t) = -\frac{A_{diff} \cdot V_{carrier}(t)}{C_f}\left[K.2 \cdot \frac{\varepsilon_0 A_{sense}\Delta d(t)}{{d_0}^2 - \Delta d(t)^2}\right] \tag{3-77}$$

The single side and the differential output voltage as a function of the displacement of the seismic mass are shown in Figure 3-26.

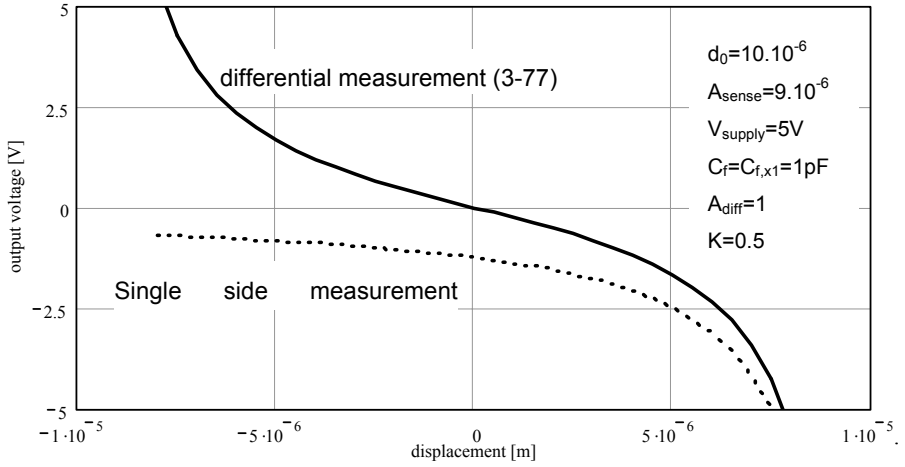

Figure 3-26: The single side and the differential output voltage of the signal modifier as a function of the mass displacement.

The linear range of ΔV as a function of Δd is limited to the displacement where the deviation between the actual $\Delta V(\Delta d)$ and a linear ΔV as a function of Δd is smaller than 1%, like the definition used in section 3.1.2.

$$(\Delta V_{out} - S_{ME} \cdot S_E.\Delta d) \times 100\% \leq 1\% \tag{3-78}$$

The sensitivity of the single side measured mechanical electrical transduction is:

$$S_{ME}.S_E = -\frac{K \cdot V_{carier} \cdot \varepsilon_0 \cdot A_{sense} \cdot A_{diff}}{C_f \cdot d_0^2} \tag{3-79}$$

and for the differential measurement:

$$S_{ME}.S_{E,diff} = -\frac{2 \cdot K \cdot V_{carier} \cdot \varepsilon_0 \cdot A_{sense} \cdot A_{diff}}{C_f \cdot d_0^2} \tag{3-80}$$

Solving equation (3-78) for the single side measured mass displacement results in a maximal mass displacement of 0.5% of the initial distance between the mass and the inner box wall to maintain a linear ratio between the output voltage and the seismic mass displacement. For the differential measurement the mass displacement is linearly measured up to 10% of the initial distance between the mass and the inner box wall.

Concluded can be that the electrical transduction of differential measured capacitors is twice as sensitive as a single capacitor and has a 20 times larger linear mechanical-electrical transduction range, than the single side measured mass displacement.
Thus if the sensor is designed in such a way that for maximum experienced accelerations (5g in our case) the mass does not displace more than 10% of the initial distance between the inner box wall and the original mass position, then the output voltage is proportional the experienced acceleration.

3.9 Conclusions

The Gyracc is based on a seismic mass enclosed by a cubic box, that is symmetrically suspended by non-linear springs of the rubber elastic material PDMS. The mass displacement as a function of the applied force is linear for displacements up to 10% of the original PDMS spring height.

The capacitance between the seismic mass and the inner box walls is a measure for the position of the seismic mass. The capacitance is measured by means of a Capacitance to Voltage Converter (CVC). The output voltage of the CVC is linearly related to a change in the measured capacitance. The relation between the mass displacement and the resulting change in capacitance can be regarded linear for displacements up to 0.5% of the initial distance between the inner box wall and the seismic mass. When measuring the differential capacitance of the capacitors on two opposite sides of the mass, displacements up to 10% of the initial distance between the inner box wall and the seismic mass can be measured linearly. Besides this 20 times increase of the linear area the sensitivity is increased by a factor of two.

The mass is brought into vibration to enable rate of turn measurements. The vibration of the mass has a certain phase shift with respect to the actuation force. The phase shift is a function of the actuation frequency.

Coriolis force is experienced during the presence of a rate of turn around an axis perpendicular to the axis of the vibration. This force will make the mass vibrate in the axis perpendicular to the axis of the actuated vibration. The amplitude of this Coriolis vibration is a measure for the experienced rate of turn. Furthermore the phase shift between the applied and Coriolis vibrations is a measure for the direction of the rate of turn. The Coriolis vibration amplitude of the mass in a symmetric inertial sensor with a quality factor of 1 is approximately $3/100{,}000^{th}$ of the 10 µm initial spring height per rad/s. In this particular case the Coriolis vibration amplitude is 0.03% of the actuated vibration amplitude.

With the analysis of the position of the mass it is possible to deduce the accelerations and rates of turn experienced by the system. To differentiate between signals of accelerations and rates of turn, the seismic mass should vibrate at a frequency well above the frequency range in which accelerations occur. Furthermore the mass should not vibrate at the resonance frequency of the system, because it will be impossible to separate the Coriolis signal from the damped resonance vibration, which occurs after a mechanical disturbance of the system.

Coriolis signal measurement is to be performed with a lock-in amplifier, because this instrument measures the amplitude as well as the phase shift of the Coriolis signal with respect to the actuated vibration with high accuracy.

Dual axis rate of turn sensing is possible with a mass vibrating along one axis. Tri-axial rate of turn can be measured by means of a mass that is vibrating along a circular pathway.

3.10 References

[1] Lötters, J.C., Thesis, University of Twente, "A Highly Symmetrical Capacitive Triaxial Accelerometer", ISBN 90-365-0982-3, 1997.

[2] Treloar, L.R.G., The physics of rubber elasticity, Clarendon Press, 1975

[3] Morse, P., Ingrad, K.U., Theoretical acoustics, Mc Graw-Hill, New York, 1st edition, 1968

[4] Veyola, T., Kuisma, H., Lahdenpera, J., "The influence of gas surface interaction on gas-film damping in a silicon accelerometer", Sensors and Actuators A, vol. 66, pp. 83-92, 1998.

[5] ABCR Research Chemicals and Metals, catalogue, Kalsruhe, Germany, 1994.

[6] Meriam, J.L. and Kraige, L.G., Book: "Engineering Mechanics Vol.2", ISBN: 0-471-84912-X, 1987.

[7] Lötters, J.C., Olthuis, W. and Bergveld, P., A sensitive differential capacitance to voltage converter, Instrumentation and Measurement (1999), pp. 89-96

Appendix A

APPENDIX CLOSED BOX DAMPING ESTIMATION

In the Gyracc a cubic mass is vibrating in a closed box. In section 3.1.3, the damping inside the Gyracc is estimated by means of reciprocating plates as there is no "standard" solution for the Gyracc's geometry.
In this appendix the damping inside the Gyracc is calculated with the finite element model of the Aplac simulation package [1]. This package simulates the damping of flat geometries. To estimate the damping inside the Gyracc its 3D geometry is therefore reshaped into a flat/simplified structure.

A.1 Simplified structure

The first step in simplifying the structure is by means of dividing the sensor into parts with identical damping characteristics. For small signal analysis the air damping on the upper plane and the lower plane of the mass is identical.

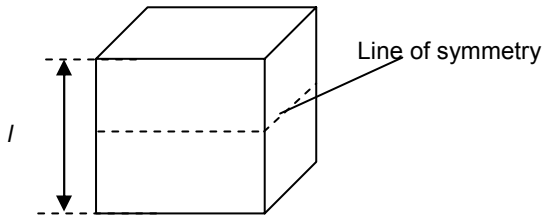

Figure A-1: Line of symmetry of the sensor.

At the line of symmetry the pressure of the air is a constant, which is equal to the atmospheric pressure. The damping above the line of symmetry is equal to the damping below the line of symmetry.
The lower and upper half of the sensor can be divided into four equally behaving areas (Figure A-2a). There is no net airflow between the four areas. If the influence of the 90-degree bend in the flow channel is ignored, then the lower half of the cube can be converted into one single plane (Figure A-2b).

Only one quarter of the area has to be simulated, due to symmetry. The resulting damping is 1/8 of the damping of the whole cube. In the Aplac simulation the finite difference mode, realizing the modified Reynolds equation, is used. It has been implemented as an electrical equivalent circuit. The model has been described in [2], but here additional boundary conditions (flow=0) and a possibility for arbitrary excitation is added. The boundary conditions are shown in the Figure A-2. The excitation area is l/2 x l/2 and the two other areas act as "tubes" where the air is forced to flow.

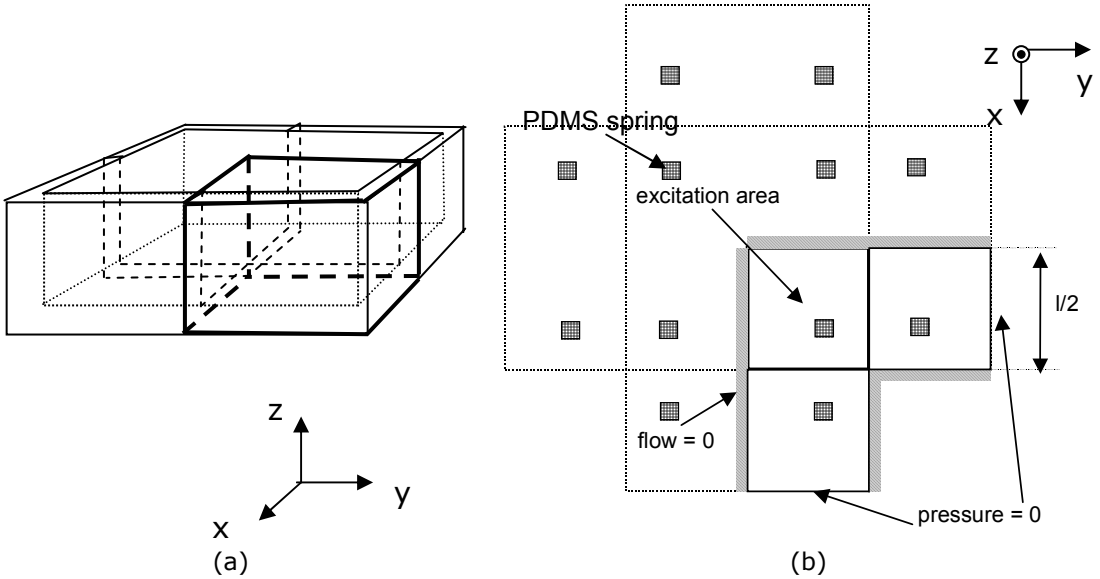

Figure A-2: (a) The original 3D shape of the Gyracc (b) the simplified flat geometry.

The damping in our system will be larger than the standard damping, but smaller than the to be simulated closed box damping, because the Gyracc model will neither contain a fully open nor a perfectly closed box.

A.2 Simulation results

A grid of 41x41 elements was used in the simulation of the pressure distribution due to the airflow according to the Reynolds equation, with and without the possible effects of the blocking effects of the springs. The resulting pressure distribution (at low frequency) is shown in Figure A-3. The contribution of 300µm x 300µm PDMS springs is included.

This figure shows that the pressure in the middle of the actuated side shows a maximum and the end of the flow tubes have a pressure equal to atmospheric pressure. The three discontinuities show the position of the springs (no air, no pressure).

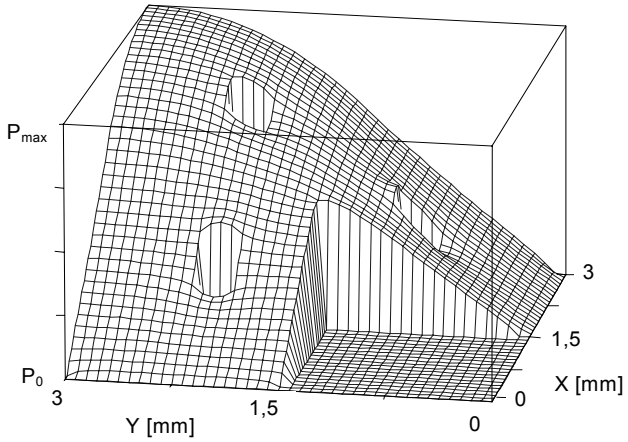

Figure A-3: The pressure distribution of the air during displacement of the mass in the z-direction.

The following figures show the frequency response of the gas-damped cubic mass for an air gap height of 20, 10 and 5μm. For every air gap height the frequency response is calculated for:

- Near vacuum, with the closed box damping model.
- Atmospheric pressure, with the closed box damping model.
- Atmospheric pressure, with squeezed film damping model, as explained in section 3.1.3.

The mass vibration is excited with a 1g sinusoidal acceleration. The output is the amplitude of the displacement in μm dB scale.

Values used in the simulations: input force amplitude: 1g (10 m/s^2), l=3mm, gas viscosity=18.5×10^{-6} Pa.s, mean free path at 101kPa: 58.5nm, mass: 220 mg, pressure: 1.22 kPa and 101kPa, effective spring coefficients: Kr= 5500, 11000 and 22000 N/m.
Figure A-4a shows the amplitude of a vibrating mass suspended by 20 μm high springs, as a function of the vibration frequency. The vibration amplitude at resonance in the closed box model is half the amplitude as compared to the "standard" squeezed film damping model. For the spring heights of 10 and 5 μm the frequency response can not be regarded as being a standard squeezed film problem anymore. The frequency response shows a drastic decrease in vibration amplitude.
The damping and quality factor of the vibrating systems shown in Figure A-4, are calculated with equations 3-33 and 3-34. The result is shown in Table A-1.

Table A-1: The quality and damping factor of the vibrating mass for systems with an air gap height of 5, 10 and 20 μm at 101 kPa atmospheric pressure.

Air gap height	reciprocating plates	closed box model	Ratio
5 μm	Q=0.42; b= 5.2 Ns/m	Q=0.075; b= 29.3 Ns/m	5.6
10 μm	Q=1.2; b=1.3 Ns/m	Q=0.3; b=5.2 Ns/m	4.0
20 μm	Q=2.4; b=0.5 Ns/m	Q=1.8; b=0.6 Ns/m	1.2

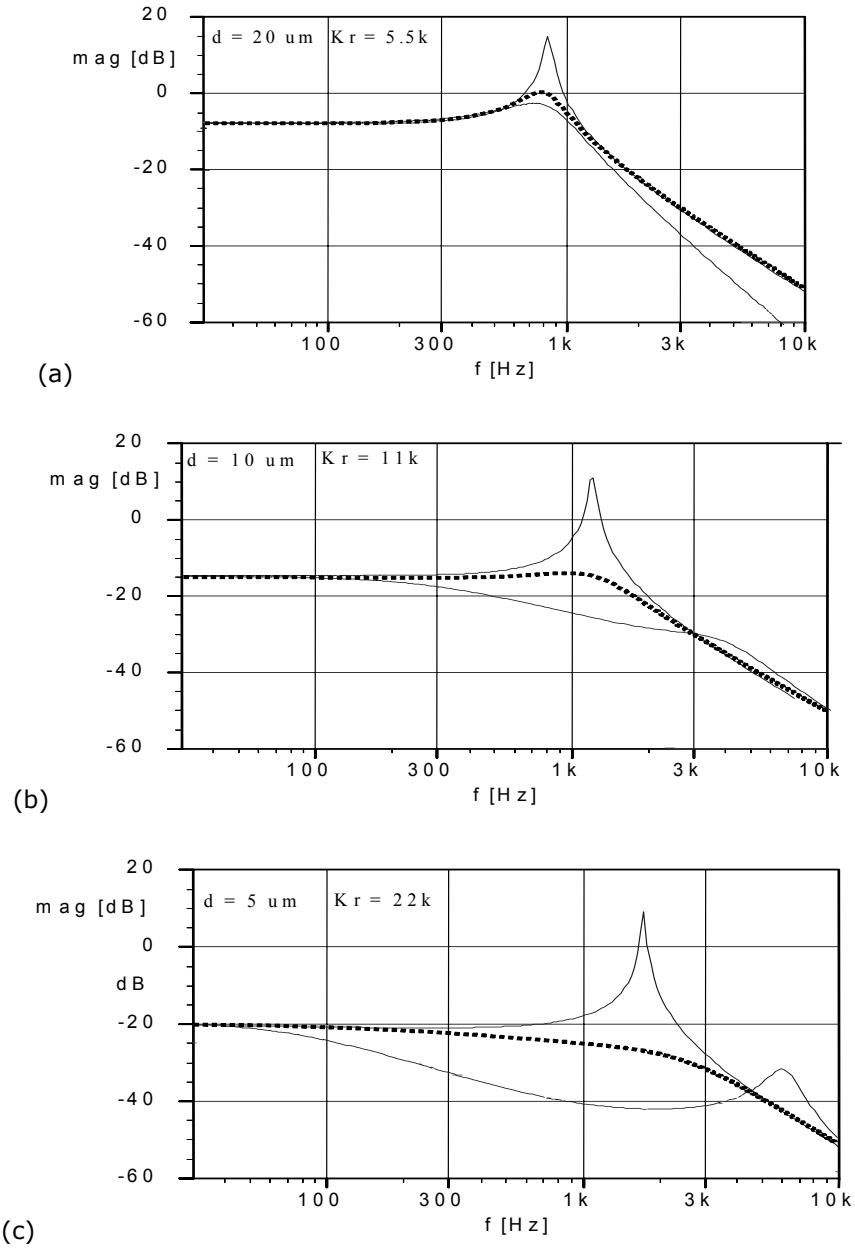

Figure A-4: The vibration amplitude of the mass as a function of the vibration frequency for three different heights of the air gap (a,b,c) for an squeezed film damping model (dotted line), near vacuum (upper line) and 1 Atm air pressure (lower line).

Concluded can be that the damping in a fully closed box with a vibrating mass, can not be estimated with the squeezed film damping equation for the Gyracc with an air gap height less than 20 µm.

A.3 References

[1] Aplac Solutions Corporation, Aplac [7.6], 2000 Ref. Type: Computer Program.

[2] Veijola, T., et al., Equivalent-circuit model of the squeezed gas film in a silicon accelerometer, Sensors an Actuators, vol. 48, pp. 239-248, 1995.

Chapter 4

4 THE ACTUATOR

In the previous chapter the theory of the Coriolis effect has been treated. It was assumed that the mass inside the sensor box was vibrating. The actuation of this vibration should be realized without a fundamental change in the design of the inertial sensor.

4.1 The maximum actuation force

The inertial sensor is designed such that the mass displaces linearly during the experience of accelerations within the limits of ±50 m/s^2. The maximum force for which the mass displaces linear is therefore:

$$F_{\max} = a_{\max} \times m_{mass} \tag{4-1}$$

with

F_{max}	=	*The maximum force for which the mass should be displaced linearly*	*[N]*
a_{max}	=	*the maximum acceleration to be measured*	*[m/s^2]*
m_{mass}	=	*weight of the seismic mass*	*[kg]*

The ribs of the mass have equal length (l), because the mass has a cubic shape. The weight of the seismic mass is calculated by:

$$m_{mass} = l^3 \times \rho_{material} \tag{4-2}$$

with

m_{mass}	=	*weight of the seismic mass*	*[kg]*
l	=	*rib length of the seismic mass*	*[m]*
$\rho_{material}$	=	*mass density*	*[kg/m^3]*

There are two possibilities to actuate the mass without modification of the design of the sensor: electrostatic and electromagnetic actuation. For electrostatic actuation the mass should be of an electrically conducting material and for magnetic actuation the mass should conduct magnetic flux. The metal "steel 37 (ST37)" is conducting and is commonly used in electromagnetic circuits. Its mass density (ρ_{ST37}) is $7.8.10^{3\ kg}/_{m^3}$.

The maximum force for which a linear displacement of the ST37 mass occurs as a function of the rib length of the mass is shown in Figure 4-1.

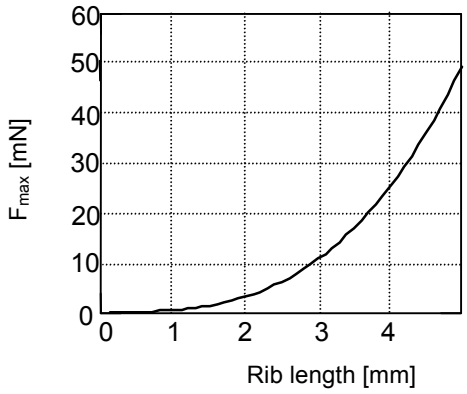

Figure 4-1: The displacement force (F) as a function of the size of the cubic shaped mass with a rib length (l) for St37 at a_{max}= 50 m/s^2.

From Figure 4-1 it can be seen that for a cubic shaped seismic mass with a 3 mm rib length, the maximum force should be 11 mN. The following sections show whether these forces can be reached by means of electrostatic and/or electromagnetic actuation methods.

4.2 The optimal spring constant in the Gyracc

The sensitivity (S) of the sensor is depending on the displacement of the mass as a function of the spring constant (k) of the sensor. For a high sensitivity the spring constant should be as low as possible. But based on sections 3.1.2 and 3.8.6 it can be stated that the output voltage of the CVC is linear until the experienced force compresses the PDMS springs for 10%.

$$\Delta d_{\max} = \frac{d_0}{10} \tag{4-3}$$

To obtain the maximum sensitivity of the sensor the spring should be compressed to 10% during the maximum force to be measured. With this knowledge the optimal spring constant can be found,

$$k_{optimal} = \frac{F_{\max}}{\Delta d_{\max}} \tag{4-4}$$

By substitution of equation (4-1) and (4-3) in equation (4-4), the optimal spring constant as a function of the height of the springs is found to be:

$$k_{optimal} = \frac{10 \cdot m \cdot a_{\max}}{d_0} \tag{4-5}$$

4.3 Electrostatic actuation of the seismic mass

A potential difference between the mass and a sensor plate (Figure 4-2) will result in an electrostatic force that pulls the mass towards this specific sensor

plate. By applying a sinusoidal potential between the mass and the sensor plate the mass can be brought into vibration.

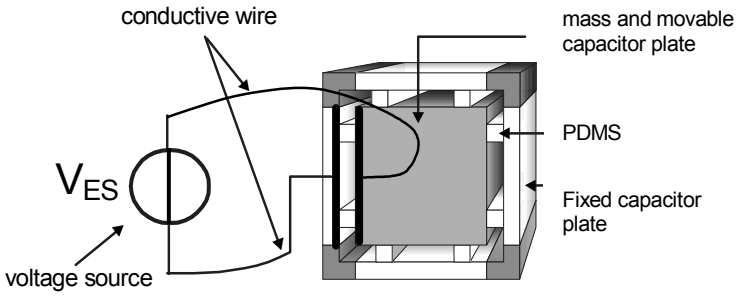

Figure 4-2: The sensor with the voltage source connected to a conductive sensor plate and the conductive mass.

The electrostatic force between two plan parallel positioned conducting plates is:

$$F_{ES} = \frac{\varepsilon_0 \varepsilon_r . A_{plate} \cdot V_{ES}^{\ 2}}{2 \cdot d^2} \qquad (4\text{-}6)$$

with

FES	=	*the electrostatic force between two conducting surfaces*	*[N]*
ε0	=	*the dielectric constant of vacuum 8.85419.10-12*	*[F/m]*
εr	=	*the relative dielectric constant of the medium between the surfaces*	*[-]*
Aplate	=	*the area of the conducting surfaces*	*[m2]*
VES	=	*the voltage difference between the conductive surfaces*	*[V]*
d	=	*the distance between the conductive surfaces*	*[m]*

The electrostatic force (F_{ES}) produced as a function of the voltage (V_{ES}) for three different plate distances is shown in Figure 4-3a. The force (F) necessary to move the seismic mass a certain distance (Δd) is calculated using equation (4-4). This force (F) has to be realized by the electrostatic force (F_{ES}), therefore:

$$F_{ES} = F \qquad (4\text{-}7)$$

The initial thickness of the PDMS structures (d_0) plus the mass displacement (Δd) results in the distance (d) between the two conductive plates, as mentioned in equation (4-6).

$$d = d_0 + \Delta d \qquad (4\text{-}8)$$

Rewriting and substitution of the previous equations yields the necessary voltage between the mass and the sensor plate, as a function of the initial PDMS height:

$$V_{ES} = (d_0 + \Delta d) \cdot \sqrt{\frac{2 \cdot \frac{\Delta d}{d_0}.10.m.a_{\max}}{\varepsilon_0 \varepsilon_r . A_{plate}}} \qquad (4\text{-}9)$$

A_{plate}	=	*area of mass side (9.10^{-6} for the Gyracc)*	$[m^2]$
m	=	*weight of seismic mass (220.10^{-6} for steel 37)*	$[kg]$
a_{max}	=	*the maximum acceleration for which the mass-displacement should be linear*	$[m/s^2]$

The voltage necessary to obtain a certain mass displacement is shown in Figure 4-3b.

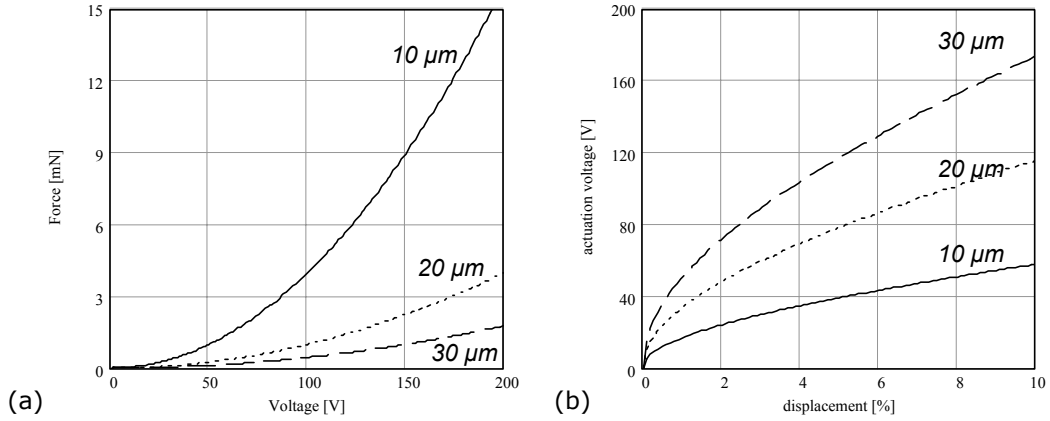

Figure 4-3: (a) The ES-force as a function of the voltage for 3 different plate distances with a plate area of 3×3×3 mm. (b) The voltages to be applied to displace the mass a certain percentage of the initial PDMS height for 3 different plate distances.

Figure 4-3b shows that the electrostatic voltage necessary for attracting the mass is proportional to the distance between the mass and the capacitor's plate. This is due to the fact that the PDMS spring constant depends on the PDMS thickness (equation (4-5)).

4.3.1 Non contact electrostatic attraction

With the configuration as described above it was assumed that there is an electric contact with the mass. A possibility to get rid of this (interfering) connection is by means of applying a voltage between two capacitor plates located adjacent to each other on the sensor plate with areas A_1 and A_2 respectively (see Figure 4-4). This voltage will be divided over the two related capacitances $\varepsilon A_1/d$ and $\varepsilon A_2/d$ respectively. Because the resulting electrostatic forces F_1 and F_2 is independent of the sign of the voltage as is clear from equation (4-6), the final result will be attraction of the seismic mass.

The total electrostatic attractive force, F_{ESNC}, by which the seismic mass is attracted, is equal to:

$$F_{ESNC}=F_1+F_2 \qquad (4\text{-}10)$$

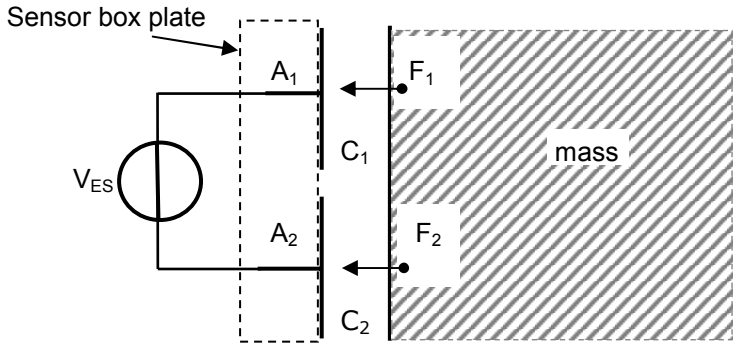

Figure 4-4: Wireless electrostatic attraction of the seismic mass.

The attractive force is a function of the potential difference between the fixed capacitor plate with area A_1 and the mass and the capacitor plate of A_2 and the mass. The potential differences over these capacitors are:

$$V_{C1} = \frac{A_2}{A_1 + A_2} \cdot V_{ES}$$

$$V_{C2} = \frac{A_1}{A_1 + A_2} \cdot V_{ES} \qquad (4\text{-}11)$$

Substitution of equation (4-10) and (4-11) in (4-6) results in:

$$F_{ESNC} = \frac{\varepsilon_0 \varepsilon_r}{2 \cdot d^2} \cdot \frac{A_1 \cdot A_2}{A_1 + A_2} \cdot V_{ES}^{\ 2} \qquad (4\text{-}12)$$

with

F_{ESNC}	=	*the electrostatic force between sensor plate and mass*	*[N]*
A_1	=	*the plate area of capacitor C_1*	*[m^2]*
A_2	=	*the plate area of capacitor C_2*	*[m^2]*
V_{ES}	=	*the voltage across C_1 + C_2*	*[V]*

With $A_1+A_2=A_{total}$ the electrostatic force between the contacted and the non-contacted configuration can be compared (equation (4-6) and (4-12)):

$$\frac{F_{ESNC}}{F_{ES}} = \frac{A_1 \cdot A_2}{(A_1 + A_2)^2} \qquad (4\text{-}13)$$

The maximum ratio is reached for $A_1=A_2$. In this situation the force is 4 times lower than in the situation of the directly contacted seismic mass. Concluded can be that the applied voltage has to be twice the voltage of the contacted configuration to reach the same mass displacement.

4.3.2 Sinusoidal voltage excitation

A voltage between the mass and the sensor plate will result in an attractive force, independent of which of the two elements is positive or negative with

respect to the other. For this reason an alternating voltage signal with a certain frequency will not result in a mass displacement with the same frequency, but with twice the actuation frequency. The displacement of the mass due to a sinusoidal electrostatic force can be calculated by using equations (4-12), (4-5) and (4-8).

$$\Delta d = \frac{F_{ESNC}}{k_{opt}} = \frac{\varepsilon_0 \varepsilon_r . \frac{A_1 \cdot A_2}{A_1 + A_2} \cdot V_{ES}^{\ 2}}{2 \cdot (d_0 + \Delta d)^2} \cdot \frac{d_0}{10 \cdot m \cdot a} \qquad (4\text{-}14)$$

Figure 4-5 shows the mass displacement as a function of an applied sine wave voltage. The used parameters are: an initial PDMS thickness of d_0=10 µm, A_1 and A_2 of 4.5 mm^2 and a sine wave amplitude of 30 V.

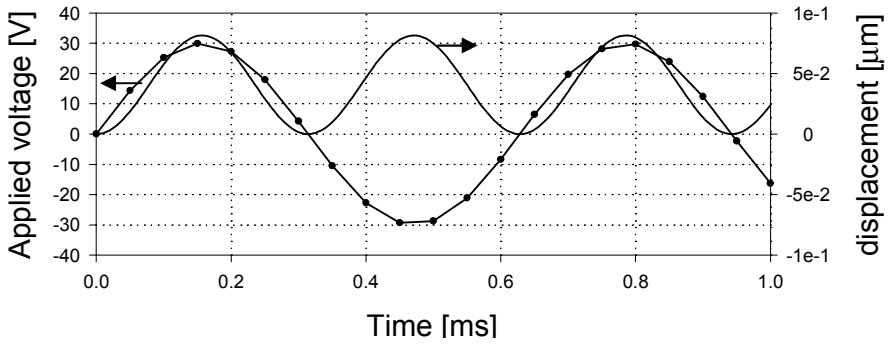

Figure 4-5: The movement of the mass (solid line) and the applied voltage signal (dotted line) as a function of the time.

The resulting movement of the seismic mass has twice the frequency of the applied sine wave. The shape of the movement is the square of a sine wave. The square of a sine wave results in a perfect cosine wave with the double frequency of the original sine wave, and an offset (equation (4-15)),

$$\sin^2 \omega \cdot t = \frac{1}{2}\left(1 - \cos 2\omega \cdot t\right) \qquad (4\text{-}15)$$

An advantage of the double frequency of the movement as compared to the applied actuation signal is that the measured movement of the mass can be separated from the actuation signal by means of filtering techniques.

It is also possible to let the mass vibrate in the same frequency as the applied voltage signal. This can be accomplished by giving the applied signal an offset, which makes the signal continuously positive or negative. This is shown in Figure 4-6. The result is a non-harmonic displacement of the mass.

Applying the voltage signal at one side of the sensor system has the advantage that the oscillating displacement of the seismic mass can be measured with the sensor plate on the opposite side of the mass. A disadvantage is that the mass can only be moved towards the conductive plate (only attraction is possible) and

not towards the sensing plate, which limits the possible amplitude of the movement.

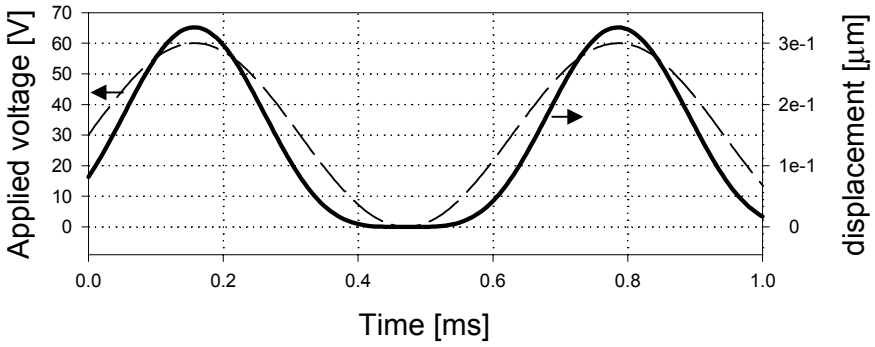

Figure 4-6: The movement of the mass (solid line) and the applied voltage signal with an offset (dotted line) as a function of the time.

It is possible to apply the voltage alternatively between the conductive plates on both sides of the mass. This will open the possibility to increase the amplitude of movements. A disadvantage is that it is more complex to measure the resulting movements of the seismic mass in the present construction.

4.4 Electromagnetic actuation of the seismic mass

Instead of electrostatic excitation of the mass it is also possible to generate vibration of the seismic mass by means of magnetic forces. A possible construction for the GyrAcc is shown in Figure 4-7.

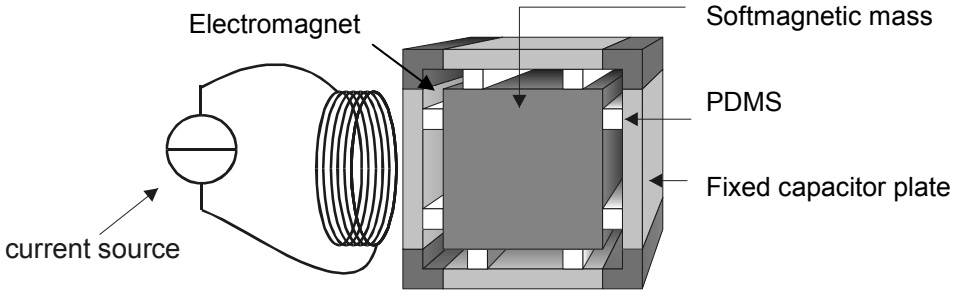

Figure 4-7: An electromagnet that can attract the mass inside the inertial sensor

A disadvantage of the addition of an electromagnet is the enlarged volume and weight of the Gyracc. An advantage is that the capacitive displacement sensing on which the sensor relies will not experience interference with the electromagnetic actuation, in contrast to the high voltages of the electrostatic actuation. Therefore the rest of this chapter will fully be devoted to electromagnetic actuation of the mass.

4.4.1 Electromagnets in micromachined sensors

The most interesting way to make an electromagnet is a planar coil made in the capacitor plates. Positioning a coil on top of a silicon plate has been done by a number of researchers [1,2,3,4]. Wagner and Benecke [1,2] presented a micro-actuator based on a planar coil and a moving permanent magnet mounted on a micromachined silicon suspension (Figure 4-8). Although a permanent magnet is not an option in the design of the triaxial inertial sensor, it is still interesting to know the force values that can be achieved by the application of planar coils, constructed in silicon.

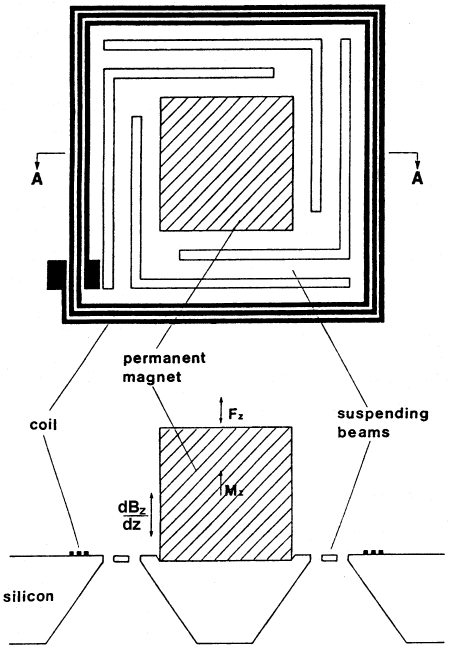

Figure 4-8: A schematic view of the electromagnetic actuator presented by Wagner and Benecke [2]

The actuator is driven by the vertical force F_z [N], with magnetization M_z [T] and volume V [m^3] of the magnet.

$$F_z = M_z \int \frac{d}{dz} H_z dV \qquad (4\text{-}16)$$

H_z [A/m] is the vertical component of the magnetic field produced by the planar coil. A square-shaped planar coil was designed with 17 turns, resulting in an EM-force on the magnet with dimensions of 1.5x1.5x1.0 mm^3 and a magnetization of 1.0 Tesla. Figure 4-9 shows the force as a function of the distance between the plane of the coil and the center of the magnet, during a 300mA actuation current. It is clear that this design can not approach the required force for the Gyracc (11 mN).

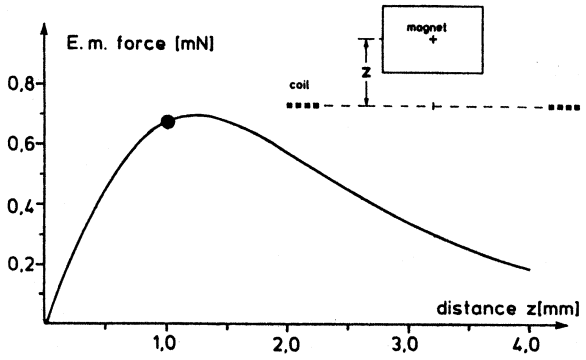

Figure 4-9: Electromagnetic force of the actuator designed by Wagner and Benecke during a 300mA actuation current [2].

A comparable approach is reported by Affane and Birch [3]. They used a planar coil in combination with a permanent magnet as a middle-ear implant hearing device. Figure 4-10 shows the schematic diagram.

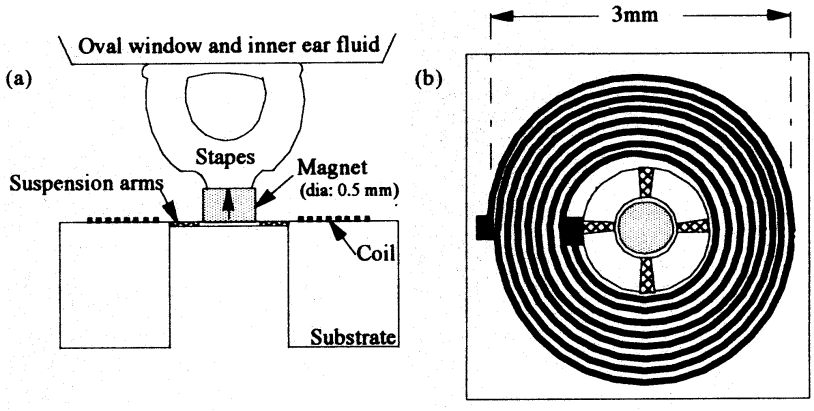

Figure 4-10: Schematic diagram of the proposed device of Affane and Birch [9], (a) cross section and (b) top view

With a 3 turn coil with a diameter of 2.5 mm, a 3.2 mm^3 magnet with a remanent magnetism of 1.15 T and a current of 2.5 mA, the resulting force is shown in Figure 4-11.

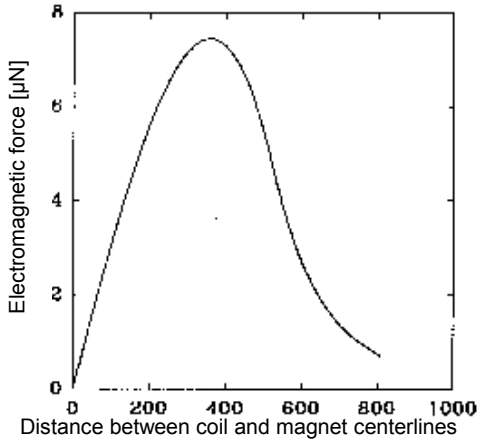

Figure 4-11: Force vs. distance characteristic of the device of Affane and Birch [3]

Even with adjustments of these parameters, the force will not be strong enough to actuate the seismic mass in the Gyracc.

The most powerfull electromagnet is presented by Fullin et al. [4]. They designed a micro relay, which consists of a "U-core", together with two planar multi-layered Cu-coils connected in series for generating a magnetic flux, thus realizing a higher NI product.

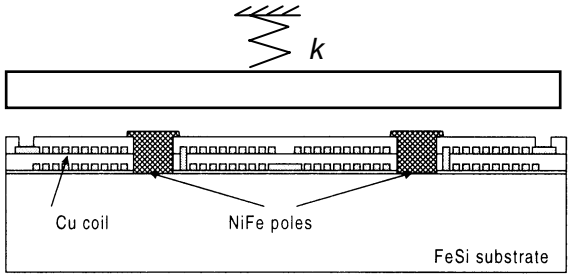

Figure 4-12: The multi-layer planar electromagnet design of Fullin et al. [4].

Figure 4-13 shows a comparison between an analytical calculation and a 2D finite-element analysis simulation, with a NI (product of number of turns and current) of 1.8 AT.

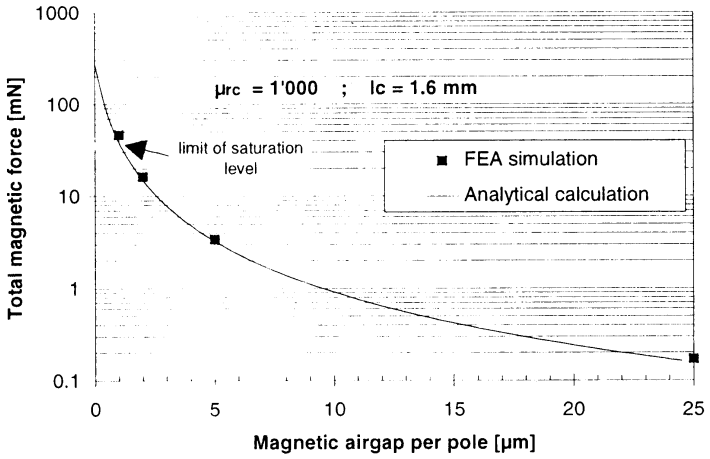

Figure 4-13: Comparison between analytical calculation and FEA simulation of the microrelay of Fullin et al. [4]

Figure 4-13 shows that forces in the order of 10 mN can be achieved by a planar coil construction, applying the U-core concept. Nevertheless the integration of a coil in the sensor plates of the Gyracc is not a realistic option. It can just deliver large enough forces but the construction is too complicated in combination with the capacitive displacement detection. To increase the force of an electromagnet the current through the coil could be increased or the number of turns of the coil. The increase of the current is limited to a certain current density, due to the generation of heat, but the number of turns can be increased if the electromagnet is positioned outside (unlimited space) the inertial sensor box. Therefore in the following paragraph a number of electromagnet designs with an external coil will be compared.

4.4.2 Electromagnet designs with an external coil

The possible actuation force of four electromagnet designs is estimated in this section. The dimensions of the magnet designs are not optimized, but the four electromagnets have in common:

- A distance of 150 micrometer from the iron seismic mass, which is the distance of the outer side of the sensor box to the mass.
- A 10 turn copper coil
- The copper wire carries 1A

A schematic drawing of an implementation of the electromagnet in the sensor-system is shown in Figure 4-14 and the force by which the mass inside the inertial sensor is attracted is calculated by MagNet, which is a finite element electromagnet simulation program [5]. Although the designs of the presented electromagnets are not optimized, the simulations will give an insight of the forces possible in these designs.

4.4.2.1 A coil at one side of the inertial sensor box

The first possible electromagnetic actuation is by means of a coil next to the inertial sensor box as shown in Figure 4-14a.

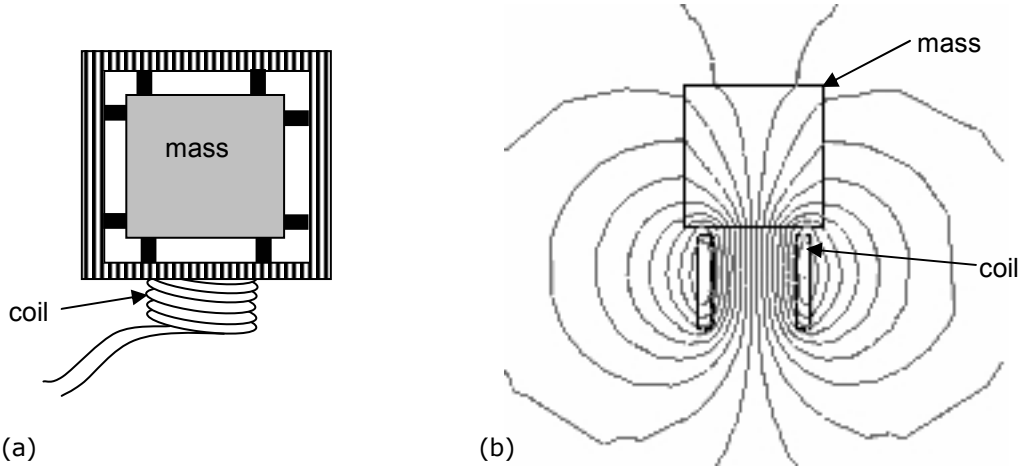

Figure 4-14: (a) Electromagnetic actuation by means of a coil outside the inertial sensing box (b) magnetic field lines of the actuated electromagnet

The attraction force of the coil on the iron mass is 22.8 μN (as calculated by MagNet). A variation on this concept is realized by providing the coil with an iron (soft magnetic material) core. This resulted in a force of 107.3 μN. A disadvantage of these designs is that the coil radiates its magnetic field around the wiring of the electronics far beyond the volume of the seismic mass (Figure 4-14b), which might have a negative effect on the mass position detection.

4.4.2.2 A coil around the inertial sensor box

In this actuating concept the coil is wrapped around the inertial sensor box. Figure 4-15 shows this concept for the three axes.

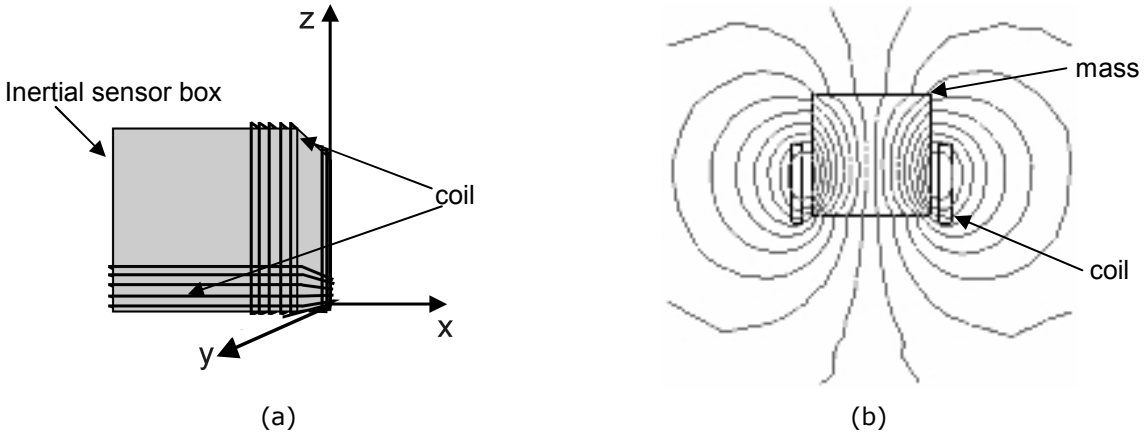

Figure 4-15: (a) Inertial sensor box wrapped in square-shaped coils for actuation in three axes (b) magnetic field lines during the actuation of one of the coils.

The attraction force of the coil on the iron mass is 37.6 μN (as calculated by MagNet). As with the previous mentioned design the coil around the inertial sensor box has the disadvantage that the coil radiates its magnetic field beyond the volume of the seismic mass (Figure 4-15b).

4.4.2.3 U-core electromagnet at one side of the inertial sensor

In a U-core electromagnet the electromagnetic field lines are guided through a soft magnetic material (iron).

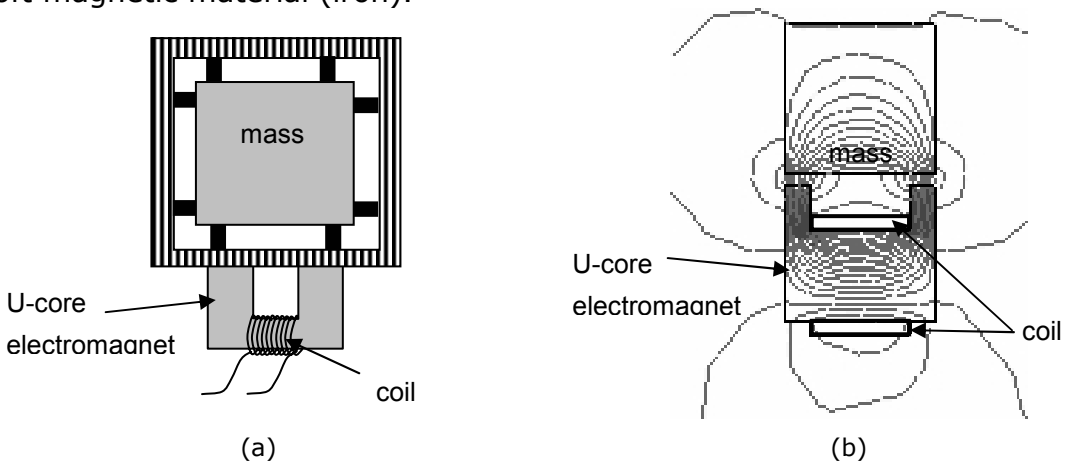

Figure 4-16: (a) The U-core besides the inertial sensor box (b) magnetic field lines during the actuation of the U-core.

Simulating this configuration with the same coil as in the other simulations and with arbitrary U-core dimensions, a force of 1.4 mN is calculated. In a U-core construction almost all flux lines are trapped within the core and the seismic mass (see Figure 4-16b).

4.4.2.4 An E-core electromagnet at one side of the inertial sensor

A different shape of the U-core electromagnet is found in the shape of an E-core, as shown in Figure 4-17a.

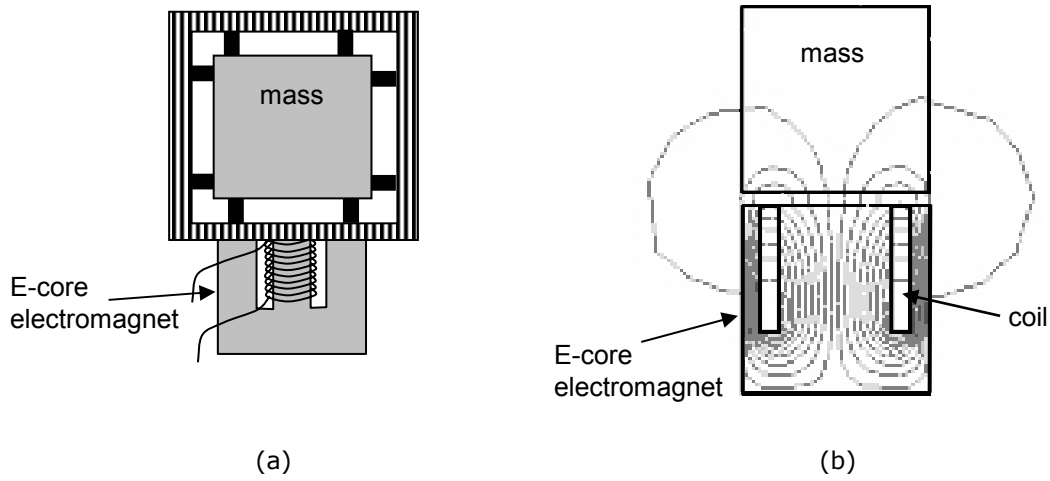

Figure 4-17: (a) The E-core besides the inertial sensor box (b) magnetic field lines during the actuation of the E-core.

Simulation of an E-core electromagnet resulted in a force of 2.3 mN. As for the U-core electromagnet most field lines are trapped within the sensor system.

With elongating the middle leg of the electromagnet through a plate of the inertial sensing box the magnetic resistance in the pathway is further reduced and a larger force can be achieved. When implementing a longer middle leg of the E-core through the sensor plate the seismic mass will be more attracted by the middle element of the E-core than the outer elements, which might reduce a possible wobbling effect of the mass.

4.4.3 Conclusions

Implementation of electromagnetic actuation in silicon based micromachining techniques has been realized by a number of groups. In most of the performed experiments the micro electromagnetic actuator existed of a planar coil that was designed to induce forces on a permanent magnet. The realized force by the mentioned techniques is well below the force necessary in the Gyracc. A different electromagnetic actuator was developed for the use in a micro relay. This electromagnet consisted of a magnetic field line conductor (soft magnetic material) and is able to attract a keeper of a soft magnetic material with a force in the milli-Newton range.

Four electromagnet designs have been suggested and a rough estimation of the force acting on the mass within the inertial sensor is made. Table 4.1 summarizes the forces calculated by the simulation program MagNet.

A great deal of the magnetic field is guided through free space around the coil shaped electromagnets, possibly inducing a current in the wiring of the capacitive distance detection system, which is in the vicinity of the electromagnet. Furthermore the actuation force of the coil shaped

electromagnet is much lower than for the U- and E-core electromagnets, which contain a magnetic field conductor.

Table 4.1: Simulated forces of the different electromagnet approaches, using the design conditions as given in section 4.4.2.

Electromagnet approach:	Shown in:	Force on the seismic mass
Coil without a core at one side	Figure 4-14	23 μN
Coil with a core at one side		107 μN
Coil around the sensor	Figure 4-15	38 μN
U-core at one side	Figure 4-16	1.4 mN
E-core at one side	Figure 4-17	2.3 mN

The U- and E-core electromagnets have the advantage that there is little radiation of the magnetic field, which could disturb the electronics in the vicinity. The magnetic flux in the U- and E-core magnets stays within the system and contributes to the necessary force. With the possibility to elongate the middle-leg of the E-core magnet this electromagnet is put under further investigation.

4.5 The actuation force of the E-core electromagnet

Because the mass is to be actuated, without changing the construction of the accelerometer, the electromagnet is placed externally along one of the axes to realize the actuation force (F) in that direction, as shown in Figure 4-18.

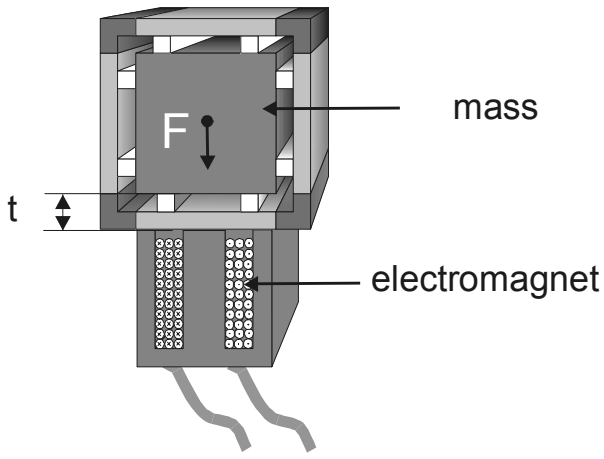

Figure 4-18: Cross section of the inertial sensor in combination with an E-core magnet

In the previous chapter finite element methods (MagNet) were used to calculate the force the electromagnet is applying to the mass at a certain distance (t). This is not a suitable tool for fast estimation of the influence of changes in design parameters. Therefore a lumped segment model of the electromagnet is made for simulation and optimalization purposes.

4.5.1 The lumped segment model of the E-core magnet

The stepwise transformation of the electromagnet into a lumped segment model is shown in Figure 4-19. Figure 4-19 shows a cross section of the electromagnet in combination with the seismic mass (keeper). For convenience we use the term E-core for this electromagnet, although the outer legs of the E-core are joined. The lines in the figure show the magnetic flux lines through the soft magnetic materials and the air gap between the poles of the electromagnet and the seismic mass. In the lumped segment model the magnetic flux between the poles of the electromagnet and the seismic mass is assumed to be uniform.

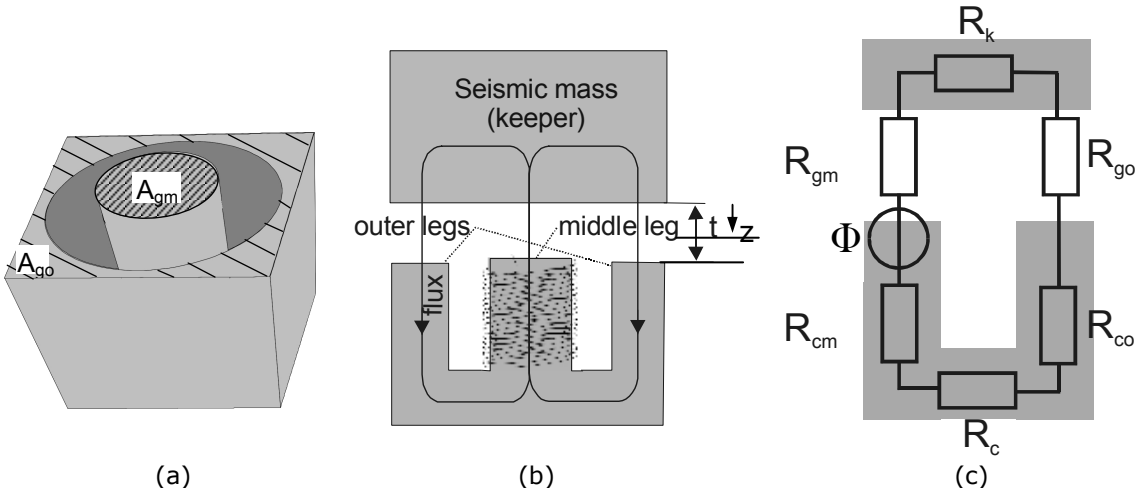

Figure 4-19: (a) A three-dimensional view of the E-core electromagnet (b) Cross-sectional view of electromagnetic fieldlines through the E-core electromagnet and seismic mass (c) The lumped segments of the model.

The different elements in Figure 4-19 are:

A_{gm}	*the area on top of the electromagnet 's central leg*	$[m^2]$
A_{g0}	*the area on top of the electromagnet 's outer leg*	$[m^2]$
R_k	*the reluctance of the keeper (the seismic mass)*	$[H^{-1}]$
R_c	*the reluctance of the standing leg of the E-core*	$[H^{-1}]$
R_{co}	*the reluctance of the outer leg*	$[H^{-1}]$
R_{cm}	*the reluctance of the middle leg*	$[H^{-1}]$
R_{go}	*the reluctance of the air-gap of the outer legs*	$[H^{-1}]$
R_{gm}	*the reluctance of the air-gap of the middle leg*	$[H^{-1}]$
Φ	*the magnetic flux*	$[Wb]$

The magnetic flux of the electromagnetic actuator passes different segments in the magnetic-circuit. Each segment has its specific reluctance (magnetic resistance) and can be calculated with equation (4-17) [5].

$$R_i = \frac{l_,}{\mu_0 \mu_{r,i} A_i} \qquad (4\text{-}17)$$

with,

$\mu_{r,i}$	= *the relative magnetic permeability of segment "i"*	*[-]*
μ_0	= *magnetic permeability of vacuum 1.25664.10^{-6}*	*[H/m]*
A_i	= *the cross area of segment "i"*	*[m^2]*
l_i	= *the length of segment "i"*	*[m]*

A current through the coil around the soft magnetic material will induce a magnetic flux through the magnetic circuit, which is equal to:

$$\Phi = \frac{N \cdot I}{\sum R_i} \tag{4-18}$$

with

N	= *the number of turns of conductive wire (the coil) around the pole of magnetic soft material.*	*[-]*
I	= *the current through the coil*	*[A]*

The seismic mass is pulled towards the electromagnet because the electromagnetic circuit wants to reduce the loss of energy in the electromagnetic circuit as much as possible. The relation between the energy W (J) in the magnetic circuit and the magnetic flux Φ (Wb) is given by equation (4-19).

$$W = \frac{1}{2} \cdot NI \cdot \Phi \tag{4-19}$$

The force produced in the z-direction (Figure 4-19b) is equal to the change in circuit energy as a function of the displacement of the keeper in the z-direction.

$$F_z = -\frac{\delta W}{\delta z} \tag{4-20}$$

The energy in the circuit is a function of the reluctance of all segments. Only the reluctance of the air-gap between the poles of the electromagnet and the keeper is a function of z. The dimensions of the E-core electromagnet and seismic mass are necessary to calculate all reluctances before the electromagnetic force can be calculated. Figure 4-20 specifies the variables used in the calculations.
The total reluctance of the elements (R_v), which are independent of the distance between the mass and the electromagnet, are given in equation (4-21), using Figure 4-19c:

$$R_v = R_k + R_{co} + R_c + R_{cm} \tag{4-21}$$

with

$$R_k = \frac{l_k}{\mu_0 \mu_{rk} A_k}, R_{co} = \frac{l_{co}}{\mu_0 \mu_{rco} A_{co}}, R_c = \frac{l_c}{\mu_0 \mu_{rc} A_c}, R_{cm} = \frac{l_{cm}}{\mu_0 \mu_{cm} A_{cm}}$$

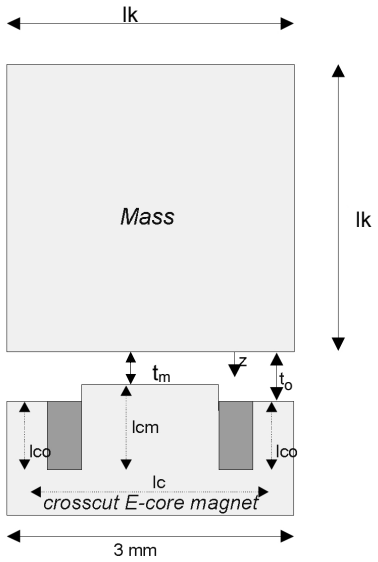

Figure 4-20: Cross-sectional view showing the dimensions of the E-core electromagnet and the seismic mass

The reluctance of the elements that are depending on the mass displacement in the z-direction are:

$$R_{gm} = \frac{t_m - z}{\mu_0 A_{gm}}$$
$$R_{go} = \frac{t_o - z}{\mu_0 A_{go}} \qquad (4\text{-}22)$$

Combining equations (4-19), (4-21) and (4-22) results in:

$$W = \frac{(NI)^2}{2\sum_i R_i} = \frac{(NI)^2}{2\left(\frac{t_m - z}{\mu_0 A_{gm}} + \frac{t_o - z}{\mu_0 A_{go}} + R_v\right)} \qquad (4\text{-}23)$$

The following equation can be used to calculate the force produced by an E-core electromagnet:

$$F_z = -\frac{\delta W}{\delta z} = -\frac{(A_{go} + A_{gm}) \cdot (NI)^2}{2\mu_0 A_{go} A_{gm}\left(\frac{t_m A_{go} + t_o A_{gm}}{\mu_0 A_{go} A_{gm}} + R_v\right)^2} \qquad (4\text{-}24)$$

with

F_z *= the attractive force of the electromagnet* *[N]*

Equation (4-24) shows an estimation of the force produced by an electromagnet at a certain distance from the seismic mass. The closer the middle and outer leg are positioned to the seismic mass the larger the attractive force will be. For this

reason two differently shaped electromagnets are combined with the inertial sensor and are taken into consideration.

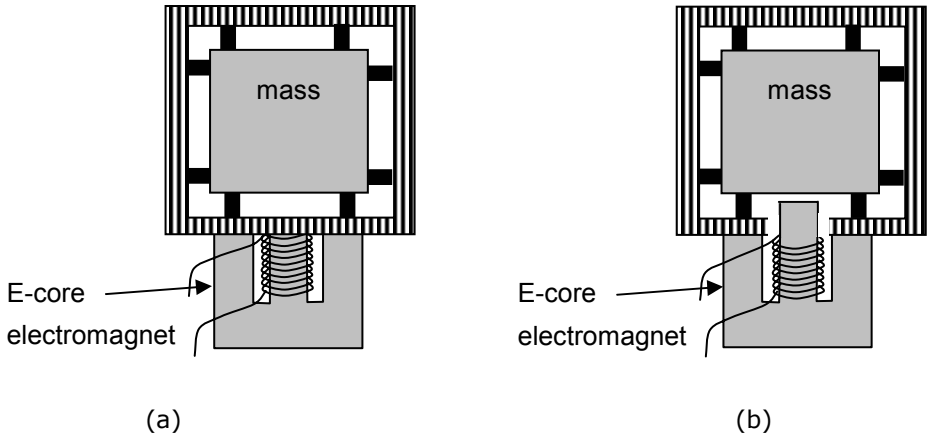

Figure 4-21: Cross-sectional view of a (a) standard e-core magnet and of an (b) E-core magnet with extended middle leg.

The difference between the electromagnets in Figure 4-19 is the longer middle leg of the electromagnet in figure b as compared to figure b, which results in a smaller distance between the seismic mass and the middle leg of the electromagnet. Note that a hole in the housing has to be available for the extended middle leg of the electromagnet. If both electromagnets are actuated with the same actuation current, then the electromagnet with the extended middle leg will have a larger attractive force on the seismic mass.

Example: The electromagnets shown in Figure 4-21 are realized (see Chapter 6). The attractive force of these two electromagnets is calculated with equation (4-24) and the dimensions of these practically realized electromagnets are used. For one electromagnet $t_{m1}=t_{o1}=150$ µm and for the other electromagnet $t_{o2}=150$ µm and $t_{m2}= 50$ µm. The attractive force of the electromagnet with extended middle leg shows to be approximately 5 times larger than for the electromagnet without the extended middle leg.

Equation (4-24) shows that the force is, besides of course a function of NI, for a great deal depending on the surfaces A_{go} and A_{gm} [m^2], which are the surface areas of respectively the outer- and middle legs of the E-core. The influence of the separate parameters will be discussed in the following section.

4.5.2 The maximum force of the E-core electromagnet

In case the E-core magnet and keeper (seismic mass) as shown in Figure 4-19 would be realized of an ideal magnetic material, then the reluctance in the soft magnetic material would be zero. In this case the electromagnetic force, as calculated in equation (4-24), can be re-written as:

$$F_{EM} = \frac{(A_{gm} + A_{go})(A_{gm}A_{go})}{(t_m A_{go} + t_o A_{gm})^2} . \tfrac{1}{2} \mu_0 (NI)^2 \qquad (4\text{-}25)$$

4.5.2.1 The NI product

The NI product in equation (4-25) is the product of the current through the coil and the number of turns the coil consists of. Thus the NI product is the total amount of current flowing through the cross sectional area of the electromagnet (Figure 4-22).

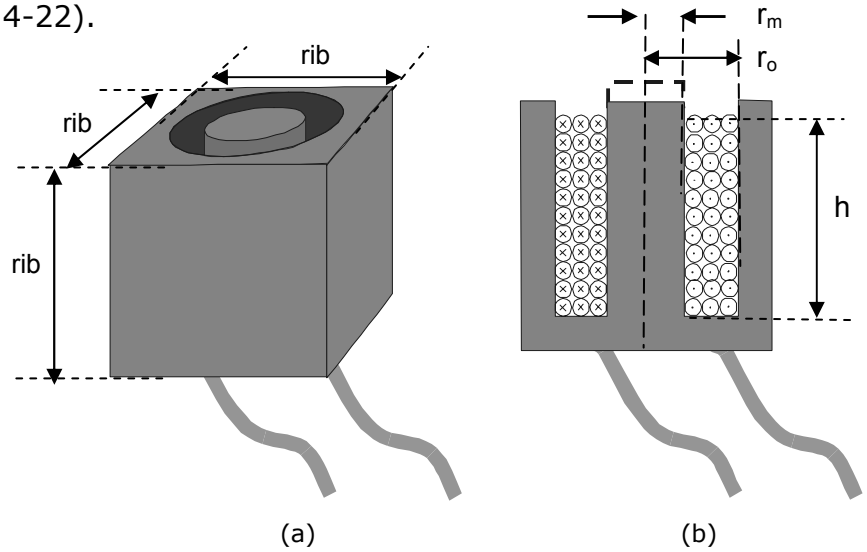

Figure 4-22: (a) Sketch of the electromagnet. (b) Cross-section of the electromagnet that shows the area of the NI product

The cross section is $h \times (r_o - r_m)$, but this area is not completely filled by current conducting copper wire.

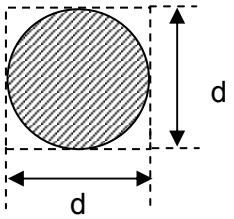

Figure 4-23: Cross-sectional view of a copper wire showing the effective area.

The ratio between the available area and the copper wire is the fill factor (FF). In case the wire of the coil is stacked as shown in Figure 4-22b, then the maximum fill factor is:

$$FF = \frac{d^2}{\pi\left(\frac{d}{2}\right)^2} = 0.78 \qquad (4\text{-}26)$$

The total possible ampere-turns (NI) can be calculated by means of equation (4-27),

$$NI = J \cdot FF \cdot (r_o - r_m) \cdot h \qquad (4\text{-}27)$$

with

J	=	*the current density*	$[A/m^2]$
r_o-r_m	=	*available thickness of the coil*	*[m]*
h	=	*height of the coil*	*[m]*
FF	=	*fill factor*	*[-]*

4.5.2.2 The size of the pole areas

The total available area at the top side of the electromagnet (A_{total}) is distributed over the coil and the pole areas A_{go} and A_{gm}. It will be determined for which ratio of these areas the largest electromagnetic force is reached. The pole areas are written as a function of the radians r_o and r_m (see Figure 4-22b).

$$A_{gm} = \pi \cdot r_m^{\,2} \qquad (4\text{-}28)$$

$$A_{go} = A_{total} - \pi \cdot r_o^{\,2} \qquad (4\text{-}29)$$

with,

A_{total}*= the total available area (rib×rib)* $[m^2]$

In case the middle leg and the outer leg of the electromagnet are at equal distance to the mass (t_o=t_m), then a maximum in the force as calculated by equation (4-25) is reached when A_{gm}=A_{go}. In this case the relation between r_o and r_m is:

$$r_o = \sqrt{\frac{A_{total} - \pi \cdot r_m^{\,2}}{\pi}} \qquad (4\text{-}30)$$

Substitution of equation (4-30) in equation (4-29) and subsequently in equation (4-25), results in a radius of the inner-leg of the electromagnet (r_m), which is 0.22 times the rib-length of the electromagnet. With equation (4-30) this results in a radius r_o, which is 0.53 times the rib-length of the electromagnet. Then, unfortunally, the coil would exceed the dimensions of the cubic shaped mass (Figure 4-25a).

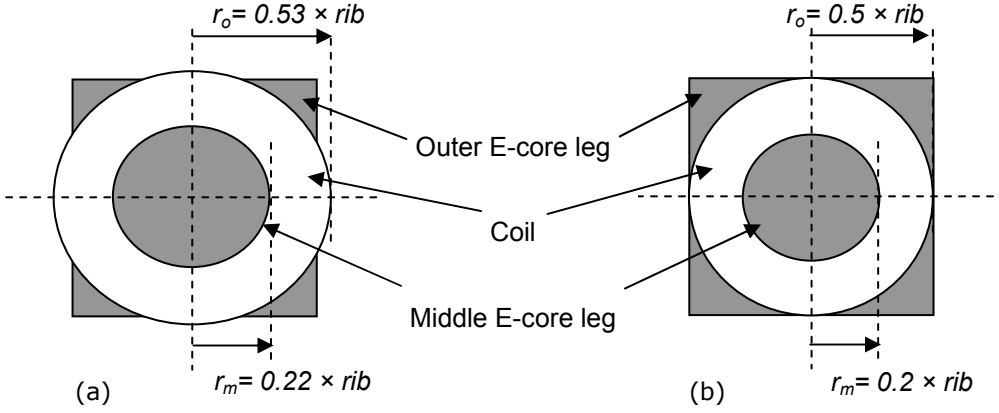

Figure 4-24: Top view of the E-core electromagnet with (a) optimized relation between the pole areas and the NI product, but exceeding the dimensions of the cube (b) optimized relation between the pole areas and the NI product, within the available space.

This is an undesired situation and therefore the maximum radius of the outer dimensions of the coil is limited to:

$$r_o = \frac{rib}{2}$$

The normalized force of an E-core electromagnet acting on the seismic mass as a function of the radius r_m of the middle leg is shown in Figure 4-25.

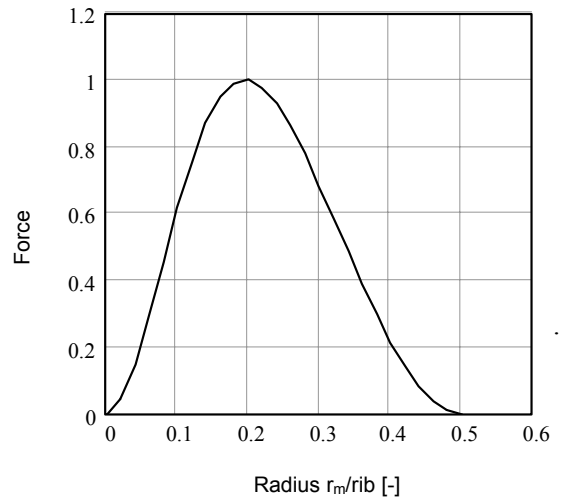

Figure 4-25: Force of E-core electromagnet for different values of r_m, here r_o=½ rib and t_o=t_m. Note: the maximum force normalized to 1.

In this new situation the maximum in the force is reached for an inner-leg with a radius (r_m) of 0.20×rib-length of the cubic shaped E-core magnet (Figure 4-24b).

4.5.2.3 The maximum force

Now all parameters are known for the design of an idealized electromagnet with a maximum attractive force. In Equation (4-25) the following parameters can be substituted:

$$\left.\begin{aligned} A_{gm} &= \pi \cdot (0.2 \cdot rib)^2 \\ A_{go} &= rib^2 \cdot (1 - \frac{\pi}{4}) \\ t &= t_m = t_o \\ NI &= J \cdot FF \cdot (\frac{rib}{2} - \frac{rib}{5}) \cdot h = J \cdot 0.78 \cdot 0.3 \cdot rib \cdot h \end{aligned}\right\} \quad (4\text{-}31)$$

which results in the following equation for the maximum force of the electromagnet:

$$F_{EM-MAX} \leq 2.7 \cdot 10^{-9} \cdot \frac{rib^4 \cdot h^2}{t^2} \cdot J^2 \quad (4\text{-}32)$$

For a cubic shaped electromagnet the height (h) of the E-core is equal to the length of the rib (rib):

$$F_{EM-MAX} \leq 2.7 \cdot 10^{-9} \cdot \frac{rib^6}{t^2} \cdot J^2 \qquad (4\text{-}33)$$

Figure 4-26 shows the absolute maximum force produced by a 3×3×3 mm^3 electromagnet for different current densities (J) as a function of distance t (Figure 4-20).

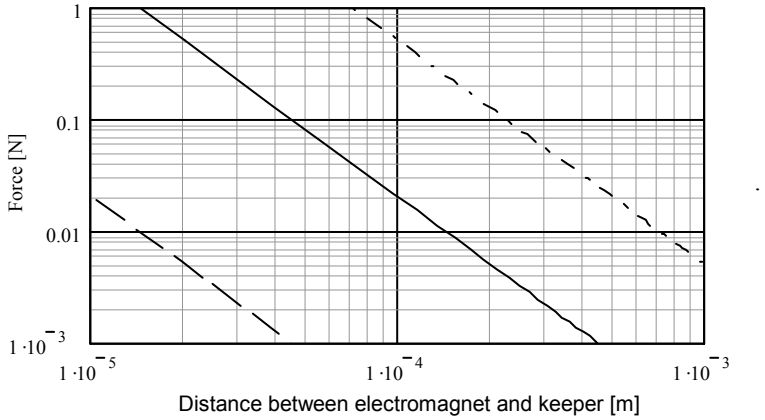

Figure 4-26: The absolute maximum force (F) of cubic shaped 3×3×3 mm^3 E-core electromagnet as a function of the distance (t) to the keeper for different current densities (J).

Figure 4-26 is a helpful graph for fast estimation of the minimum current density through the copper coil of the electromagnet in order to obtain the required force, as a function of the air gap (t). The shown maximum force is only limited by the reluctance of the air gap between the magnet and the mass. Note that for more accurate force estimations the reluctance of the yoke and mass have to be accounted for by substitution of equation (4-31) in equation (4-24).

4.6 Conclusions

The optimal mechanical sensitivity of the inertial sensor, with still a linear relation between the mass position and the sensor output signal, is reached when the seismic mass displaces 10% of the initial spring height during the maximum acceleration to be measured. This is realized by choosing the right spring constant in combination with the weight of the seismic mass.

The sensitivity of the sensor to rates of turn is a function of the actuated vibration amplitude. The higher the amplitude of this vibration, the higher the sensitivity of the sensor to rates of turn. The amplitude of the vibration is chosen to be 10% of the initial gap distance between the inner box walls and the mass, for reasons explained above.

The 3×3×3 mm^3 seismic mass is made of steel ST37, because this material can be used for electromagnetic as well as electrostatic actuation. The sensor is designed in such a way that the force acting on the mass to reach the maximum vibration amplitude is equal to the force acting on the mass during the experience of the maximum acceleration (50 m/s^2), being 11mN.

Electrostatic actuation is realized by applying a potential difference between the surfaces of two conducting objects. In the Gyracc the surface areas are the inner box wall and the opposing surface of the seismic mass. A potential can be applied to the seismic mass with or without the use of an electrical connection to the seismic mass. Calculations showed that a potential difference of 60V has to be applied to generate a force of 11 mN to two opposing surface areas of 3×3 mm^2 at a distance of 10µm. If this potential difference is to be realized without an electrical connection to the seismic mass then the potential difference should be 120V, which is regarded to be a too large voltage to be useful in biomedical applications.

Geometries of several electromagnets, positioned outside the inertial sensor, are discussed. The most efficient electromagnet showed to be the E-core magnet, which is a geometrical variation on the U-core magnet. An optimally designed E-core electromagnet with outer dimensions of 3×3×3 mm^3 realizes an attractive force of 11mN with an actuation current with a density of 11 A/mm^2.

4.7 References

[1] Wagner, B. and W. Benecke, "Magnetically Driven Microactuator: Design Considerations", Microsystem Technologies 90, Berlin, 1990, p.838, Springer-Verlag 1990.

[2] Wagner, B. and W. Benecke, "Microfabricated actuator with moving permanent magnet", Proceedings IEEE Micro Electro Mechanical Systems, Nara, Japan, 1991.

[3] Affane, W. and T.S. Birch, "A microminiature electromagnetic middle-ear implant hearing device", Sensors and Actuators A, A46-47, 1995, p.584-587.

[4] Fullin, E., J. Gobet, H.A.C. Tilmans and J. Bergqvist, "A new basic technology for magnetic micro-actuators", Proceedings IEEE Micro Electro Mechanical Systems, jan. 25-29 1998, Heidelberg, Germany.

[5] Software-package MagNet 5.2.3 by Infolytica, Montreal, 1996

Chapter 5

5 SIMULATIONS OF GYRACC BEHAVIOR

This chapter shows simulation results of the vibration behavior of the seismic mass during the experience of rate of turn in the two and three dimensional space.

5.1 Introduction

The mechanical behavior of the Gyracc is analyzed by means of the simulation program 20sim [1]. The Gyracc consists of the 3D inertial sensor as described in chapter 3 and is actuated with the electromagnet described in chapter 4. The sensor is divided into a number of subsystems for implementation in the simulation program. The subsystems are shown in Figure 5-1.

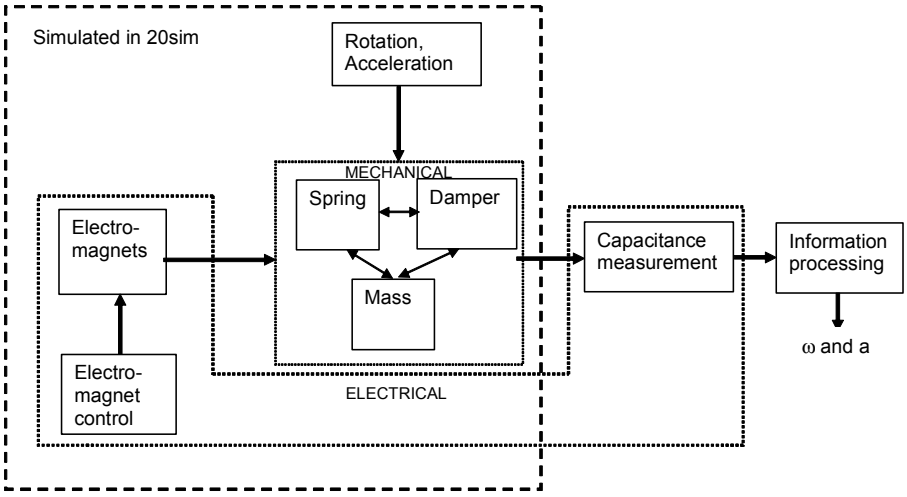

Figure 5-1: The specific subsystems of the Gyracc, which is simulated in the simulation package 20sim.

The goal of the simulation is to show the movement of the electromagnetically actuated sensor's seismic mass during the experience of acceleration and rate of turn. The simulation program should be flexible with respect to changes in the configuration of the model and should be able to solve non-linear differential equations (the non-linear PDMS springs). For this reason the simulation program 20sim is used. It solves differential equations numerically by means of the Runge-Kutta 4 method. The rotations are implemented in a vectorized representation of the mass-spring-damper system.

5.2 The simulation parameters

The subsystems of the Gyracc shown in Figure 5-1 are provided with the following simulation parameters:

5.2.1 Mass

The mass is considered to be a point mass, which experiences a force that is equal to:

$$F_{mass}=m.a \tag{5-1}$$

with

F_{mass}	*Force acting on the mass*	*[N]*
m	*mass of the seismic mass*	*[kg]*
a	*acceleration experienced by the mass*	*[m/s²]*

The simulations are performed with a mass weight of 220 mg.

5.2.2 Spring

The force-compression relation of the PDMS springs surrounding the point mass obeys equation (3-21), with PCR=0:

$$F_{spring} = GA_{PDMS}\left[\frac{2\cdot\Delta d}{d_0}+\frac{1}{\left(1-\frac{\Delta d}{d_0}\right)^2}-\frac{1}{\left(1+\frac{\Delta d}{d_0}\right)^2}\right]\cdot\left(1+\frac{2}{3}\right) \tag{5-2}$$

with

F_{spring}	*the applied force to the springs*	*[N]*
Δd	*the displacement of the mass*	*[m]*
d_0	*the initial thickness of the PDMS structures*	*[m]*
G	*the shear modulus of the spring*	*[N/m²]*
A_{PDMS}	*the area of the of the PDMS spring structures*	*[m²]*

The simulations are performed with: G= 250.000 N/m^2, A_{PDMS}= 4.10^{-8} m^2 and d_0= 10 µm.

5.2.3 Damper

The damping force acting on the mass (F_{damper}) is a function of the mass displacement velocity.

$$F_{damper}=b.v \tag{5-3}$$

with

F_{damper}	*the damping force caused by the damper*	*[N]*
b	*the damping constant*	*[N.s/m]*
v	*mass displacement velocity*	*[m/s]*

The simulations are performed with a damping constant of 1.4 N.s/m, which is the squeezed film damping. Some simulations are also performed with a damping constant of 2.8 N.s/m to get an impression of the consequences of a larger damping constant. This is because Appendix A showed that the damping in the symmetrical mass-spring-damper system is expected to be larger than the damping predicted by the use of squeezed film damping only.

5.2.4 Electromagnet

The force produced by an electromagnet, with optimized pole areas (substitution of equation 4-31 into equation 4-25), acting on the mass is equal to:

$$F_{EM} = 5.10^{-8} \cdot \frac{rib^2}{t^2} \cdot (N.I)^2 \qquad (5\text{-}4)$$

with

F_{EM}	*the force produced by the electromagnet*	*[N]*
rib	*rib length of the mass and electromagnet*	*[m]*
t	*the electromagnet to mass distance*	*[m]*
N	*the number of coil wire turns*	*[-]*
I	*the actuation current*	*[A]*

The simulations are performed with a 3mm rib length, 115 coil wire turns and a distance of 165 µm between the electromagnet and the seismic mass.

5.3 Single axis simulation

The simulations are executed with the parameters mentioned in the previous paragraph. In this paragraph the vibration of the mass along the actuation axis is investigated.

5.3.1 Seismic mass actuation

Figure 5-2 shows the electromagnetic force acting on the seismic mass and the resulting displacement of the mass as a function of the actuation current.

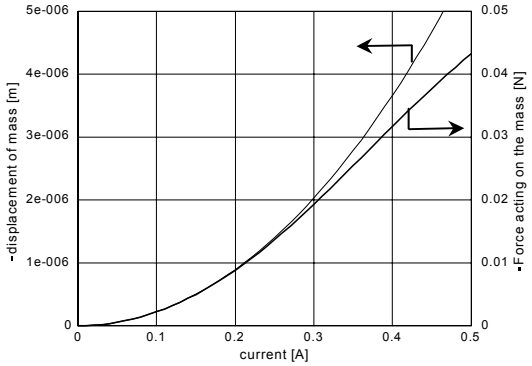

Figure 5-2: The mass displacement and force acting on the mass as a function of the applied current

Figure 5-2 shows a quadratic behavior in the current-force relation of the electromagnet. Furthermore it can be concluded that the mass displaces proportionally to the experienced force for displacements up to approximately 1µm, which corresponds to a 10% compression of the PDMS springs and an actuation current of approximately 200 mA for this example.
Figure 5-3 shows the force on the mass and the mass displacement for a sine-wave current of 1 mA and 100 mA actuation respectively.

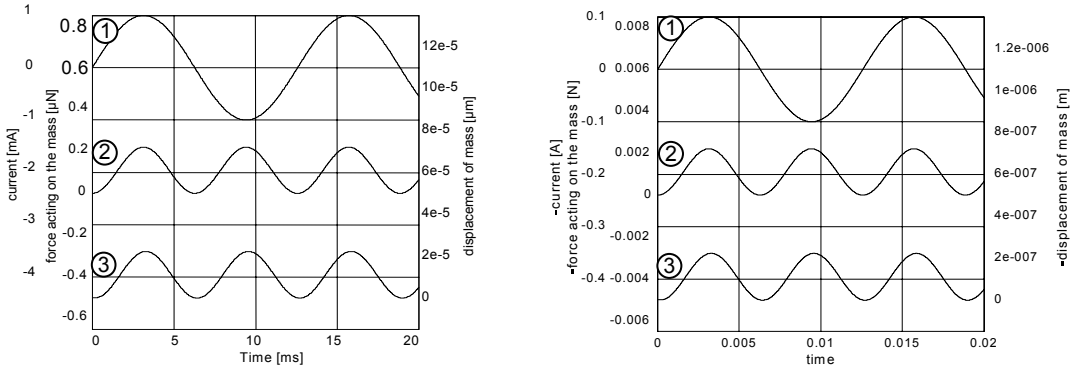

i=1 mA, b= 1.4 Ns/m, ω=1k rad/s i=100 mA, b= 1.4 Ns/m, ω=1k rad/s

Figure 5-3: The force (②) produced by the electromagnet as a function of the current (①) and the resulting movement of the mass (③).

Figure 5-3 shows that the force produced by the electromagnet is twice the frequency of the actuation current. A current amplitude of 1mA results in a force of 0.1 µN. A current amplitude of 100mA results in a force of 1 mN, which shows that the displacement is a square function of the actuation current as expected from Figure 5-2 for currents smaller than 200 mA.

5.3.2 Amplitude as a function of damping and frequency

Using equation (3-30) it can be calculated that the resonance frequency for the inertial sensor with 10 µm high PDMS and a damping constant of 1.4 Ns/m is 5944 rad/s and for the system with 2.8 Ns/m the resonance frequency is 2227 rad/s. The following figures show the movement of the mass for frequencies below the resonance frequency (2000 rad/s) and above resonance frequency (8000 rad/s), for a damping constant of 1.4 N.s/m and of 2.8 N.s/m.

Figure 5-4 shows that the resulting vibration of the mass has an offset displacement. This offset has its origin in the fact that the force produced by the electromagnet is the square of the sinusoidal actuation current ($I = \hat{i} \cdot \sin(\omega t)$).
Substitution of this sinusoidal current in equation (5-4) results in:

$$F_{EM} = 5.10^{-8} \cdot \frac{rib^2}{t^2} \cdot N^2 \cdot \hat{i}^2 \cdot [1 - \cos(2\omega t)] \qquad (5\text{-}5)$$

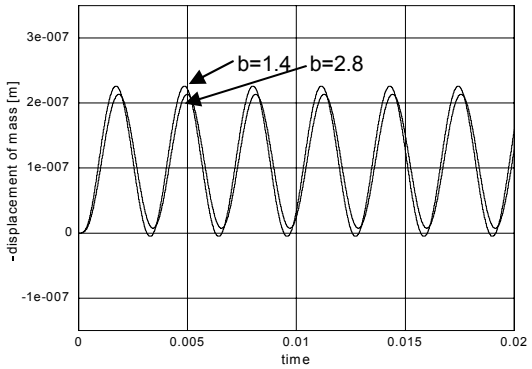

i=100 mA, b= 1.4 and 2.8 Ns/m, ω=2k rad/s

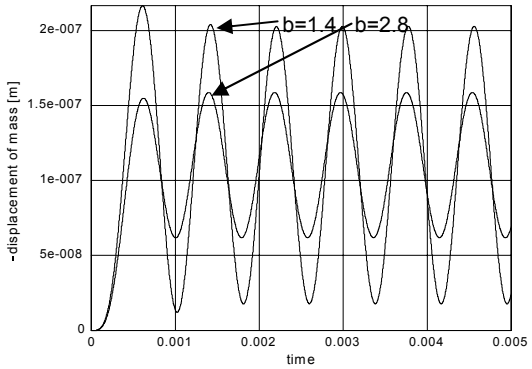

I=100 mA, b= 1.4 and 2.8 Ns/m, ω=8k rad/s

Figure 5-4: The vibration of the mass for two frequencies (2k and 8k rad/s) with two different damping constants (1.4 and 2.8 Ns/m).

Thus the electromagnetic force acting on the mass consists of a time dependent and a time independent part. The offset in the vibration of the mass is a function of the actuation current and is independent of the actuation frequency and damping constant.

Due to this offset force the springs between the mass and the electromagnet are pre-compressed and the opposite spring is extended. This non-symmetry of the PDMS springs results in an increase of the force-displacement relation (see Figure 3-5), which results in a rise of the spring constant and the resonance frequency as a consequence. The top-top amplitude of the vibration is a function of the damping constant and the actuation frequency. The top-top amplitude of the vibration for different actuation currents as a function of the frequency is shown in Figure 5-5.

Figure 5-5a shows the frequency response of the mass-spring-damper system. It is interesting to see that the top-top amplitude of the vibration reaches a plateau for the actuation frequencies between 5000 and 6000 rad/s. This is most likely due to the non-linearity of the spring constant. Figure 5-5b shows a comparable frequency response. Note that the vibration amplitude is higher for this higer actuation current. Figure 5-5c shows the frequency response for a 500 mA actuation current. This figure shows that the resonance frequency of the system is approximately 6500 rad/s, which is higher than for lower actuation currents. From this it can be concluded that the resonance frequency of the system is actuation current amplitude dependent.

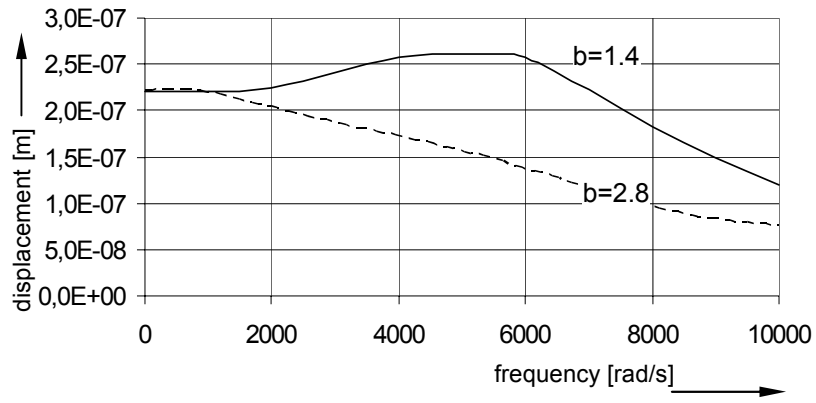

(a) i=100 mA, b= 1.4 and 2.8

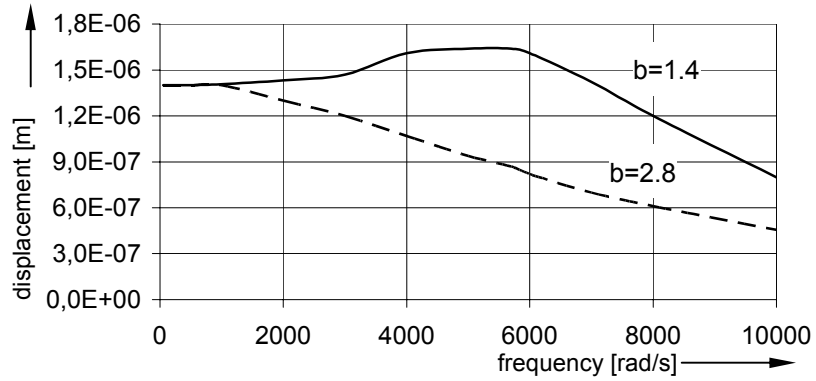

(b) i=250 mA, b= 1.4 and 2.8

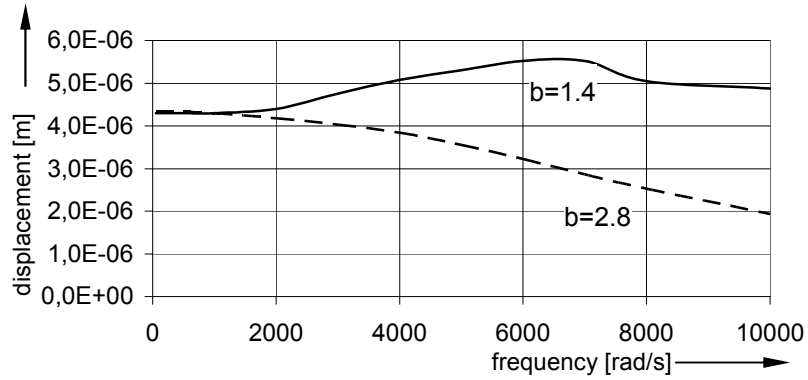

(c) i=500 mA, b= 1.4 and 2.8

Figure 5-5: Vibration top-top amplitude for two damping constants as a function of vibration frequency for 3 actuation currents.

5.3.3 High current actuation

The mass is brought into vibration with a sine-wave current with an amplitude of 1A (b=1.4 Ns/m).

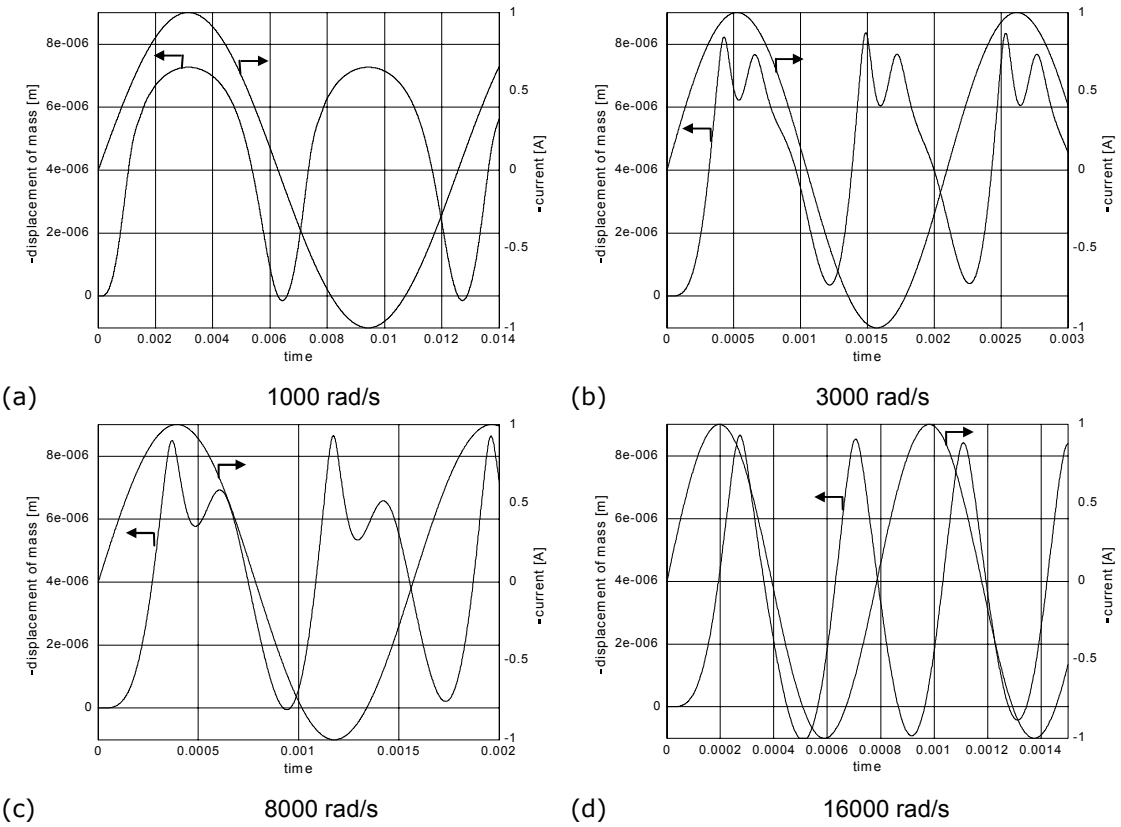

Figure 5-6: Actuation of the mass vibration with a relatively large actuation current at different frequencies.

Figure 5-6a shows the movement of the mass during sinusoidal actuation with a large current at a frequency well below its resonance frequency. The mass is pulled firmly into the non-linear springs as a result. The resulting mass movement is not sine wave shaped. At higher actuation frequencies the mass vibrates at higher harmonic frequencies (Figure 5-6b and c), which is a result of the non-linear behavior of the mass spring damper system. For a more or less sine-wave shaped vibration of the mass, the mass has to vibrate at the resonance frequency belonging to the actuation current. The resonance frequency for an actuation amplitude of 1A is about 16.000 rad/s, which is at least twice the frequency of resonance for small actuation currents.

5.3.4 Sine wave and pulse actuation

The electromagnets can be actuated by means of an actuation current with different shapes. The effect of a sine-wave actuation is compared with that of a pulse actuation at different actuation frequencies (i= 1mA, b=1.4), as shown in Figure 5-7.

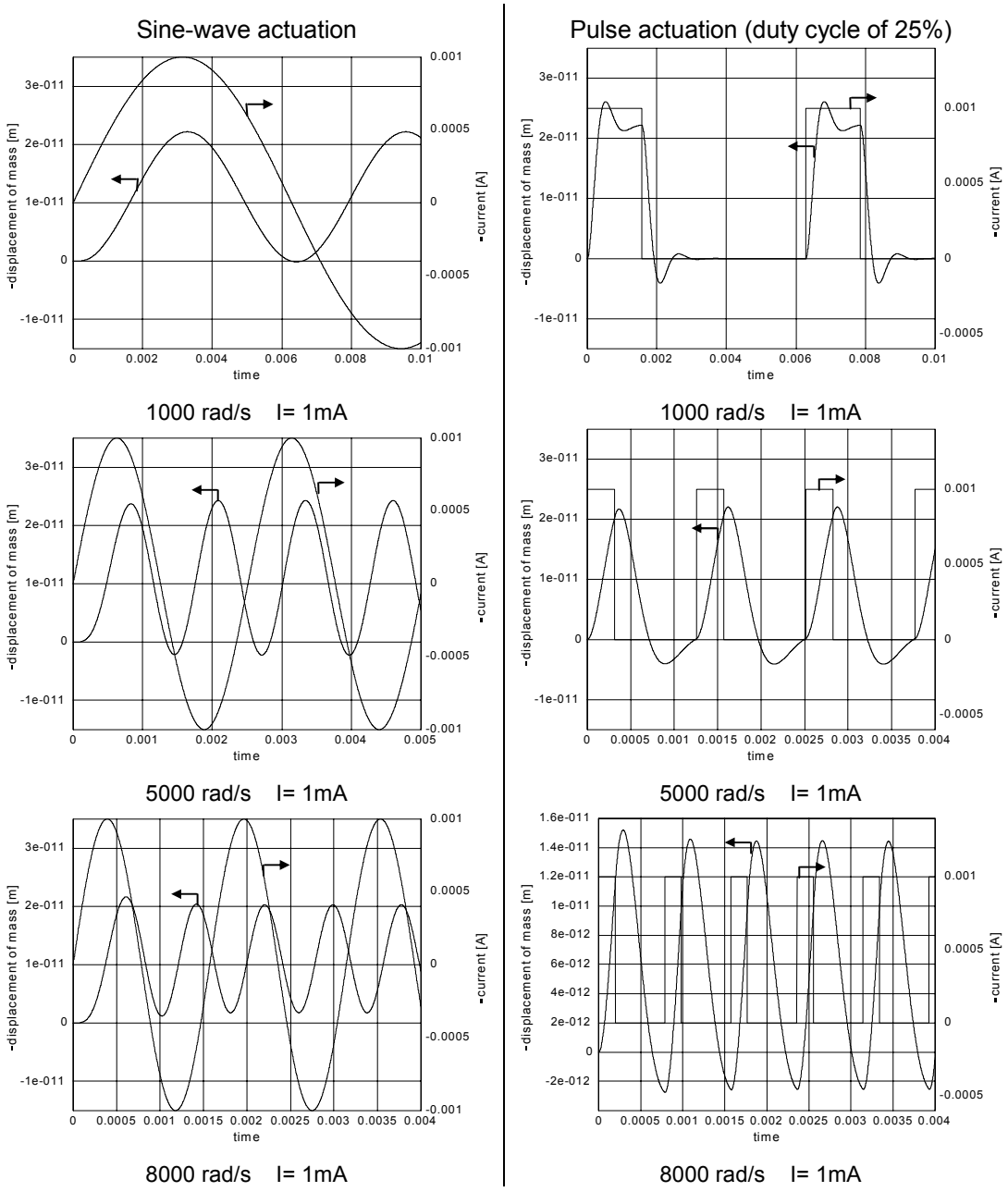

Figure 5-7: Sine wave and pulse actuation at different frequencies

Both actuation methods show a difference in amplitude of the resulting displacement as a function of the frequency. A sine-wave actuation results in a smooth (well controlled) vibration of the mass. The pulsed actuation of the mass results in a less fluent movement of the mass. However, for frequencies equal to or higher than the mass-spring-damper resonance frequency, the mass vibrates almost sine-wave shaped.

5.3.5 Tuning the resonance frequency

Section 5.3.2 showed that the resonance frequency of the vibrating mass is a function of the actuation amplitude of the electromagnet. The resonance

frequency of the mass can also be tuned by providing the sine-wave actuation current with a DC-offset current. The DC offset current provides the electromagnet with an offset force. This offset force attracts the mass thus compressing the PDMS springs at one side and stretches the springs on the opposite side. The spring constant around this new position of the mass is a function of the offset displacement of the mass. The simulated resonance frequency of the vibrating system as a function of the DC offset current is shown in Figure 5-8. The resonance frequency at different offset currents is deduced by taking the time period of the damped vibration, which occurs after applying the DC current to the electromagnet.

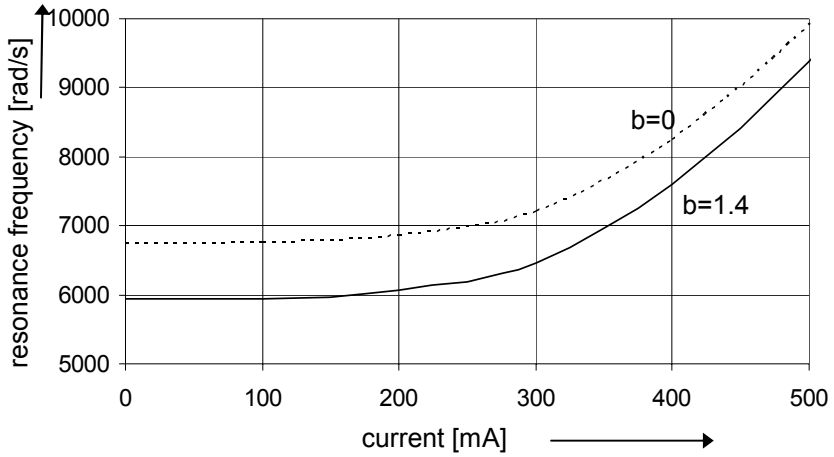

Figure 5-8: The simulated resonance frequency as a function of the DC-offset current for b=0 and 1.4 N.s/m.

Figure 5-8 shows that an offset in the actuation current results in a change in the resonance frequency. It is therefore possible to increase the resonance frequency of the mass by means of applying a DC offset current.

5.3.6 Conclusions

With the simulation results shown in this section, the following conclusions can be made for a mass actuated by an electromagnet:

- A sine wave actuation is preferred over a pulsed actuation, because sine wave actuation results in a more fluent vibration.
- A pure AC actuation current will result in a vibration frequency of the mass which is twice the actuation frequency.
- The mass vibrates around an offset position, which is a function of the actuation amplitude.
- The maximum amplitude in the vibration of the mass is reached at its resonance frequency.
- The maximum vibration amplitude of the mass is not reached at one single frequency, but shows a plateau for a range of frequencies.
- The resonance frequency increases with the amplitude of the sine wave current.

- Providing the actuation sine-wave current with a DC offset current increases the resonance frequency.

5.4 The Coriolis simulation

This section shows the vibration pathway of a mass that experiences rate of turn. The electromagnet actuates the mass in its x-axis and the rotations are performed around the z-axis, which will result in a Coriolis vibration of the mass in the x-y plane. The y-axis is being expressed as being the Coriolis axis. The movement of the mass in the Coriolis direction is not calculated by means of solving an equation, but by rotation of the mass spring damper system around an axis.

5.4.1 Coriolis amplitude as a function of the rate of turn.

In this simulation the system is rotated in the x-y plane without the experience of external accelerations. Figure 5-9 displays the movement of the vibrating mass in the actuation direction (x-axis) as well as the vibration in the Coriolis direction (y-axis) during a rate of turn of 1 rad/s. The electromagnet is actuated with a sinusoidal current with 10 mA amplitude and an angular frequency of 1000, 5000 and 8000 rad/s.

Figure 5-9, 1b, 2b and 3b represent the vibration pathway in the x-y plane of the mass, at different vibration frequencies. The startup of the vibration is represented by the line, which originates from coordinates (0,0). The difference in shape of the elliptical pathway in the three cases is mainly due to the phase shift between the vibration in actuation direction and the vibration in the Coriolis direction. The phase shift is a function of the vibration frequency. This is in agreement with the expectation as described in chapter 3, section 3.2.3. If the vibration frequency of the mass in the actuation axis (x-axis) is equal to the resonance frequency of the mass in the Coriolis direction, then the phase-shift between the two movements is 180^0. This results in a vibration along a straight line (Figure 5-9 2b). The amplitude in the Coriolis direction is about $2/10.000^{th}$ of the amplitude in the actuated direction during an experienced rate of turn of 1 rad/s.

Figure 5-10 shows the vibration pathway of the mass for different experienced rates of turn (-10, -5, 0, +5 and +10 [$^{rad}/_{s}$]) at an angular vibration frequency of 1000 rad/s.

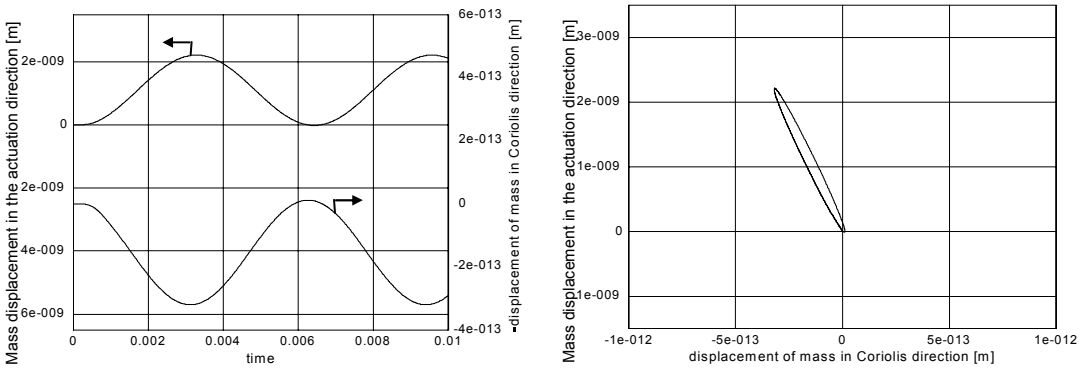

(1a) i=10 mA, b= 1.4 ω=1000 rad/s, Ω=1 rad/s (1b)

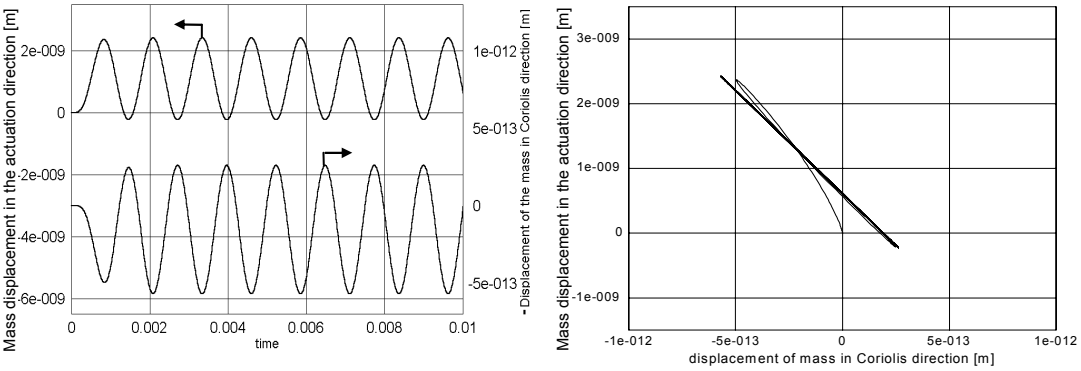

(2a) i=10 mA, b= 1.4, ω=5000 rad/s, Ω=1 rad/s (2b)

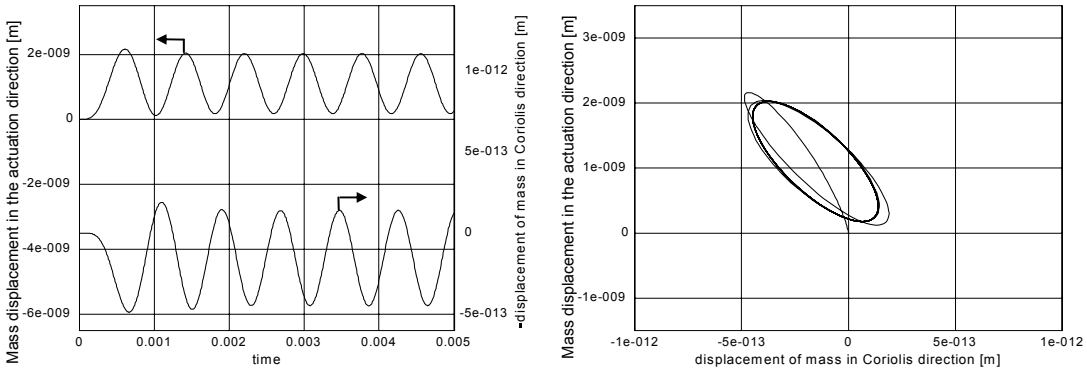

(3a) i=10 mA, b= 1.4, ω=8000 rad/s, Ω=1 rad/s (3b)

Figure 5-9: The first column shows the vibration in the x and y-axis at different vibration frequencies, during the experience of 1 rad/s rate of turn. The second column shows the corresponding vibration pathway of the mass in the x-y plane.

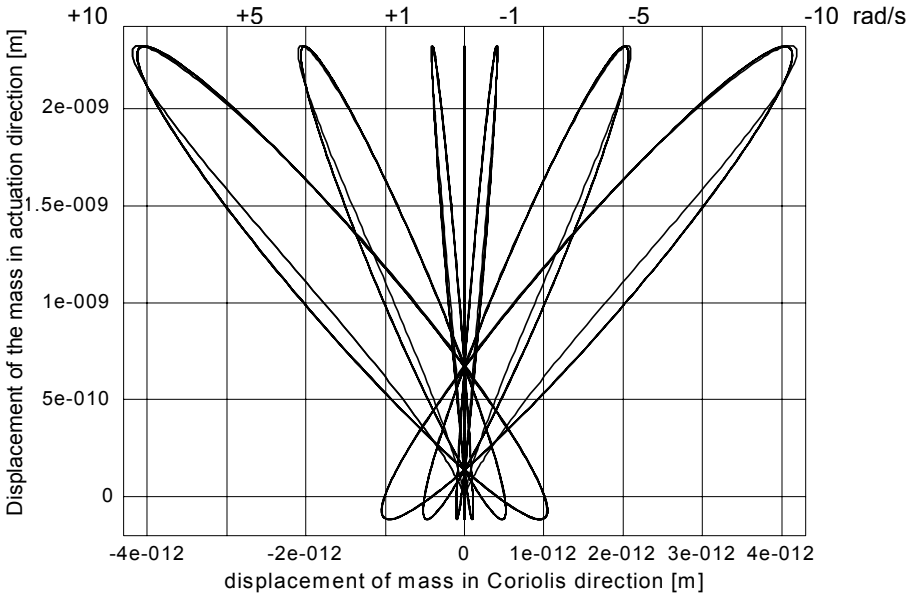

Figure 5-10: The vibration pathway of the mass for different experienced rates of turn

Note that the amplitude of the vibration in the actuated direction is independent of the experienced rate of turn. The amplitude in the Coriolis direction rises in proportion with the experienced rate of turn. Positive or negative experienced rates of turn result in different pathways of the mass, but with the same Coriolis amplitude. Figure 5-11 shows the top-top amplitude of the Coriolis vibration as a function of the experienced rate of turn.

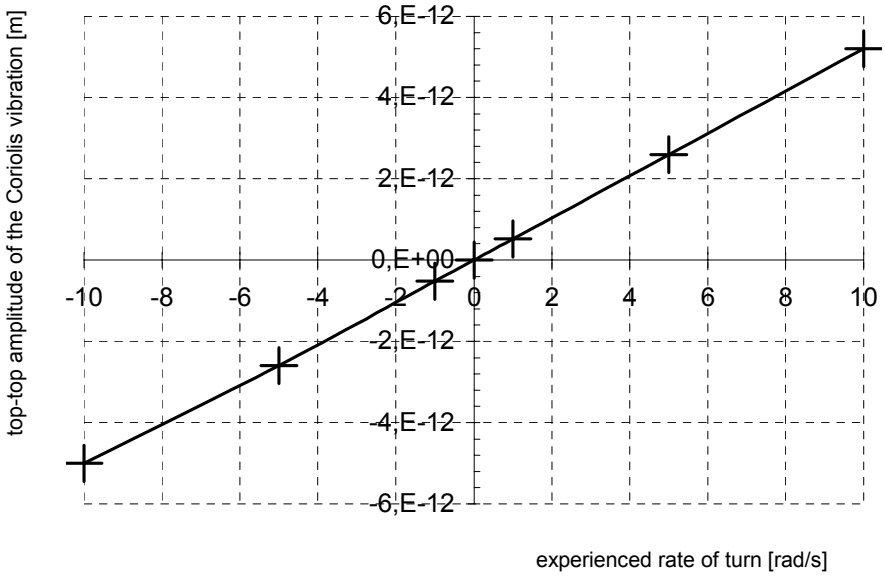

Figure 5-11: The top-top amplitude of the Coriolis vibration as a function of the experienced rate of turn for a 1000 rad/s vibration frequency.

The relation between the Coriolis amplitude and the experienced rate of turn is clearly linear.

5.4.2 The maximum rate of turn

In this simulation the system is exposed to a wider range of rates of turn than in the case shown in Figure 5-10. The goal is to investigate how the vibration pathway of the mass behaves under high rates of turn.

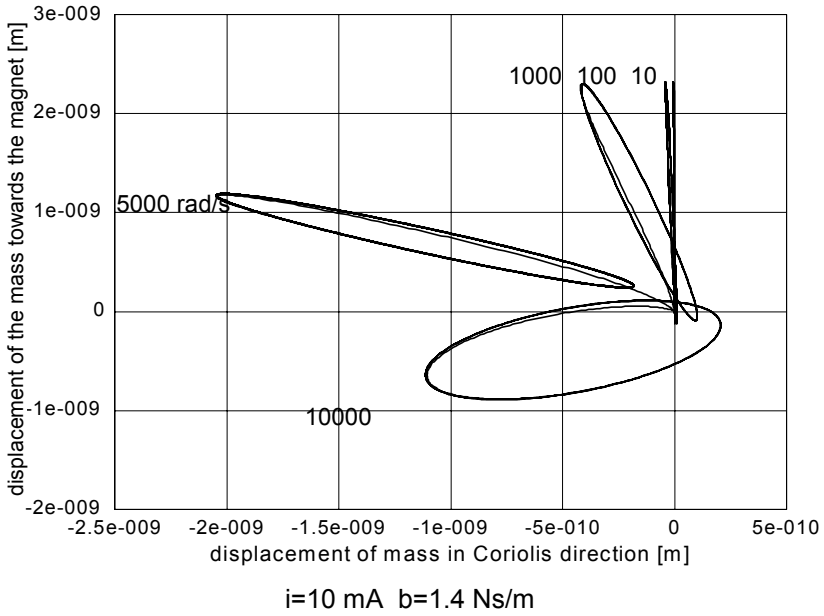

Figure 5-12: The vibration pathway of the mass under a number of rates of turn.

Figure 5-12 shows that the amplitude of the vibration in the actuated direction holds at least for rates of turn up to 1000 rad/s. For higher rates of turn like 5000 rad/s the amplitude in the actuated direction decreases. On the other hand, the amplitude in the Coriolis direction still increases for higher rates of turn, but at a rate of turn of 10.000 rad/s the Coriolis vibration also decreases in amplitude. A possible reason for the lowered amplitude is the out of phase vibration of the mass with respect to the actuation frequency in the x-axis.

Note that this example nicely shows why the first order approximation of the Coriolis force (equation 3-43):

$$F_{c,y}(t) = -2m.\Omega(t)\hat{x}\omega\cos(\omega t) \qquad (5\text{-}6)$$

only holds for Ω [rad/s] << ω [rad/s].

5.4.3 Influence of cross axis movement of the mass

The following example shows the movement of the seismic mass due to a misaligned actuation. The misaligned electromagnet realizes an actuation force in the y-axis direction, which is 0.5 % of the actuation force in the x-axis.

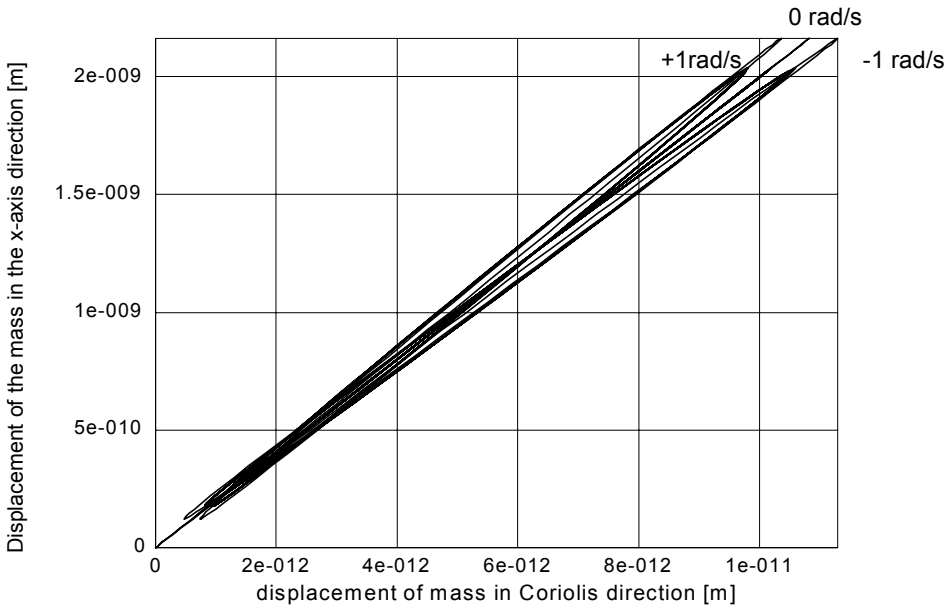

Cross-axis force =0.5% of F_{act} x-axis, Ω =0, +1 and –1 rad/s, ω = 3000 rad/s, i=10 mA, b=1.4 Ns/m

Figure 5-13: Vibrating mass pathway while the mass experiences cross-axis actuation, with and without the experience of a rate of turn.

The Coriolis amplitude is super-positioned on top of the cross-axis movement of the mass. Figure 5-13 shows that the amplitude of the vibration in the actuated direction is not influenced by the experienced rate of turn, but the amplitude in the Coriolis direction is increased or decreased by the experience of positive or negative rates of turn. The absolute change in amplitude of the y-axis signal is independent of the existence or non-existence of cross-axis movement. But the relative change in the amplitude of the y-axis signal is 5% at the given cross-axis movement of 0.5%. In case the cross-axis actuation force would be 5% then the change in signal in the Coriolis axis would only be 0.5% of the signal at an experienced rate of turn of 1 rad/s.

5.4.4 The influence of gravity

Up to now all simulations were conducted without the experience of accelerations on the system. In practice however the mass will experience gravitational force which results in a certain offset displacement. In this simulation the vibrating mass experiences gravitation in the x and y-axis during a rotation. The setup of the simulated situation is shown in Figure 5-14. The actuated vibration frequency is 200Hz, the actuation current amplitude is 10 mA and the system experiences a 2 rad/s rate of turn in the simulations.

The force acting on the mass due to the earth's gravity is calculated by means of: $F_{xy} = m.g.\sin(\alpha)$, the resulting force in the x-y plane during a rotation just out of plane of the earth surface (α=1°) is 0.03 mN and for the rotation perpendicular to the earth surface (α=90°) the force is 2.2 mN.

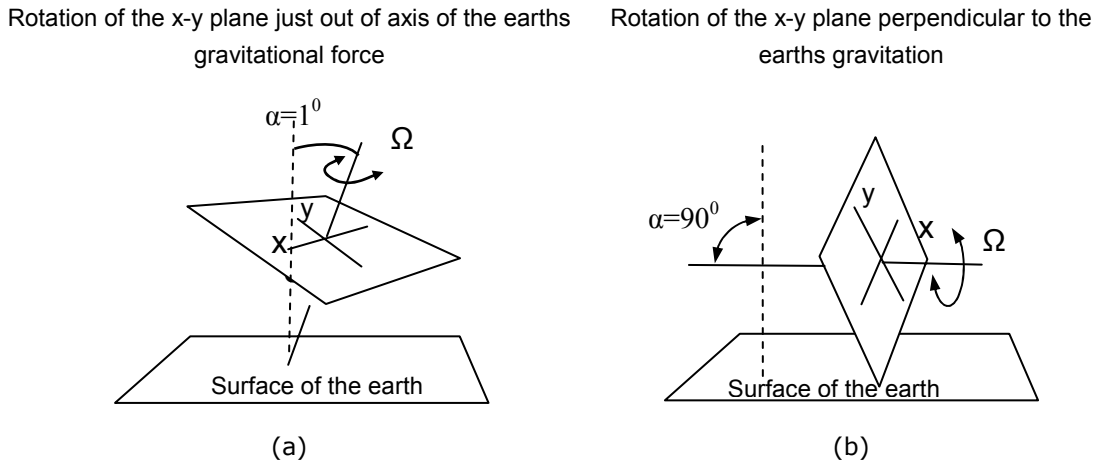

Figure 5-14: (a) Rotation of the x-y axis around an axis, with a 1^0 angle with the axis perpendicular to the earth surface ($\alpha=1^0$). (b) Rotation of the x-y plane perpendicular to the earth surface ($\alpha=90^0$).

The rotation perpendicular to the earth surface simulates the mechanical movements during roll (and pitch) of the Gyracc. Figure 5-15 shows the vibration pathway of the mass along the actuated and the Coriolis axis for these two situations.

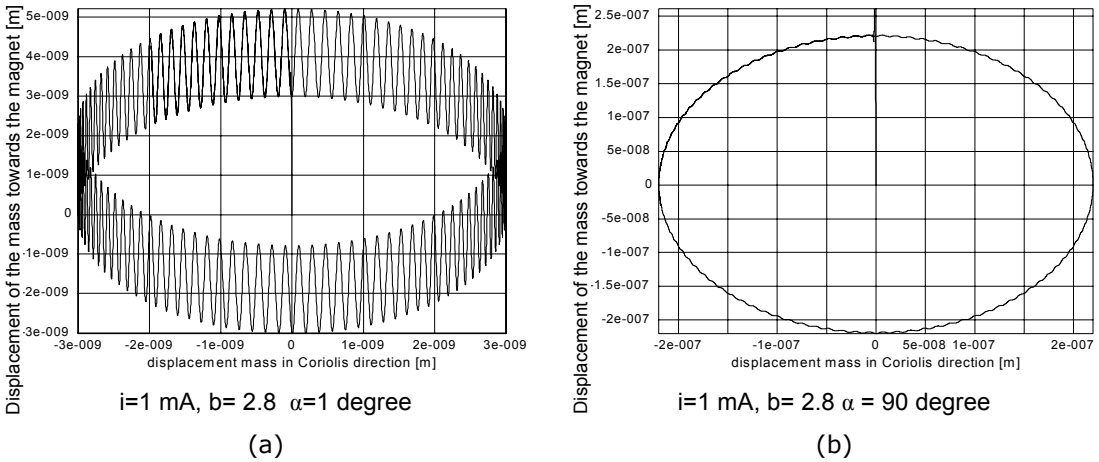

Figure 5-15: The vibration pathway of the mass in the x-y plane during a 360^0 rotation (a) just out of plane of the earth-surface (b) perpendicular to the earth surface.

The mass displacement in the Coriolis- and actuated direction are strongly influenced by the gravitational force acting on the vibrating mass. The circular shape represents the position of the mass during a full 360^0 rotation. Figure 5-16 shows the position of the mass along the actuated axis and the perpendicular Coriolis axis as a function of time for a whole 360^o rotation. The low-frequentcy wave with an angular frequency of 2 rad/s represents the displacement of the mass due to gravitation. The high frequency vibration (200Hz) on top of it is the actuated vibration of the mass. In Figure 5-16a the actuated vibration in the x-axis direction is clearly visible on top of the

displacement due to earth gravity. Note that the actuation induces an offset position of approximately 1.10^{-9} m. Figure 5-16b shows the individual axis as a function of the time for a rotation perpendicular to the earth surface. In this figure the actuation vibration is hardly visible. Here the displacement due to the earth gravity is much larger than the actuated vibration amplitude.

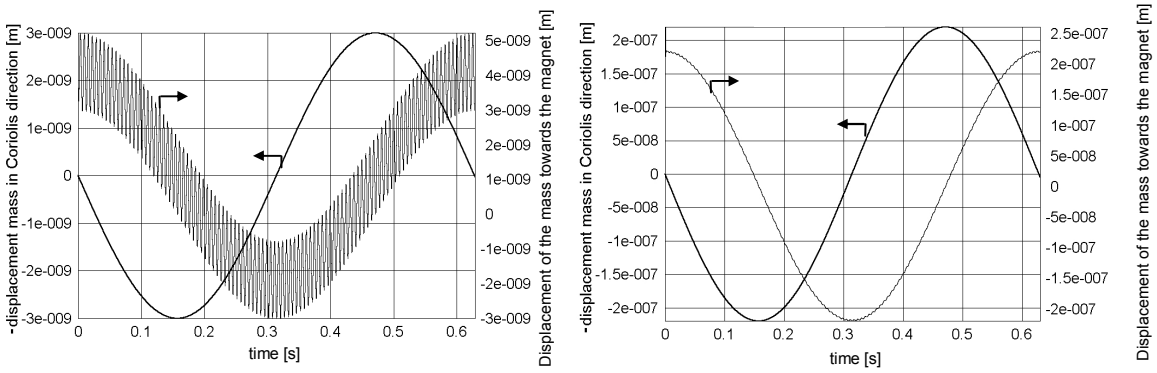

Figure 5-16: The vibration in the actuated and the Coriolis axis. (a) just out of plane of the earth's surface (b) perpendicular to the earth surface.

The vibration in the y-axis direction due to the Coriolis forces, induced by the experienced rate of turn, is not visible in both cases. Therefore an enlargement of the y-axis signal is made for both situations. The results are shown in Figure 5-17.

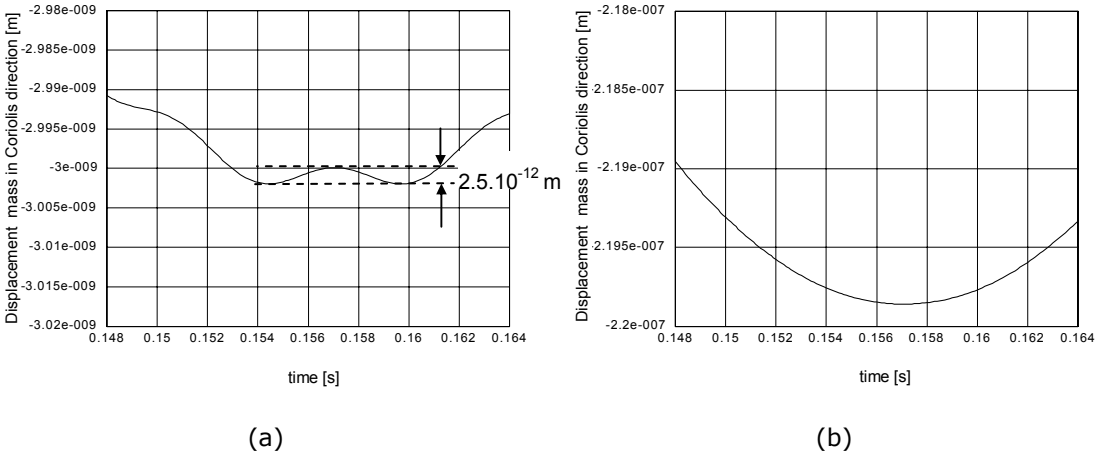

Figure 5-17: Close-up of the movement in the Coriolis-axis (a) just out of plane of the earth-surface (b) perpendicular to the earth surface.

The vibration in the y-axis due to the experienced rate of turn is visible for the just out of plane case. Figure 5-16 shows that the top-top amplitude due to the earth gravity is about 6.10^{-9} m. Figure 5-17 shows that the top-top amplitude due to the Coriolis force is approx. $2.5.10^{-12}$ m. Therefore the amplitude ratio of these to be measured signals is 1/2000.

During the rotation of the x-y plane perpendicular to the earth surface the top-top amplitude of the mass displacement is approximately 4.10^{-7} m. Therefore

the Coriolis displacement, which is not visible, is approximately 1/200.000th of the total to be measured signal.

The presence of gravitation during the experience of a rate of turn does not seem to be a problem, but the electronics that translate the displacement into a voltage needs to have a very high resolution. The high frequent Coriolis signal has to be separated from the low frequent acceleration signal to reduce the signal window before amplification can take place.

5.4.5 Conclusion

With the simulation results shown in this section, the following conclusions can be made for a vibrating mass, experiencing a rate of turn.

- The Coriolis amplitude is a function of the rate of turn and the frequency of operation.
- The vibrating mass pathway is a function of the rate of turn and of the frequency of operation
- The mass vibrates along a straight line when the vibration frequency of the mass in the actuation direction is equal to the resonance frequency in the Coriolis axis (y-axis).
- The absolute amplitude of the Coriolis signal is equal for positive and negative rates of turn.
- The maximum frequency of the to be measured rate of turn should be below the angular frequency of the vibrating mass.
- Cross axis movement of the mass has no influence on the Coriolis amplitude itself, but the relative change of the signal in the y-axis is reduced.
- The experience of gravitation or accelerations does not influence the Coriolis signal itself, but the relative change of the signal in the y-axis is reduced, requiring a properly designed electronic detection circuit.

5.5 Triaxial simulation

The simulations performed in this section make use of a different simulation model than the simulations performed in the previous sections. The previously mentioned 20sim model was only able to simulate the dynamic properties of the mass movements in the actuated direction and in an axis perpendicular to this axis. A 3D model of the Gyracc is implemented in Labview® [2] by Luinge [3]. The model contains the same parameters as the 20Sim model, but does not account for non-linear springs, electromagnetic force-distance relation and gravitational and acceleration forces.

5.5.1 Triaxial rate of turn measurement

In these simulations the mass is not solely actuated by an electromagnet in one direction, but also by an electromagnet perpendicular to the first actuation axis,

with a mutual phase shift of 90^0 as described in chapter 3. The resulting vibration pathway of the mass is shown in Figure 5-18.

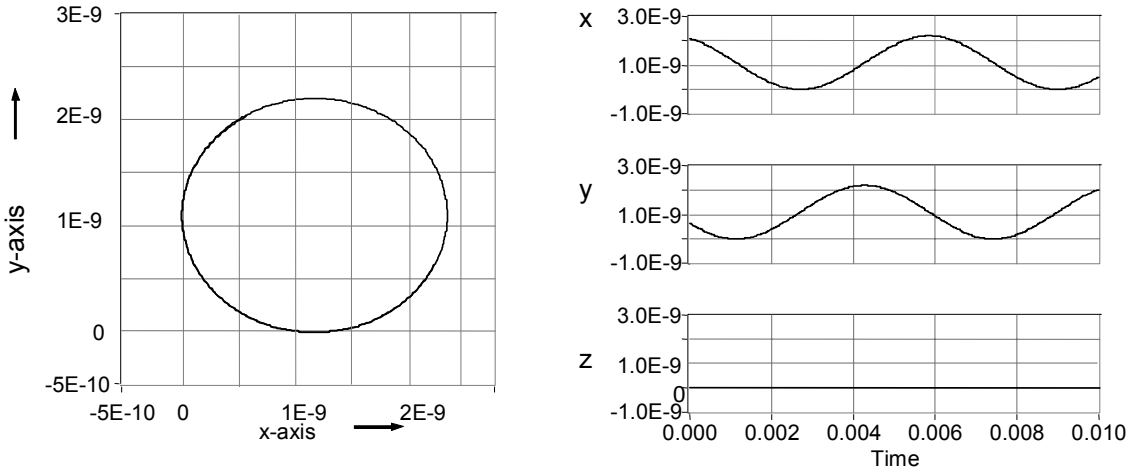

Figure 5-18: Circular vibration of the mass in the x-y plane without the experience of a rate of turn.

5.5.1.1 Rotation around the z-axis (Yaw)

The circular vibration in the x-y plane is exposed to a rate of turn around the z-axis of 1 rad/s. The circular vibration pathway of the mass only changes a very small amount. The small change in vibration pathway is not visible. Therefore the following figures will show the change in the pathway of the mass with respect to the pathway while the mass was not experiencing a rate of turn (Figure 5-18) and this is shown in Figure 5-19.

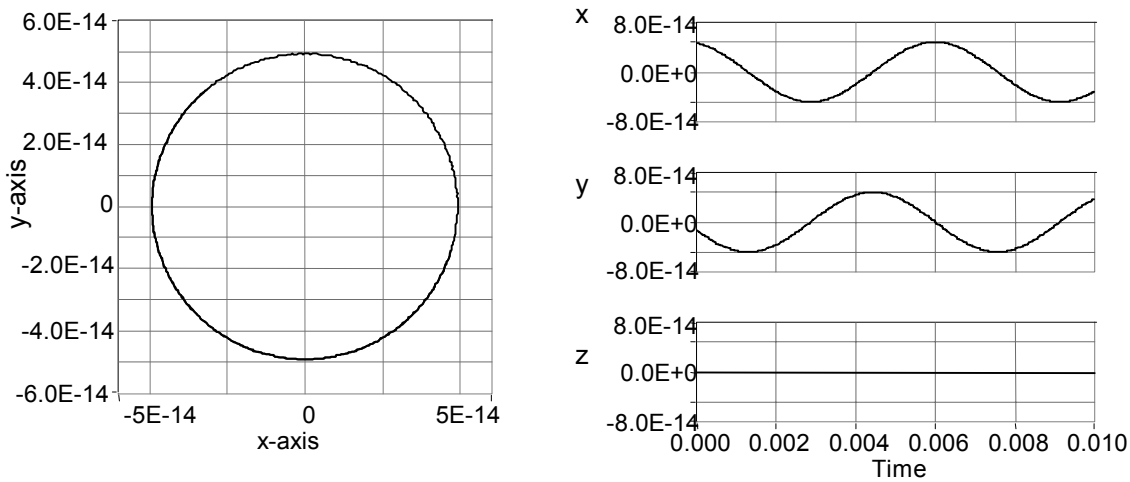

Figure 5-19: Change in mass pathway for a 1 rad/s rate of turn around the z-axis.

A rate of turn around the z-axis shows an increase in the amplitude in the x- and y-axis with respect to the $\Omega=0$ case of approximately 5.10^{-14} [m]. There is no additional movement in the z-axis.

5.5.1.2 Rotation around the x-axis (Roll)

The following figure shows the change in pathway of the mass for a 1 rad/s rate of turn around the x-axis.

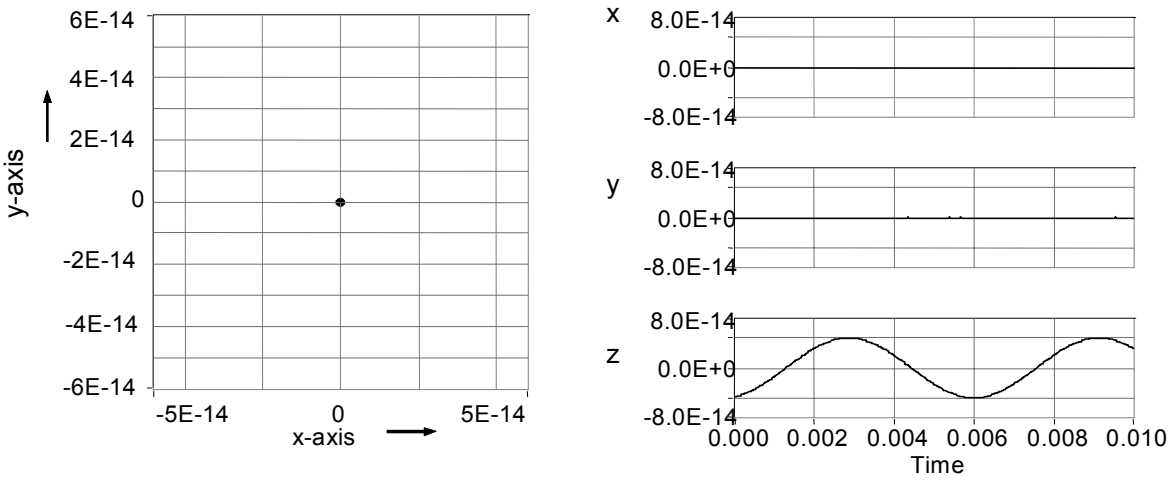

Figure 5-20: Change in mass pathway for a 1 rad/s rate of turn around the x-axis.

The rate of turn around the x-axis results in a vibration in the z-axis, which is in phase with the actuated vibration in the x-axis. The movements in the x-y plane are not influenced by the rotation around this axis.

5.5.1.3 Rotation around the y-axis (Pitch)

A rotation around the y-axis results in the change in pathway as shown in Figure 5-21.

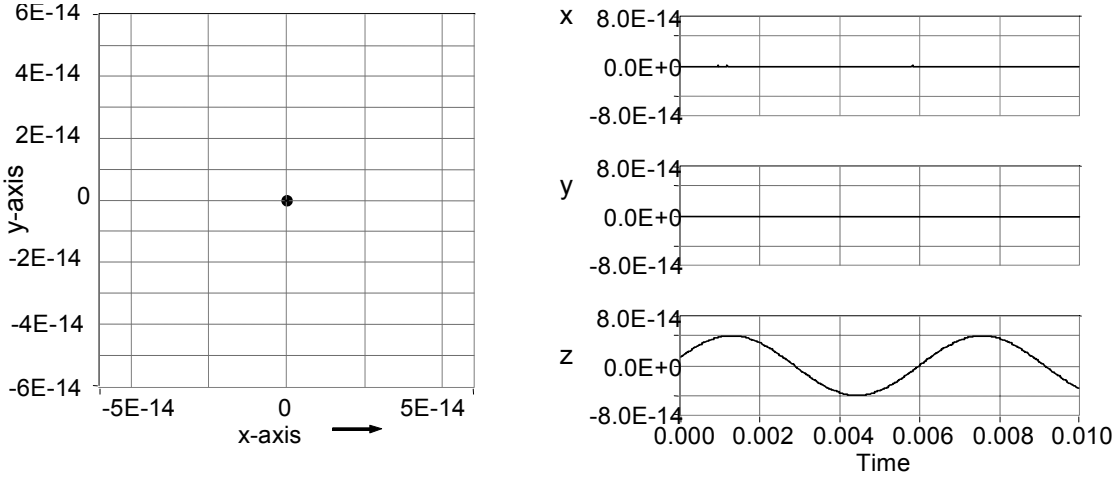

Figure 5-21: Change in mass pathway for a 1 rad/s rate of turn around the y-axis.

A rate of turn around the y-axis also results in a vibration in the z-axis. The vibration along the z-axis is in counter-phase with the actuated vibration in the y-axis (Figure 5-18).

5.5.1.4 Rotation around the x, y and z-axis

A rate of turn around the [1,1,1] axis is shown in Figure 5-22.

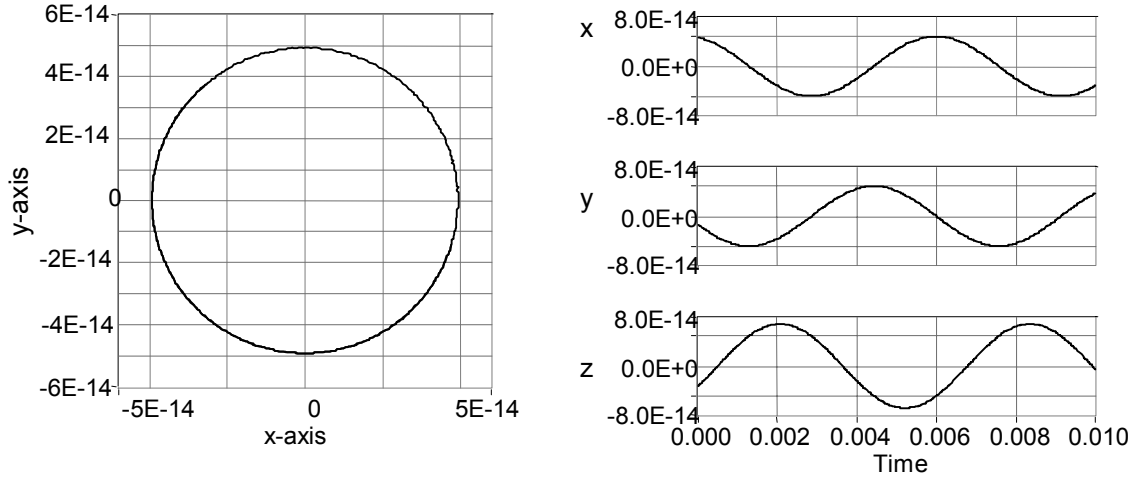

Figure 5-22: Change in mass pathway for a 1 rad/s rate of turn around the [1,1,1] axis.

As a result of the simultaneous rotation around the x, y and z-axes all three axes show changes in movement. In this case the maximum amplitude of the vibration in the z-axis is at a different phase with respect to the vibration in the actuated direction.

The rotation around the [1,1,1] axis is a summation of the rotation around the x, y and z-axis. The amplitude of the movements in a specific axis at a specific phase with the actuation vibration is a measure for the experienced rate of turn. It will be hard to subtract the amplitudes of the signals at their specific phase with the applied vibration. Note that these simulations are performed on a system with linear springs and actuation.

5.5.2 Conclusions

With the simulation results shown in this section, the following conclusions can be made of a mass that is vibrating in a circular pathway.

- With a circular vibration pathway of the mass it is possible to detect rotations around all three axes.
- Rotation around the x-axis as well as rotation around the y-axis results in a vibration in the z-axis.

5.6 Conclusions

To make the seismic mass of the mass-spring-damper system vibrate in a well defined way the electromagnet is to be positioned at a relatively large distance from the mass and is to be actuated with a sinusoidal current that is small enough to make the mass vibrate in its linear region. The angular frequency of the vibration should be well above the maximum to be measured rate of turn. The Coriolis amplitude can be best detected if the cross axis sensitivity is as low as possible. Combined acceleration and rate of turn sensing is not a fundamental problem, but it has its influence on the design of the detection electronics. With a circular vibration of the mass, obtained by two

electromagnets, the rotation around the three axes of the 3-Dimensional space can be detected.

5.7 References

[1] 20Sim 3.0, ControlLab Products B.V, bond graph simulation package, Enschede, Netherlands, 1993.

[2] Labview 6.1, Multi-purpose data analysis software, National Instruments, Austin, Texas, 1998.

[3] Luinge H., Thesis: "Inertial Sensing of Human Movement", Twente University Press, ISBN 9036518237, Enschede, The Netherlands, 2002.

Chapter 6

6 DESIGN AND REALIZATION

This chapter shows the practical implementation of the theoretically described Gyracc.

6.1 Inertial sensor structure

The theoretically described sensor has to be realized. Therefore a sensor is designed which approaches the sensor described in theory as close as possible. The sensor consists of an orthogonal cubic mass, which is enclosed by springs inside a box. The inner walls of the box are covered with capacitor plates to detect the position of the mass with respect to the inner walls of the box by means of capacitive detection [1]. The minimum size by which a cubic mass is manually handled well is about 3×3×3 mm^3. For the required mass displacement sensitivity the distance between the 3×3×3mm^3 mass and the inner box-walls should be about 10 micrometer. The seismic mass, the height of the springs, the distance between the inside of the box walls and the seismic mass is now specified and equal for each axis. Simulations showed that a non-orthogonal mass is a source of cross-axis movement, which results in undesired cross axis sensitivity [2]. An orthogonal mass cannot be realized by means of micromachining because of the limited aspect ratio during the etching processes. Therefore the 3D inertial sensor is constructed with an orthogonal mass produced by means of precision engineering instead of micromachining. This precision engineered mass is symmetrically suspended by the rubber elastic material PDMS inside a box (Figure 6-1).

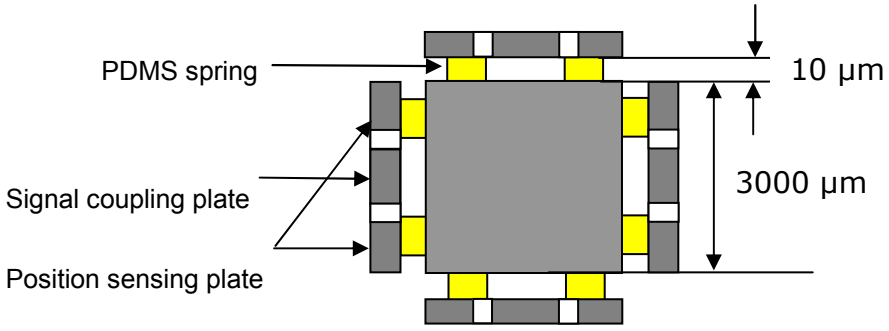

Figure 6-1: Cross-section of the 3D inertial sensor box.

Lötters realized this inertial sensor concept as a triaxial accelerometer [3]. Its mechanical construction is summarized in paragraph 6-3. In that design the mass consisted of tungsten. To extend the triaxial accelerometer with the possibility to sense rate of turn, an actuator has to be added to the construction

to let the mass vibrate. The design of this actuator (an electromagnet) is described in section 6.2. This also implies that in this case the mass should be made from a ferromagnetic material. The construction of the original triaxial accelerometer appears to be unsuitable for the rate of turn sensor, therefore two new designs for an inertial sensor box are shown and described in paragraph 6.4 and 6.5, both with their own advantages and disadvantages.

6.2 The electromagnet

The electromagnet proposed in section 4.5 is realized by means of precision engineering. In the centre of an iron cube of 3 x 3 x 3 mm^3 a hole with a depth of 2.6 mm and a diameter of 2.6 mm is milled (Figure 6-2a). A hole with a diameter of 1 mm was drilled in the center of this cavity and another hole was drilled in the bottom of the core close to the outer wall as a through hole for the copper wires of the coil (Figure 6-2b). The inner leg of the E-core, with a diameter of 1mm and a length of 3.1 mm, is lowered in the center hole. For a solid fixation the core is heated up, resulting in a small expansion of the hole diameter after which the middle leg is put in the hole (Figure 6-2c). The middle leg is fixed during the cooling down of the core. With this methode one is able to construct an E-core magnet with any desired length of the middle leg of the E-core (Δh_{ml}). The coil, which is lowered over the middle leg (Figure 6-2d), consists of copper wire, coated with an enamel insulation layer with a total diameter of 115µm.

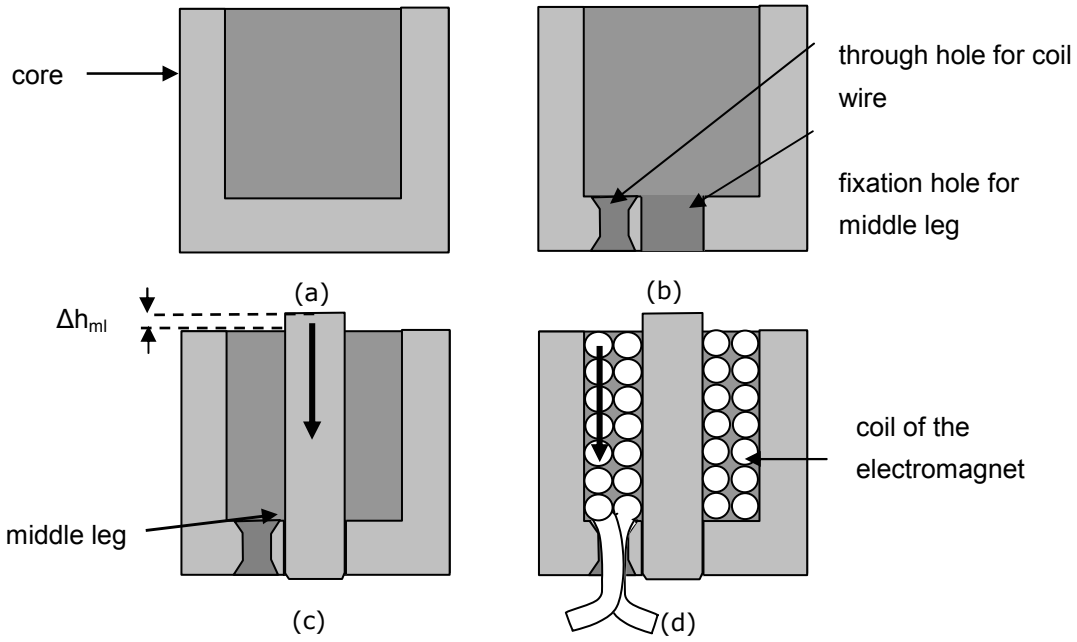

Figure 6-2: Cross-section of the different processing steps for the realization of the E-core electromagnet.

The coil is shaped around a 1mm thick axle, which is covered by a thin paper layer. The coil is wound in such a way that its height is approximately 20 turns

and its width is approximately 6 turns, resulting in a coil of 118 turns. This coil is heated up and the enamel becomes soft and sticky. After cooling down the enamel around the wire will harden again and the coil is fused to a whole. The coil can be removed from the assembly axle, because the paper layer prevents the coil form sticking to the axle. The resulting coil can easily be shifted over the inner leg of the E-core electromagnet, with the connection leads put through the hole in the case bottom. Figure 6-3 shows a picture of the realized electromagnet.

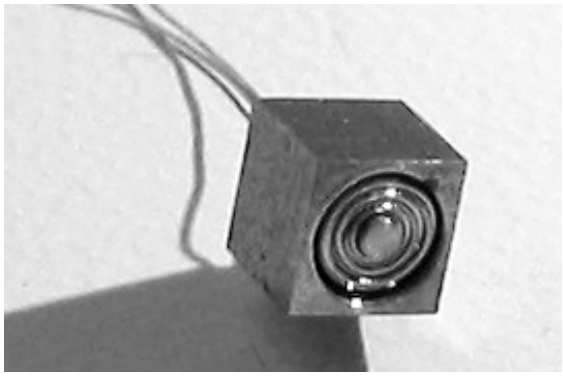

Figure 6-3: The electromagnet of the Gyracc with outer dimensions of 3×3×3 mm³

6.3 The original triaxial accelerometer

In the triaxial accelerometer design as described by Lötters [3], the sensor plates surrounding the mass (Figure 6-1) are made of silicon plates, kept in position by means of a tungsten housing. The six sensor plates are interconnected by means of flexible polyimide (PI). A cross-section of the realized construction is shown in Figure 6-4.

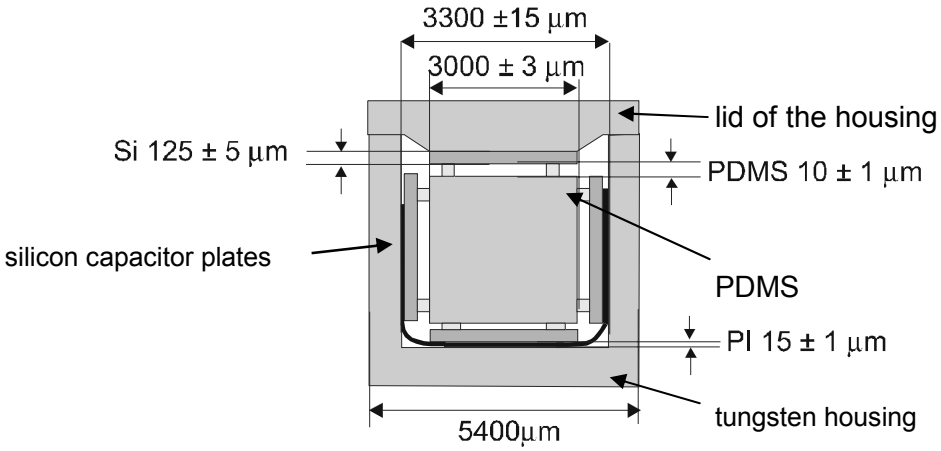

Figure 6-4: Cross-section of the original triaxial accelerometer [3]

The mass and housing were made of tungsten and were shaped by means of spark-erosion, a precision engineering technique. With this technique one is able to make small 3D-structures out of an electrically conducting material. The inner dimensions of the housing have a precision of 3300 ± 15 µm. The orthogonal

cubic tungsten mass has a precision of 3000 ± 5 µm. After spark erosion the masses were polished and could eventually reach a precision of 3000 ± 3 µm. Lötters was not able to find a company that was able to make a tungsten cubic mass with an error smaller than 3 µm. The masses as well as the tungsten housing made by spark erosion showed to be non reproducible, although they were from the same batch. The PDMS structures, the polyimide layer and the silicon sensor plates are made by means of micromachining and have a reproducible error.

6.3.1 Assembly

The mass and sensor plates are lowered in the tungsten housing and ultimately covered with a tungsten lid. With the given realistic deviations in the size of the elements (Figure 6-4) there is a reasonable chance that sensor plates are not well positioned with respect to the seismic mass. In case the inner box dimensions are too large then a sensor plate might be positioned as shown in Figure 6-5. Therefore slices of 5 µm Teflon (DuPont corp.) were put between the sensor plate and the tungsten housing to overcome this type of over-dimensioning.

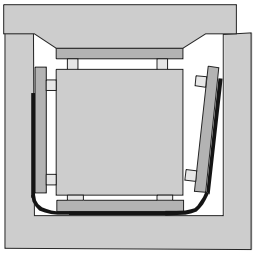

Figure 6-5: The result of an over-dimensioned sensor housing

The poor positioning of sensor plates are a source of cross-axis sensitivity and difference in sensitivity of the axes, as already observed by Lötters [4].

6.3.2 Discussion and conclusions

In the first place this original construction is unsuitable for the application of an externally positioned electromagnet, because the seismic mass is made of tungsten, which is a non-magnetic material. Even if the mass would be exchanged by a ferro-magnetic material (like iron) then this construction would still be unsuitable for an externally positioned electromagnet. This is because of the large distance between the mass and the outside of the tungsten box. Furthermore the sensor is not reproducible due to the large errors in the dimensions of the seismic mass and the housing mass with respect to the 10 µm thick PDMS springs and thus the desired distance between the mass and the capacitor sensing plates. Moreover the parasitic capacitances of the design are large because of the small distance between the backside of the sensor plate and the electrically conducting housing of the sensor. An advantage is the robust design of the box.

6.4 Sensor box with pre-defined dimensions

Although the tungsten housing does not influence the magnetic field ($\mu_r \approx 1$) the triaxial accelerometer excludes the possibility of electromagnetic actuation of the mass, because of the large distance between the mass and the outside of the sensor box. Furthermore the sensor can not be realized reproducibly, because of the non-reproducibility of the inner dimensions of the tungsten box. Therefore, a new design is proposed. Figure 6-6 shows a construction of the sensor in which no additional housing of the sensor is necessary.

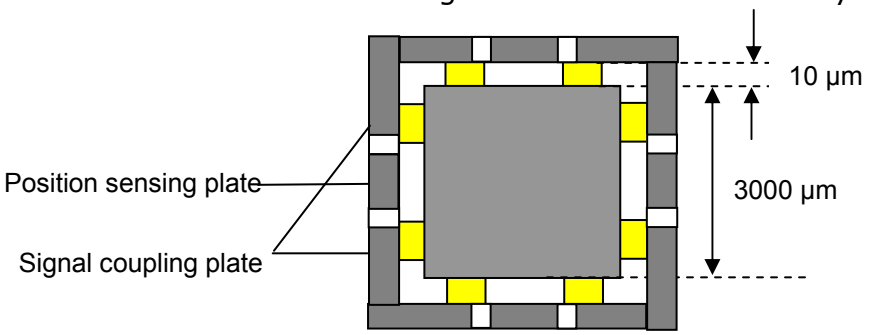

Figure 6-6: Sensor box with integrated capacitor sensor plates

All six sensor-plates are designed equally and are of well-defined dimensions achievable by micromachining. The sensor plates have crenellations, which makes it possible to shape the plates into a box structure like a 3D-puzzle [5]. A simplified representation of the shape of the box walls is shown in Figure 6-7a. These two plates can be positioned perpendicular to each other, but the degree of accuracy in positioning is poor (Figure 6-7b). However, the plates will be positioned perpendicular by adding a third plate. The three orthogonal positioned sensor plates result in a corner-piece of the box (Figure 6-7c). Combining two of these corner pieces results in an orthogonal box, which can enclose the mass.

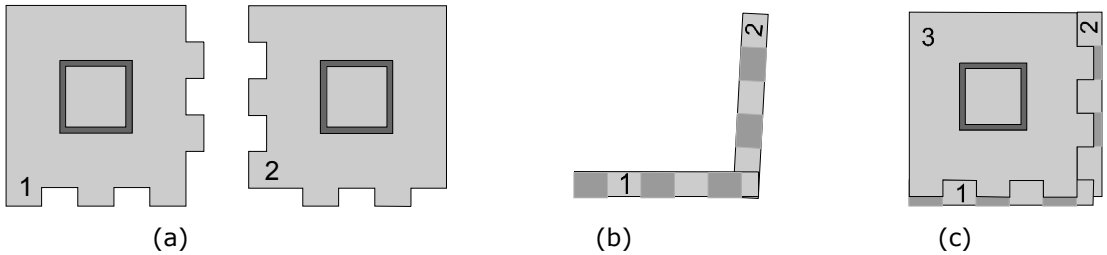

Figure 6-7: (a) two sensor plates (b) two almost orthogonal positioned sensor plates (c) three orthogonal positioned sensor plates

6.4.1 Assembly

The box walls are made of equally shaped sensor plates, which consist of a capacitor input coupling plate, a capacitor sensing plate and the PDMS springs (Figure 6-8a). Different from the original design of Lötters [3], the inner plate is now meant for sensing and the outer plate for the input signal. These outer

capacitor coupling plates are electrically connected to each other, by means of the electrically conducting silver epoxy H-20 Epotec. This electrical connection between the coupling plates reduces the coupling-signal bond wires from six to one. Assembly of half boxes with several plate thicknesses showed that the minimal thickness of the 3 mm × 3 mm plate should be 120 µm for convenient handling during assembly of the half boxes in a dedicated Pyrex assembling device (Figure 6-8b), in which the three separate plates are positioned and held by means of vacuum nozzles.

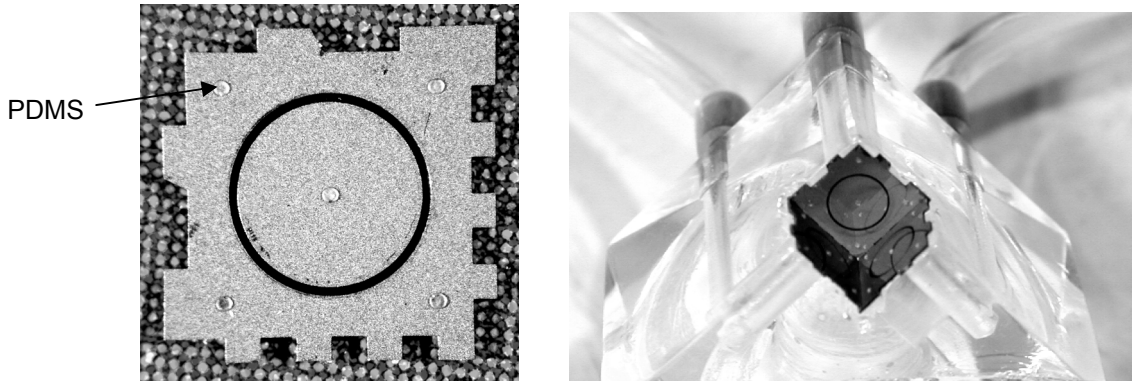

Figure 6-8: (a) One of the six equal 120 µm thick silicon box plates (b) Three orthogonal positioned sensor plates in the assembly device.

After assembling a half box, the assembly device and the half box are placed in an oven at 80^0C for 3 hours to harden the epoxy. The lower half-box is positioned in a 45^0 angle and the mass is lowered on top of the PDMS structures. Ultimately the upper half-box is lowered and glued on top of the structure (Figure 6-9a).

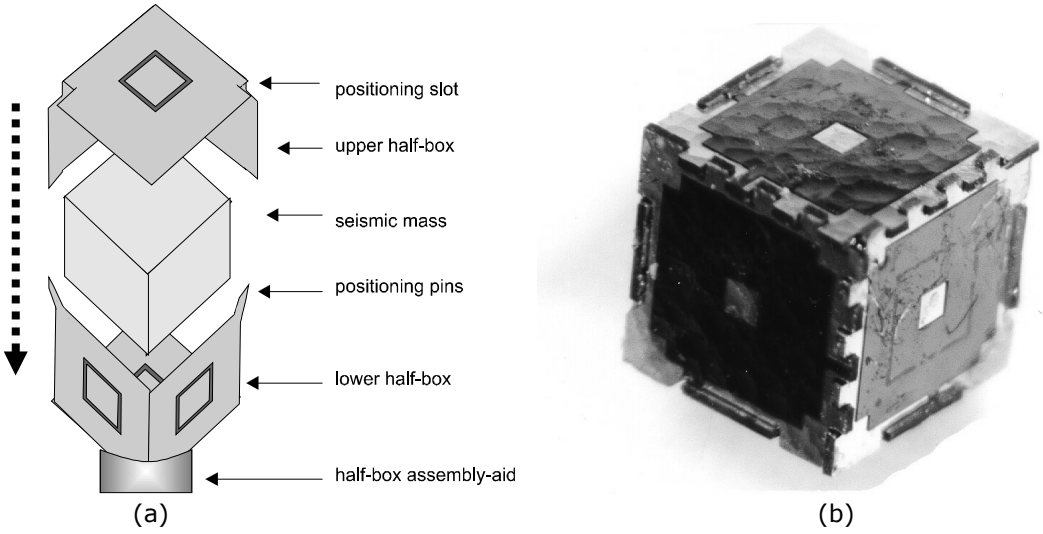

Figure 6-9: (a) Three-dimensional view of assembling the two half boxes (b) the assembled inertial sensor box.

The positioning of the two half boxes is controlled by sliding the box-halves along each others positioning pins. Figure 6-9b shows a close-up of the complete assembled silicon box with the mass inside. A fully assembled inertial sensor box, connected with gold bond wires to the top of a DIL package is shown in Figure 6-10.

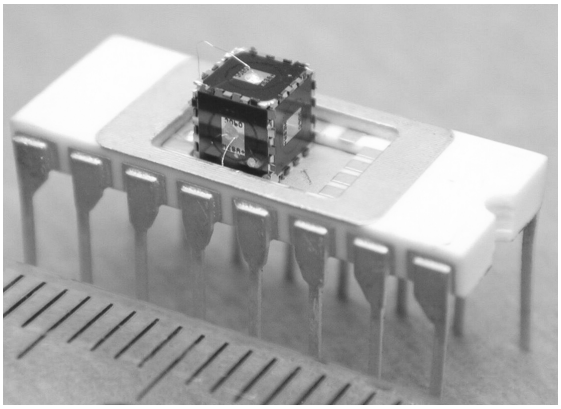

Figure 6-10: The 3D inertial sensor box with pre-defined dimensions.

Figure 6-12a shows a cross section of the inertial sensor box in combination with the electromagnet. The inertial sensor is glued on top of the DIL package by means of hot melt glue and the electromagnet is positioned by gluing a 120 µm thick silicon plate as a mechanical support between the electromagnet and the DIL package.

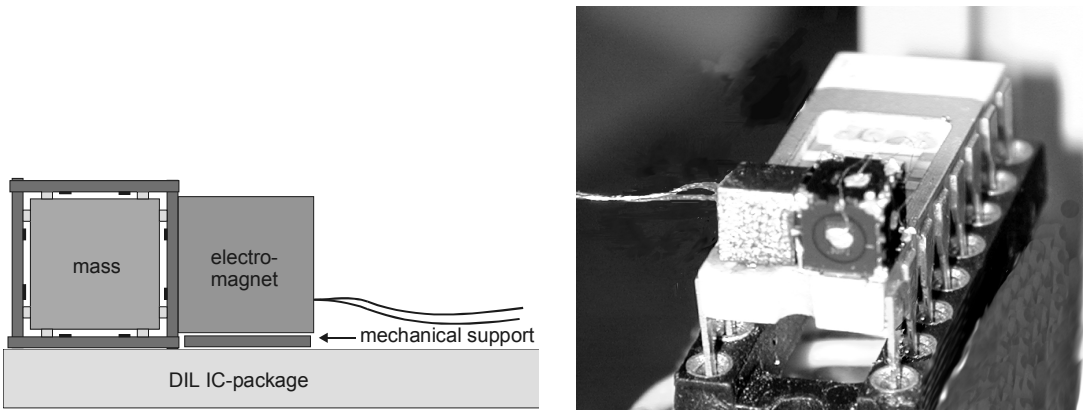

(a) (b)

Figure 6-11: (a) Cross-section and (b) picture of the inertial sensor in combination with the electromagnet.

Figure 6-11b shows the inertial sensor box in combination with the electromagnet, resulting in the Gyracc.

6.4.2 Capacitor plate distance

The mass displacement sensitivity is depending on the distance between the capacitor plates on the inner-walls of the box and the mass. This distance is equal to the height of the PDMS structures. The minimal height of the PDMS

structures is a function of the accuracy in the dimensioning of the elements. Figure 6-12 shows the PDMS height in the best-case and worst-case scenarios. In case there are no dimensional errors in the size of the elements, the height of the PDMS should be L_{perf} [m]. In case the inner dimensions of the box would be maximal and the mass smallest in size, the PDMS should have a maximum height L_{max} [m].

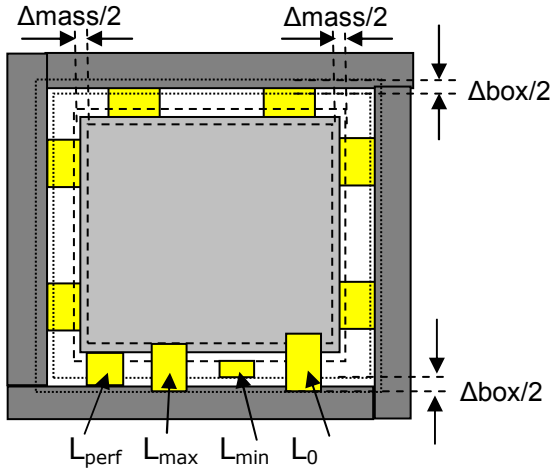

Figure 6-12: The possible heights of the PDMS structures

In case the inner dimensions of the box are minimal and the mass maximal, then the PDMS should have a minimum height L_{min} [m].

$$L_{max} = L_{perf} + \Delta_{mass}/2 + \Delta_{box}/2 \quad (6\text{-}1)$$

$$L_{min} = L_{perf} - \Delta_{mass}/2 - \Delta_{box}/2 \quad (6\text{-}2)$$

During the experience of inertial forces, the mass will compress PDMS structures at one side of the mass and decompress the springs at the opposite side of the mass. The spring constant of the springs is chosen in such a way that the maximum displacement of the mass is 10% of the height of the springs. Therefore the springs should be made 10% higher than the maximal possible distance between the inner box walls and the mass (L_0), to be certain that the springs do not lose contact with the mass during the experience of accelerations.

$$L_0 \geq L_{max} + 10\% \, L_{max} \quad (6\text{-}3)$$

Because PDMS is flexible in the 0% until 40% compression range [6], therefore the next equation should hold:

$$L_{min} \geq 0.6 \times L_0 \quad (6\text{-}4)$$

Combining equations (6-1), (6-2), (6-3) and (6-4) results in:

$$L_0 \geq 3.33 \times [\Delta_{mass} + \Delta_{box}] \quad (6\text{-}5)$$

With a maximal error in the dimension of the mass (Δ_{mass}) of 3 µm and a maximal error in the box (Δ_{box}) of 2 µm this would result in a minimum PDMS height of 17 µm.

The air gap of 17 µm will hold for a mass with a maximum error of 3 µm, but in practice it showed that the available masses have a larger dimensional error and that it was hard to keep Δ_{box} within the 2 µm range. Therefore we looked at another inertial sensor box construction that is less dependent on variation in the dimensions of the elements.

6.5 Dimension-tolerant sensor box design

The sensitivity of the capacitive detection of the movement of the mass is greatly influenced by the distance between the mass and the inner box wall. This section describes the design of an inertial sensor with a distance between the mass and the inner box walls that is independent of deviations in the size of the mass or the surrounding box.

6.5.1 Theory

In the dimension-tolerant design it is assumed that only the mass has fixed dimensions. The capacitor plates surrounding the mass (Figure 6-13a) are positioned at a certain distance from the mass wall and eventually fixed in their position by bars glued in the corners, as shown in Figure 6-13b.

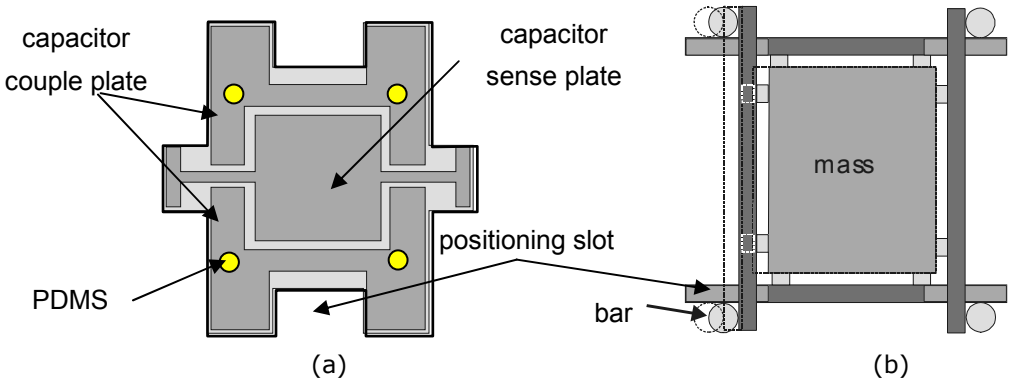

Figure 6-13: (a) Front view of capacitor plate box wall. (b) Cross-section of the dimension tolerant inertial sensor box.

Figure 6-13b shows that with the proposed structure the slot in the wall plate takes care of deviations in the size of the mass. The assembly of the six sensor plates around the seismic mass is realized manually. It is necessary to load all PDMS structures equally during assembly for a well-defined spring constant on all sides of the mass [7].

The distance between the mass and the capacitor plate can be chosen in advance by placing distance keepers next to the PDMS spring structures. Figure 6-14 shows the different phases of assembling the inertial sensor. First the box plates will be positioned around the mass (Figure 6-14a), secondly the plates will be fixed in their position by interconnecting the plates with bars (Figure 6-14b) and finally the distance keepers should be taken away or shrunk, resulting in release of the mass (Figure 6-14c). The deviation in the distance

between the sensor plate and the mass is equal to the deviation in the height of the distance keepers.

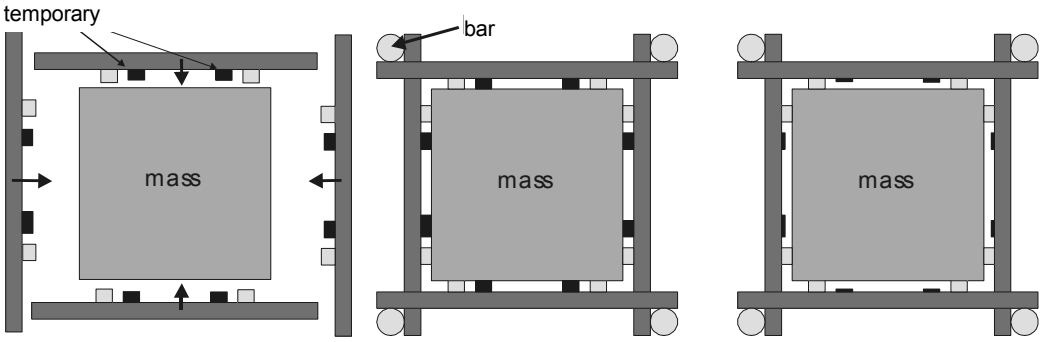

Figure 6-14: Cross-section of the inertial sensor during the different assembly phases

6.5.2 Temporary mechanical support

Some micro-mechanical devices need a temporary mechanical support during fabrication. A well-known method is the use of a sacrificial layer. Non of the known sacrificial layers can be used in the mass adapting box, because removing the sacrificial layer would result in dissolving of the PDMS structures or the aluminum of the capacitor plates. Therefore instead of a sacrificial support, polyimide (PI) probimide 7810 (Olin microelectronic materials) is applied as a temporary mechanical support layer. Not fully cured probimide is a rigid material, with the ability to shrink 40% of its original height by means of a temperature treatment (curing). The shrinking of the probimide is not fully homogeneous and the rim of the structure will shrink less than the centrally situated probimide (Figure 6-15a).

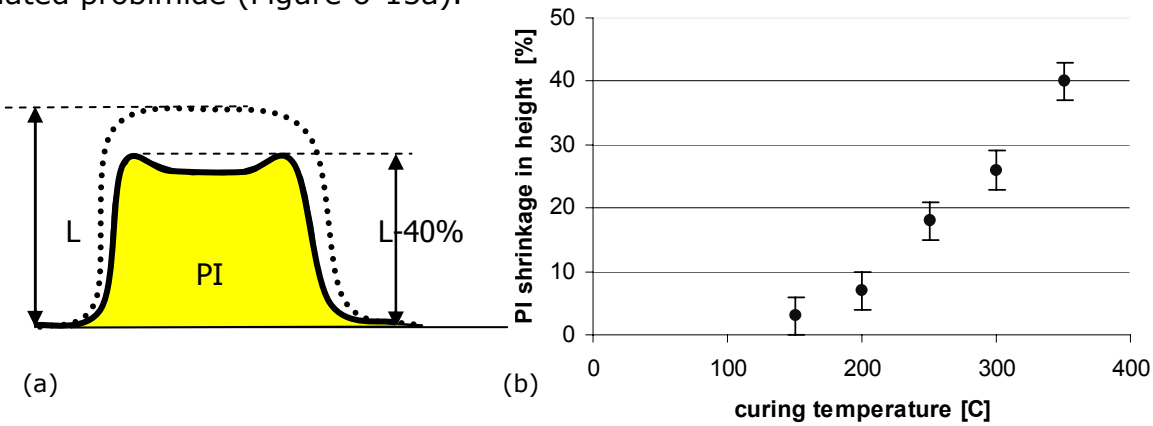

Figure 6-15: (a) Cross-section of a polyimide bump, before and after curing at 350^{0}C. (b) The measured shrinkage of the height of the polyimide (PI) as a function of the temperature.

The shrinking percentage in height of the probimide bumps as a function of one hour at different curing temperatures is shown in Figure 6-15b. Shrinkage of 40% is reached at a temperature of 350^{0}C. At temperatures above 350^{0}C the PI partly burned, which resulted in PI bumps with an undefined height. For this

reason one should stay below this temperature. For an assembled inertial sensor the PI height should at least be lowered for 10%, which is the maximum mass displacement for which the sensor output is linear. From Figure 6-15b it can be concluded that this is reached for temperatures of 225^0C and higher. A temperature of 250^0C is chosen to realize shrinkage of at least 10%. In order to use this type of temperature sensitive support, it should be investigated whether or not the PDMS spring structures can withstand the temperature treatment. Therefore, using a Dektak surface profiler, the flexible behavior of a PDMS bump is compared before and after the exposure to 250^0C. The result is shown in Figure 6-16. It can be concluded that the Young modulus of the PDMS is not affected by exposures up to at least 250 ^{0}C.

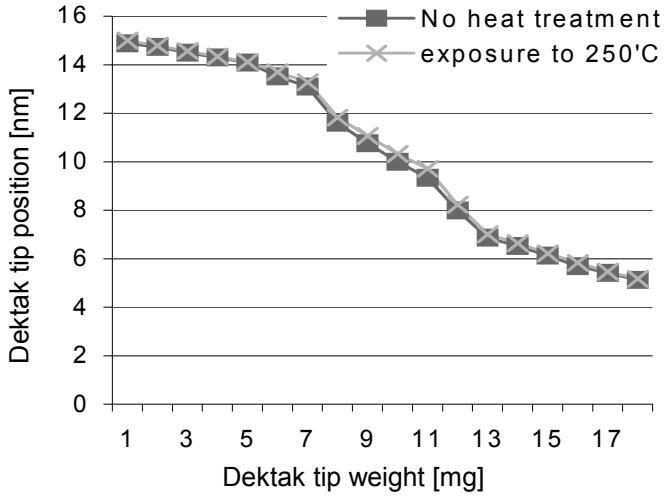

Figure 6-16: The compression of a PDMS bump before and after the exposure to 250^{o}C as a function of the Dektak tip pressure.

The ultimate procedure of applying the temporary mechanical support by probimide is shown in Figure 6-17. Two plates should enclose a mass with PDMS springs on top. During assembling the plates stop when the PI structures adjacent to the PDMS structures reach the mass (Figure 6-17b). The plates are fixed at this position and the complete structure is heated up to 250 ^{0}C. As a result the PI shrinks and the mass can move freely within the spring construction (Figure 6-17c).

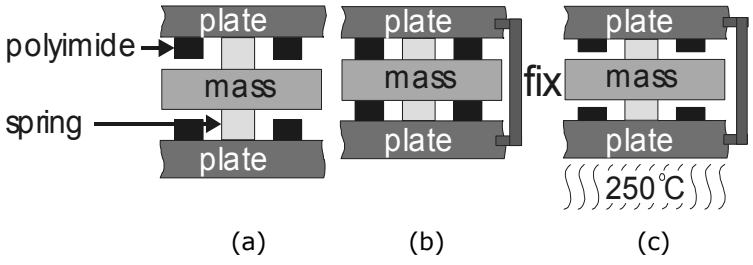

Figure 6-17: Assembly phases of a mass-spring system, with temporary PI support

6.5.3 Cleanroom processing

Besides the change in the design of the inertial sensor box, the sensor plates of the sensor box with adaptive dimensions are made of glass instead of silicon. This has been done for the following reasons:

- The capacitor couple and sense plate of the silicon sensor plates are interconnected by Polyimide, which is a material that has some flexibility. Therefore the capacitor plate in the center is not rigidly fixed.
- Less parasitic capacitance remains between the 1μm thick aluminum capacitor coupling area and the capacitor sense area on the glass plate, as compared to the 120 μm thick silicon capacitor plates. The sensitivity of the sensor will benefit from the reduction of the parasitic capacity.

The design of the glass plates of the dimension tolerant box is shown in Figure 6-18. This section describes the cleanroom-processing steps to realize the plates. The processing steps are schematically shown in Figure 6-19. A microscope covering glass of 50×45 mm^2 and a thickness of 140 μm is intensively cleaned. After cleaning an amorphous silicon layer is deposited on the glass plate as an HF etching mask. Therefore the glass plate is put in the PECVD reactor at a temperature of 200 ^{0}C, which is a relatively low temperature to prevent the glass from large mechanical stress. The amorphous silicon grows in 80 minutes on top of the glass-plate under the condition that the plasma is a 50W HF field containing 1500 sccm 2% SiH_4 in N_2 at a pressure of 500 mT. The etching pattern in the amorphous silicon is realized by spinning Olin 90/17 photoresist, at a speed of 4000 rpm for 20 seconds, on top of the amorphous silicon. After baking the photo resist for 2 minutes at 95 ^{0}C, the glass etch pattern is copied into the Olin photo-resist layer using an exposure time of 6 seconds (Figure 6-19a). The photo-resist is developed and the non-exposed photo-resist is flushed away. The remaining photo-resist is hardened by 10 minutes post baking at a temperature of 120 ^{0}C. The uncovered amorphous silicon is removed by means of reactive ion etching with the following processing parameters: 20/5/5 sccm $SF_6/CHF_3/O_2$ at a pressure of 20 mT at 60W for 2 minutes (Figure 6-19b). The remaining photoresist is removed by means of exposing the plate to a 2 mbar oxygen plasma at 150 ^{0}C for 10 minutes (Figure 6-19c). Next the aluminum layer for the capacitor plates is deposited as well as the PI layer and selectively illuminated by the HF etching mask. First one side of the plate is covered by a 1μm aluminum layer in the sputter bell, after this the unnecessary parts are etched away in order to realize the aluminum capacitor plates. Removing the unnecessary parts is realized by covering the aluminum layer with photoresist Olin/90/17 applied by spinning at 4000 rpm for 20 seconds and pre-baking for 2 minutes at 95 ^{0}C. The photoresist is exposed for 6 seconds through the capacitor plate mask (Figure 6-19d). The photoresist is developed for 50 seconds and pre baked for 2 minutes at a temperature of 120 ^{0}C. The uncovered aluminum is etched away in two minutes by Al-etch at a

temperature of 40 ^{0}C (Figure 6-19e). The remaining photoresist is removed with acetone. The surface of the glass plate with aluminum capacitor plates is cleaned in a 120 W oxygen plasma at a pressure of 2 mbar for 1 minute (Figure 6-19f).

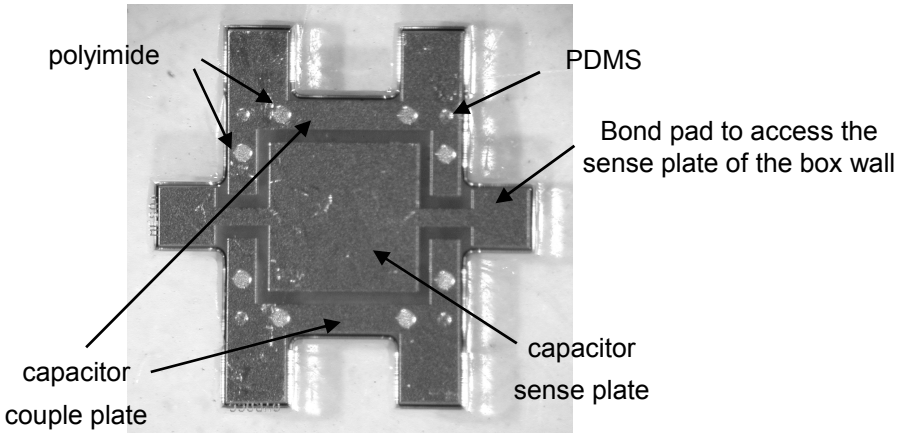

Figure 6-18: Picture of the glass sensor box wall, with PDMS and PI bumps on top

A 9.2 µm thick Olin/probimide 7510 layer is put on top of the aluminum structures for the temporary assembly support bumps by spinning for 32 seconds at a speed of 2500 rpm. The probimide is dried by pre-baking the glass-plate on top of a 95 ^{0}C plate for 5 minutes and further hardened at a temperature of 112 ^{0}C for 12 minutes. The probimide is exposed for 5 seconds to realize the assembly support bumps (Figure 6-19g). The probimide is developed by dipping the plate for 3 minutes in HTR-D2 nr.1 and successively 30 seconds in developer nr. 2. The residual probimide is removed ultrasonically with IsoPropyl Alcohol (IPA). The wafer is dried and the probimide is hard paked for 10 minutes on a 120^{0}C plate. Measurements with a Dektak showed that the probimide bumps had a height of 9,2 µm +/- 0,5 µm. The next step is applying PDMS structures on the glass plate. Placing the glass plate in 120 W oxygen-plasma, at a temperature of 120 ^{0}C for 20 seconds cleans the plate. Before bringing on the PDMS, a primer layer (TMSPM) is applied at a temperature of 60 ^{0}C. The PDMS (RMS-033) is applied by spinning for 2 minutes and 15 seconds at a speed of 3200 rpm for a 10 µm high layer (Figure 6-19h). This 10 µm thick layer cannot be put in the mask aligner because it is sticky and might stick to the exposure mask, thus damaging the fragile PDMS layer. Therefore the PDMS layer is covered with a 23 µm thick Mylar foil. Then the PDMS layer is exposed for 1000 seconds (9mW/cm^2). After another 20 minutes the Mylar foil is removed and the PDMS is developed in xylane for 30 seconds. The whole plate is flushed with IPA and dried. Measurements with the Dektak showed that the height of the PDMS structures was 10 +/- 0,5 µm.

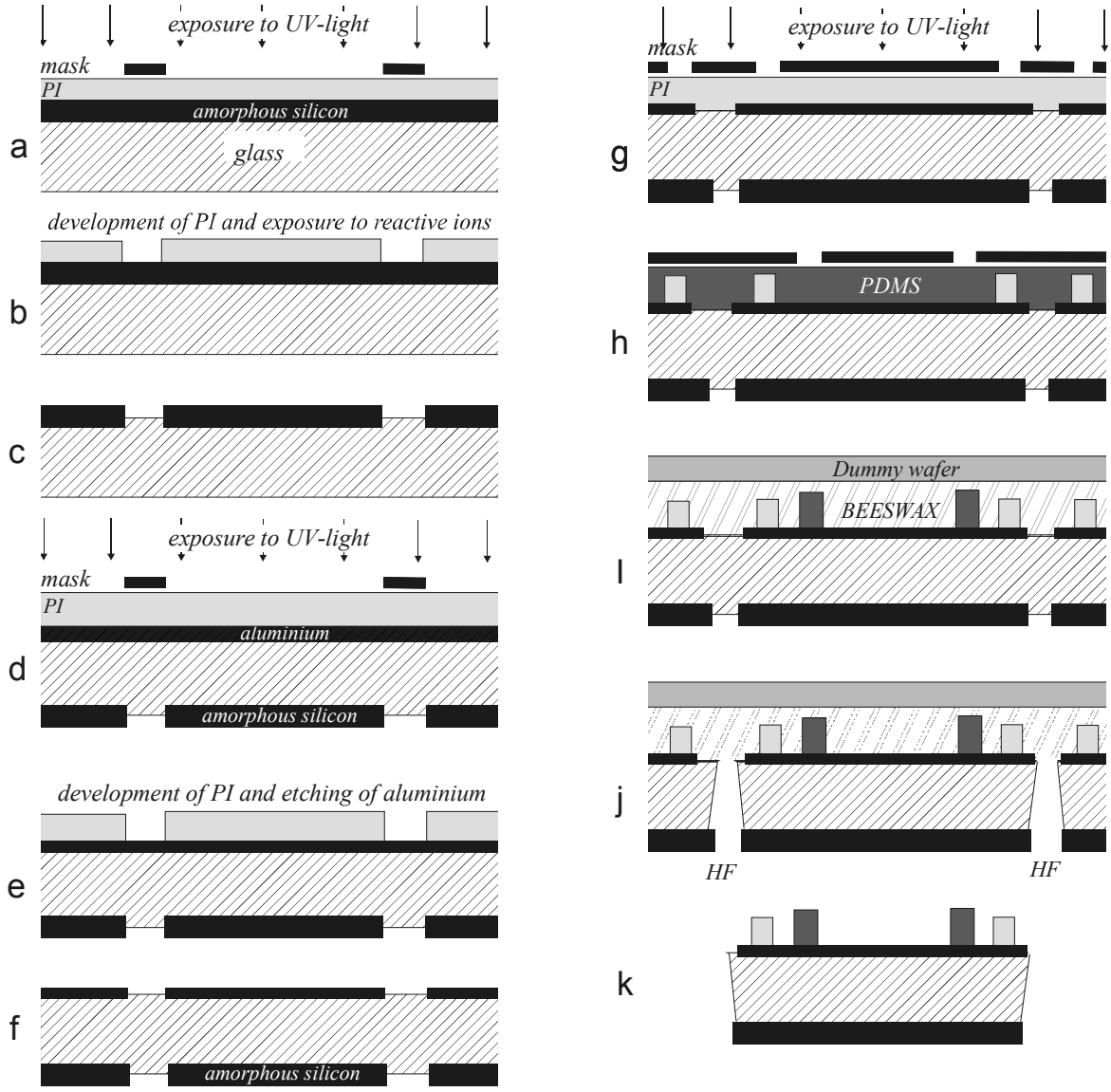

Figure 6-19: Processing steps of glass sensor box plates

The next step in the processing is separating the box plates from the glass plate. The probimide and PDMS structures are protected from the HF by a protective layer of beeswax and a dummy wafer (Figure 6-19i). This sandwich of the glass plate and dummy wafer, with the beeswax in between is dipped in 25% HF solution. After 25 minutes the HF is etched through the 140 µm thick glass plate and the sensor box plates are separated, but still stick in the beeswax on top of the dummy wafer (Figure 6-19j). The wafer with the separated chips is dipped in a benzene solution at 40 ^{0}C and agitated with ultrasonic sound to release the chips. As a last processing step the chips are flushed with IPA and dried on top of a tissue (Figure 6-19k).

6.5.4 Assembly

The inertial sensor is assembled in the dedicated assembly device shown in Figure 6-20a. First one of the sensor box plates is put on the bottom of the

assembly device, with the PDMS and PI bumps on the topside. The cubic iron mass is cleaned with ethanol and positioned on top of the PDMS and PI structures. Next, four plates are positioned around the mass. Screws on the assembly device displace the sensor plates in the direction of the mass until the PI bumps reach the mass. These four plates are mechanically interconnected with small glass bars, glued in the corners of the glass plates with Hysol. As a follow up the top plate is positioned and glued to the four vertically positioned plates with glass bars. Now the assembly device, with the mass and plates is put in an oven at 80 ^{0}C for 30 minutes to dry. After removing the device from the oven the screws release the inertial sensor and the sensor is turned upside-down to glue the lower plate of the sensor. After positioning of the last four glass bars, the sensor is positioned in the oven again to dry the glue. After this the construction is put for one hour in an oven with a temperature of 250^{0}C to shrink the temporary mechanical PI support.

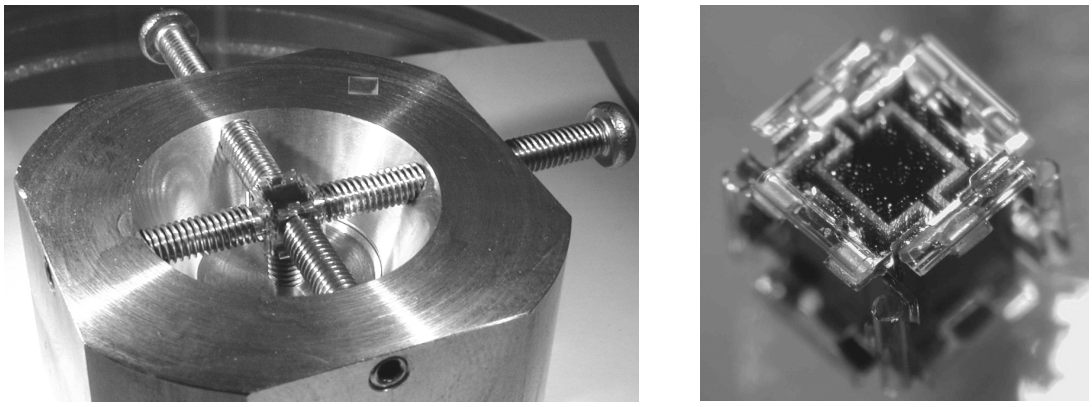

(a) (b)

Figure 6-20: (a) The inertial sensor in its dedicated assembling aid. (b) A close-up of the inertial sensor box.

After the mechanical construction of the sensor is ready (Figure 6-20b), the sensor box is glued on top of a DIL IC package. In total seven wires have to be connected from the sensor to the bond pads on the DIL IC package. The six sense plates are connected to the DIL package by means of gold bond wires. The coupling areas on the sensor plates are interconnected by means of gold bond wires thus only one bond wire has to be connected to the DIL package.
The fully assembled 3D inertial sensor with an adaptive box design is shown in Figure 6-21. Now the sensor can be used as a triaxial accelerometer. This specific inertial sensor has a hole in one of its walls to make it able to connect an electromagnet with an extended middle leg to this inertial sensor (see Figure 6-22).

The electromagnet is glued on one side of the sensor box to extend the sensing capabilities with rate of turn measurement.

To realize a solid mechanical construction, the electromagnet is not solely glued to the sensor box, but is also mechanically fixed on top of a support platform (Figure 6-23a).

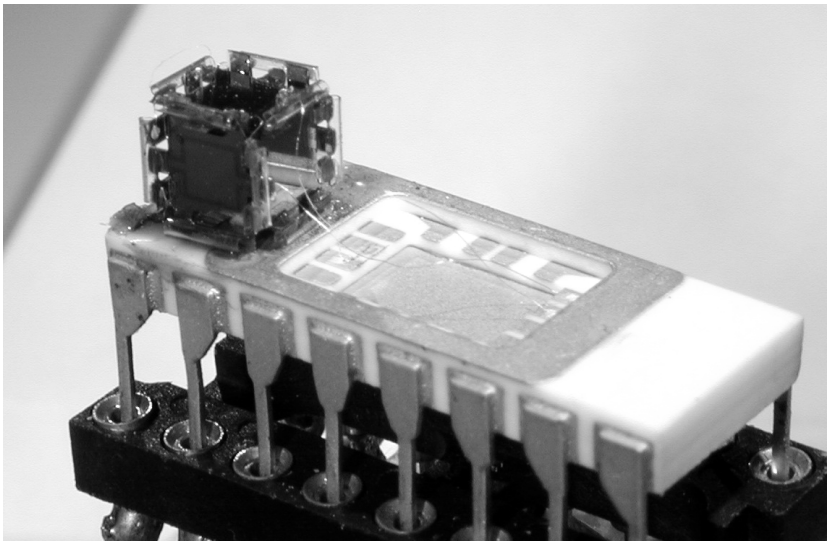

Figure 6-21: The fully assembled inertial sensor

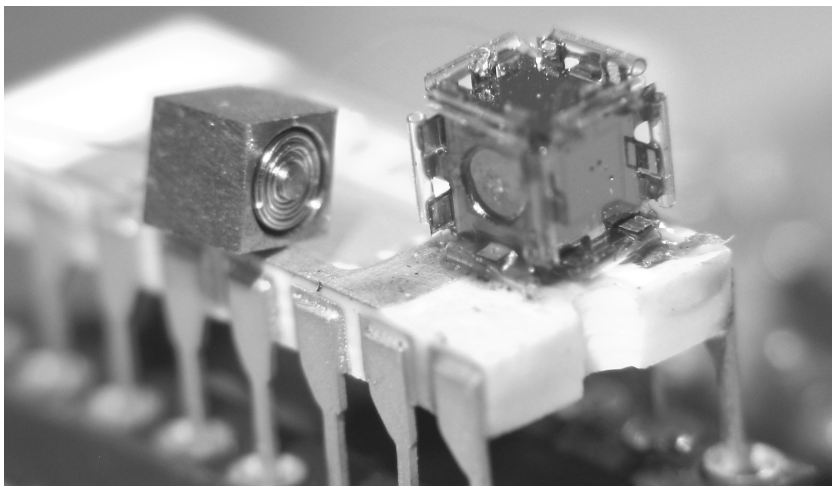

Figure 6-22: An inertial sensor with a spare area (right) for the E-core electromagnet with an extended middle leg (left).

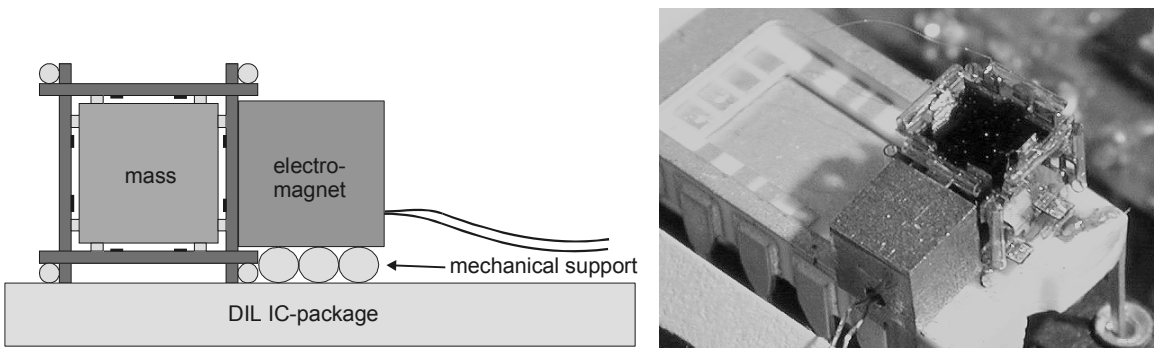

(a) (b)

Figure 6-23: (a) The electromagnet fixed to the inertial sensor. (b) The fully assembled Gyracc.

The Gyracc with its DIL-IC packaging (Figure 6-23b) can finally be connected to the electronics.

6.5.5 Discussion

The yield of 3×3×3 mm^3 tungsten masses with an absolute error less than 3 micrometer was 10% on a batch of 20. The minimum error in iron masses with a dimension of 3×3×3 mm^3 was 6 micrometer. Note that iron masses are less reproducible than tungsten masses, because iron is a softer material than tungsten. The harder the electrically conducting material the more precise the material can be shaped by spark erosion. With the help of equation (6-5) it can be concluded that the distance between the sensor plates and the mass should be at least 20 micrometers for an iron mass inside a box with exact inner dimensions.

The adaptive sensor box could be made from silicon as well as glass. Glass plates etched by means of HF etching are less reproducible than the reactive ion etching (RIE) etched silicon sensor plates. However the shape of the sensor plates is not a critical step in the design of the adaptive box design. Furthermore the electrical insulation of the glass results in less parasitic capacitance in the sensor. Sensors with different height of the air gap, between the mass and the box plates, can be made with the same cleanroom processes and etching masks.

6.6 Conclusions

An electromagnet and two construction designs of the inertial sensor have been realized. The first realized inertial sensor consists of an iron mass enclosed in an orthogonal silicon box with exact inner dimensions. The advantage of this design is that the electrical interconnection of the capacitor coupling plates of the six silicon walls drastically reduced the wiring from the sensor box to the DIL package as compared to the original triaxial accelerometer, which consisted of a tungsten housing.

The design of the orthogonal silicon box with exact inner dimensions is such that the thickness of the silicon plates is of no influence on the inner dimensions of the box. The minimum distance between the mass and the inner walls of the capacitor sensing box is a function of the variation in the size of the mass and sensor plates. A disadvantage is that the sensor is less robust than the design of the original triaxial accelerometer. Although the seismic mass is made by spark erosion it was shown that the produced masses had a dimensional error of several micrometers.

A dimension tolerant design is introduced that by-passed this problem. With this design it is possible to make a well-defined gap between the mass and the inner walls of the sensor box, independent of the dimensional error of the mass. In this design the plates are positioned around the mass, with a required distance between the mass and the inner walls of the sensor plates by means of a pillar

of polyimide (probimide 7810) as a temporary spacer. After total assembly of the inertial sensor box the polyimide releases the mass by means of shrinking by high temperature exposure. After the release of the mass the polyimide bumps remain next to the PDMS pillars and protect the springs from crushing during the experience of excessive accelerations (mechanical overload protection).
After full assembly, the sensor box is mounted on top of the DIL package and interconnected by means of gold wiring. In this state a triaxial accelerometer is constructed. After mounting the electromagnet besides the inertial sensor it may function as a rate of turn sensor as well. The distance between the electromagnet and the seismic mass is equal to the thickness of the sensor plate plus the height of the PDMS springs.

6.7 References

[1] Lötters, J.C., Olthuis, W. and Bergveld, P., A sensitive differential capacitance to voltage converter, Instrumentation and Measurement (1999), pp. 89-96

[2] Ansel, Y., Lerch, Ph., Renauld, Ph., Mode coupling aspects in a vibrating gyroscope, S&A A 62 (1997), pp. 576-581

[3] Lötters, J. C. et al., Design, fabrication and characterization of a highly symmetrical capacitive triaxial accelerometer, S&A A 66, Issues 1-3, 1 April 1998, Pages 205-212

[4] Lötters, J. C., Thesis: "A Highly Symmetrical Capacitive Triaxial Accelerometer", ISBN: 90-365-0982-3, 1997

[5] Kooi, B.J., Bomer, J., Olthuis, W. and Bergveld, P., Realization of an orthogonal cubic silicon box for a triaxial accelerometer, International Workshop on Micro Fabrication IWMF (2000), pp. 175-178

[6] Lötters, J.C., Olthuis, W. and Bergveld, P., The mechanical properties of the rubber elastic polymer polydimethyl-siloxane for sensor applications. Micromechanics and Microengineering (1997), pp. 145-147

[7] Olthuis, W., Kooi, B.J., Bomer, J.G. and Bergveld, P., Load to capacitance transfer using different spring elements in capacitive transducers, S&A A 85 (2000) 256-261

Chapter 7

7 MEASUREMENTS ON THE GYRACC

This chapter describes the measurements and their results that are performed on the inertial sensor box, the electromagnet and the capacitance to voltage converter (CVC), separately and combined.

7.1 Characterization of the electronic measurement system

7.1.1 The transfer function of the CVC

The position of the mass inside the sensing box is determined by means of the differential Capacitance to Voltage Converter (CVC) as designed by J.C. Lötters [1]. The basic circuit of the CVC is shown in Figure 7-1. The CVC is completely symmetrical and consists of two frequency-independent half AC-bridges, which act as AM modulators, two AM demodulators and an instrumentation amplifier, which rejects common mode signals.

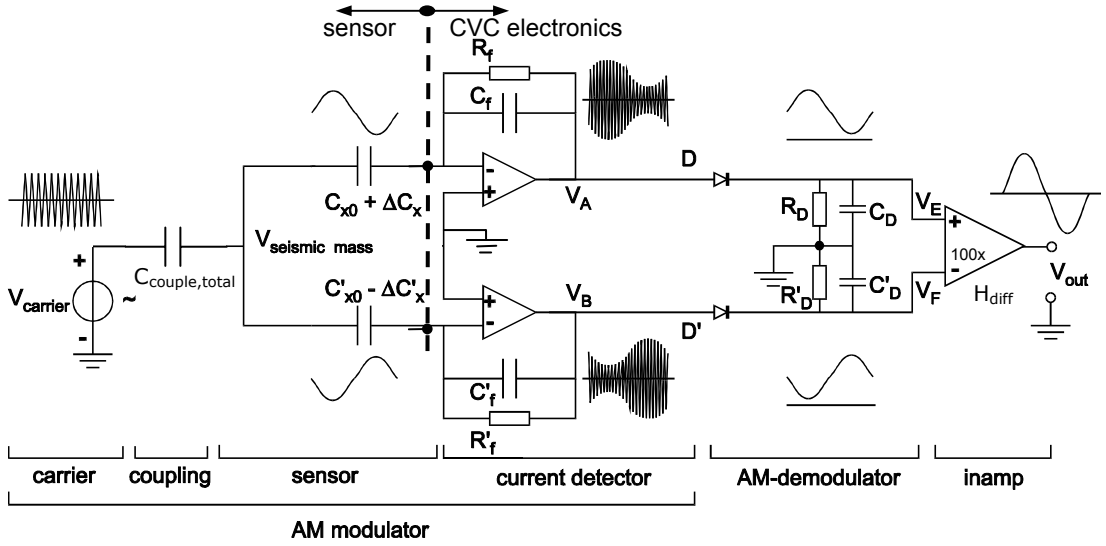

Figure 7-1: Basic circuit of the differential capacitance to voltage converter, including typical signal waveforms (see J.C. Lötters [1]).

The differential capacitance to voltage converter is driven by a voltage source with a 100 kHz carrier frequency ($f_{carrier}$) and 3.5 V_{tt} amplitude ($V_{carrier}$), which is capacitively supplied to the seismic mass of the inertial sensor. The CVC is originally designed to measure accelerations of the mass in the range from zero to 50 Hz.

It would be useful if the CVC electronics could also measure vibrations of the seismic mass in the kHz range, which is the range where the resonance frequency of the seismic mass is to be expected. Therefore a frequency sweep until 3kHz with amplitude of 50 mV_{tt} is super-positioned on top of the $3.5V_{tt}$ carrier wave, and applied to one of the ports of the differential CVC via a 1.5 pF capacitor. The amplitude and phase transfer of the three CVC's representing the x, y and z-axis, are shown in Figure 7-2.
The amplitudes of the three different axes differ due to differences in adjustment of the adjustable capacitors C_f of the corresponding CVC's.

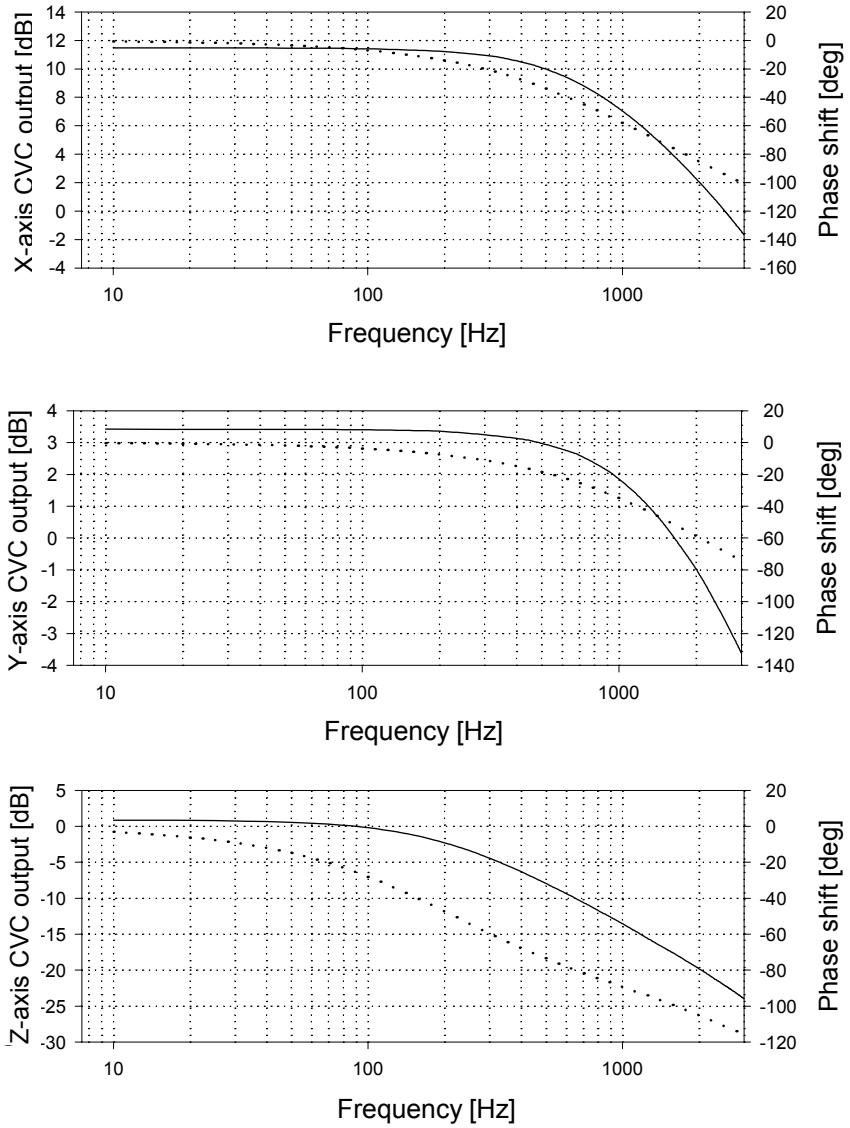

Figure 7-2: The transfer of a 50 mV_{tt} modulated signal on top of a 100kHz, $3.5V_{tt}$ carrier wave, coupled into the CVC via a 1.5 pF capacitor. Solid line: RMS amplitude, dotted line: phase.

From the results shown in Figure 7-2 it may be concluded that the CVC works well in all three axis in the zero until 50 Hz range. The attenuation in the three

axes is less than 20dB for frequencies up to 2kHz. For frequencies above 50 Hz there is clearly a phase shift between the input signal and the measured output signal. Concluded may be that the output of the CVC will represent vibration of the mass with some attenuation, but the phase of the output signal is not the actual phase of the vibration to be measured.

7.1.2 Noise level during measurements

The inertial sensor box with fixed dimensions in combination with its electronics and electromagnet is positioned on top of the rotating platform (see paragraph 7.4.1). The influence of Brownian noise and other interfering signals radiating into the y-axis signal of the sensor system, being the axis in which the Coriolis displacement is expected to be, as a function of the frequency is shown in Figure 7-3. Noise measurements are performed during no rate of turn (fat line), -6.3 rad/s and +6.3 rad/s (thin lines). During these measurements the electromagnet is not actuated.

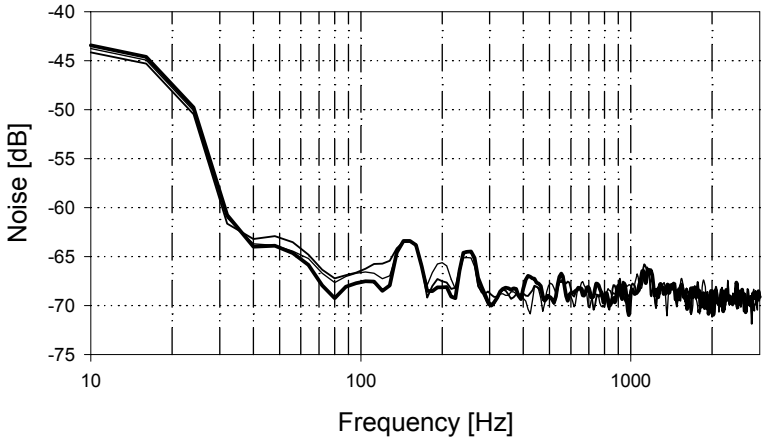

Figure 7-3: The noise in the y-axis of the silicon sensor with 30 µm PDMS springs as a function of the frequency.

The FFT spectrum of three different experienced rates of turn of the rotation platform for a frequency range from 10 until 3000 Hz is considered to be equal. Therefore, it can be concluded that the noise caused by the rotary contacts of the rotating platform (see 7.4.1) is independent of the rate of turn. The noise level for frequencies above 100 Hz is about –65 dB, which is equal to 0,5 mV_{RMS}. As a consequence only signal amplitudes higher than 0,5 mV_{RMS} can directly be measured and periodic signals with amplitudes below 0,5 mV can only be detected by means of filtering. Note that filtering will reduce the bandwidth of the sensor.

7.2 Acceleration measurements

Two types of inertial sensors are used for the Gyracc. First the silicon box inertial sensor with 30 µm high PDMS springs (further referred to as sensor Type 1) and secondly the glass sensor box with 10 µm high PDMS springs

(further referred to as sensor Type 2). A more detailed specification of the Gyracc is described in Table 7-1.

Table 7-1: Construction parameters of sensor Type 1 and 2.

Type 1 *(Silicon box Gyracc)*	**Type 2** *(Glass box Gyracc)*
Silicon box Gyracc with 120µm Silicon plates	Glass box Gyracc with 140µm glass plates
PDMS springs: 4 disk shaped dots with a radius of 50µm and a height of 30 µm on each side of the mass.	PDMS springs: 4 disk shaped dots with a radius of 50µm and a height of 10 µm on each side of the mass.
Sense plates connected to the CVC X-axis: only on the side opposite of the electromagnet. Y-axis: both sides of the box Z-axis: both sides of the box	*Sense plates connected to the CVC* X-axis: only on the side opposite of the electromagnet. Y-axis: both sides of the box Z-axis: both sides of the box
Construction details: The silicon box fully encloses the mass	Construction details: The glass box encloses the mass, but has slits of approximately 100 µm between the glass plates surrounding the mass. Furthermore there is a 1.5 mm diameter hole in the center of the glass plate for the extended middle leg of the electromagnet. The middle leg of this specific electromagnet exceeds the outer leg with 75 µm.

7.2.1 Acceleration measurement results

The Gyracc should measure accelerations as well as rotations. The acceleration frequency response of the sensors is measured by positioning them on top of a shaker unit, as described in [2]. The shaker unit vibrates with a frequency sweep from 10 Hz up to 3 kHz with an acceleration amplitude of 5 m/s^2. Before applying accelerations to the Gyracc the output of the electronics is adjusted to zero volt by adjusting the capacitors C_f of the CVC's. Figure 7-4 shows the acceleration response of sensor Type 1. The carrier signal is a 100 kHz AC sine wave with 3.5 V_{tt} amplitude.

As can be observed in Figure 7-4, the amplitude of the transfer function for accelerations until a frequency of 100 Hz is almost constant for all three orthogonal axes. In the higher frequency range one or more peaks are observed, which represent a higher sensitivity to accelerations at these specific frequencies. This frequency dependence is different for all three axes.

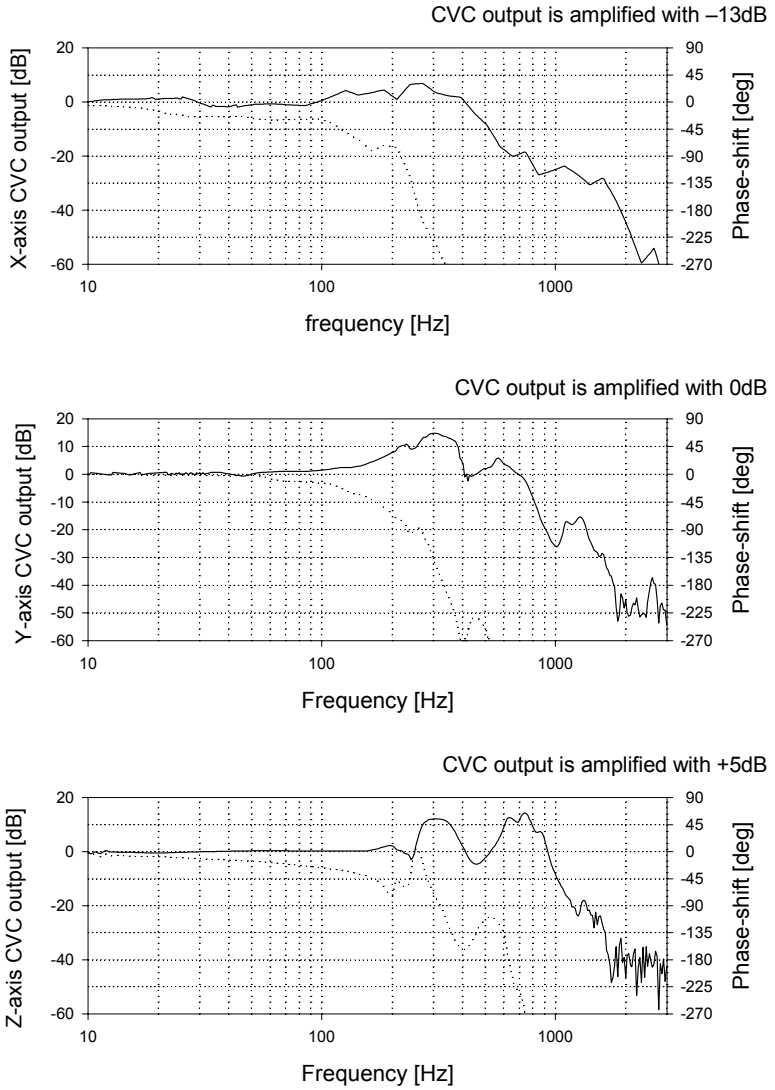

Figure 7-4: The output per axis of the sensor Type 1 as a function of the frequency for a 5 m/s^2 acceleration applied in its three axes. Solid line: amplitude, dotted line: phase.

Under the assumption that this constant response is valid for accelerations in the range from –50 m/s^2 up to +50 m/s^2 it can be concluded that Gyracc sensor Type 1 can perform well as an accelerometer in the frequency range until 100 Hz for the three orthogonal axes.

Figure 7-5 shows the acceleration measurement results of sensor Type 2. The carrier signal is a 100 kHz sine wave with 2V$_{tt}$ amplitude.

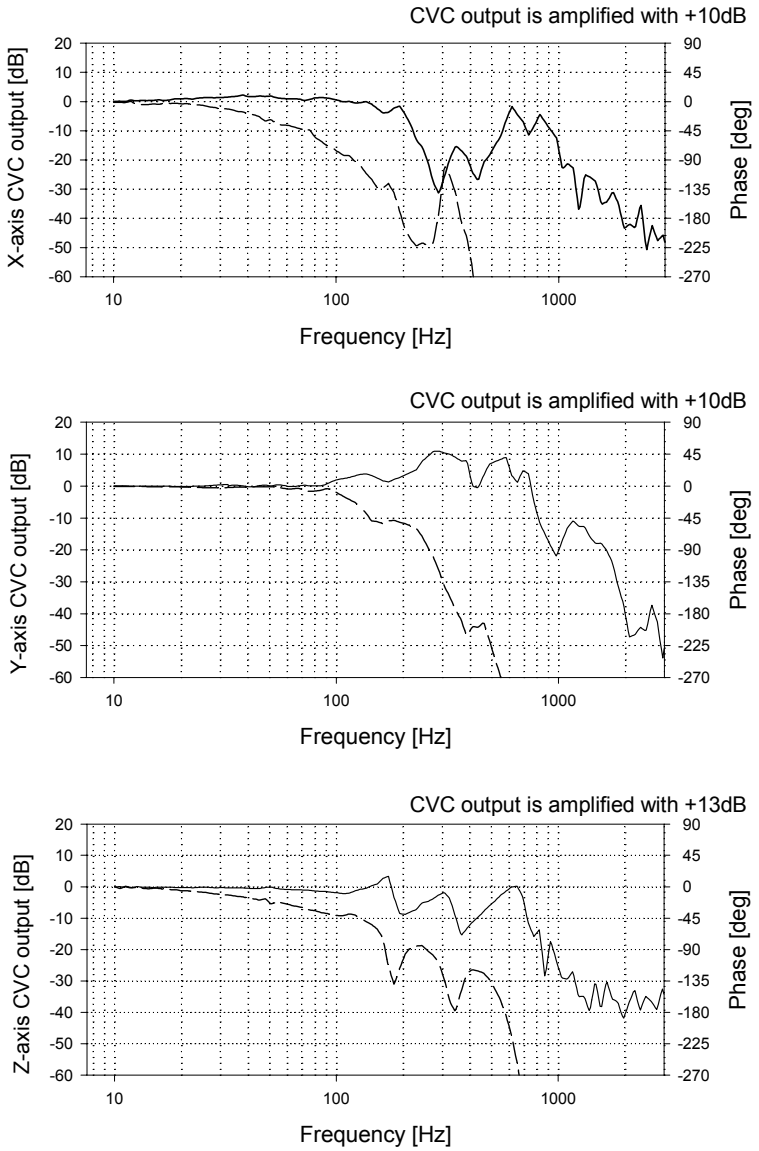

Figure 7-5: The output per axis of sensor Type 2 as function of the frequency due to a 5 m/s^2 acceleration applied in its three axes. Full line: amplitude, dotted line: phase.

As with sensor Type 1, sensor Type 2 has a constant sensitivity for frequencies up to 100 Hz for all axes and can therefore also perform as a triaxial accelerometer. Furthermore it can be noticed that the sensitivity in the three axes (as shown by the amplification factor) is more equal as compared to sensor Type 1. Most probably this is due to the fact that the construction procedure delivers more accuracy in dimensions.

7.3 Actuation of the mass

The seismic mass inside the Gyracc is to be brought into vibration by means of the electromagnet as explained in chapter 4. In this paragraph the vibration of the mass is measured as a result of the electromagnetic actuation.

Therefore the force acting on the seismic mass should be measured. This measurement is realized by fixing the electromagnet in a holder at a certain distance (d) from the 220 mg iron mass that is positioned on top of an electronic weight balance (OHaus corp. Type: Adventurer) (Figure 7-6).

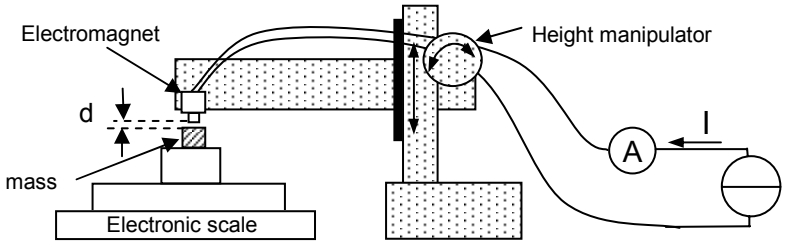

Figure 7-6: The measurement setup for the electromagnetic force measurement.

The electromagnet is actuated with a DC-current so that the mass experiences a pulling force. The pulling force of the electromagnet acting on the seismic mass is calculated by means of:

$$F_{EM,I} = g \cdot [m_0 - m_I] \qquad (7\text{-}1)$$

$F_{EM,I}$	*= force produced by the electromagnet, actuated by a current of I A.*	*[N]*
g	*= earth's gravitational force: 9.8*	*[N/kg]*
m_0	*= mass measured during no-actuation of electromagnet*	*[kg]*
m_I	*= mass measured during an actuation current of I Amp.*	*[kg]*

The current-distance-force relation between the electromagnet and the seismic mass is shown in Figure 7-7. Further the electromagnetic force is calculated with equation 4-25.

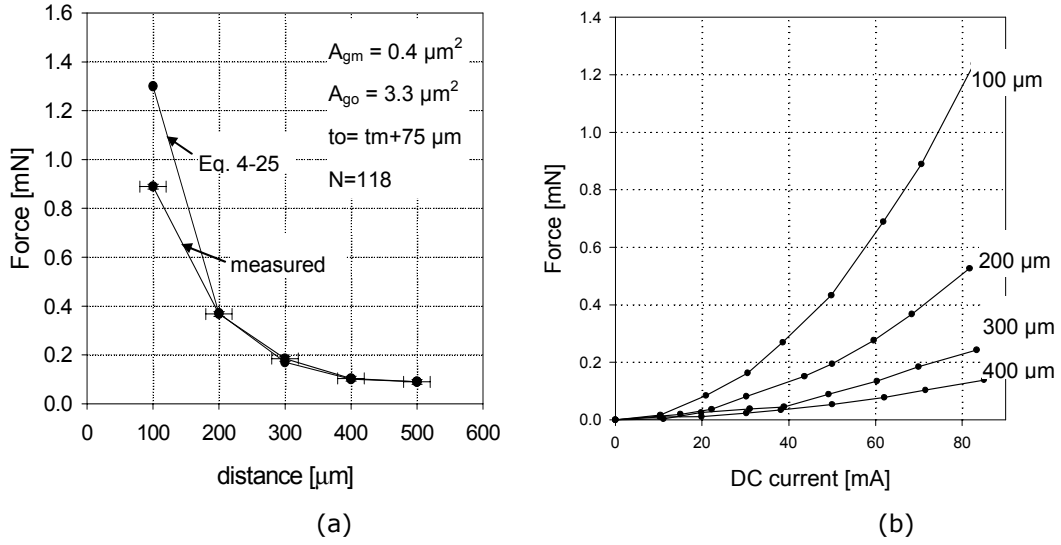

Figure 7-7: The actuation force of the electromagnet as function of (a) the distance, with actuation current of 70 mA (b) the current at different distances.

Figure 7-7a shows that the actuation force quadratically decreases with the distance and Figure 7-7b shows that the actuation force of the electromagnet quadratically increases with the actuation current both as expected from Equation 4-25.

7.3.1 Mass displacement by electromagnetic actuation

The seismic mass inside the inertial sensor box is displaced by means of the electromagnet that is positioned next to the inertial sensor box (Figure 6-11). Figure 7-8 shows the CVC output voltage due to the vibrating mass inside the silicon sensor box, which is electro magnetically actuated with a 100 Hz current with a amplitude of 25 mA_{RMS} and 50 mA_{RMS}.

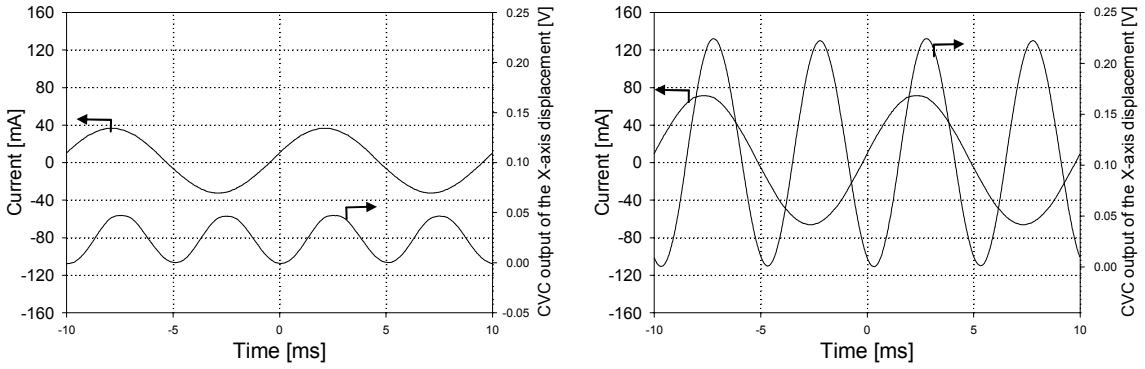

Figure 7-8: The measured CVC output due to mass vibration as a function of time (a) at 25 mA_{RMS} and (b) at 50 mA_{RMS} actuation current.

The measured vibration frequency of the mass is twice the frequency of the actuation current. Furthermore, it can be noticed that the amplitude of the vibration due to the 50 mA current is four times larger than the amplitude of the vibration with the 25 mA actuation current, as expected.

In the following graphs the amplitude and phase dependence of the vibrating mass as a function of the actuation frequency of the electromagnet in the x-axis direction is measured by means of a spectrum analyzer. For the phase measurement it is required that the actuation as well as the resulting vibration frequency have the same frequency. To realize this, the AC actuation current is super-positioned on top of a DC current; see also section 4.3.2 for a comparable solution.

To investigate the vibration behavior of the Type 1 sensor an offset current of 35 mA DC and a 25 mA_{RMS} AC current are super-positioned and the resulting response is shown in Figure 7-9.

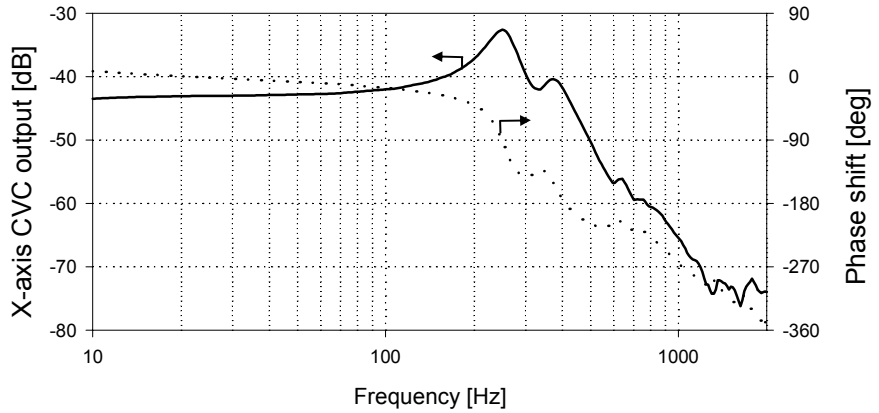

Figure 7-9: The amplitude and phase shift of the vibrating mass as a function of the actuation frequency for sensor Type 1.

For the frequency response of the Type 2 sensor an offset current of 20 mA DC and a 15 mA_{RMS} AC current are super-positioned and the result is shown in Figure 7-10.

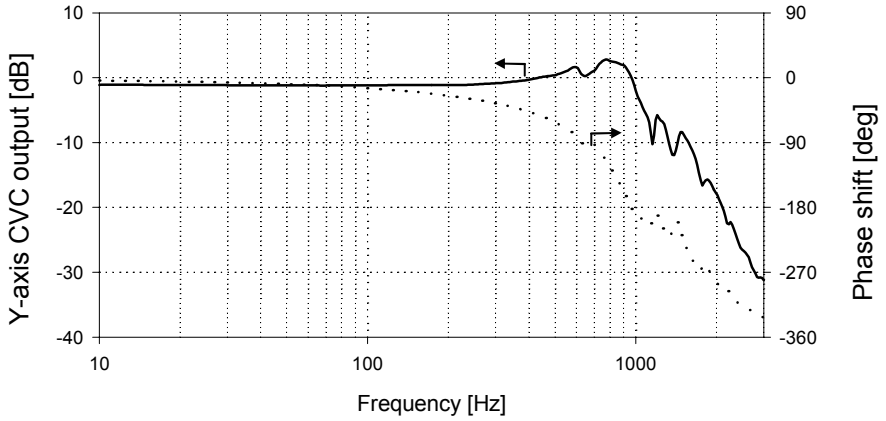

Figure 7-10: The amplitude and phase shift of the vibrating mass as a function of the actuation frequency for sensor Type 2.

The transfer functions in Figure 7-9 and Figure 7-10 may be compared with those of Figure 7-4 and Figure 7-5 respectively. Note that the bandwidth of the CVCs amplification circuitry is limited to frequencies up to 100 Hz. The transfer functions of the electromagnetically actuated sensors show a more smooth behavior as compared to the transfer functions measured by means of the acceleration measurement on top of the shaker unit. This could mean that the mechanical construction of the sensor unit, including its electronic CVC detection system, attached to the shaker unit has quite a large influence on the transfer of mechanical vibrations.

7.3.2 Cross-axis movement of the actuated mass

The electromagnet is meant to initiate a vibration of the seismic mass along the x-axis. But there will also be a certain amount of vibration perpendicular to the x-axis, due to inevitable non-symmetry in the sensor construction. The resulting

cross-axis signal in the y and z-axis is measured. The electromagnet of sensor Type 1 is actuated with a 35mA DC + 25mA$_{RMS}$ AC current. The results are shown in Figure 7-11.

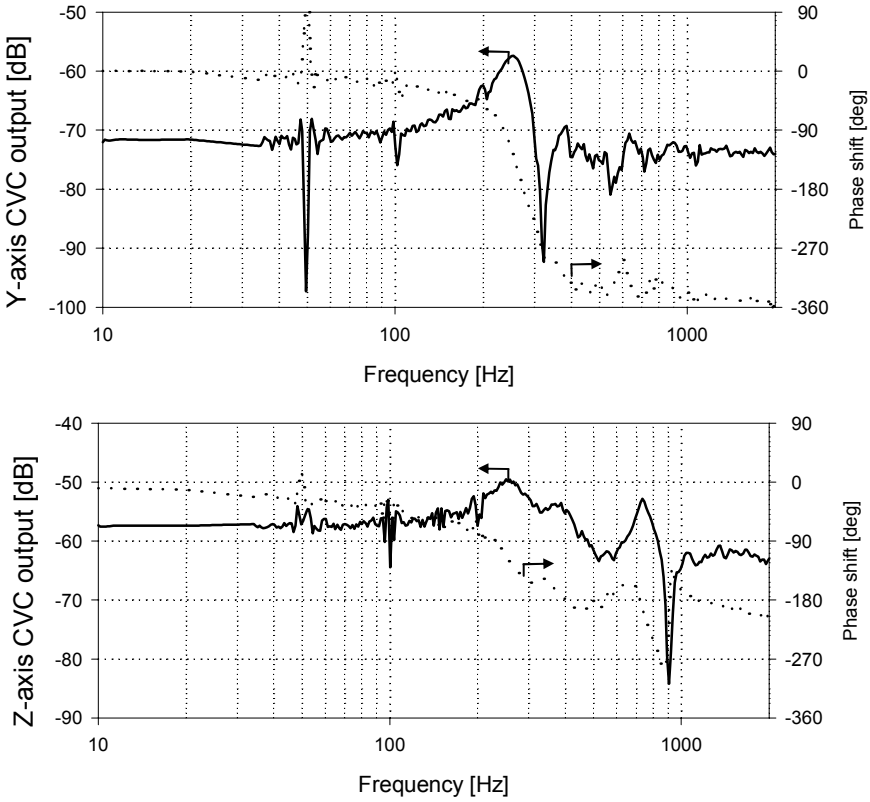

Figure 7-11: The result of cross axis movement due to actuation in the x-axis of the Type 1 sensor.

The graphs in Figure 7-11 show a frequency dependent cross axis signal in the y and z-axis. The cross axis signal from the x-axis to the y-axis is dramatically reduced at a frequency of about 310 Hz and the smallest cross axis signal in the z-axis is experienced at a frequency of 900Hz. The exact cross axis signal for these frequencies are presented in Table 7-2. Note that Figure 7-11 also shows signal peaks at multiplications of 50 Hz. These disturbances occur because the Gyracc is not electromagnetically shielded from the environment.

Table 7-2: The cross axis sensitivity in the y and z-axis due to the actuation in the x-axis for sensor Type 1.

Frequency	V_{x-y}	V_{x-z}
[Hz]	%	%
0-100	3.5	20.0
310	0.3	19.8
900	31.2	6.2

At 310 and 900 Hz the electromagnetic force almost fully counter-acts the cross-axis movement in these axes. It might be that the remaining signal in the

y and z-axis has an electrical noise or parasitic origin. The difference in the frequencies for which the cross axis signal is minimal is probably mainly due to the difference in the mass-spring-damper system in the specific axis. Coriolis vibrations during an experienced rate of turn should result in the largest signal change at the frequencies with the minimum cross axis sensitivity.

The cross axis movement of the mass is also measured for the Type 2 sensor. The electromagnet is actuated with a 20mA DC + 15mA$_{RMS}$ AC current. The results are shown in Figure 7-12.

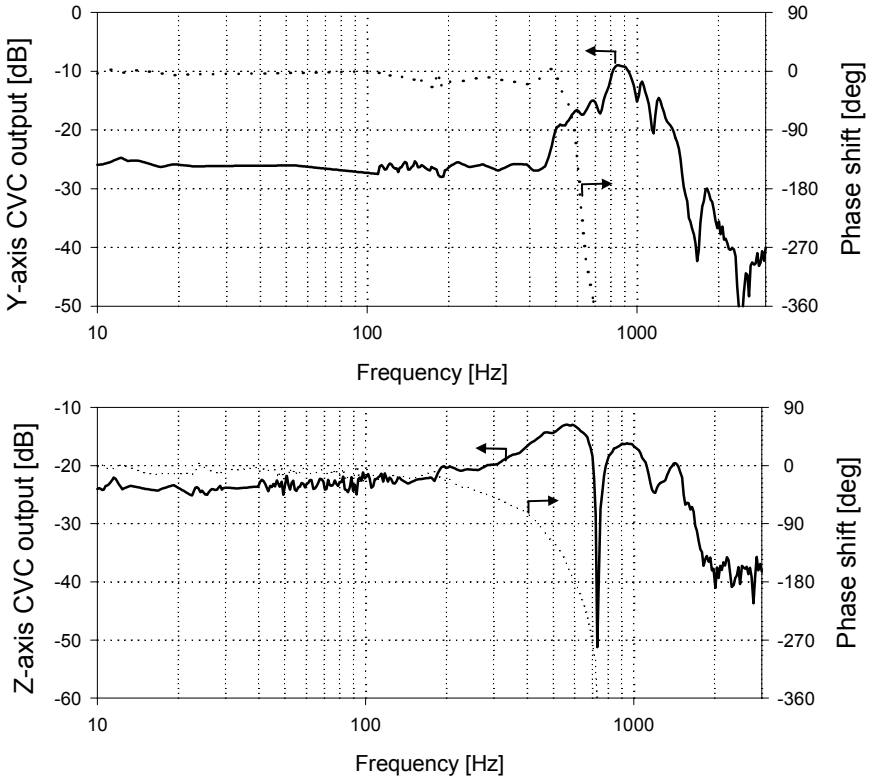

Figure 7-12: The cross axis movement during actuation in the x-axis of the Type 2 sensor.

The y-axis does not show to have a very specific frequency at which the sensor has an absolute minimum in cross axis sensitivity. For this reason the cross axis signal will be calculated for several frequencies, see Table 7-3. The z-axis shows to have minimum cross axis sensitivity at a frequency of 750 Hz.

Table 7-3: The cross axis sensitivity in the y and z-axis due to the actuation in the x-axis for sensor Type 2.

Frequency	V_{x-y}	V_{x-z}
[Hz]	%	%
0-100	5.6	7.1
400	5.0	14.0
750	11.0	0.2
1300	3.2	40.0

From Table 7-2 and Table 7-3 it can be concluded that sensor Type 2 has lower cross axis sensitivity for the frequency range from 0-100Hz as well as for the specific minimum cross axis sensitivity frequencies. With this knowledge the z-axis of sensor Type 2 is expected to have the largest Coriolis vibration sensitivity.

7.3.3 Damping and resonance frequency determination

The damping constant and resonance frequency can be determined by means of applying a force step to the system. Therefore, the seismic mass is attracted by means of a 25 mA DC current and subsequently released. After the current step the mass freely vibrates in the box.
The step response of sensor Type 1 and sensor Type 2 are shown in Figure 7-13a and Figure 7-14a respectively, whereas Figure 7-13b and Figure 7-14b show an enlargement of the damped vibration.

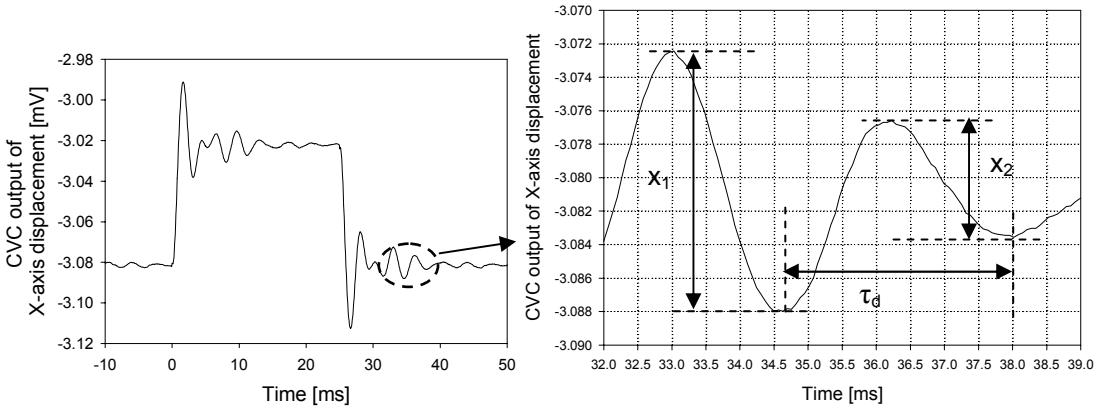

(a) (b)

Figure 7-13: The damped vibration of sensor Type 1.

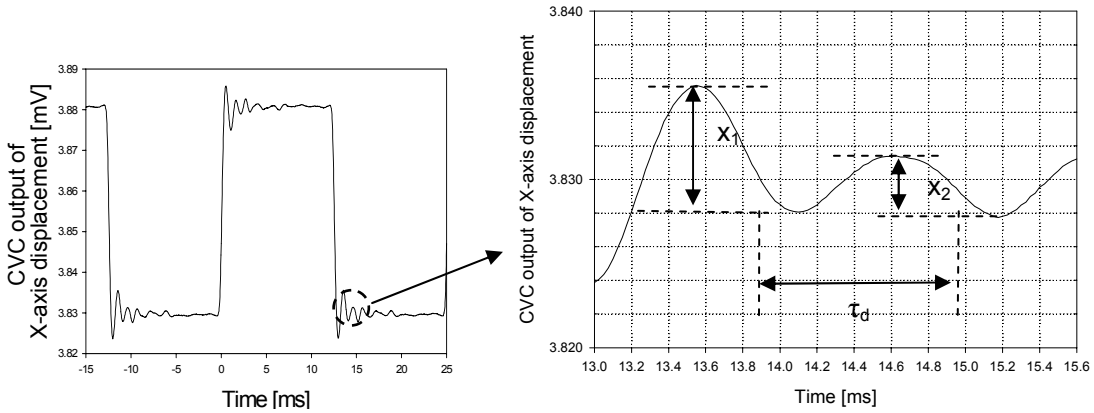

(a) (b)

Figure 7-14: The damped vibration of sensor Type 2.

The resonance frequency and the damping constant of these two systems can be determined from the parameters as given in Figure 7-13b and Figure 7-14b [3]. The resonance frequency of the damped sine wave is found with:

$$\omega_d = \frac{1}{\tau_d} \tag{7-4}$$

with

τ_d = *period time of the damped vibration* *[s]*

The natural resonance frequency can be retrieved with:

$$\omega_n = \frac{\omega_d}{\sqrt{1-\zeta^2}} \tag{7-5}$$

with

ω_d = *damped vibration frequency* *[s]*
ζ = *damping ratio* *[-]*

$$\zeta = \frac{\ln\left[\frac{x_1}{x_2}\right]}{\sqrt{(2\pi)^2 + \left(\ln\left[\frac{x_1}{x_2}\right]\right)^2}} \tag{7-6}$$

with

x_1 = *amplitude of the first vibration* *[V]*
x_2 = *amplitude of the successive vibration* *[V]*

The damping constant of the system is:

$$b = \zeta \cdot 2 \cdot m \cdot \omega_n \tag{7-7}$$

with

m = *weight of the mass* *[kg]*

The mechanical quality factor in the specific axis can be found by rewriting equation 3-33 to:

$$Q = \omega_n \cdot \frac{m}{b} \tag{7-8}$$

Table 7-4 shows the characteristic parameters of the two sensors.

The damping constants of the system are the damping constants for a mechanical vibration along the x-axis. The damping constants in the y and z-axis may differ due to small differences in symmetry of the construction. The measured damping constant of 0.4 Nm/s for the Type 1 sensor is ten times higher than theoretically calculated 0.04 Nm/s. This could be due to the difference in damping effect of airflow around the mass in the fully closed box (Appendix A) as compared to the damping effect of two enclosing plates (Equation 3-26). The measured damping of the Type 2 sensor of 0.4 Nm/s is less than half of the damping expected by theory (1,1 Ns/m, equation 3-29). The hole in the sensor plate of sensor Type 2 through which the middle leg of

the electromagnet is positioned, partly accounts for the lower than expected damping.

Table 7-4: The theoretical and experimentally determined x-axis vibration parameters of sensor Type 1 and Type 2.

Design parameters	Equation	Sensor Type 1	Sensor Type 2
A_{PDMS}	-	$4x \pi x(50\mu m)^2$	$4x \pi x(50\mu m)^2$
G_{PDMS}	-	250.10^3 N/m^2	250.10^3 N/m^2
D_0	-	30 µm	10 µm
PCR	-	0	0
M	-	220.10^{-6} kg	220.10^{-6} kg
A_{plates}	-	3mm x 3mm	3mm x 3mm
Theoretical system parameters			
K	3-23	2616 N/m	7850 N/m
B	3-29	0.04 N.s/m	1.12 N.s/m
f_n	3-31	549 Hz	951 Hz
F_0	3-30	549 Hz	860 Hz
Q	3-33	19.0	1.2
Realized system parameter			
F_0	7-4	295 Hz	870 Hz
B	7-7	0.4 N.s/m	0.4 N.s/m
f_n	7-5	330 Hz	883 Hz
K	3-31	944 N/m	6765 N/m
Q	7-8	1.1	3.0

The measured resonance frequency of both sensors is lower than calculated by theory (equation 3-30). It might be that the shear modulus of the PDMS is lower than the literature value of 250.10^3 N/m^2 [1]. In general it can be said that the Type 2 is more in line with the theory. It might have to do with the elimination of the influence of the size of the mass.

7.4 Rate of turn measurements

7.4.1 The rotation platform

Figure 7-15 shows the rotation platform for rate of turn measurements specifically designed and fabricated for this purpose. It consists of a rotating platform with a diameter of 30 cm. The Gyracc can be mounted on top of the platform connected to the external supply and measurement apparatus via rotary contacts. The platform can rotate clock wise and counter clock wise with a maximum rate of turn of 8 rad/s.

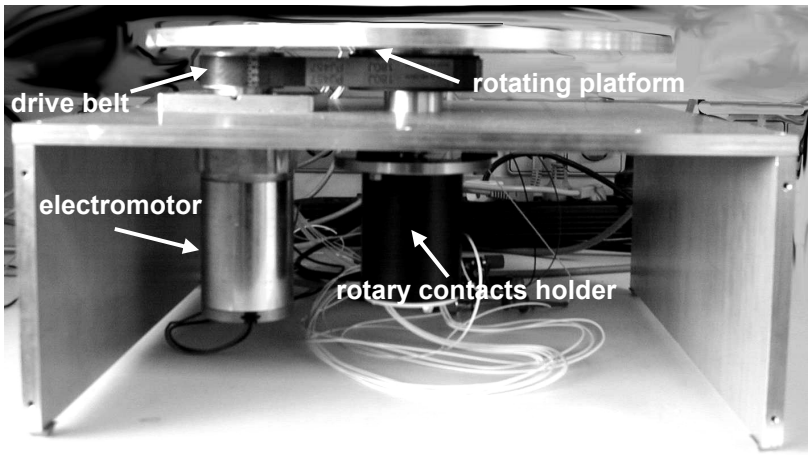

Figure 7-15: The rotation platform.

The specifications of the platform are shown in Table 7-5.

Table 7-5: The rotation platform parameters.

Rate of turn	-8 $^{rad}/_{s}$ until +8 $^{rad}/_{s}$
2 Amp. rotary contacts	8
6 Amp. rotary contacts	4
plateau diameter	30 cm
power supply	–12V +12V
Current	0.5 A

The bottom side of the rotating platform is provided with an alternating black and white pattern. An infrared light emitting diode and receiver is mounted on the base of the platform. The rate of turn of the rotating platform is known by measuring the frequency of the alternating black and white pattern. A frequency of 18 Hz is equal to 2π rad/s. A schematic representation of the measurement set-up is shown in Figure 7-16.

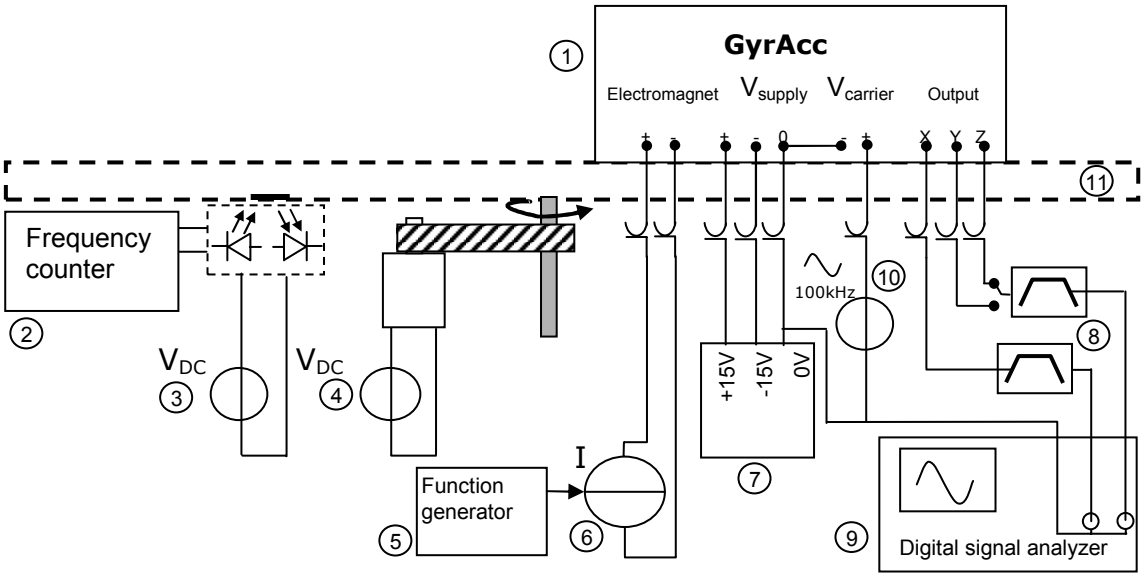

1. Gyracc
2. Frequency counter
3. Power supply for IR LED reflection tranciever
4. Voltage supply for rotating platform motor
5. Function generator to deliver input signal for the electromagnet current source.
6. Current source for the electromagnet
7. Voltage supply for the Gyracc electronics
8. Band pass filter (2x)
9. Digital oscilloscope to analyze the signals
10. 100 kHz Carrier signal
11. Rotating platform

Figure 7-16: Schematic representation of the measurement set-up of the Gyracc on top of the rotating platform.

7.4.2 Coriolis signal measurements

In this section some basic measurements are performed to show the Coriolis effect in the y-axis signal at two different mass vibration frequencies. The measurements are performed with sensor Type 1. The Gyracc is positioned on the rotating platform (Figure 7-17), with its seismic mass positioned in the center of the rotating platform.

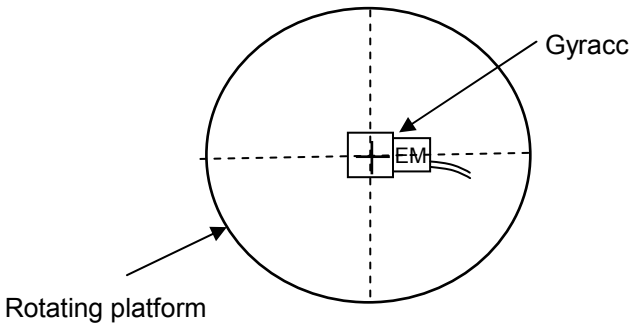

Figure 7-17: The Gyracc on top of the rotating platform.

The C_f capacitors of the CVCs are adjusted such that the x-and y-axis have the same sensitivity. The mass is electro magnetically actuated with a 75mA current

at a frequency of 250 Hz. Figure 7-18 shows the movement of the mass in the actuation axis (x-axis) and the perpendicular Coriolis axis (y-axis) at a rate of turn of –6 rad/s, 0 rad/s and +6 rad/s. The x- and y-axis signals are band pass filtered between 200 and 400 Hz. The signals are retrieved by averaging 512 measured curves of the HP digital oscilloscope. This was necessary because the y-axis Coriolis signals are in the noise level region of the measurement (see paragraph 7.1.2).

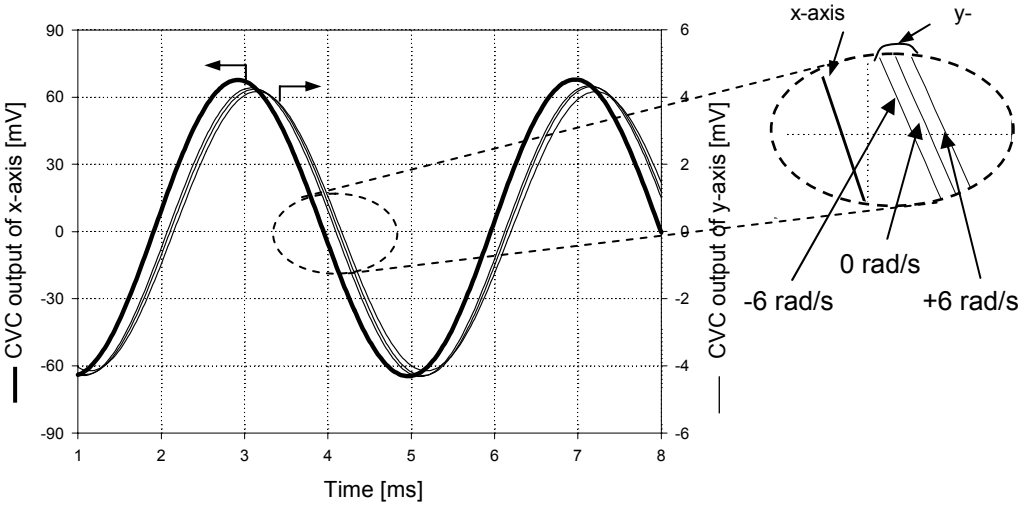

Figure 7-18: The vibrations of the mass in the x-axis (actuation) and y-axis (Coriolis) for a rate of turn of –6 rad/s, 0 rad/s and +6 rad/s, with a close-up on the upper right.

Measurements of the movement in the Coriolis direction are triggered with the movement in the actuated (x-axis) direction, which is the bold line in Figure 7-18. The y-axis signal during no rate of turn is the cross axis signal. The figure shows a phase shift in the y-axis signal with respect to the x-axis signal due to the Coriolis effect, which is induced by the experienced rate of turn.

The contribution of the Coriolis force in the movement of the mass is found by subtracting the cross axis movement in the y-axis, the 0 rad/s signal, from the experienced +6 rad/s and –6 rad/s. These differential signals are shown in Figure 7-19.

Figure 7-19 shows that a clockwise and a counter clockwise rate of turn result in anti-phase vibrations in the y-axis. The Coriolis amplitude is 0.2 mV at a rate of turn of 6 rad/s, which is 5% of the total y-axis signal amplitude. The sensitivity of the Gyracc at this actuated vibration frequency is approximately 32μV per rad/s. Note that the CVC output stage has an amplification factor of 100.

The vibration amplitude of the Coriolis signal is a function of the vibration amplitude in the applied x-axis direction. In this particular case the Coriolis contribution in the y-axis signal is 0.3% of the CVC output signal in the actuated x-axis. The CVC output signal in the y-axis is measured differentially and the x-axis signal is measured single sidedly. When the displacement amplitudes are to be compared then the output voltage in the x-axis is generated by twice the

mass displacement as compared to the y-axis. This results in a Coriolis vibration amplitude which is 0.15% of the actuated amplitude during the experience of a 6 rad/s rate of turn. The Coriolis amplitude at a rate of turn of 1 rad/s would then be approximately 0.03% of the amplitude in the actuated direction.

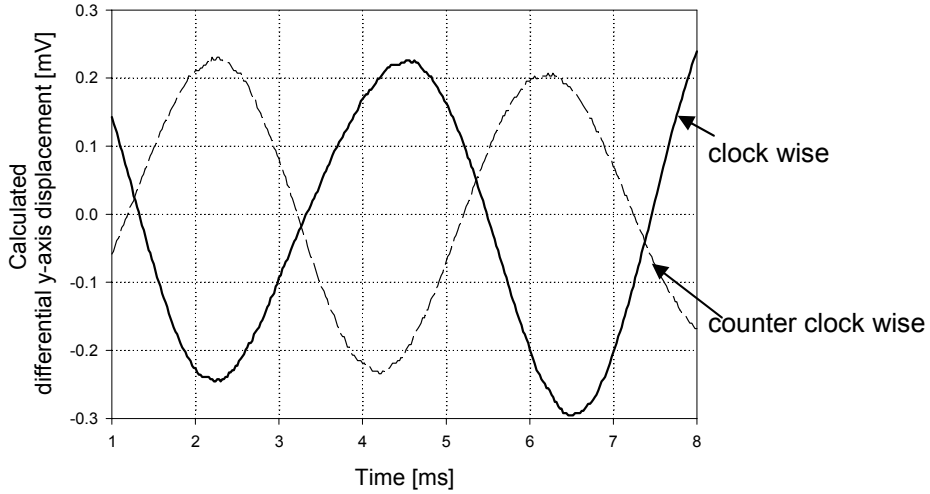

Figure 7-19: The Coriolis contribution to the y-axis signal during the 6 rad/s (solid line) and the –6 rad/s rotation (dashed line) at a 250 Hz frequency operation.

In Figure 7-20 the mass is actuated with a frequency of 335 Hz. This is the frequency in which the cross axis movement of the mass in the y-axis direction is low. The x- and y-axis signals are band pass filtered between 250 and 450 Hz.

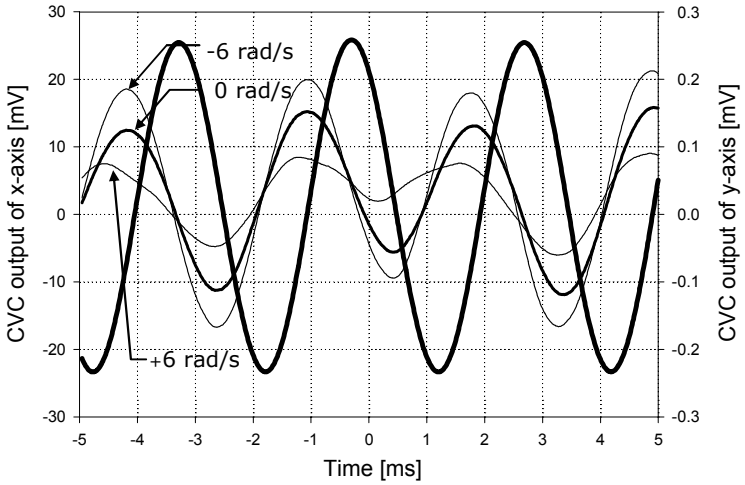

Figure 7-20: The x and y-axis amplitude at a vibration frequency of 335 Hz during a rate of turn of –6 rad/s , 0 rad/s, +6 rad/s.

Figure 7-20 shows the change in the y-axis signal due to the experience of the rate of turn. At this frequency of operation the Coriolis contribution has a large impact on the amplitude of the y-axis signal. The contribution of the Coriolis force in the movement of the mass is found by subtracting the cross axis movement in the y-axis (during the 0 rad/s rate of turn) from the experienced +6 rad/s and –6 rad/s. These differential signals are shown in Figure 7-21.

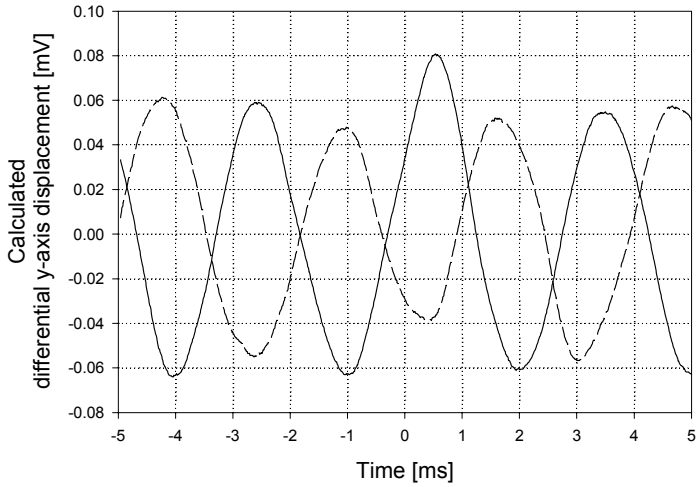

Figure 7-21: The Coriolis contribution to the y-axis signal during the 6 rad/s (solid line) and the –6 rad/s rotation (dashed line) at an operation frequency of 335 Hz.

The Coriolis amplitude is 0.06 mV at a rate of turn of 6 rad/s, resulting in a sensitivity of 10μV rad/s. Note that the differential CVC has an amplification factor of 100. The relative change of the y-axis signal due the contribution of the Coriolis signal is depending on the amount of cross axis movement in the y-axis. The change in amplitude in the y-axis due to 6 rad/s rate of turn the Coriolis signal is 33%. At this 6 rad/s rate of turn the measured Coriolis signal is 0.3% of the measured actuation signal. The actual Coriolis vibration amplitude during a 1 rad/s rate of turn is then approximately 0.03% of the actuated vibration amplitude, for the same reasons as mentioned for the 250 Hz measurement.

Concluded can be that the Coriolis vibration amplitude is approximately 0.03% of the actuation vibration amplitude for both operating frequencies, during a 1 rad/s rate of turn. Note that this result is achieved although the relative change in the y-axis signal for both operation frequencies was completely different.

7.4.3 Rate of turn measurement with the lock-in amplifier

The contribution of the Coriolis effect is buried in the noisy signal of the y-axis (see also 7.1.2), but because the Coriolis signal has the same frequency as the frequency of the vibration in the actuation axis the Coriolis signal can be retrieved by means of a lock–in amplifier. Furthermore a lock-in amplifier is able to average the measured signal over a time span τ.

The Gyracc with its three CVC circuits is connected to the lock-in amplifier in such a way that the measured x-axis displacement is used as the reference and the Coriolis signal (y-axis) as the input signal for the lock-in-amplifier (Figure 7-22).

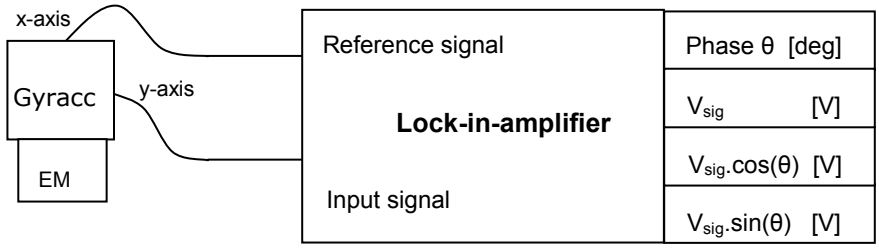

Figure 7-22: The Gyracc connected to a lock-in-amplifier.

For the experiments the dual phase Princeton Applied Research 830-model lock-in amplifier is used, which is able to measure:

- The phase difference between the vibration in the x-axis (actuation) and the vibration in the y-axis (Coriolis).
- The amplitude of the y-axis signal at the reference frequency.
- The amplitude of the y-axis signal at the reference frequency at a specific phase angle with respect to the reference signal (V_{sig}.cos(θ) as well as V_{sig}.sin(θ)).

During the rate of turn measurements with the Gyracc, the phase difference between the vibration in the x- and y-axis vibration is measured (phase θ [deg]) as well as the amplitude of the y-axis signal (V_{sig} [V]).

7.4.4 Rate of turn measurement results

Sensor Type 1 is positioned in the center of the rotating platform (see Figure 7-17). The electromagnet is actuated with a current of 75 mA and the mass is vibrating at a frequency of 280 Hz. Now the rotating platform is put three times to a number of rates of turn ranging from –8 rad/s up to +8 rad/s. The output of the lock-in-amplifier as a function of the rate-of-turn experienced by the Gyracc is shown in Figure 7-23. The time constant (τ) of the lock-in amplifier is set to 300 ms, which limits the rate of turn measurement bandwidth to approximately 1.8 Hz.

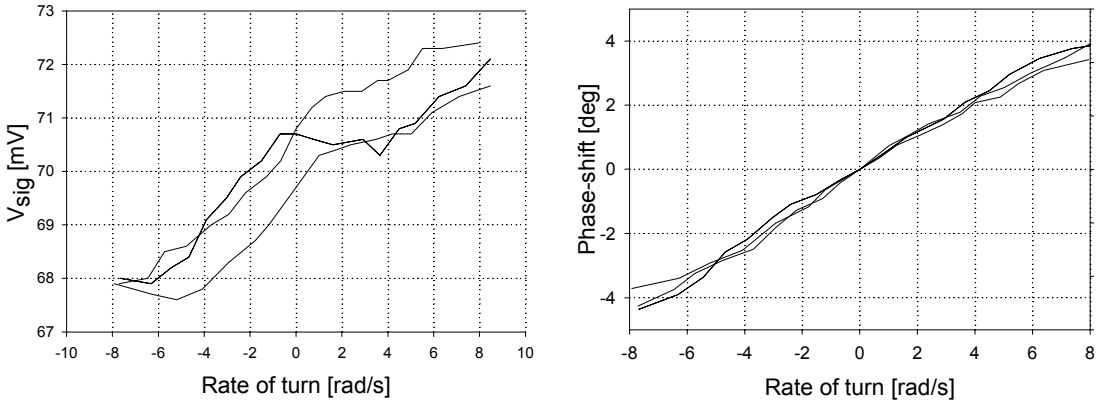

Figure 7-23: (a) The amplitude of the y-axis signal and (b) the phase shift of the y-axis signal as a function of the rate of turn around the z-axis for the Type 1 sensor.

Figure 7-23 shows that the change in amplitude of the y-axis signal as well as the phase-shift between the two vibrations represent the rate of turn. Comparing Figure 7-23a and b it may be concluded that the phase shift is a more reliable representation of the rate of turn, because the phase shift signal is less noisy and more reproducible. The three phase shift measurements show a phase sensitivity of about 0.5^0 per rad/s.

The fluctuations and time dependent amplitude of the y-axis is probably due to vibrations produced by the turntable. These vibrations are super imposed on top of the actuation and Coriolis vibration. If the amplitude of the vibration in the x-axis (actuation axis) is increased due to (unwanted) vibrations in the turntable then this will also result in an higher amplitude of the Coriolis signal in the y-axis (Equation 3-44b). This effect will have no effect on the phase shift between the x- and y-axis vibrations. This might be the reason that phase measurement is less noisy.

The phase shift experiment is also performed on sensor Type 2. The experiment is repeated for different vibration frequencies of the mass. The vibration frequencies are 400, 750 and 1300 Hz. The results are shown in Figure 7-24a, b and c respectively.

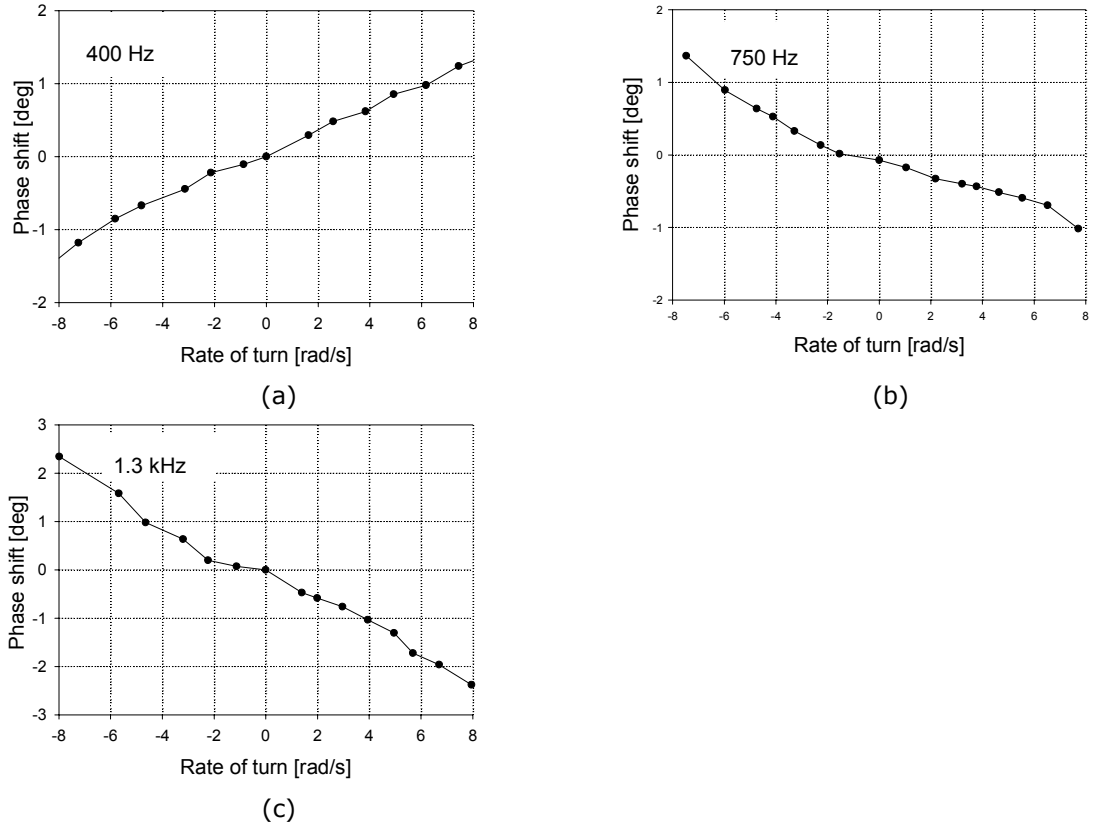

Figure 7-24: The y-axis phase shift as a function of the rate of turn for sensor Type 2 at a vibration frequency of (a) 400Hz, (b) 750Hz and (c) 1.3 kHz.

The sensitivity of the sensor Type 2 differs for the different vibration frequencies. The phase sensitivity of the 400, 750 and 1300 Hz vibration

frequencies are respectively: 0.16^0 per rad/s, $-0{,}13^0$ per rad/s and -0.28^0 per rad/s. At the vibration frequency of 400 Hz the phase sensitivity is positive and at the operation frequencies of 750 Hz and 1.3 kHz the sensitivity is negative. This is due to the phase dependency of the Coriolis signal with respect to its natural resonance frequency, as described in section 3.3 and shown in Figure 3-15 d and e. Note that for a certain frequency between 400 Hz and 750 Hz the phase shift between the vibration in the x-axis and vibration in the y-axis is independent of the rate of turn. At this specific frequency the Coriolis signal will be in phase with the cross axis movement and only the amplitude of the y-axis signal will change.

In the previous measurements the Gyracc was rotated around its z-axis and the amplitude was measured in its y-axis. In the following measurement rotations around the Gyracc's y-axis will be applied and the vibrations in its z-axis will be measured. Therefore the Gyracc, together with the CVC circuits, is put on its side (90^0 rotated around its x-axis) and positioned centrally on the rotation platform. Measurement results for sensor Type 1 and 2 are shown in Figure 7-25.

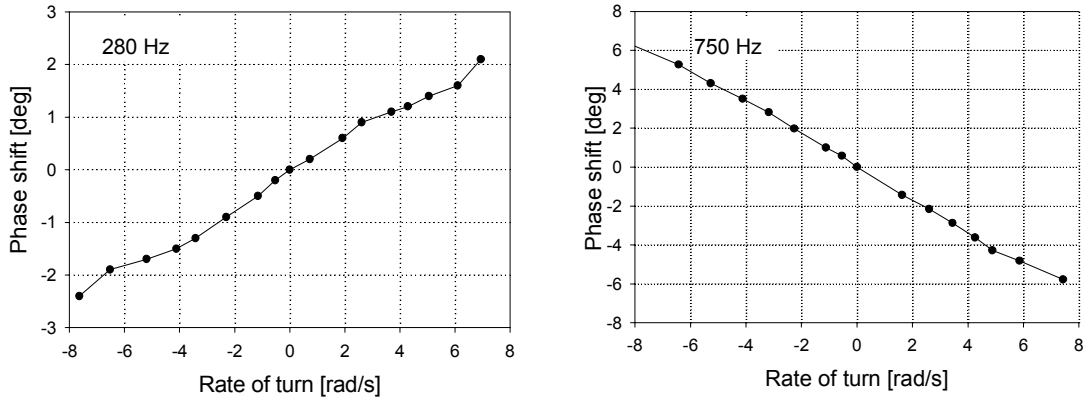

(a) (b)

Figure 7-25: (a) the phase shift of the z-axis signal as a function of the rate of turn around the y-axis for sensor Type 1 and (b) similar for sensor Type 2.

The mass in sensor Type 1 is vibrating at a frequency of 280 Hz and is actuated by a current of 75 mA current. The mass in the Type 2 sensor is vibrating at a frequency of 750 Hz and is actuated by a current of 60 mA. The sensitivity of sensor Type 1 is about 0.33^0 per rad/s and sensor Type 2 has a sensitivity of about -0.83^0 per rad/s. This higher sensitivity was to be expected from the low cross axis sensitivity (Table 7-3) for this frequency. In conclusion it can be said that both sensors are capable of measuring rotations around the z-axis as well as the y-axis.

7.4.5 Rate of turn sensing with centrifugal forces

A gyroscope should measure the experienced rate of turn independently of the position on top of the rotating platform. In the previous section the Gyracc was positioned in the center of the rotating platform and now the Gyracc is positioned 10 cm off-center on the rotating platform (Figure 7-26), with the electromagnet pointing to the center of the rotating platform.

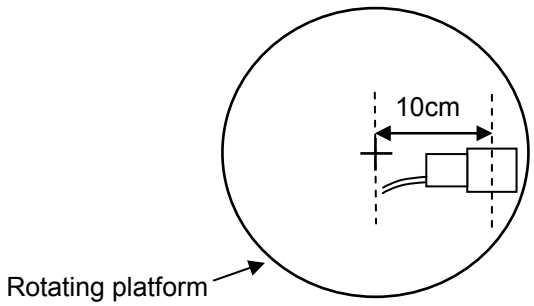

Figure 7-26: The position of the sensor on top of the rotating platform.

Rate of turn measurements performed with this setup will also introduce centrifugal forces on the seismic mass. After placing the Gyracc at this new position the vibrating behavior of the seismic mass showed to have changed. Some rates of turn have been applied to the system at different actuation frequencies. The following actuation frequencies showed to give noticeable shift responses. The electromagnet of sensor Type 1 is actuated with a current of 75mA and is vibrating with a frequency of 320 Hz. The electromagnet of sensor Type 2 is actuated with a current of 60 mA and is vibrating with a frequency of 700 Hz. Their phase-shift as a function of the rate of turn is shown in Figure 7-27.

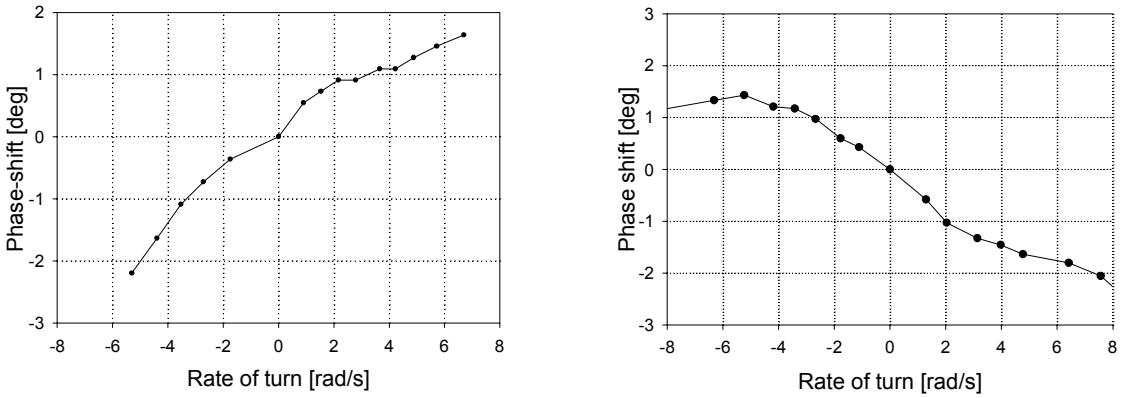

(a) (b)

Figure 7-27: The phase shift of the y-axis signal as a function of the rate of turn around the z-axis (a) for sensor Type 1 and (b) sensor Type 2.

Both figures show that the phase-shift as a function of the experienced rate of turn is less linear for both sensors than with the sensor placed centrally. In addition the mean sensitivity of sensor Type 1 is decreased from 0.5^0 per rad/s to 0.3^0 per rad/s. The sensitivity of Sensor Type 2 increased from 0.16^0 per rad/s to 0.25^0 per rad/s. Concluded can be that the centrifugal forces have an influence on sensing the rate of turn. An increase in the rate of turn increases the centrifugal force, which results in an increase in the distance between the seismic mass and the electromagnet and in an increment of the spring constant in the actuation direction, both having their influence on the phase and amplitude of the vibration.

In the following measurements the Gyracc is positioned with its electromagnet in the direction of the rotation, see Figure 7-28. Now the distance between the mass and the electromagnet will not be influenced by the centrifugal forces, but the mass is pressed against the outer wall of the box, in the same axis as the Coriolis vibration is to be expected.

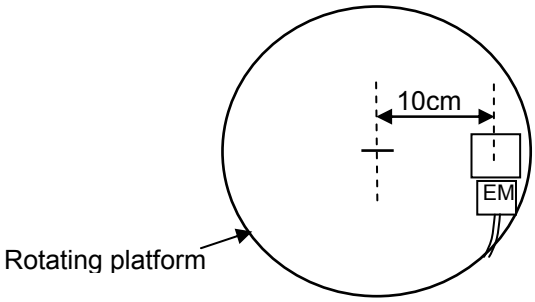

Figure 7-28: The position of the sensor on top of the rotating platform.

The phase-shift of the vibration in the y-axis with respect to that of the x-axis as a function of the rate of turn for sensor Type 1 and Type 2 is shown in Figure 7-29.

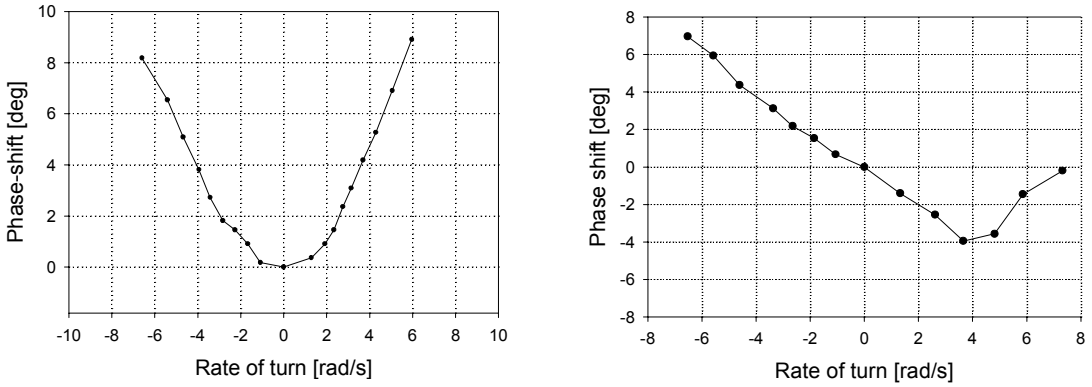

(a) (b)

Figure 7-29: The phase shift of the y-axis signal with respect to the x-axis signal as a function of the rate of turn around the z-axis for (a) sensor Type 1 and (b) sensor Type 2.

Although these measurements are performed with the same currents and frequencies as used in Figure 7-27, the results are different as compared to the results of Figure 7-27. It might be that during the compression of the springs, due to the centrifugal forces the resonance frequency of the mass in this specific axis changes. The change in resonance frequency of this specific axis results in a phase shift of the vibration in the y-axis with respect to the vibration in the x-axis. It might very well be that the phase shift dependency for centrifugal forces is larger than the phase shift due the Coriolis force.

7.5 Conclusions

The Gyracc is able to measure triaxial accelerations and the rate of turn around two axes, using one electromagnet. The electronic circuitry, originally designed to measure frequencies up to 50 Hz, was able to detect vibrations up to 1 kHz. The electromagnet assembled next to the inertial sensor box is able to attract the seismic mass. The frequency of the vibration of the seismic mass is twice the frequency of the actuation current of the electromagnet.
Although the actuation with the electromagnet is solely intended to initiate vibrations in the actuation axis, the mass also induced a small vibration in the perpendicular axes. The percentage of this cross axis sensitivity is a function of the vibration frequency of the seismic mass.

The Coriolis vibration amplitude during a 1 rad/s rate of turn is typically about 0.03% of the amplitude in the actuation direction. As the Coriolis amplitude is below the noise level of the system, the Coriolis signal is to be detected by means of signal averaging. The Coriolis signal is super-imposed on top of the cross axis movements of the mass. If the mass is actuated at a frequency for which the cross axis movement of the mass is low, then the Coriolis contribution is more easily detected.

The Coriolis signal on top of the cross axis movement of the mass induces a phase shift, a change in amplitude or a combination of these two in the axis where the Coriolis displacement is to be expected. It is shown that phase shift in the signal is a more reproducible measurement than amplitude measurement. A lock-in-amplifier is the ideal measurement instrument to retrieve this phase shift. During the measurements the lock-in amplifier used a low pass filter with a time constant of 300 ms, which limited rate of turn sensing to a frequency of 1.8 Hz.

The measurements have been performed with two differently constructed Gyraccs. In one construction the seismic mass was enclosed by 30µm high PDMS springs inside a silicon box and in the other design the seismic mass was enclosed by 10 µm high PDMS springs in a glass box. Both sensors showed comparable performance. The sensor with 10 µm high PDMS springs was operated with an actuation current of 60 mA and the sensor with 30 µm high PDMS springs was operated with an actuation current of 75 mA.

A point of attention is the rate of turn sensitivity for accelerations (and centrifugal forces) of the sensor. It seems that during simultaneous experience of rotation and accelerations the phase sensitivity of the sensor to accelerations overrules the sensitivity to rates of turn. It might be that at certain frequencies of operation this sensitivity is reduced to zero.

It can be concluded that both Gyracc designs can perform as a triaxial accelerometer and a dual axis rate of turn sensor.

7.6 References

[1] Lötter, J.C., Olthuis, W., Veltink, P.H., Bergveld, P., "A sensitive differential capacitance to voltage converter for sensor applications", IEEE Instrumentation and Measurements Vol. 48, pp. 9-96, 1999.

[2] Lötter, J.C., Thesis: "A Highly Symmetrical Capacitive Triaxial Accelerometer", ISBN 90-365-0982-3, 1997.

[3] Meriam, J.L. and Kraige, L.G., Book: "Engineering Mechanics Vol.2", ISBN: 0-471-84912-X, 987.

Chapter 8

8 CONCLUSIONS AND SUGGESTIONS FOR FURTHER RESEARCH

In this chapter the main conclusions are drawn of the research and development of the Gyracc, followed by some open items in the section with suggestions for further research.

8.1 Conclusions

There is a market for sensors that are able to detect rates of turn and accelerations in the three dimensional space for the determination of position and orientation. A measurement system which is able to measure these 6 degrees of freedom is called an Inertial Measurement Unit (IMU). IMUs consist of a combination of sensors. The sensors with the smallest outer dimensions are based on the inertial properties of mass and are fabricated with MEMS techniques. The majority of the MEMS sensors are only able to measure rate of turn around one single axis or accelerations in one or two directions. MEMS devices that are able to detect dual axis rate of turn consist of two smartly integrated single axis rate of turn sensors. No MEMS devices with combined acceleration and rate of turn sensing properties are presently available. However, the Gyracc is able to measure accelerations and rates of turn in all directions and around all axes by analyzing the vibrating behavior of one single symmetrically suspended seismic mass. The outer dimensions of the sensing element are approximately 3.3×3.3×6.3 mm^3 and could be an alternative for IMUs that consist of several individual sensors.

8.1.1 Sensitivity and linearity

The Coriolis forces experienced by the seismic mass of the Gyracc are low. Therefore the mechanical sensitivity of the sensor is made as large as possible. With the overall boundary condition that the error in the accuracy of the measurement should be no larger than 1% the following specific conditions must be met:

- A single side PDMS suspended seismic mass is allowed to displace proportional to the experienced force over a distance equal to maximally 1% of the original PDMS spring height.
- A two sided by PDMS enclosed seismic mass is allowed to displace proportional to the experienced force over a distance equal to maximally 9% of the original PDMS spring height.

- The capacitance between the seismic mass and one of the inner box walls is proportionally to the distance over a displacement range of maximally 0.5% around the initial distance.
- The differential capacity between the seismic mass and two opposite of each other positioned inner box walls is proportional to the distance over a displacement range of maximally 10% around the initial distance.

A combination of these effects results in a differential capacity which is proportional to the forces experienced by the mass, for mass displacements up to 10% of the original PDMS height. The mechanical sensitivity in combination with differential capacitive measurement is 40 times larger then the sensitivity reached by using single side suspension and capacitive measurement.

8.1.2 Realized sensor constructions

Two different mechanical sensor constructions were developed consisting of a combination of MEMS and precision engineered elements, being the sensor box with predefined dimensions and the dimension tolerant sensor box design. Both sensors showed to be able to measure accelerations as well as rates of turn.

In the sensor box with predefined dimensions all capacitive position detection plates on the box walls are interconnected by means of electrically conducting glue, which drastically reduced the amount of electrical interconnections between the capacitor plates and the electronics, as compared with the original triaxial accelerometer of Lötters. The box walls were made of 6 equally shaped silicon plates, which were separated by means of reactive ion etching. The dimensions of the sensor box are determined by the dimensions of the seismic mass. Calculations showed that the distance between the box inner walls and the seismic mass should be no less than 30 µm, caused by the tolerances in the dimensions of the seismic mass. A smaller distance could result in large compression forces in the PDMS springs, resulting in mechanical fixation of the mass.

An electrostatic actuation potential of 120V would be necessary to actuate the mass over a distance of 30 µm, which is too large for biomedical applications. As a result electromagnetic actuation was introduced. During the project the idea developed to realize a dimension tolerant box, which was insensitive to the dimensional tolerances of the seismic mass and thickness of the box walls. The dimension tolerant sensor box consists of six equally shaped KOH etched glass walls. Although the costs of a sensor are not of interest for a fundamental research project, it is nice to express that for this type of box less expensive precision engineered seismic masses and micromachined box walls can be used.

Several electromagnet constructions have been analyzed for their actuation force. The largest actuation force can be realized by means of an electromagnet with an E-shaped core. This type of electromagnet also showed to have the lowest fringing of magnetic fields. Theoretically an E-core electromagnet with dimensions of 3×3×3 mm^3 can reach an actuation force of 11mN. An E-core electromagnet has been produced not conform to the optimized dimensions and realized a force of 1 mN during a 70mA actuation current.

8.1.3 Probimide as a temporary support.

A concept of temporary supporting the flexible PDMS pillars with stiff probimide pillars was introduced. The temporary support opened the possibility to assemble the Gyracc accurately although there is a spread in assembly forces. After the full assembly the probimide pillars were shrunk by means of heat, with the free to move suspended mass as a result. Furthermore the shrunk probimide pillars function as a mechanical overload protection to prevent the PDMS pillars from crushing during the experience of excessive accelerations.

8.1.4 The Coriolis-signal

A vibrating mass will experience a force in the direction orthogonal to its vibration axis, during the experience of a rate of turn, further referred to as the Coriolis axis. This force causes a vibration in the Coriolis axis. This Coriolis vibration will be added to the vibrations already present in the Coriolis axis. These already present vibrations may be caused by accelerations, mechanical cross axis sensitivity or disturbances. The already present mechanical cross axis signal is frequency dependent. The Coriolis signal may influence the signal in the Coriolis axis in its amplitude or phase with respect to the actuation vibration. The vibration signal in the Coriolis axis may mainly change the existing amplitude of the vibration or the phase of the signal. Thus the phase or amplitude sensitivity depends on the frequency of operation.
The amplitude and phase of the Coriolis signal are always a function of the rate of turn and the actuated vibration amplitude and frequency. If the actuated amplitude is not controlled, then it might vary in amplitude due to external disturbances. This will also result in a change of amplitude of the Coriolis signal. Therefore the Coriolis signal can best be determined by measuring the phase between the actuation and the Coriolis signal by means of a lock-in amplifier.

8.1.5 Theory, Simulations and Practice

The theory shows that a symmetrical system, with a quality factor of 1, will cause a Coriolis amplitude of 0.03% of the actuation amplitude during the experience of a 1 rad/s rate of turn. This relation is also found during the simulations and measurements. Simulations and practice show that, during the experience of a rate of turn, a larger mechanical cross-axis sensitivity between the actuation axis and the Coriolis axis results in a lower change in the Coriolis

signal, but theory and practice both show that the absolute contribution of the Coriolis force is independent of this cross axis sensitivity.

8.1.6 Triaxial accelerometers and dual axis rate of turn sensing

A symmetrically suspended mass in combination with one single electromagnet has been realized and shows to be able to measure accelerations in three axes and rates of turn around two axes.

8.1.7 Triaxial acceleration and rate of turn sensing

Theory showed that it is possible to realize an inertial sensor which is able to measure accelerations as well as rotations in the 3 dimensional space by using a single suspended mass which vibrates in at least two different axes.
The vibrations in the different axes may be induced sequentially or simultaneously. Realizing a vibration of the mass in the separate axes sequentially, results in a continuous start and stop of the vibrations which highly limits the bandwidth of the sensor. The bandwidth of a continuously vibrating mass is not limited by this phenomenon. Simulations are performed on a mass which is actuated in two orthogonal axes simultaneously. The vibration in the two orthogonal axes is out of phase, which results in a circular vibration pathway of the mass. Rotating the inertial sensor around its three major axes results in a Coriolis vibration in the to be expected axes. Such a sensor will result in an IMU which is able to measure rotations as well as accelerations around a single point.

8.1.8 The influence of accelerations

The phase difference between the vibration in the Coriolis axis and the vibration in the actuated axis shows to be sensitive to accelerations, in the form of centripetal forces. Both produced sensors show to be sensitive to the centripetal force, but sensor Type 1 shows the largest sensitivity. It might be that actuation in sensor Type 2 results in a larger actuation amplitude and that therefore the influence of the centripetal force is lower. An increase of the actuation force will result in a larger Coriolis vibration, but such amplitude may mask the phase sensitivity to accelerations. A solution to this problem may be to subtract the phase shift caused by the experienced acceleration, because the experienced acceleration is known in this sensor.

8.1.9 Frequency of operation

The experience of a mechanical disturbance in one of the axes of the Gyracc will result in a vibration of the seismic mass at its resonance frequency. If this disturbance takes place in the Coriolis axis then this will result in a damped vibration at the resonance frequency in the Corilis axis. If the Coriolis signal would be at the same frequency as the resonance frequency, then the Coriolis signal generated by the experience of a rate of turn can not be separated from

the signal resulting from the mechanical disturbance. For this reason the single mass rate of turn sensor should not operate at its resonance frequency. In contrast to most MEMS based rate of turn sensors the Gyracc does not need to vibrate at its resonance frequency to sense the small signal amplitude generated by the Coriolis forces. Therefore the Gyracc is to be expected to be less sensitive to mechanical disturbances. The minimum measurable rate of turn is determined by the noise level of the electronic measurement system as shown in Figure 7-3.

8.2 Suggestions for future research

8.2.1 Dedicated electronics

A dedicated electronic system should be developed to simultaneously measure accelerations and rate of turn signals. The acceleration system should measure the low frequencies of the signal and the rate of turn sensing electronic system should only measure the Coriolis vibration.

8.2.2 Algorithm to increase accuracy

It might be possible that the accuracy of the rate of turn measurement can be increased by an algorithm which combines the rate of turn signal with the acceleration signal, because both signals are based on the position of the same mass.

8.2.3 Decrease rate of turn sensitivity to accelerations

During the experience of a rate of turn the vibration of the mass in the Coriolis direction showed to be phase sensitive to centrifugal forces. This is possibly due to a change in the spring constant of the springs surrounding the mass or by a change in damping constant. One of the following methods might overcome this effect:

- Apply an increased vibration actuation force.
- Apply an algorithm which compensates for the experienced accelerations.
- Use a different actuation vibration frequency.
- Apply amplitude measurement instead of phase measurement.
- Keep the seismic mass at a fixed displacement range by means of force feed back, which would need the use of dual side actuation.

8.2.4 Relation between sensitivity and energy consumption

Electrostatic and electromagnetic actuation can provide actuation of the seismic mass in the inertial sensor, without changing the concept of the symmetrical triaxial sensor. An actuation force of 11mN would be the optimal force to actuate the 3x3x3 mm^3 iron mass in the inertial sensor.

For an inertial sensor with 10 µm high PDMS springs an electrostatic actuation potential of approximately 120 Volts should be applied to reach the required 11mN. Such a potential is considered to be a too high potential for biomedical applications. Therefore the inertial sensor is actuated by a 3x3x3 mm^3 E-core shaped electromagnet positioned next to the inertial sensor. An optimally designed electromagnet can reach forces up to 11mN.

The electromagnet realized in practice was not conform to the optimal dimensions and could produce only an actuation force of 1mN with an actuation current of 60mA. An optimal electromagnet would consume less power during a 1mN actuation force. Further an optimal electromagnet can reach a higher actuation force resulting in a higher rate of turn sensitivity.

8.2.5 Electrostatic actuation

A 1mN actuation force of the electromagnet resulted in a measurable rate of turn. The 1mN actuation force can also be reached with an electrostatic actuation potential of 35V, which seems reasonably low for biomedical applications. The costs of an electrostatically actuated Gyracc will be lower than an electromagnetically actuated Gyracc, while the overall dimensions are also smaller.

SUMMARY

There is a need for systems that can sense motions in the 3D-space for position and orientation determination. In the biomedical field such a sensing system should ultimately be small enough for implantation in human beings (Chapter 1).

The smallest available motion sensors are based on the inertial properties of mass (Chapter 2). These small 6-degrees of freedom measurement systems consist of several individual inertial sensors. The total volume of such an Inertial Measurement Unit (IMU) is several cubic centimeters. This is too large for implantation. Therefore in this thesis a prototype of a sensing element with IMU measurement properties is presented with a volume of several cubic millimeters. In this sensor the inertial forces on only one single seismic mass are measured. This sensor is called Gyracc, which is short for gyroscope and accelerometer.

The Gyracc is based on the triaxial accelerometer developed by Dr. Ir. J.C. Lötters. The triaxial accelerometer consists of a cubic seismic mass which is suspended by polydimetyhylsiloxane (PDMS) springs inside a box. The position of the seismic-mass with respect to the inner box walls depends on the inertial forces experienced by the seismic mass. The inner-walls of the box contain capacitor plates which in combination with a dedicated Capacity to Voltage Converter (CVC) can measure the position of the conducting mass with respect to the inner box walls.

The triaxial accelerometer is extended with rate of turn sensing capability by actively actuating the seismic mass into a vibration (Chapter 3). The vibration is achieved by means of an E-core electromagnet (Chapter 4). During the experience of rate of turn in the axis perpendicular to the actuated vibration the seismic mass will experience a Coriolis force. This Coriolis force will result in a vibration perpendicular to the actuated vibration of the seismic mass. The amplitude and phase of this Coriolis vibration is a measure for the experienced rate of turn.

The mechanical as well as the electrical sensitivity of the inertial sensor had to be optimized to be able to sense the small mass displacements induced by Coriolis force. The non-linear spring constant of the rubber elastic polydimethylsiloxane (PDMS) springs and the non-linear characteristics of the capacitive measurement system partly compensate each other, thus increasing the linear range of the complete system.

The different parameters of the mass-spring-damper system are optimized and used as an input for a simulation model of the Gyracc. Simulations show that rate of turn sensing around the three major axes of the Gyracc is possible by actuating the seismic mass in a circular pathway. The circular pathway of the mass is realized by two perpendicularly positioned actuators (Chapter 5).

The described inertial sensor is realized with micromachined sensing plates, with PDMS springs on top, a precision engineered seismic mass and an electromagnet. The initial compression of the PDMS-springs, which enclose the seismic mass, is of large influence on the Gyracc's rate of turn sensitivity. Two different mechanical constructions of the Gyracc are realized in which the initial compression of the springs is controlled (Chapter 6).
In the first design the initial height of the PDMS springs exceeds the total dimensional tolerance in the construction by far, resulting in an upper limit in compression of the springs after assembly. In the second design the tolerances in the mechanical components have no influence on the initial compression of the PDMS at all. During the assembly of this Gyracc the initial compression of the flexible PDMS springs is limited by a structure positioned nearby the flexible PDMS springs. This structure is a bump of stiff polyimide. After assembly the polyimide is shrunk by means of temperature treatment, which results in the release of the fixed seismic-mass. Furthermore, for the first design silicon is used as the basic material, whereas for the second design glass is used. An E-core electromagnet with outer dimensions of 3x3x3 mm^3 is designed (Chapter 4) and realized to actuate the seismic mass inside the mass-spring-damper system (Chapter 6).

Both realized Gyraccs show to perform as expected from the theory (Chapter 7). Phase measurements between the Coriolis vibration and the actuated vibration show a more stable representation of the experienced rate of turn than using the Coriolis amplitude. The single side actuated Gyracc proves to be a triaxial accelerometer with dual axis rate of turn sensing properties.

SAMENVATTING

Er is een behoefte aan sensorsystemen die de positie en oriëntatie van objecten bepalen zonder voortdurend gebruik te maken van referentiepunten uit de omgeving. Bij bepaalde geneeskundige toepassingen bestaat de wens om zo'n systeem uiteindelijk dusdanig klein te maken dat dit in de mens geïmplanteerd kan worden (Hoofdstuk 1).

Een, zich in de 3-dimensionale ruimte verplaatsend, object ervaart een combinatie van versnellingen in en rotaties rond zijn drie hoofdassen. De kleinste systemen die al deze 6 vrijheidsgraden kunnen meten zijn gebaseerd op het principe van massatraagheid. Zo'n systeem (Inertial Measurement Unit of IMU) bestaat uit verscheidene kleine sensoren en is in totaal enkele kubieke centimeters groot (Hoofdstuk 2). Dit is te groot om in het menselijk lichaam te implanteren. In dit proefschrift wordt een prototype van een sensing-element van enkele kubieke millimeters beschreven met IMU meeteigenschappen. Dit sensing-element bepaalt de bewegingen in zijn 6 vrijheidsgraden door het meten van massatraagheid aan slechts één seismische massa. Deze sensor wordt verder Gyracc genoemd, wat een samenvoeging is van de eerste drie letters van Gyroscoop en accelerometer.

De Gyracc is gebaseerd op de door Dr. Ir. J.C. Lötters ontwikkelde 3-assige versnellingssensor. Deze sensor bestaat uit een doosje met daarin een verend opgehangen kubische massa. Een op de massa uitgeoefende kracht zal tot een verandering in de afstand tussen de massa en de binnenzijden van het doosje leiden. De binnenkant van het doosje is voorzien van condensatorplaten, die in combinatie met een speciaal ontworpen capaciteit naar spanningsomzetter de positie van de massa ten opzichte van de binnenwanden van het doosje bepalen.

Door de verend opgehangen massa in trilling te brengen blijkt het ook mogelijk te zijn om rotatiesnelheden te meten (Hoofdstuk 3). Tijdens het ondervinden van rotaties loodrecht op de trilrichting van de massa zal de massa een Coriolis-kracht ervaren. Deze Coriolis-kracht resulteert in een trilling loodrecht op de opgelegde trilling. De amplitude en fase van deze Coriolis-trilling ten opzichte van de opgelegde trilling zijn een maat voor de draaisnelheid van de Gyracc.

De mechanische en de elektrische gevoeligheid van de sensor zijn geoptimaliseerd zodat de door de kleine Coriolis-krachten geïnduceerde trillingen een maximale amplitude bereiken. De niet lineaire polydimethylsiloxane (PDMS) veren en de niet lineaire eigenschappen van

capacitieve metingen compenseren elkaar gedeeltelijk. Dankzij dit fenomeen wordt de lineaire gevoeligheid voor versnellingen aanmerkelijk vergroot.

Simulaties tonen aan dat rotaties rond de drie hoofdassen van de Gyracc gemeten kunnen worden als de seismische massa een cirkelvormige beweging in het sensordoosje maakt. Deze cirkelvormige beweging wordt gerealiseerd met twee haaks op elkaar geplaatste actuatoren (Hoofdstuk 5).

De in de theorie beschreven inertiële sensor is gerealiseerd en opgebouwd uit een constructie van fijn mechanische, micro mechanische en in de cleanroom gefabriceerde onderdelen, alle met hun specifieke toleranties in de afmetingen. De mate van initiële compressie van de PDMS veren waarmee de massa is opgehangen is van grote invloed op de gevoeligheid van de Gyracc. Er zijn twee verschillende constructies ontworpen en gerealiseerd die beide de initiële compressie tot een vastgesteld maximum beperken (Hoofdstuk 6). In het eerste ontwerp is de afstand tussen de massa en de binnenzijde van de behuizing dermate groot, dat toleranties in de afmetingen van de massa en de behuizing nauwelijks invloed hebben op de initiële compressie van de PDMS veren. In het tweede ontwerp is de initiële compressie van de veren onafhankelijk van de toleranties in de afmetingen van de massa en de behuizing. In dit ontwerp bevindt zich een polyimide structuur naast de PDMS veren. Deze polyimide structuren bepalen de maximale compressie van de veren tijdens assemblage. Na assemblage wordt het geheel verhit waardoor de polyimide structuur krimpt en de massa vrij komt te hangen. In het eerste ontwerp is gebruik gemaakt van een silicium behuizing en in het tweede ontwerp van een glazen behuizing.

Om de massa in trilling te brengen is een elektromagneet met uitwendige afmetingen van 3x3x3 mm^3 ontworpen (Hoofdstuk 4) en gerealiseerd (Hoofdstuk 6).

De twee gerealiseerde Gyraccs gedragen zich zoals in de theorie beschreven is (Hoofdstuk 7). Metingen laten zien dat een Gyracc met een enkelzijdig geactueerde massa een 3-assige versnellingssensor combineert met een 2-assige rotatiesnelheidssensor is. Het faseverschil tussen de Coriolis-trilling en de magnetisch opgelegde trilling blijkt rotatiesnelheden beter te representeren dan uitsluitend de amplitude van het Coriolis-signaal.

DANKWOORD

Zoals een oosterse wijze ooit tegen me zei: “Bart, all writing starts with sitting down”, dat heb ik bij deze gedaan.

Ik heb mijn verblijf in de BIOS groep als zeer aangenaam ervaren. Dit was mede te danken aan: “Ik heb het druk, maar ik help je graag” Sjouke Hornstra. “Ik krijg die chip wel aan de praat en als er nog een druppel koffie in de pot zit, dan is ie van mij” Hans Albers. De uitvinder Ad Sprenkels. “Ik klaar dat klusje wel ff” fietser Björn Timmer. “Om dit probleem op te lossen zal ik es even aan de binnenkant van mijn ogen kijken” heer Erik Faber. “Alles moet tegelijk en jullie zijn allemaal zoooo saai” party animal Koen van Delft. “Meester Jager wat een mooie dag”, het zonnetje van de leerstoel Dorothee Hermes. “Ik ga echt niet lopen als ik het ook vanachter m’n PC kan doen” Sebastiaan Herber. “Zo’n meetinstrument hebben we nog wel ergens staan”, de man die alles op zijn ware waarde weet te schatten Ed Droog.

Door het van hogerhand op mijn kamer plaatsen van een aantal buitenlandse schonen kregen deze dames een op shocktherapie beruste inburgeringscursus. Eén van hen was de Amerikaanse ‘Holy Yoly’ Yolanda Fintschenko, zij was, onnavolgbaar, degene die het meeste werk in acht uur tijd kon verzetten. Daarnaast had ik het genoegen de Italiaanse Petra Mela op de kamer te hebben mogen ontvangen; zij is een vrouw pur sang. En dan is er nog mijn trouwste kamergenote, de Vietnamese jonkvrouwe, Dam Thi Van Anh (alias: Annie). Iedereen maar denken dat ze pas na twee jaar een beetje Nederlands kon verstaan NOT! Met haar oosterse wijsheden heeft ze mij een rijker mens gemaakt.

Geert Langereis liet me zien dat ook “normale” mensen promotieonderzoek kunnen doen. Hij was het lichtend voorbeeld dat liet zien dat je er, naast het promoveren, ook best een vrouw en twee kinderen op na kunt houden.

Alle nieuwe Bios-ers, alle niet Bios-ers aan het einde van de gang en de automotive mensen in Almelo wil ik bedanken voor hun interesse in mijn proefschrift. Met name Arjan Kölling voor zijn onverstoorbare interesse in de voortgang van het geschrevene, hij deed dit waarschijnlijk om zijn vriend Albert van den Berg een dienst te bewijzen. Verder wil ik alle mensen bedanken die ik voor de verdediging heb uitgenodigd, eenieder weet zelf wel wat zijn/haar bijdrage in het geheel geweest is.

Bovenstaande mensen zijn allemaal heel aardig geweest, maar hebben actief nul komma niets bijgedragen aan het voor je liggende proefschrift. Ter jullie informatie: het proefschrift is datgene dat voor dit dankwoord gedrukt staat. Lees het maar eens door, want daar leer je nog es wat van. Ter stimulatie heb ik in een van de hoofdstukken een verwijzing naar een heerlijk drankje staan. Diegene die ‘m als eerste vindt, krijgt deze van me.

Zo, het is hoog tijd om de mensen eens te bedanken die al die bladzijden hiervoor voorzien hebben van enige wetenschappelijke waarde, want ere wie ere toekomt.

Piet Bergveld en Wouter Olthuis als tweetal. Al tijdens mijn afstuderen wist ik dat jullie een eenheid zijn met een hoogwaardig intern differentieel. Jullie werken gescheiden, maar toch helemaal samen. Zelfs de overbrenging naar mijn mechanismen liep lekker soepel. Piet, dit is dan het laatste proefschrift waar jij het zaaien en oogsten van hebt mogen begeleiden. Dankzij jouw manier van begeleiden heb ik me kunnen ontwikkelen tot een vrij mens en daar ben ik je dankbaar voor. Wouter, zonder een onvertogen woord te hebben laten vallen heb jij mijn rapporten keer op keer bekeken en voorzien van opbouwend commentaar. Ik heb hier veel van geleerd. Naast dit talent ben je ook nog eens een leuk en goed mens.

Peter Veltink wil ik bedanken voor het vertrouwen dat hij in me had toen hij me naar Canada stuurde om wat hand- en spandiensten in een revalidatiecentrum te verrichten. Hier heb ik het gebrek aan kleine 3D-bewegingssensoren aan den lijve mogen ondervinden en kwam ik zo uiteindelijk bij biosensoren terecht.

Joost Lötters was mijn voorganger en had mijn taken al op voorhand vormgegeven. Bij zijn vertrek heeft hij veel nuttige onderdelen achtergelaten, waardoor ik een kickstart kon maken.

Met Emiel Dijkstra kon ik de elektrotechnische uitdagingen bespreken en de onverwachte meetproblemen terugvoeren naar basale elektronische effecten.

Henk Luinge kon me altijd precies vertellen waar ik welke vibratieformule kon vinden. Dat hij binnen 5 minuten de specificaties van het rotatieplatform doorberekende heeft veel indruk op me gemaakt. Regelmatig heb ik gedacht dat we onze projectverantwoordelijkheden moesten ruilen.

Mijn vrienden Sebastian Böhm en Heiko van der Linden verdienen een speciale aankondiging in dit geheel, bij deze.

Sebastian Böhm is de man die ogenschijnlijk alles kan, ach wat nou ogenschijnlijk, het is echt waar. Hij weet altijd precies waar de mensen te vinden zijn die je nodig hebt om een klus snel te klaren. Jouw invulling van het AIO-schap me heeft laten zien dat het is wat je er zelf van maakt. Dat middagpauzes zelfs nuttig besteed kunnen worden met een queste naar een bier dat het lekkerst smaakt bij kamertemperatuur is nog steeds van onschatbare waarde.

Heiko leek in eerste instantie veel op het type westerling waar m’n ouders me vroeger voor gewaarschuwd hadden; heel direct, geen blad voor de mond en van porselein had hij al helemaal nooit gehoord. Hij bleek een grote ongeslepen edelsteen, die in de loop der jaren flink gepolijst is. Het is echt ongelooflijk over hoeveel uiteenlopende onderwerpen hij het fijne weet. Vooral dankzij hem heb

ik de emotionele rollercoaster van het promoveren zonder permanente beschadiging doorstaan.

De studenten Wico Hopman, Thijs Engels, Boudewijn de Jong en Lodewijk van Hoesel, kwamen op het moment dat ik dacht "is dit 't nu wel helemaal?". Leuk dat Wico, Boudewijn en Lodewijk AIO zijn geworden, dan heeft 't in ieder geval niet aan mij gelegen. Lodewijk en Thijs zijn zelfs teruggekomen voor nog een opdracht. Aan Lodewijk is het te danken dat er een 20Sim model van de Gyracc is gemaakt, waarin zelfs rotaties worden gesimuleerd (H5). Aan Thijs is het te danken dat er een indeling in de jungle van de micromechanische gyroscopen is te maken (H2).

Jarmo Hietanen is acknowledged for bringing me in contact with Timo Veijola. Timo Veijola performed vibration simulations in the 3D mass spring damping model developed by himself, which is part of the Aplac simulation program (Appendix Chapter 3).

Leon Raanhuis heeft de verschillende elektromagneetconfiguraties doorgefloten, waardoor we tot een eenduidig antwoord konden komen over de mogelijkheden van elektromagnetische actuatie.

Johan Bomer en Ton Verloop ben ik zeer dankbaar voor hun strijdvaardige inzet voor het feilloos realiseren en in elkaar zetten van respectievelijk de cleanroom en de fijn-mechanische onderdelen. Door jullie inzet heeft het er nog van mogen komen dat er ook metingen aan de Gyracc zijn verricht.

Heiko van der Linden en Jeroen Schipper wil ik bedanken voor het willen optreden als mijn paranimfen.

Lieve Anita, eigenlijk behoor jij helemaal vooraan in het dankwoord te staan. Zonder jouw permanent liefdevolle ondersteuning had het voor je liggende er waarschijnlijk nooit gelegen.

Mijn schatjes Peter en Sophie wil ik via deze weg even de groetjes doen.

Bedankt allemaal! Oei, bijna vergeten: Elvis U2.

ABOUT THE AUTHOR

Berend Jan Kooi (1970), better known as Bart Kooi, studied Electrical Engineering at the University of Twente. In 1997 he started his PhD work at the biomedical sensors research group of Piet Bergveld and designed a miniature sensor which is able to measure movements in the free 3D space. In 2002 Bart Kooi started as a sensor design engineer at Texas Instruments Holland B.V. and is involved in the development of pressure- and gas sensors for the automotive industry.

B.J.Kooi@alumnus.utwente.nl